ARMADA

Applying Reliable Methods to Analyse and Deflect an Asteroid

M.F. van Amerongen
J. Anckaert
P.M. van den Berg
J.M. Fisser
J.M. Heywood
A. Hutan
T.A.J. Meslin
U.B. Mukhtar
A.S. Parkash
J. Ramos de la Rosa

Final Review
Design Synthesis Excercise

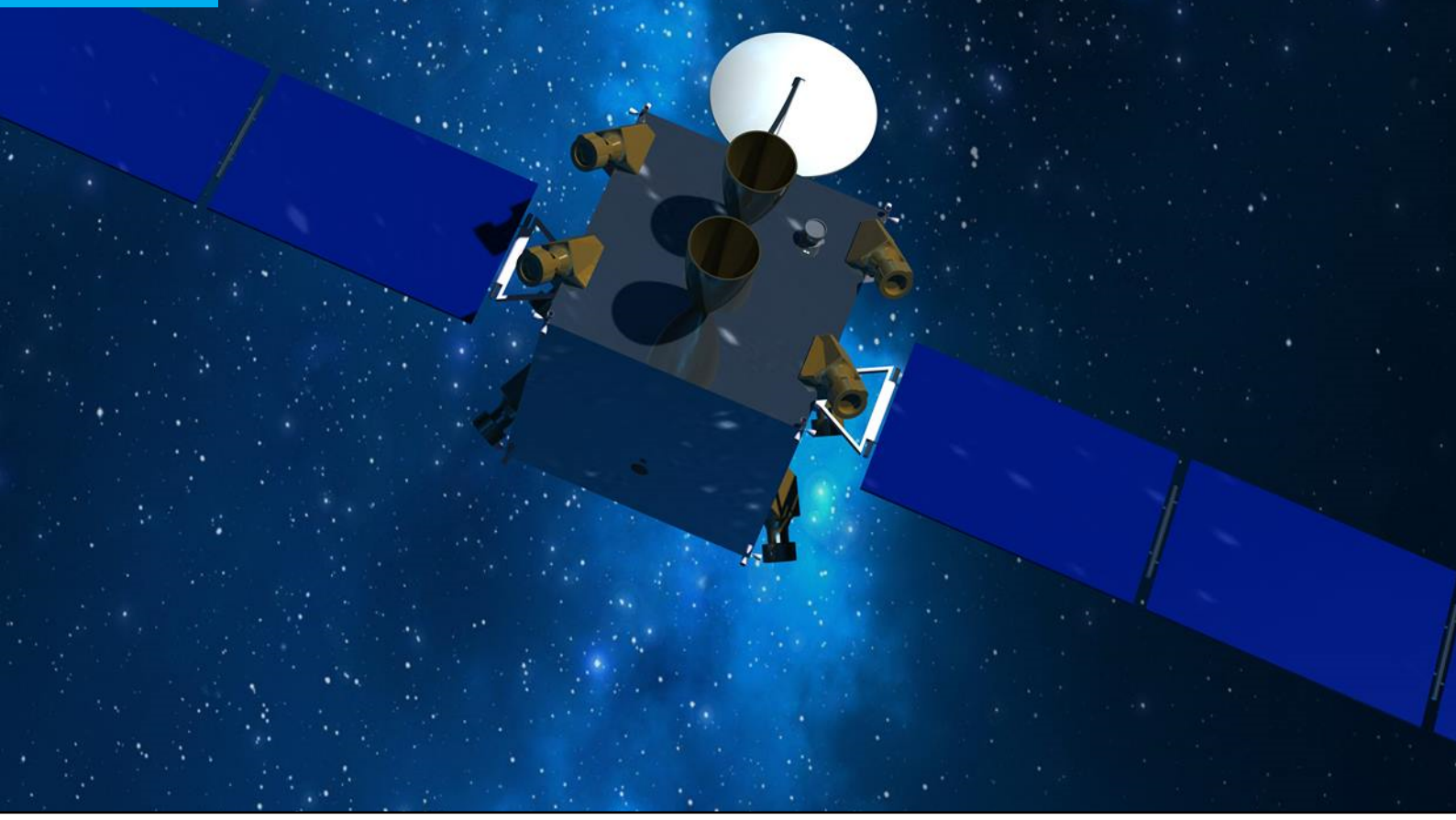

TU Delft Delft University of Technology

Aerospace Engineering

June 29, 2016

(This page is intentionally left blank.)

Mission to a Small Near-Earth Object

Final Review
Version 1.0

Delft University of Technology

Faculty of Aerospace Engineering

June 29, 2016

by

Group 03

M.F. van Amerongen	4295196
J. Anckaert	4304411
P.M. van den Berg	4207696
J.M. Fisser	4290089
J.M. Heywood	4219554
A. Hutan	4195744
T.A.J. Meslin	4220269
U.B. Mukhtar	4206363
A.S. Parkash	4278356
J. Ramos de la Rosa	4228596

Supervisors:	Dr.ir. E.J.O. Schrama	Astrodynamics and Space Missions
	Dr. A. Menicucci	Space Systems Engineering
	J.S. Bahamonde MSc.	Flight Performance and Propulsion

TU Delft Delft University of Technology

Lists of abbreviations

ADCS	Attitude Determination and Control System
APL	Applied Physics Laboratory (of the Johns Hopkins University)
APM	Antenna pointing mechanism
ARMADA	Applying Reliable Methods to Analyse and Deflect an Asteroid (mission name)
AU	Astronomical unit
BER	Bit error rate
BPSK	Bipolar phase-shift keying
C&DH	Command and data handling
CNR	Carrier-to-noise ratio
CPU	Central processing unit
DSE	Design Synthesis Exercise
DSN	Deep Space Network
DST	Deep space transponder
EIRP	Effective isotropic radiated power
ESA	European Space Agency
FEEP	Field-emission electric propulsion
HPBW	Half-power beam width
HRM	Hold-down and release mechanism
IR	Infrared
JPL	Jet Propulsion Laboratory
MMH	Monomethylhydrazine
NASA	National Aeronautics and Space Administration
NEAR	Near Earth Asteroid Rendezvous (NASA/APL mission)
NEO	Near Earth object
O/F	Oxidizer fuel ratio
OBC	On-board computer
OQPSK	Offset quadrature phase-shift keying
QPSK	Quadrature phase-shift keying
RPA	Rocket Propulsion Analysis v1.2 lite edition
RTG	Radioisotope Thermoelectric Generator
SNR	Signal-to-noise ratio
SSPA	Solid state power amplifier
TT&C	Telemetry, tracking & command
TWTA	Travelling wave tube amplifier

Nomenclature

a	Semi-major axis	km
A_s	Enlightened surface area	m^2
B	Bandwidth	Hz
C	Carrier power	W
c	Speed of light	$m\,s^{-1}$
C_{ch}	Channel capacity	s^{-1}
C_{req}	Capacity required	J
d	Distance	m
D_{cap}	Battery capacity degradation coefficient	-
D_{cell}	PV cell degradation coefficient	-
D_{inher}	Inherent degradation coefficient	-
DC_{ttc}	Duty cycle of TT&C	-
E	Eccentric anomaly	rad
e	Eccentricity	-
E_{cell}	PV cell efficiency	-
E_{dc}	Battery discharge efficiency	-
c	Frequency	s^{-1}
F	Force	N
F_g	Gravity force	N
F_{path}	Path loss factor	-
F_{pow}	Power factor for power system	-
F_{rel}	Reliability margin factor	-
G	Standard gravitational parameter	$m^3 s^{-2}$
g_0	Sea level gravitational acceleration on Earth	$m\,s^{-2}$
h	Angular momentum	$km^2\,s^{-1}$
i	Inclination angle	rad
I_{sp}	Specific impulse	s
L	Thruster moment arm	m
L_{DoD}	Limit on depth of discharge	-
M	Mean anomaly	rad
M_{ast}	Mass of Apophis	kg
m_{avg}	Average spacecraft mass	kg
MF	Margin factor	-
$\dot{m}_{ion}$	Ion thruster mass flow rate	$kg\,s^{-1}$
M_{prop}	Propellant mass	kg
N	Noise power	W
n	Mean motion	$rad\,s^{-1}$
n_{tr}	Number of thrusters	-
P	Orbital period	s
P	Power	W
P_{charge}	Battery charging power	W
P_{req}	Power required	W
P_{ttc}	Power required for TT&C	W
P_{ion}	Ion thruster power	W
P	Surface reflectance	-
r	Radius	km
R_i	Spacecraft-object(i) distance	m
r_{ast}	Radius of Apophis	m
S_0	Solar constant at 1AU	$W\,m^{-2}$
S_{in}	Solar input flux	$W\,m^2$
T	Temperature	K
T	Torque	N m
t	Time	s
T_{cycle}	Operational cycle duration	s
T_{redun}	Redundancy time duration	s
T_{req}	Thrust required (for Ion thrusters)	N
t_{dump}	Momentum dumping time	s
t_p	Deflection time	s
V	Absolute Velocity	$km\,s^{-1}$
v	Velocity component	$km\,s^{-1}$
$V_{e,ion}$	Ion thruster exhaust velocity	$m\,s^{-1}$
α_{exh}	Thruster exhaust plume angle	°
α_{mis}	Thruster misalignment angle	°
α_T	Thruster angle	°
γ	Flight path angle	rad
Δc	Distance center of mass and pressure	m
ΔX	Deflection distance	m
η_{ion}	Ion thruster efficiency	-
θ	Angle local vertical and z-axis	rad
θ	True anomaly	rad
θ	Pitch angle	rad
$\ddot{\theta}_{slew}$	Slew acceleration	$rad\,s^{-2}$
θ_{slew}	Slew angle	rad
λ	Wavelength	m
μ	Gravitational parameter	$m^3\,s^{-2}$
ϕ	Solar incidence angle	rad
φ	Roll angle	rad
ψ	Yaw angle	rad
Ω	Right ascension of ascending node	rad
ω	Argument of periapsis	rad

List of Figures

List of Tables

Preface

This report presents the Final design of the Design Synthesis Exercise (DSE) to 'Capture a Small Asteroid and Change its Orbit' at the Faculty of Aerospace Engineering at Delft University of Technology. The bachelor programme 'Aerospace Engineering' comprises several projects enabling students to explore aeronautics and space from different kinds of perspectives. The Design Synthesis Exercise serves as the conclusion to this programme. During this final project students integrate their previously obtained knowledge and skill to examine a specific design problem in groups of ten students for the duration of eleven weeks. This final report is the last in a series of four and documents the detailed design of the concept that was chosen in the mid-term report.

We would like to thank our tutor E.J.O. Schrama and coaches A. Menicucci and J.S. Bahamonde for their valuable and continuous support throughout the whole project. We would also like to acknowledge K. Kumar, T.B. Bahamon, D.M. Stam, R. Noomen, J.Bouwmeester and D. Dirkx for their valuable input.

M.F. van Amerongen (4295196)
J. Anckaert (4304411)
P.M. van den Berg (4207696)
J.M. Fisser (4290089)
J.M. Heywood (4219554)
A. Hutan (4195744)
T.A.J. Meslin (4220269)
U.B. Mukhtar (4206363)
A.S. Parkash (4278356)
J. Ramos de la Rosa (4228596)

Delft, May 2016

Summary

The probability of an asteroid impacting the Earth at any point in time is so small that it is almost negligible, but when looking at the consequences of such an impact, it is clear that the risk it poses is not. Given sufficient mass and velocity, an asteroid impact could potentially cause the extinction of the human race. Furthermore, although most celestial bodies do not have a high impact probability, interaction with planets they go close to can dramatically increase that probability.

Considering these destructive consequences, it is important for this issue to be addressed by the scientific community. As such, this report aims at designing the chosen deflection method in light of a technology demonstration. Doing such a demonstration would allow for a validation/rejection of the chosen concept, which would help in the design of any future deflection mission. It is necessary to note that the choice of concepts has already been restricted through a preliminary trade-off.

In order to effectively demonstrate the reliability and applicability of the deflection method, the Apophis asteroid is chosen, which not only poses one of the highest impact risks, but is also representative of a majority of Near Earth Objects. This will allow for an investigation into the effectiveness of the chosen method and its applicability for future missions. Once the target was selected, different design concepts were evaluated. From these, a final choice was made, the gravity tractor concept being selected as it was the design choice which better met the mission requirements. The subsystems were subsequently designed based on their performance constraints, and specific components were chosen. The launcher was selected based on a ΔV budget, obtained from modelling the transfer trajectory to Apophis. In addition, the final spacecraft layout was optimised depending on the size and temperature range of each component. Instruments with high power consumption were placed further apart, and components with higher masses where placed as close as possible to the spacecraft's central body-axis, in order to keep the centre of mass close to the z-axis. Next, a power and mass budget could be computed, and checked for compliance with the requirements. Moreover, a thorough design analysis was done to identify, quantify, and mitigate the risks of the mission so as to increase the reliability of the whole spacecraft. A cost estimation of the full system was also performed and checked for compliance against the allocated budget. Finally, the future design phases were discussed, evaluating the spacecraft's production plan, ground operations and logistics, as well as an extensive market analysis.

In conclusion, the Apophis asteroid was chosen for the mission from a trade-off of relevant Near Earth Objects during baseline. The gravity tractor was finally selected as the most optimal deflection method from a range of three options evaluated at Mid-term. The final design will have a final mass of 559 kg, with a maximum power required of $2308W$, and a total cost of $419M\$$. A preliminary market analysis was performed to identify possible customers (space agencies) and competitors (AIDA, Hayabusa Mk.2, and ARM). The subsystems were then preliminarily sized for the chosen concept. Furthermore, risk management and a sustainability analysis were carried out to check that the ARMADA mission will fulfil all its objectives without harming or endangering the future of humanity. Finally, the future phases of the design, such as the production plan, and operations and logistics, were described.

Contents

1. Introduction

Roughly 66 million years ago the era of the dinosaurs ended when an asteroid impacted the Earth, killing 75% of all plant and animal species on Earth. In 2013 the town of Chelyabinsk, Russia, was violently woken up by a meteorite entering the Earth's atmosphere, releasing the energy equivalent of 500 kilotons of TNT [41]. This event raised the question: Will we succumb to the same fate as the dinosaurs? With the potential consequences of an asteroid impact being enormous, the need to develop the technology required to deflect an asteroid is evident.

The aim of this project is to design a mission that demonstrates technology capable of reducing the risk of an NEO impacting Earth within the next 100 years. Or, in other words: "Applying Reliable Methods to Analyse and Deflect an Asteroid" or ARMADA, which was chosen as the name for the mission. The asteroid 99942 Apophis has been chosen to be the subject of this demonstration, since it has an orbit quite similar to Earth's and is also amongst the asteroids posing the highest risk to Earth according to NASA [42]. Moreover, Apophis has been studied extensively from Earth, which means that more information is available about it in comparison to other asteroids. Therefore the risk of the mission is reduced.

The purpose of this report is to document the final, but still preliminary, design of the ARMADA mission and give an overview of the design process between the mid-term and final review. The gravity tractor concept was chosen to perform the deflection objective and a scientific payload is included in order to have the ability to investigate the characteristics of Apophis. The different subsystems will be worked out in more detail and a final layout of the mission will be given. To reach the objectives, the ARMADA team used the following process: First of all, an initial mass estimation for the complete spacecraft, including dry mass and propellant mass, was determined. This mass is iterated, taking into account the different subsystems in order to obtain a final mass estimate for the spacecraft, which includes all individual masses of the subsystems. Models or simulations were made for the complex computations, and their results were used for the subsystem sizing and component selection. An overall sustainable approach was taken throughout the design process. Finally, an extensive mission analysis, including market and sensitivity analysis, and risk assessment, was carried out.

The structure of the report is as follows: Chapter 2 presents the overall mission overview including a timeline and functional analysis of the mission. Then, the astrodynamics are handled in Chapter 3. In this chapter, the transfer trajectory and different orbits as well as launcher selection are given. The next chapter gives an elaboration on the gravity tractor concept including a preliminary mass estimation for the spacecraft. Chapter 5 handles the scientific part of the mission, which consists of different scientific objectives that the ARMADA mission was set to perform and the instruments which will accomplish those objectives. Chapters 6 to 12 elaborate on the detailed subsystem designs, including the propulsion, ADCS, C&DH, communications, thermal control, power and structures systems. Each of these include the set requirements for the subsystems, used methods for the sizing and final results of the specific design process. After all the subsystems are sized and their components are chosen, an overall configuration of the spacecraft can be produced, which can be found in Chapter 13. This chapter also concludes the technical part of the report an design process. Chapter 14 elaborates on the design analysis, which includes the risk management, RAMS and sensitivity analysis, sustainable approach and compliance matrix. A final cost estimation for the ARMADA mission is given in Chapter 15. Then, as the ARMADA design is still in its early development phase, a chapter including all proposed future activities, such as production or development logic is included. This is Chapter 16. Finally, a concise conclusion and some further recommendations for the future are included in Chapter 17.

2. Mission Overview

2.1 Asteroid selection

In order to demonstrate the technology of deflecting an asteroid, an appropriate asteroid for deflection was to be found. A number of asteroids were selected and a trade-off was performed to find the most suitable one. One of the requirements for the mission was that it must deflect an asteroid which may pose a risk to Earth within the next 100 years. This directly omitted a large number of asteroids from NASA's asteroid database [42]. The remaining asteroids were traded off based on their impact danger, size, and relative velocity. From this trade-off the asteroid 99942 Apophis came out as the most appropriate for the proposed mission. The asteroid selection process is explained more elaborately in the baseline report [43].

2.2 Mission timeline

The ARMADA mission will be separated into six phases, namely: Launch and preparation, Transfer, Injection, Observation, Deflection and, lastly, Disposal. The duration of these phases and their progression in time is illustrated in Figure 2.1. The deflection time is dependent on the mass of Apophis, as for a minimum mass, the deflection is minimum. The observation time is the minimum time needed.

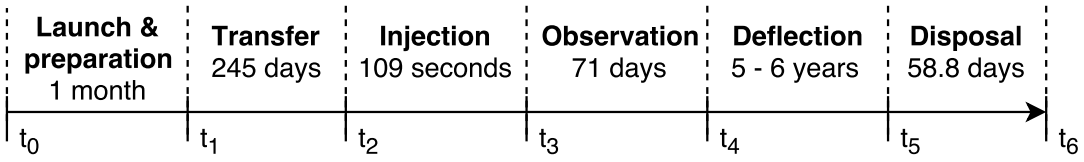

Figure 2.1: Mission timeline

It is necessary to note that the launch date, corresponding to t_1 is 21/04/2021. This represents the most favourable launch window for the time-frame above, as will be explained in Chapter 3. The disposal time is estimated by calculating the time it would take the ARMADA spacecraft to impact Apophis when its engines get turned off, through the use of Newton's law of universal gravitation. The observation period required is 71 days, however the phase is planned to last for 6 months so as to account for any additional observations of elements of interest. This phase will itself be separated into sub-phases.
A more detailed explanation of the observation, transfer and deflection phases will be shown in Section 8.2, where the data rates for the different segments are also explained.

2.3 Functional analysis

In this chapter, a functional analysis of the system is carried out in order to give a better overview of what the mission encompasses during its lifetime. Two different methods are used to analyse the functions of the ARMADA mission, a functional flow diagram and the functional breakdown. In this manner, the functions are first illustrated in the order they are performed, then the loops and common elements are taken out to create the breakdown diagram.

A functional flow block diagram represents the functional flow of the system functions from the functional breakdown diagram in a graphical way. As opposed to the breakdown diagram, it is time-sequenced. It gives a step-by-step representation of the system functions. The diagram is separated into several levels. From top level, each step downwards details the functions more. Three levels of detail are shown Figure 2.2. An important thing to mention is that for a diamond node, an arrow coming out vertically corresponds to the negative option, whilst arrows emerging horizontally correspond to a positive response. Furthermore, it is necessary to note that, for the observation function that is detailed in Figure 2.2, the data produced by these sensors will always be stored before the other functions occur, following the flow described for storing data.

The idea behind the functional breakdown structure seen in 2.3 is to display all the functions composing the system in an AND tree. The functions present here are solely the functions of the system itself, including the subsystem functions, of course. There is no sequence of events in this structure - the functions are simply listed. The order in which the functions are mentioned bares no relevance to the order in which they are executed.
It is necessary to note that Figure 2.3 illustrates the specific functions of the spacecraft itself. This means that the aim of the mission is to have all commands and functions fully automated, with commands from the ground station being issued only when external input is necessary. The only ground station specific commands are signalling the beginning and end of the observation and deflection phases.

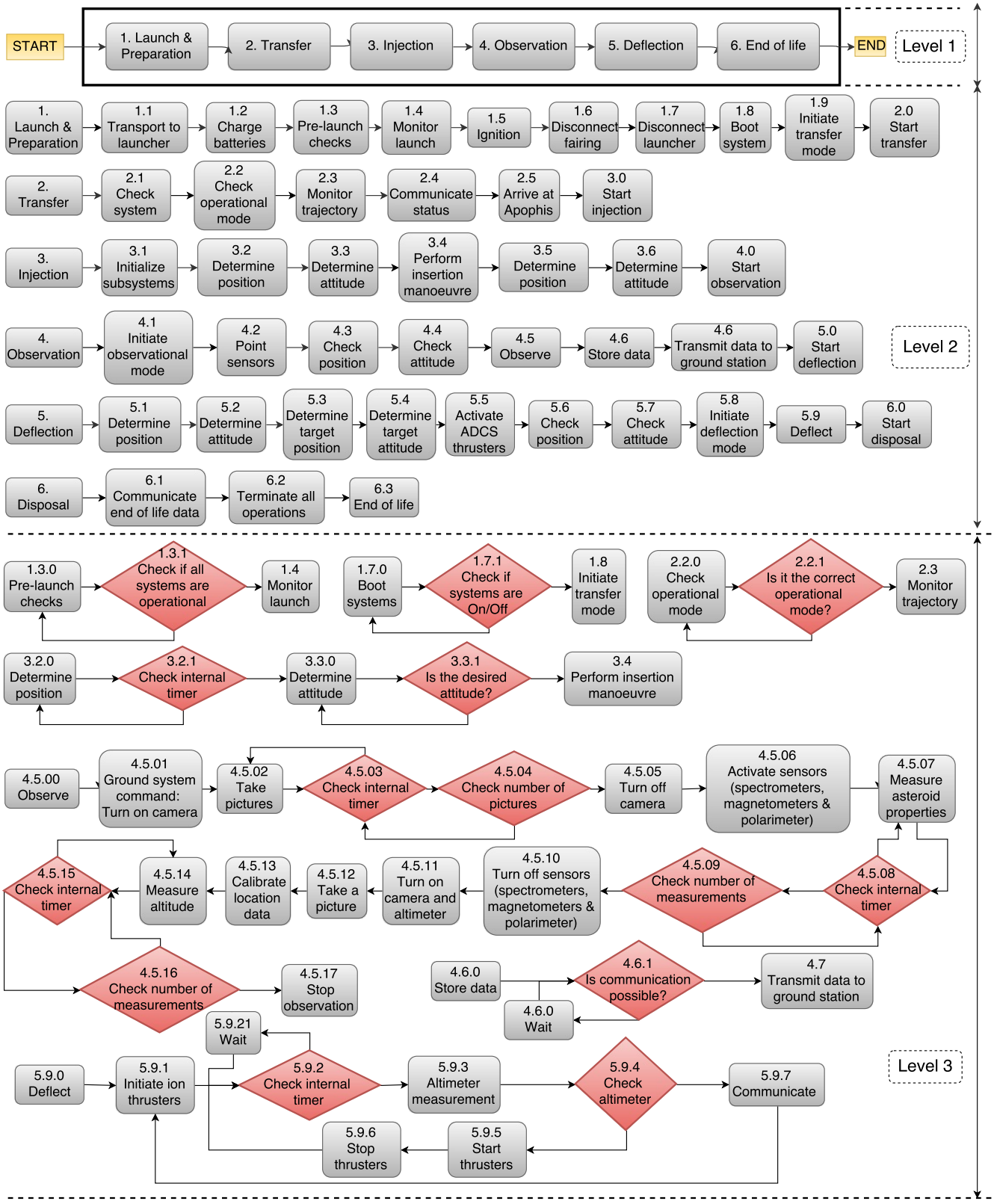

Figure 2.2: Functional flow block diagram

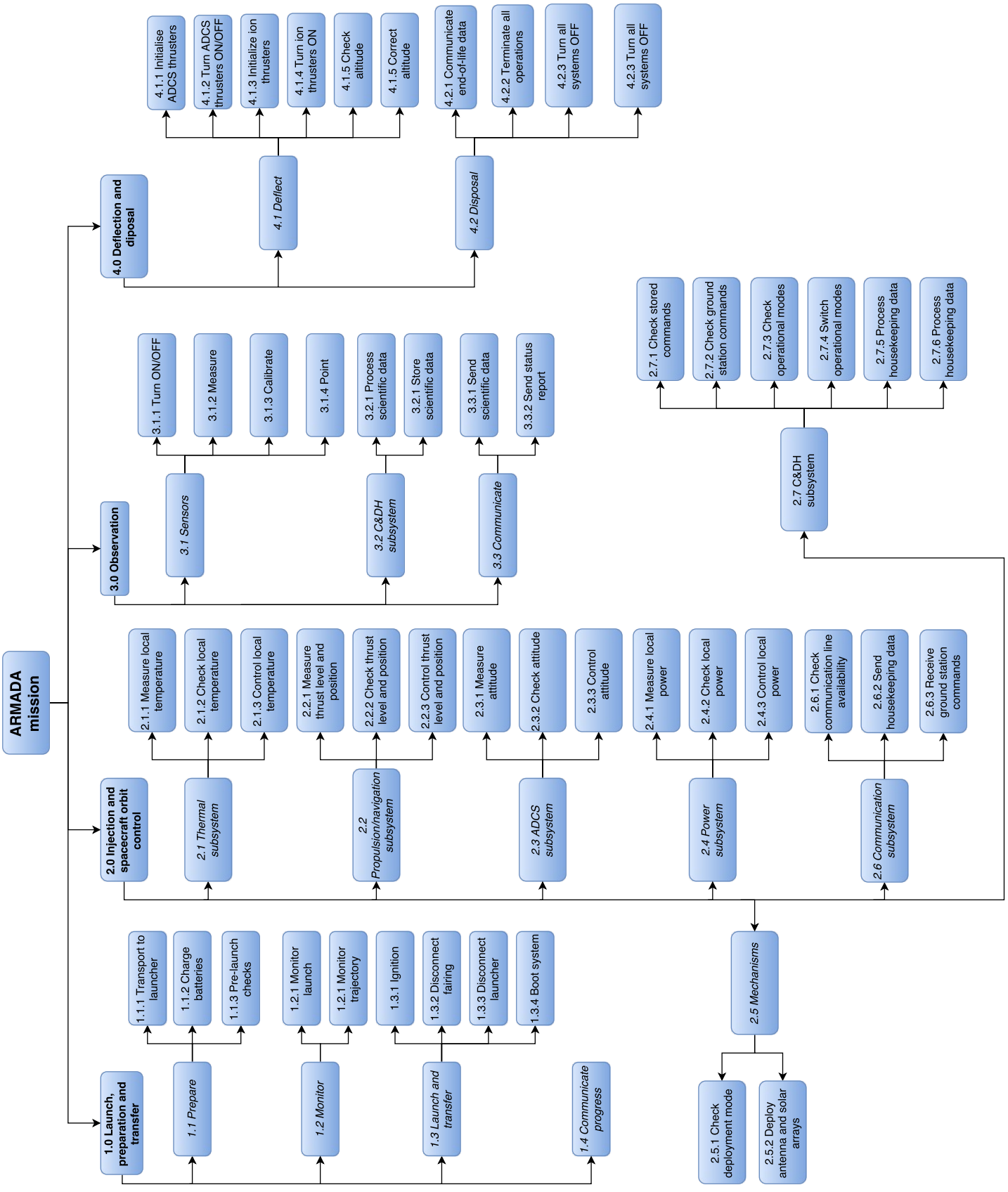

Figure 2.3: Functional breakdown structure

3. Astrodynamics

In this chapter, the astrodynamical aspects of the mission are discussed. This includes the method used to simulate the positions of the bodies of interest relative to a selected frame, and to find the trajectory from Earth to the asteroid. In the end, this analysis is mainly performed to find the velocity change required to reach the asteroid, and to investigate the different environments during the mission.

3.1 Model of the solar system

In this section, an overview of the coordinate system is given, as well as the position and velocity determination of orbiting bodies in this system.

Coordinate system

In order to determine a trajectory from a point to a point, the first step is to choose a coordinate system. This can be either in Cartesian or polar coordinates and is dependent on the problem to be solved. In the model used here, the main model will be described using a heliocentric Cartesian coordinate system. This is a conservative choice, as an orbit of any body around another significantly larger one can be described by six Kepler elements. These elements are mainly dependent on the shape of the orbit, and the mass of the orbited body. In this case, the main orbits of interest are that of Earth, Venus, and the asteroid Apophis, which all orbit the Sun. When describing the orbits of planets, the first important element is the distance to the center or orbited body, and the second is the variation of this distance. These are described by the semi-major axis or a and eccentricity for elliptical orbits, for which the eccentricity e is between 0 and 1. The semi-minor axis or b is used for relations between the angles [1], but in principle depends on the first two. These elements, together with the true anomaly θ determine the location of the orbiting body in two dimensions.
Furthermore, it is necessary to choose a reference plane. In this case, the ecliptic plane is chosen, in which the orbit of the Earth is. The other orbit paths have a certain inclination i with reference to this plane. The coordinate system is thus a Cartesian system based on the heliocentric ecliptic plane, or in other words: The orbit of the Earth lies in the z = 0 plane. The other orbits can then be identified by the location at which their path cross this plane, and then the relative location of their closest point to the Sun, also called perihelion. The first is described by the right ascension of the ascending node, or Ω. The latter is described by the argument of periapsis, or ω. The final element then identifies the location on this orbit at a certain time, and can be expressed in multiple ways. In this case, the mean anomaly at epoch M_0 is chosen, as information provided by NASA generally contains this last element. This is the angle of position a body on a circular orbit about the orbited body in the orbit plane would have at the same time as the considered body in the eccentric orbit. Due to the circular reference orbit, this angle will travel with a constant speed, the mean motion n [1].
This last element allows for determining the position of a body on a certain point in time. To express this point in time, the time elapsed since a certain reference time is used. In the presented model, the J2000 Julian Day system is used. In this system, every Julian day covers exactly 24 hours, which take 3600 seconds. The reference time used is at noon on the first of January, 2000. This time is set to have an exact value of 2451545.0 Julian Days [1].

Kepler orbit equations

In the orbital plane, the orbit can be described with several equations. The first is expressed in Equation 3.1, where the radius r or distance to the focus point is described in terms of the varying true anomaly θ. This equation is one of the mathematical forms of Kepler's first law [1]. The absolute velocity can then be described by the Vis Viva equation, seen in Equation 3.2, where $\mu = GM$ is the standard gravitational parameter, or the gravitational constant G times the mass of the orbited body M [44, 1].

$$r = \frac{a(1-e^2)}{1+e\cos\theta} \tag{3.1}$$

$$\frac{V^2}{2} = \frac{\mu}{r} - \frac{\mu}{2a} \tag{3.2}$$

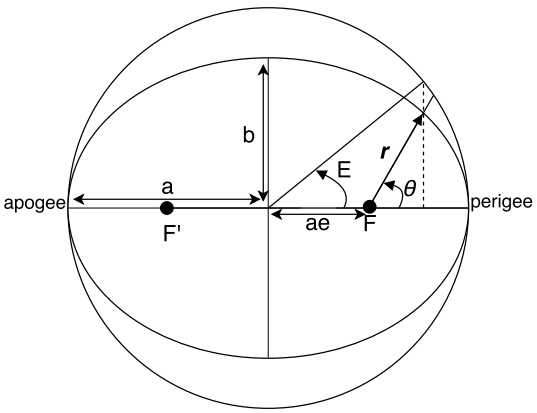

Figure 3.1: The Kepler orbital elements in two dimensions, showing r, θ, a, b, e, and E

As mentioned before, the position in the orbit on a certain time can be evaluated from the mean anomaly, which is found at a time t using

Equation 3.3 [1], where t_0 is the starting epoch.

$$M = M_0 + n(t - t_0) \tag{3.3}$$

For the elliptic orbits considered here, this mean anomaly can be expressed in terms of the eccentric anomaly E, with is the angle between the center of the orbit, or the intersection of the semi-major and semi-minor axis, and the projected point on the circle. The eccentric anomaly can be found using Equation 3.4. However, no simple analytical solution is possible. Therefore an iterative function can be used to calculate the eccentric anomaly from the mean anomaly, Equation 3.5 is used for the model [44, 1], which is derived by using Newton's method. It converges for orbits with low eccentricities, as the ones considered, as well as the desired transfer trajectory. The value of the mean anomaly is used as a first guess for the eccentric anomaly. Other methods include using power series, or using Bessel functions [1].

$$M = E - e \sin E \tag{3.4}$$

$$E_{i+1} = E_i + \frac{M - E_i + e \sin E_i}{1 - e \cos E_i} \tag{3.5}$$

If the eccentric anomaly is found, the true anomaly θ can be found using Equation 3.6.

$$\tan \frac{\theta}{2} = \sqrt{\frac{1+e}{1-e}} \tan \frac{E}{2} \tag{3.6}$$

Using Equation 3.1 the relative position in the plane is thus fully determined. To describe the motion in Cartesian coordinates, the two-dimensional position vector as seen in Equation 3.7 can be used.

$$\begin{bmatrix} x \\ y \\ z \end{bmatrix} = \begin{bmatrix} r \cos \theta \\ r \sin \theta \\ 0 \end{bmatrix} \tag{3.7}$$

In-plane Velocity calculation

From the location and orbit elements, the velocity components can be found. The first important notice is that the angular momentum h of an orbit is constant in any (stable) orbit. This angular momentum can be found using Equation 3.8 [1], where $r_p = a(1 - e)$ is the radius at periapsis. Using again the polar coordinates in the orbit plane, the velocity can be expressed in two components, v_r and $v_\perp$, the radial and tangential velocity, respectively. These can be computed using Equation 3.9 [1]. The Cartesian components of the velocity vector can be found using Equation 3.10.

$$h = \sqrt{\mu \, r_p (1 + e)} \tag{3.8}$$

$$\begin{bmatrix} v_r \\ v_\perp \end{bmatrix} = \begin{bmatrix} \frac{\mu}{h}(e \sin \theta) \\ \frac{\mu}{h}(1 + e \cos \theta) \end{bmatrix} \tag{3.9}$$

$$\begin{bmatrix} v_x \\ v_y \\ v_z \end{bmatrix} = \begin{bmatrix} \cos \theta v_r - \sin \theta v_\perp \\ \sin \theta v_r + \cos \theta v_\perp \\ 0 \end{bmatrix} \tag{3.10}$$

From two to three dimensions

If the location at any time in an orbit is known, it is also possible to describe the locations relative to other orbiting bodies. As described before, this can be done by using the three angles Ω, ω and i. In essence, this transformation can be described as three subsequent rotations of the axis system. In this model, using these transformation matrices any point in the orbit can be described in the heliocentric ecliptic J2000 coordinate system. The in-plane coordinate system is denoted by $\bar{x}\bar{y}\bar{z}$, while the heliocentric ecliptic coordinate system is denoted by XYZ, where the X axis points at the Vernal Equinox Υ. The transformation matrices for the subsequent rotations are based on the Euler angles. These are an angle Ω about the z-axis, an angle i about the x-axis and an angle ω about the z-axis, respectively. The angles are defined to be positive for transformation from XYZ to $\bar{x}\bar{y}\bar{z}$, however, thus the transformation is reversed and negative angles are used. The final transformation matrix of the position and velocity vectors from any orbital plane, for example that of Apophis, to the heliocentric plane is calculated using 3.11. The resultant matrix is shown in Equation 3.12 [1]. The product of this matrix and the in-plane vector of an orbit then results in a vector in the heliocentric ecliptic coordinate system.

$$\boldsymbol{Q}_{\bar{x}X} = \boldsymbol{R}_z(-\Omega)\boldsymbol{R}_x(-i)\boldsymbol{R}_z(-\omega) \tag{3.11}$$

$$\boldsymbol{Q}_{\bar{x}X} = \begin{bmatrix} \cos\Omega\cos\omega - \sin\Omega\sin\omega\cos i & -\cos\Omega\sin\omega - \sin\Omega\cos\omega\cos i & \sin\Omega\sin i \\ \sin\Omega\cos\omega + \cos\Omega\sin\omega\cos i & -\sin\Omega\sin\omega + \cos\Omega\cos\omega\cos i & \cos\Omega\sin i \\ \sin\omega\sin i & -\cos\omega\sin i & \cos i \end{bmatrix} \tag{3.12}$$

Used parameters

The parameters used in the model are shown in Table 3.1, and provided by the JPL database [9] and the planetary data, both from NASA [10]. In the model, all angles are converted to radians. As some values for Apophis have an uncertainty in the order of 10^{-6}, they are rounded here to 5 significant digits. The transfer orbit will be elaborated on with the results, see Section 3.3.

Table 3.1: Orbit elements [9, 10]

Element	Sym.	Unit	Earth	Venus	Apophis	Transfer
Semi-major axis	a	AU	1.0000	0.72333	0.92228	0.94284
Eccentricity	e	[-]	0.016710	0.0067732	0.19108	0.16933
Inclination	i	°	0.00005	3.3947	3.3313	3.1955
Long. of ascending node	Ω	°	-11.261	76.681	204.46	210.51
Long. of periapsis	ω	°	102.94719	131.538	126.39	123.07
Mean anomaly	M_0	°	100.46	181.98	215.54	-105.62
Epoch	t_0	JD	2451545.0	2451545.0	2454441.5	2459325.5

3.2 Trajectory

Now that the position at every time is known, it is possible to determine a trajectory from Earth to Apophis. Theoretically, the most efficient trajectories arise by means of exactly half of an elliptic transfer orbit, that starts from its departure orbit at its periapsis and ends in an apoapsis in the arrival orbit, or vice versa. This is known as a Hohmann transfer. However, the orbits of Earth and Apophis differ quite significantly, especially considering the relative inclination angle of about 3.33°as seen in Table 3.1.

In addition, in some deep space missions, flybys are used to increase the orbital energy. However, such manoeuvres are generally done to rendezvous with objects that are either further away from the Sun, or closer. It is true that the orbit of Apophis is generally closer to the Sun, but in this report the orbits of Earth and Apophis are not considered to differ enough for a flyby to be of interest. However, in future design phases this possibility may be investigated in case the used approach is too inefficient.
The following approach is used to find the transfer trajectory. Based on the technique of patched conics, the transfer orbit is calculated from three inputs, which are known from the solar system model. These are the position vector at departure time $\boldsymbol{r}_1$, the travel time Δt, and the position vector at arrival time $\boldsymbol{r}_2$, where the last one follows from the first and second. This problem is known as Lambert's problem, shown in Figure 3.2 [1], where the $\hat{I}\hat{J}\hat{K}$ frame is the heliocentric ecliptic in the model, with the X-axis pointing to the Vernal Equinox.

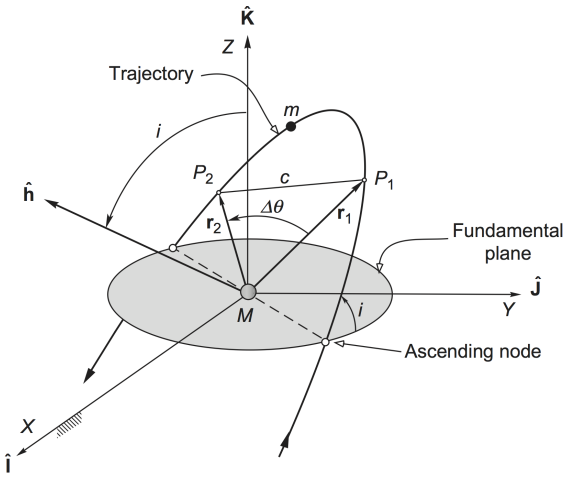

Figure 3.2: Lambert's problem, describing the path from one point to another in a set time [1]

Considered methods

Several methods to solve the Lambert's problem exist, for example a method by Gooding [45]. However, the method used in this model is the one described by Howard Curtis in [1], and is based on the works of Bate, Mueller and White (1971) and Bond and Allman (1996). An iterative method is used which includes the Kepler equations rewritten for the universal anomaly χ. These equations then hold for all different Kepler orbits, i.e. circular, elliptic, parabolic and hyperbolic. However, for the transfer trajectory, only elliptic orbits are considered as they generally result in lower velocity changes. The outcome of the solution of this method is two velocity vectors at

the two input positions.

Assumptions

The following assumptions are made in the calculation of the needed velocity changes.

- **The orbits of the bodies stay constant.** - This means that, although the gravitational attraction of all bodies in the solar system will constantly alter the path of the asteroid, this is not taken into account. Furthermore, the orbits of the planets are also taken to be constant. This assumption decreases the complexity of the problem.
- **The departure and arrival position vectors coincide with the location of the Earth and Apophis at that time** - In reality, the departure position will be at the intersection of the hyperbolic escape trajectory and the sphere of influence of Earth. The same hold for the arrival position at Apophis. This assumption will have only a minor influence on the accuracy of the trajectory. In addition, the focus of the simulation is to obtain the ΔV needed for the mission, which will not be significantly influenced by this assumption.
- **In the orbits, the spacecraft is only attracted by the body with the highest gravitational attraction** - When in the sphere of influence of Earth or Apophis, the spacecraft is only attracted by that body. Outside these during the transfer trajectory, it is only attracted by the Sun. In addition, the attraction of the Moon or other bodies in the Solar system is neglected.
- **The mass of the spacecraft is neglected** - In reality, a small mass actually orbits the barycenter together with the large orbited body. However, this is neglected, thus the barycenter is at all times at the center of mass of the orbited body.

A short description with the main idea of solving the Lambert's problem follows.

Approach

From the position vectors, the travelled angle along the transfer orbit $\Delta\theta$ from $\boldsymbol{r}_1$ to $\boldsymbol{r}_2$ can be calculated using Equation 3.13, with r_1 and r_2 the absolute radii.

$$\cos\Delta\theta = \frac{\boldsymbol{r}_1 \cdot \boldsymbol{r}_2}{r_1 r_2} \tag{3.13}$$

The orbit can be travelled in two ways, namely using a prograde and retrograde trajectory. For prograde trajectories, $i \in [0, 90]^\circ$, and for retrograde trajectories, $i \in [90, 180]^\circ$. This can be determined from Equation 3.14. For this mission, the inclination should not be changed significantly in order to find the least velocity change possible. As both the Earth's and Apophis' orbits are prograde, the considered trajectory should be prograde as well to minimise the velocity change.

$$(\boldsymbol{r}_1 \times \boldsymbol{r}_2)_Z = r_1 r_2 \sin\Delta\theta \cos i \tag{3.14}$$

If $(\boldsymbol{r}_1 \times \boldsymbol{r}_2)_Z$ is positive, then the inclination $i \in [0, 90]^\circ$, and $\Delta\theta$ is as calculated in Equation 3.13. However, if is negative, the new value for $\Delta\theta$ is $2\pi - \Delta\theta$.
The calculation of the velocities is based on the Lagrange coefficients f, g, and their time derivatives, which are unique for each set of orbit elements, and describe the velocity components at any point in time. This can be done using the relations seen in Equation 3.15.

$$\boldsymbol{v}_1 = \frac{1}{g}(\boldsymbol{r}_2 - f\boldsymbol{r}_1), \qquad \boldsymbol{v}_2 = \frac{1}{g}(\dot{g}\boldsymbol{r}_2 - \boldsymbol{r}_1) \tag{3.15}$$

These Lagrange coefficients are independent of the eccentricity, and can be determined as a function of the universal anomaly χ and z. The equations include two Stumpff functions, $S(z)$ and $C(z)$, which are defined by the infinite series as seen in Equation 3.16. Through iteration, a positive value of z can be determined for one problem, where the value for which the function $F(z)$ is zero is found. If z is positive, the trajectory is elliptic, while it is hyperbolic for negative values of z. The procedure iterates by calculating new values of z, until the change is lower than a certain set accuracy. This calculation is done using Equations 3.17a, 3.17b, and 3.17c. Note that A is entirely dependent on input, $y(z)$ is dependent on both the input and the value of z, while the others only on the value of z. The iteration to find the value of z for which $F(z)$ is zero is based on Newton's method, as seen in Equation 3.18. The derivation is however rather extensive and fully covered by Howard Curtis [1].

$$S(z) = \sum_{k=0}^{\infty}(-1)^k \frac{z^k}{(2k+3)!}, \qquad C(z) = \sum_{k=0}^{\infty}(-1)^k \frac{z^k}{(2k+2)!} \tag{3.16}$$

$$A = \sin\Delta\theta\sqrt{\frac{r_1 r_2}{1-\cos\Delta\theta}}, \qquad y(z) = r_1 + r_2 + A\frac{zS(z)-1}{\sqrt{C(z)}} \tag{3.17a}$$

$$F(z) = \left[\frac{y(z)}{C(z)}\right]^{3/2} S(z) + A\sqrt{y(z)} - \sqrt{\mu}\Delta t \tag{3.17b}$$

$$F'(z) = \begin{bmatrix} \left[\frac{y(z)}{C(z)}\right]^{3/2}\left(\frac{1}{2z}\left[C(z) - \frac{3}{2}\frac{S(z)}{C(z)} + \frac{3}{4}\frac{S(z)^2}{C(z)}\right]\right) + \frac{A}{8}\left[3\frac{S(z)}{C(z)}\sqrt{y(z)} + A\sqrt{\frac{C(z)}{y(z)}}\right] & (z \neq 0) \\ \frac{\sqrt{2}}{40}y(0)^{3/2} + \frac{A}{8}\left(\sqrt{y(0)} + A\sqrt{\frac{1}{2y(0)}}\right) & (z = 0) \end{bmatrix} \tag{3.17c}$$

$$z_{i+1} = z_i - \frac{F(z_i)}{F'(z_i)} \tag{3.18}$$

Retrieving orbital parameters for the transfer trajectory

Additionally, when solving Lambert's problem for a given departure date and travel time, the transfer trajectory orbital elements can be calculated from the departure and arrival velocities using the following equations. This is done using Equations 3.19a and 3.19b [1] for the angular momentum vector $\boldsymbol{h}$, the node vector $\boldsymbol{N}$, the eccentricity vector $\boldsymbol{e}$, and the four angles i, Ω, ω and θ. Using the equations from Section 3.1 the mean anomaly M_0 can be calculated, which is the position at departure. Finally, the semi-major axis a is calculated using Equation 3.2. Note that bold font symbols are vectors, while normal font are absolute value scalars, e.g. $r = |\boldsymbol{r}|$. A subscript x, y or z denotes the respective component of that vector.

$$\boldsymbol{h} = \boldsymbol{r}\times\boldsymbol{v}, \qquad \boldsymbol{N} = \hat{\boldsymbol{K}}\times\boldsymbol{h}, \qquad \boldsymbol{e} = \frac{1}{\mu}\left(\left(v^2 - \frac{\mu}{r}\right)\boldsymbol{r} - (rv)\boldsymbol{v}\right) \tag{3.19a}$$

$$i = \cos^{-1}\frac{h_z}{h}, \qquad \Omega = \cos^{-1}\frac{N_z}{N}, \qquad \omega = \cos^{-1}\frac{\boldsymbol{N}\cdot\boldsymbol{e}}{Ne}, \qquad \theta = \cos^{-1}\frac{\boldsymbol{e}\cdot\boldsymbol{r}}{er} \tag{3.19b}$$

In addition, the angles must be inverted if certain components of the vectors hold a negative value. This can be implemented using conditional statements as follows. If $N_y < 0$, then take $\Omega = 2\pi - \cos^{-1}\frac{N_z}{N}$. If $e_z < 0$, then take $\omega = 2\pi - \cos^{-1}\frac{\boldsymbol{N}\cdot\boldsymbol{e}}{Ne}$. If $\boldsymbol{r}\cdot\boldsymbol{v} < 0$, then take $\theta = 2\pi - \cos^{-1}\frac{\boldsymbol{e}\cdot\boldsymbol{r}}{er}$ [1].

3.3 Results

The final model was programmed in MATLAB and is visualized in a flowchart, seen in Figure 3.3. Only the basic functionality is shown, but the functions are all based on the equations given in the previous sections. From the outputs, various plots have been generated. In addition, the model output consists of the position and velocity data of Earth, Venus and Apophis, for every day from a given starting date. This can be seen in a three-dimensional view in Figure 3.5, where the orbits are plotted, including the position of the planets and asteroid at the 21st of April, 2021. The transfer orbit is also shown, which is selected based on the porkchop plots. To show the relative inclinations, a side view of the plot is shown in Figure 3.6.

From the velocity vectors at departure and arrival, an estimate of the necessary velocity change to reach this orbit can be given. The change is taken to be the absolute difference between the velocity vector of Earth at departure and the departure velocity vector, added to the absolute difference between the velocity vector of Apophis and the arrival velocity vector. To find an optimal combination of both the departure date and travel time for the lowest velocity change, a so-called pork-chop plot is generated. In this plot, regions with favourable transfer windows can be identified. In addition, a low relative arrival velocity is strongly preferred, as this would decrease the needed propellant for the orbit injection manoeuvre. For the calculation of the velocity changes, circular parking orbits at Earth and Apophis are assumed, at a height of 300 km and 1500 m, respectively. By plotting a whole region of departure dates between 2016 and 2026, it was found that a particular area of interest lies in the region of 100 to 120 days from the reference date, which is the first of January, 2021, for travel times between 200 and 250 days. This region is shown in Figures 3.7 and 3.8. It followed that the most favourable travel time is 245 days with the departure date at the 21st of April, 2021.

The transfer orbit parameters for the selected departure date and travel time can be seen in Table 3.1. The ΔV budget is then determined as shown in Table 3.2. The starting point is assumed to be a circular parking Low-Earth orbit (LEO), at a height of 300 km. The arrival point is assumed to be a circular parking orbit about Apophis, at a height of 1500 m. The velocity increments are visualised in Figure 3.4, where the sphere of influence (SOI) is indicated for both departure and arrival bodies. This is only a schematic presentation and is not to scale. The velocities for these orbits are calculated using Equation 3.2, where the semi-major axis is equal to the radius for circular orbits.

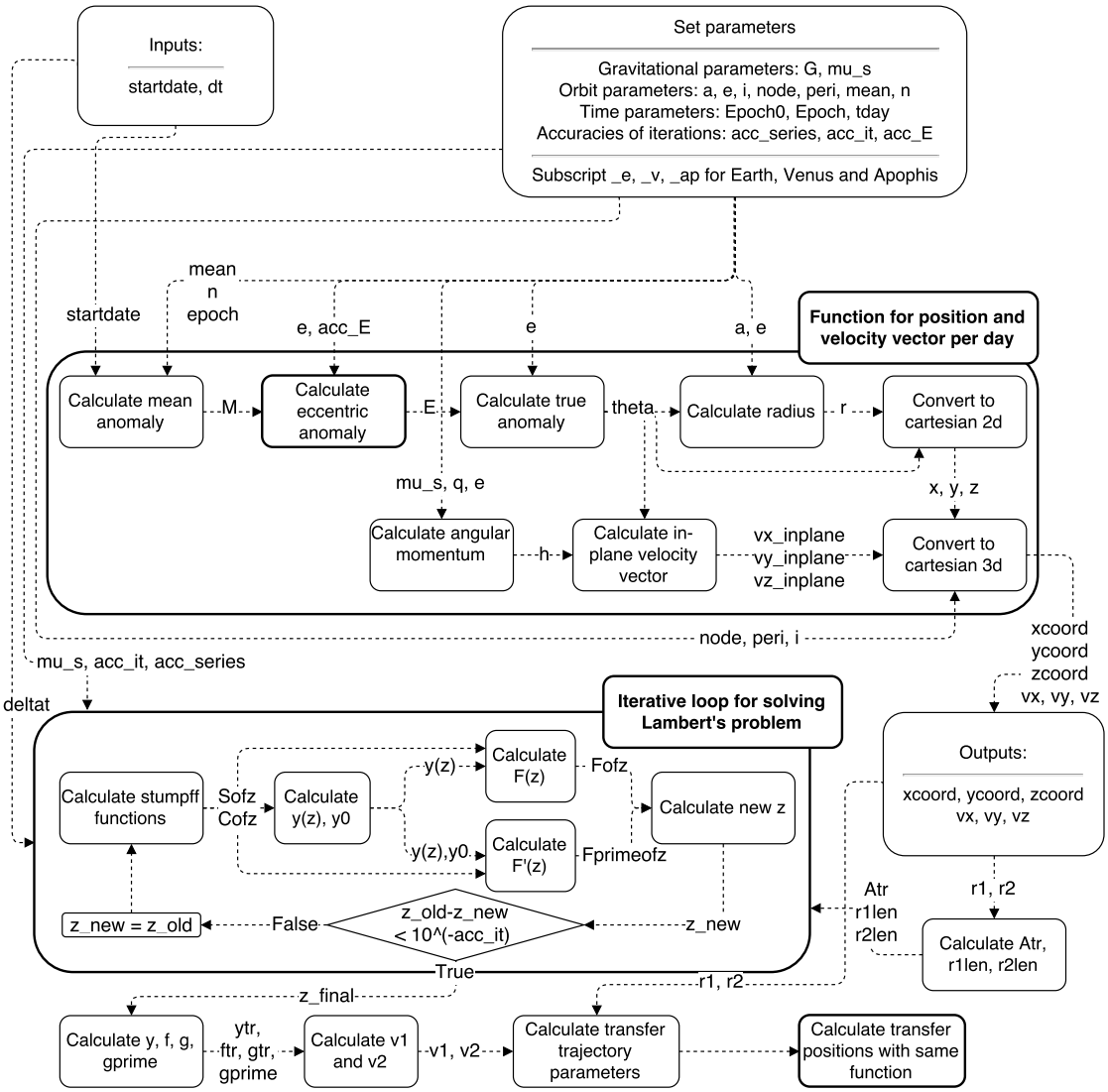

Figure 3.3: A schematic overview of the MATLAB model

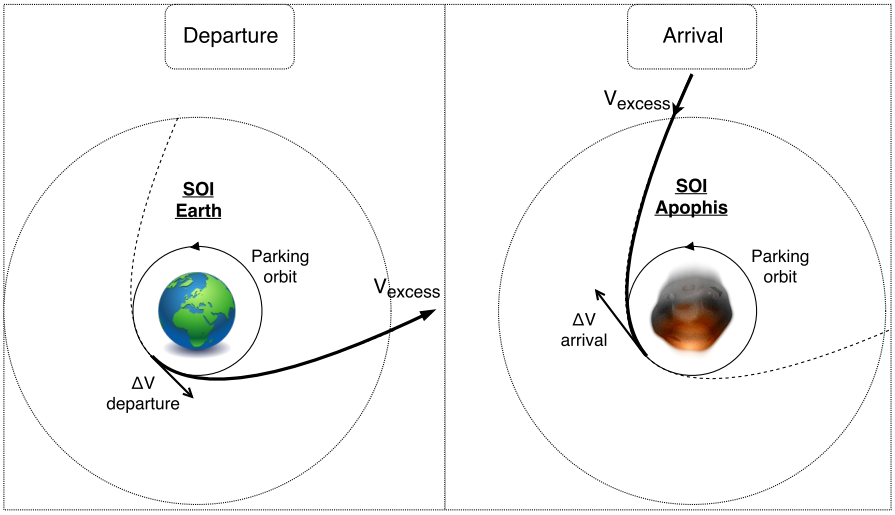

Figure 3.4: Overview of the manoeuvres at departure and arrival

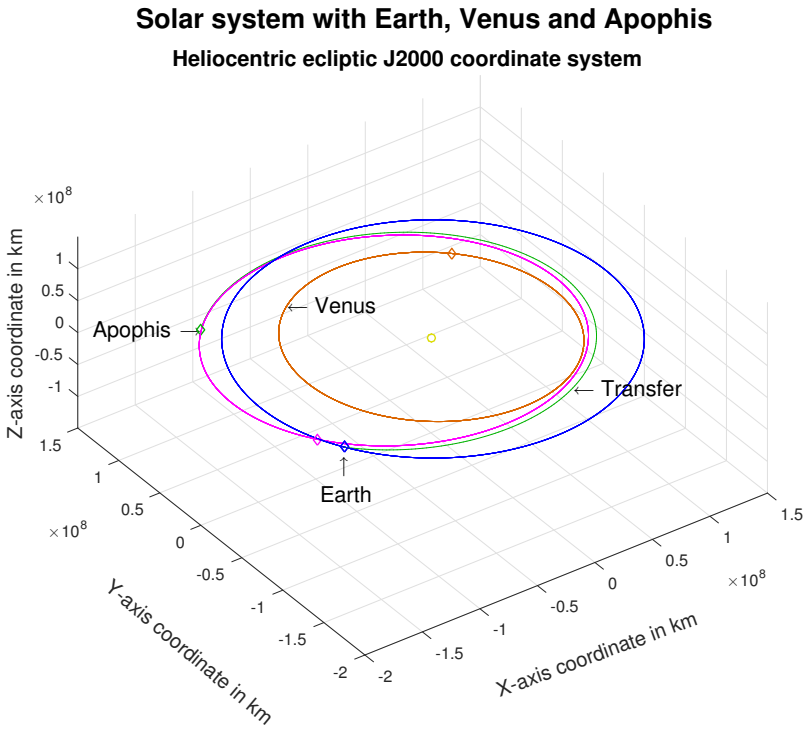

Figure 3.5: The three-dimensional model plot. The orbit colors are blue for Earth, orange for Venus, magenta for Apophis, and green for the transfer orbit when departing at 21st of April 2021 and travel for 245 days. The diamonds indicate starting positions, except for the green diamond which indicates arrival position.

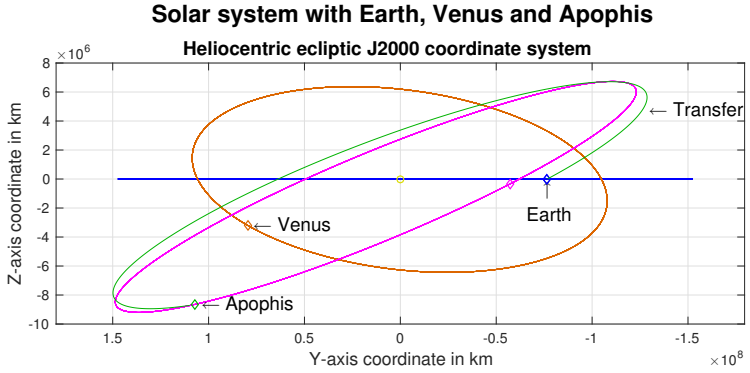

Figure 3.6: The model plot from a side-view to show the inclination, the view is towards the vernal equinox, so the bodies progress counterclockwise. Axes are not in the same scale for clarity.

Table 3.2: ΔV budget for the transfer phase, with a travel time of 245 days, departure at 21st of April, 2021.

Velocity	**Value**	**Unit**
Excess velocity at departure	5.2817	$\mathrm{km\,s^{-1}}$
Excess velocity at arrival	0.4129	$\mathrm{km\,s^{-1}}$
Parking orbit velocity at Earth	7.7299	$\mathrm{km\,s^{-1}}$
Parking orbit velocity at Apophis	2.7377e-05	$\mathrm{km\,s^{-1}}$
Velocity at departure hyperbolic periapsis	12.1408	$\mathrm{km\,s^{-1}}$
Velocity at arrival hyperbolic periapsis	0.4129	$\mathrm{km\,s^{-1}}$
ΔV for departure	4.4109	$\mathrm{km\,s^{-1}}$
ΔV for arrival	0.4129	$\mathrm{km\,s^{-1}}$
Total ΔV	4.8238	$\mathrm{km\,s^{-1}}$

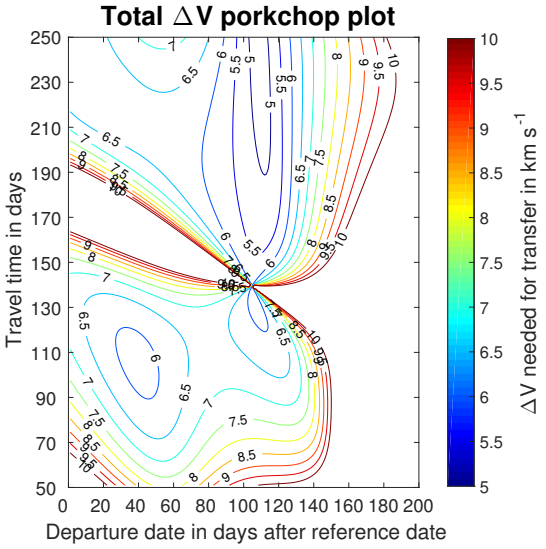

Figure 3.7: Porkchop contour plot showing the total ΔV for a range of departure dates and travel times, with reference date January 1st, 2021.

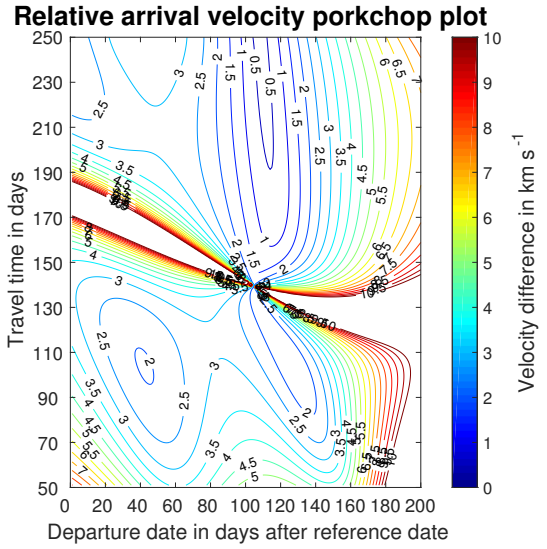

Figure 3.8: Porkchop contour plot showing the arrival velocity for a range of departure dates and travel times, with reference date January 1st, 2021

3.4 Verification of results

The verification of the results was done by performing qualitative and quantitative checks. In the code, there were different types of functions. Some of them represented a basic calculation of a function depending on the inputs, some consisted of iterations until a certain minimum difference was met, and others used to plot the results. The MATLAB compiler detects any programming typos in the program. In addition, the different functions in the model were checked for errors as well as for correct implementation of the equations as unit tests. As the orbits are plotted, a qualitative approach is to check if the orbits are sensible, for example the inclination angles and the revolution times. Furthermore, relative positions of the planets and asteroid can be checked using the NASA JPL model [9]. Also, the behaviour at extremes was assessed. The major function in the program implements the solving of the Lambert's problem. This function was successfully tested in its whole using the inputs of an example given in [1] and checking if the outputs were correct compared to the given solutions.

3.5 Launcher Selection

In order to get out of the Earth's atmosphere and on the transfer orbit to Apophis a launch vehicle is required. Multiple launch vehicles were considered and depending on the spacecraft mass a choice for a launcher was made. In Table 3.3 the launch capability to an orbit with a characteristic energy (C_3) of 27.89 is shown. This is the characteristic energy of the transfer orbit described in Section 3.3 and this energy has to be provided by the launch vehicle. Unfortunately for the Ariane 5 the C_3 curve was not available but only the launch capability to escape velocity, which corresponds to a C_3 value of zero. the Furthermore the cost and success rate, together with the total amount of launches, is given for each launch vehicle. The Data from Table 3.3 was obtained from the user manuals of each of the launch vehicles and other sources. As will be discussed in Chapter 15 the total mass of the spacecraft at launch is estimated to be 541 kg. For this mass the cheapest launch vehicle is the Soyuz (Fregat) from Arianespace with a cost of $45M. Furthermore the Soyuz is also very reliable with a 100% launch success rate out of 55 launches. Therefore the Soyuz (Fregat) was selected to launch the ARMADA mission. This Soyuz rocket will be launched from Guiana space centre in Kourou, French Guiana.

Table 3.3: Launcher specifications [11, 12, 13, 14, 15, 16, 17, 18, 19]

Launcher	**Launch capability to C_3 = 27.89**	**Cost**	**Success rate**
Europe			
Ariane 5	~4,700 kg ($C_3 = 0$)	$200M	83/85 (98%)
Soyuz (Fregat)	~660 kg	$45M	55/55 (100%)
Vega	~440 kg	$32M	6/6 (100%)
USA			
Atlas V (551)	~4,000 kg	$100M	61/62 (98%)
Delta IV Heavy	~14,220 kg	$435M	8/9 (89%)
Falcon 9	~894 kg	$62M	23/25 (92%)

4. Gravity tractor

During the mid-term review a trade-off was performed between three different mission concepts to deflect an asteroid. From this trade-off the gravity tractor was selected to be developed further. This chapter is structured as follows: firstly, the underlying concepts behind the gravity tractor will be explained. Next, the initial mass and power estimation method will be elaborated on. Finally, the procedure that was followed to find the deflection distance requirements will be explained.

4.1 Fundamental concept

In this section the fundamental concept behind the gravity tractor will be explained. As the name suggests, the main driver of the functioning of the gravity tractor is the gravity force. The force of gravity is always present between two bodies of mass. It is proportional to the mass of the bodies, and inversely proportional to the distance between the bodies squared. This is displayed mathematically in Equation 4.1.

$$F_g = \frac{GmM_{ast}}{d^2} \tag{4.1}$$

In Equation 4.1 it can be seen that the gravitational force depends on the universal gravitational constant G, the mass of the spacecraft m, the mass of the asteroid M_{ast}, and the distance d between these two bodies squared. The spacecraft hovers close to Apophis, and the gravitational force between them causes Apophis to change its orbit. Instead of hovering, the spacecraft may also be in a "halo" orbit at a certain distance from Apophis. This concept is explained in a more detailed fashion in the mid-term report [46]. The hovering concept is displayed schematically in Figure 4.1.

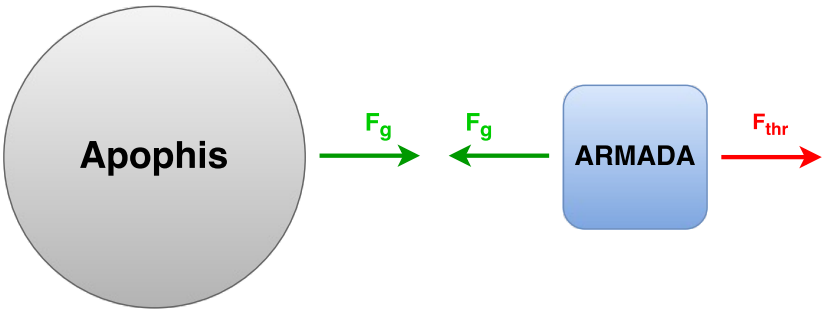

Figure 4.1: Schematic interpretation of gravity tractor concept.

From Figure 4.1 it can be seen that the gravity force that is exerted by the spacecraft on Apophis is equal (but opposite in direction) to the gravity force exerted by Apophis on the spacecraft.

According to Newton's second law, the acceleration experienced by the spacecraft will be much larger than that of Apophis, because the mass of the spacecraft is significantly lower. This means that as time goes by, the spacecraft will slowly drift towards Apophis leading to an eventual collision, which is not desired. In order to compensate for this effect, the spacecraft must thrust away with a force equal to the gravitational force. Even though this force is small compared to the gravity force we experience on earth, it must be compensated for throughout the entire mission lifetime. This force will be counteracted by means of ion engines, since they provide low thrust and have a very high specific impulse (the full trade-off will be discussed in Chapter 6). Furthermore these thrusters have to thrust under an angle in order to prevent the exhaust plumes from hitting the asteroid, which would counter the deflection manoeuvre,=. This is shown in Figure 4.2.

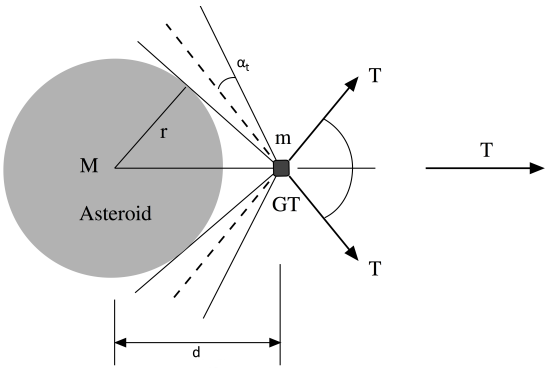

Figure 4.2: Interpretation of thruster plume effect

As the ion thrusters counteract the gravity of the asteroid, the spacecraft will stay at the same relative position with respect to the asteroid. The asteroid is pulled towards the spacecraft,

leading to the entire system (Asteroid and spacecraft) to move into the direction of the resultant force. Using this principle the asteroids orbit is slowly changed over time. Because the force used to alter the orbit only depends on the mass of the bodies and the distance between them, the deflection method is insensitive to the structure, surface properties, and rotational state of the asteroid [47]. This is an important advantage over many other deflection methods, as it can account for uncertainties regarding the physical characteristics of the asteroid.

4.2 Gravity tractor mass estimation

There are three parameters that are required in order to estimate the average mass of the spacecraft during the deflection manoeuvre: deflection time, deflection distance, and hovering altitude with respect to the asteroid. In order to ensure that the deflection can take place between two passes of the asteroid by the earth, the deflection time must be smaller than the synodic period. From [48] it was found that the synodic period of Apophis with respect to Earth is equal to 7.769 years. Furthermore, a safety factor of 1.3 was applied for the time as was discussed in the contingency management chapter in the baseline report [43]. Taking this safety factor into account yields a deflection period of 6 years. The deflection distance was chosen to be 11.8 km as will be explained in Section 4.3. From the deflection distance the thrust required by the spacecraft can be calculated, since the deflection distance is related to thrust force of the spacecraft using Equation 4.2 [49].

$$\Delta X = \frac{3}{2} A (2t_s - t_p) t_p sin\theta \tag{4.2}$$

In Equation 4.2 ΔX is the deflection distance (along the track of the orbit), A is a thrust to mass ratio $A = \frac{T}{M}$, with T the thrust of the spacecraft and M the mass of the asteroid, t_p is the time of deflection and t_s is the coasting time after the deflection manoeuvre has been performed. Because the mission goal of ARMADA is to demonstrate technology, it is important to constantly monitor the result of the deflection. This is done while hovering near the asteroid and therefore there is no coasting time and t_s can be set equal to 0. Moreover, the angle θ is assumed to be 90 degrees as this will be most efficient for deflecting the asteroid. Applying these assumptions to Equation 4.2 yields Equation 4.3 [49, 50].

$$\Delta X = \frac{3}{2} A t_p^2 \tag{4.3}$$

By using Equation 4.3 the required thrust can be calculated as function of a certain deflection time. The thrust depends on the gravitational pull of the asteroid on the spacecraft, which can be approximated using Equation 4.1. Assuming that the spacecraft mass is small compared to the mass of the asteroid, the gravity force F must be equal to the thrust T. If Equation 4.1 is now substituted into Equation 4.3, after rearranging an equation for the average spacecraft mass during the deflection manoeuvre can be derived, see Equation 4.4.

$$m_{avg} = \frac{2\Delta X d^2}{3 G t_p^2} \tag{4.4}$$

Using Equation 4.4 the mass can be plotted as function of the deflection time if a certain distance is assumed. Plotting this function for multiple distances an optimum can be found between distance, mass and deflection time. The results can be seen in Figure 4.3 for hovering distances between 1.1 and 5 asteroid radii from the asteroids center of mass with steps of 0.1.

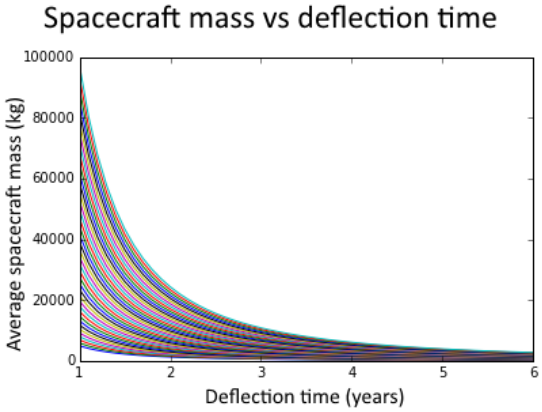

Figure 4.3: Spacecraft mass vs. deflection time

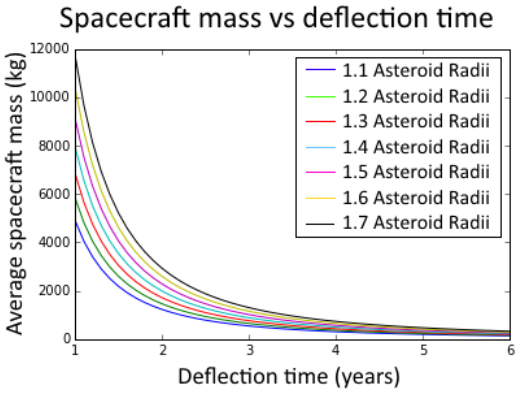

Figure 4.4: Spacecraft mass vs. deflection time for seven hovering distances

From Figure 4.3 it can already be seen that for large hovering distances and short mission times

(t<2 year), no feasible options exist, since the launch mass of the spacecraft would be far beyond the payload capability of the launch vehicles mentioned in Section 3.5. A more detailed view of the mass versus deflection time graph is given in Figure 4.4. Here, the mass versus deflection time is given for a smaller range of hovering distances.
In order to estimate the launch mass of the spacecraft (and thus be able to give an initial selection of the launcher) the average spacecraft mass is not sufficient. The mass of the fuel that is used during orbit insertion must also be taken into consideration. This can be done by means of Tsiolkovsky's rocket equation, as presented in Equation 4.5.

$$\Delta V = V_e ln(\frac{m_0}{m_e}) = I_{sp} g_0 ln(\frac{m_0}{m_e}) \tag{4.5}$$

In Equation 4.5 m_0 and m_e are the starting mass and end mass during the manoeuvre, respectively. Moreover, the fuel mass during the manoeuvre is the difference between these masses. In this case, the manoeuvre is the orbit insertion. Moreover, I_{sp} is the specific impulse which is an indication of an engine's efficiency. Typical values for I_{sp} can be found from literature, which leaves m_0 and m_e as the unknowns. It must be noted that m_e corresponds not only to the mass after the orbit injection, but also the mass at the beginning of the deflection manoeuvre. This mass can be approximated to be the average mass during the deflection, plus an additional 50% of the fuel used during the deflection. In order to do this, an expression for the fuel used during the deflection must be found. Firstly, Equation 4.6 shows the relation between Thrust T and mass flow $\dot{m}$, which can be rewritten to give a relation between thrust, fuel mass m_f and deflection time Δt.

$$T = \dot{m} V_e = \dot{m} I_{sp} g_0 = \frac{m_f}{\Delta t} I_{sp} g_0 \tag{4.6}$$

Recalling that the thrust required should be equal to the gravity force given in Equation 4.1 yields an expression for the fuel mass for the deflection manoeuvre, as shown in Equation 4.7. Note that additional terms η, an arcsine term, and α_t are taken into consideration to account for efficiency, thruster effectiveness, and thruster plume respectively.

$$m_f = \frac{GmM}{I_{sp} g_0 d^2 \eta cos(asin(\frac{r}{d}) + \alpha_t)} \Delta t \tag{4.7}$$

After having determined the fuel mass during deflection, the mass at the end of orbit insertion (and beginning of deflection) can be expressed as in Equation 4.8. This assumes that the mass flow of the fuel is constant.

$$m_e = m_{avg} + \frac{1}{2} m_f \tag{4.8}$$

Equation 4.5 can now be rearranged to find an expression for the mass at the beginning of orbit insertion. This is the mass that needs to be taken on board of the launcher, and thus constrains the launcher selection. Rearranging Equation 4.5 yields Equation 4.9:

$$m_0 = m_e e^{\frac{\Delta V}{I_{sp} g_0}} \tag{4.9}$$

By following the procedure above, estimations on launch mass, fuel mass, and dry mass can be obtained.

4.3 Gravity tractor deflection distance

In order to size the spacecraft it is important to first define some key constraints and characteristics regarding the mission. Defining these clearly leads to a smaller design space, thus allows for a more accurate design proposal in the early design phase. The deflection distance must be computed since it is a major design driver, as the acceleration given to the asteroid is directly related to the deflection distance, and this acceleration depends on the spacecraft's mass. Because this mission is a technology demonstration, the deflection distance can be chosen arbitrarily (as long as it is measurable). For ARMADA, however, it is considered that a similar mission should be readily available in the case where deflection is required to save Earth. For that reason the deflection distance is chosen in a way that it is of the same order of magnitude as a deflection distance that may be required in the future, in the case of a threat.

There is a keyhole with a diameter of 4.6 km in proximity to the Earth [51]. Currently, the orbit of Apophis indicates that the asteroid will go through this keyhole in April 2029. There is a 1 in 45000 chance that the asteroid will then return to Earth and impact it seven years later, in 2036 [52]. Because this probability is small, there is no direct need to perform a deflection mission to prevent Apophis from impacting Earth in 2036. For ARMADA, however, a deflection distance will be based on this encounter as it resembles a scenario that may happen in the future. If an asteroid does indeed pose a threat in the future, a mission similar to ARMADA can be executed in a short timeframe to deflect the threat. A schematic overview of the orbits of Earth and Apophis is given in Figure 4.5.

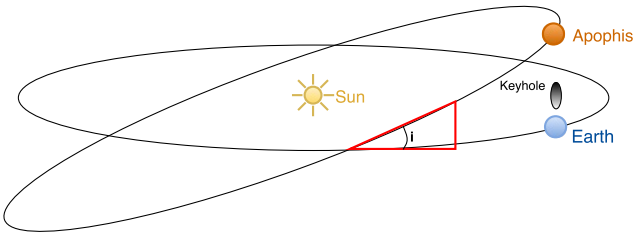

Figure 4.5: A schematic overview of Earth's and Apophis' orbits

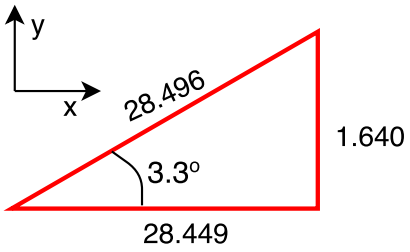

Figure 4.6: Computation of velocity components of Apophis (km/s)

Apophis will be either slowed down or accelerated in its orbit to delay its encounter with Earth [49]. Moreover, a margin for the vertical distance between the bodies is taken to be twice the diameter of the keyhole. This will ensure that the spacecraft never passes through the keyhole. In order to compute the distance with which the asteroid must be slowed down, it is important to first find the relative velocity between Earth and Apophis. The triangle highlighted in Figure 4.5 is shown in Figure 4.6. It is used to compute the velocity components of Apophis.
The velocity of Apophis is computed using Equation 3.2, and then decomposed in the direction of Earth's motion (x) and perpendicular to that (y) using the inclination of Apophis' orbit with respect to the ecliptic [52]. Earth's velocity can be computed in a similar manner, from which the relative velocity between the two bodies can be found by simple vector subtraction. This yields relative velocities of 1.004 km/s and 1.640 km/s in x and y directions respectively. Using the vertical deflection distance of 9.2 km, the delayed time can be computed. This can then be translated to a horizontal distance using the horizontal relative velocity. Using the Pythagorean theorem the required deflection can simply be computed and is found to be 11.8 km. According to [50] this distance is sufficient to ensure there will not be a future collision

5. Scientific Payload

Before deciding to use the gravity tractor for asteroid deflection, components needed for other deflection methods were considered as payload. The gravity tractor concept is based on the mass of the spacecraft itself. As the gravity tractor allows for more mass and space to carry in the craft due to the lack of a deflection payload, team ARMADA will now conduct an additional observation part, thus scientific goals are also considered. From the observation, key parameters of the asteroid such as the mass distribution and dynamical properties are determined before initiating the deflection phase. There is global scientific interest in asteroids and, as there is now room for scientific payload, additional stakeholders and goals can be included in the mission.

5.1 Scientific Objectives

In order to reduce the risk of an NEO impacting the Earth, one of two methods can be used: directly mitigating the risk through a deflection action, or reducing the uncertainties associated with NEOs. The first option was already decided upon as the main objective of the ARMADA mission. However, the array of options possible to achieve this are mainly restricted by uncertainties related to asteroid position, trajectory, mass and composition. It is thus evident that a more detailed analysis of these aspects will help in future deflection missions.
Firstly, the uncertainties regarding the orbit of NEOs can be reduced. One way to do this is to detect and count the craters present on the celestial body so as to get more information on how the asteroid was formed, its age and where it potentially comes from. This information can give insight into so-called "danger zones" that produce NEOs, helping future tracking and identification of potential hazards. Another key factor that influences the orbit of an asteroid is the Yarkovsky effect, which contributes to the normal spin and tumbling rates of such bodies. Measuring this by quantifying the effects on a small celestial body will greatly help in reducing the uncertainties related to NEO orbits. Estimations on the Yarkovsky effect can be made using the thermal properties and albedo of the asteroid.
Secondly, the composition and mass distribution of the asteroid are of great interest. Knowing the exact constituent elements and how they are distributed throughout the structure of the celestial body will greatly reduce the uncertainty associated with certain deflection methods (i.e. laser ablation and solar mirrors), where the material composition is a critical factor. Sometimes asteroids are formed through the collision of multiple such celestial bodies. Knowing the composition of this asteroid can give further insight into the formation processes of asteroids and its history, and may help lower the risk of undetected NEOs being detected too late for a non-nuclear deflection method to be used. Furthermore, knowing the internal structure of an asteroid can also mitigate the risk of creating unplanned debris with a chosen deflection method.
The shape and size of the asteroid are other critical factors. Having a detailed map of the asteroid can greatly contribute to the understanding of the implementation issues of other deflection methods that require landing or impact (i.e. railguns or impactor). Furthermore, getting an accurate measurement of the size of the asteroid will serve to validate measurements from Earth and potentially help in improving the accuracy of Earth-based measurements. In terms of the gravity tractor concept, knowing the shape and size of Apophis will help in maintaining the deflection distance required from the centre of the target body.
Another characteristic of the asteroid that would be interesting to observe, from a planetary science point of view, is the magnetic field. Generally large magnetic fields are only present in celestial bodies with an iron core, however having iron in its composition also creates a magnetic field. It is expected that a small asteroid has a small such field, however no one has actually measured this. If a more powerful magnetic field is registered than currently anticipated, this could be used in the implementation of new deflection techniques. As such, it is important to finally confirm or infirm the existence of such a field.
Finally, the albedo of an asteroid is a very important factor for such a mission. It gives a measure of reflectance, as well as giving insight into how the target was formed and where it comes from. This information is important for both the ARMADA mission, since mapping an asteroid with low albedo through cameras can be inconvenient. In addition, it may be of interest for future missions which use the concept of heat transfer and surface ablation as deflection mechanism (i.e. laser and solar mirrors concepts). And as previously mentioned, the albedo is also an important parameter for the Yarkovsky effect.

5.1.1 Requirements

The scientific requirements for the ARMADA mission are presented in table 5.1. The last column represents the sensors that fulfil the requirement. FC is framing camera, LA corresponds to the laser altimeter, IR is IR spectrometer, XS corresponds to X-ray spectrometer and PO is polarimeter.

Table 5.1: Scientific payload requirements

Identifier	Requirement	Sensor
ARMADA-SM-01	The scientific payload shall obtain images of $\geq$ 99% of the surface of Apophis with a sampling of $\leq$0.2cm per pixel.	FC
ARMADA-SM-02	The scientific payload shall obtain a topographic map of $\geq$ 99% of Apophis with a horizontal resolution $\leq$20cm and a vertical resolution of $\leq$ 10cm	FC, LA
ARMADA-SM-03	The scientific payload shall measure and map the abundance of major rock-forming minerals to $\leq$ 10% and create a compositional map of Apophis	FC, IR, XS
ARMADA-SM-04	The scientific payload shall obtain more than $\geq$ 500 spectral frames on Apophis' surface between wavelengths 360 and 2100 nm	FC, IR
ARMADA-SM-05	The scientific payload shall determine the bulk density of Apophis to $\leq$ 1%	LA, FC, IR, XS
ARMADA-SM-06	The scientific payload shall determine the tumbling spin state properties of Apophis	FC
ARMADA-SM-07	The scientific payload shall determine the albedo of Apophis with an accuracy of 99%	PO
ARMADA-SM-08	The scientific payload shall obtain the thermal properties of Apophis with an accuracy of 95%	IR
ARMADA-SM-09	The scientific payload shall determine the abundance of materials on Apophis in the $0.3 - 10.0$keV range	XS

5.2 Scientific Instruments

The following section presents the scientific instruments that will be taken on the mission in order to satisfy the stated requirements in the previous section, along with their specifications.

5.2.1 Camera Mapping

The purpose of ARMADA's framing camera is to allow a further understanding of the origin and maturation of asteroids, and hence the origin and evolution of our solar system. The framing camera will achieve this goal through the optical determination of the asteroid's optical properties. The scientific camera on-board the spacecraft can fill a wide variety of scientific objectives which are described in this section.

Physical properties

Firstly some fundamental parameters of the asteroid must to be determined. This does not only add scientific value, but it also allows for measuring dynamical properties such as the rotation period and spin-axis orientation. These must be known for the safe operation of the spacecraft during observation, and for the use of other scientific equipment on board. Additionally, the shape, mass, and bulk density of Apophis are crucial parameters for determining the dynamics of the gravity tractor deflection.
From photometric observations of Apophis, [53] found from measurements between December 2012 and April 2013, Apophis is in a state of non-principle axis rotation (tumbling). The inertial properties about its spin axes have also been determined in [53]. The first part of the scientific mission will be to validate these results, and to determine its spin state more accurately. Doppler measurements from the laser altimeter, correlated with a detailed mapping of landmarks, will be used to find the rotation rates and corresponding axes. This means that major landmarks outside of the altimeter field of view will be tracked until they are hit by the laser beam. At this point, the spin and its direction can be evaluated. A 3D shape model of Apophis can be produced using the pictures taken along with the laser altimeter, allowing the bulk density to be derived using an estimated mass found in [54], or from further measurements during the scientific mission.

Digital terrain model

From images taken by the framing camera, the global shape of Apophis can be determined. Topographic features can be modelled using photoclinometry. This method uses the different brightnesses, for example in the slopes of a crater, to create a 3D interpretation of a 2D picture. Its working is largely dependant on the direction of the light and reflectivity of Apophis' surface, but can be combined with data from the laser altimeter to create an accurate description of the asteroids topography and volume.

Geology and composition

The geological composition of the asteroid can reveal clues as to how the solar system was formed. Additionally, with the study of constituent materials, collisions, tectonics and thermal mapping, the geological history and evolution of Apophis can be studied.
A fundamental characteristic of a surface material is the light it reflects. Sunlight that lands on an asteroids surface is either scattered or absorbed by mineral grains on the surface. The fraction of this light that is absorbed or reflected back to an observer varies as a function of wavelength. This can be utilised to understand more about the composition of Apophis. The framing camera will be equipped with seven different colour bands and a panchromatic clear filter, where the wavelengths of the filters will vary from near infra-red to visible light. Variations in surface material, along with the amount of time a particular area has been exposed to space, can be determined as the light spectrum of reflected light of asteroids are sensitive to these properties in the near infra-red part of the spectrum. Iron bearing silicates, such as Pyroxene and Olivine, which are commonly found in asteroids, also have absorption bands at wavelengths near 1 and 2μm [55]. The position of a minimum in the absorption band, together with the shape and strength of the band, sheds light on the crystal structure and the abundance of that material and composition.

Camera design

The design of ARMADA's framing incorporates design points from the Dawn framing camera, the Hayabusa multi-band imaging camera and OSIRIS, the scientific camera on-board Rosetta. The designs of these instruments can be found in [56], [57] and [58] respectively.
As discussed, the camera will incorporate an 8 band filter. The filter properties and their scientific purpose can be seen in Table 5.2, where the effective wavelength λ_{eff}, the bandwidth B_f and the transmission are given for each channel.

Table 5.2: Filter specifications

Channel	$\boldsymbol{\lambda_{eff}}$	**B**	**Transmission**	**Scientific Objective**
1	360 nm	51.1 nm	78.2 %	Spectral slope near UV
2	430 nm	40 nm	$\geq$ 75%	Spectral slope visible wavelength
3	550 nm	40 nm	$\geq$ 75%	Spectral slope visible wavelength
4	750 nm	40 nm	$\geq$ 75%	Spectral slope visible wavelength
5	640 nm	520nm	5 %	Neutral Density
6	805 nm	40.5nm	69.8 %	Orthopyroxene
7	960 nm	75nm	$\geq$ 75%	Clinopyroxene
8	1041 nm	60.7nm	$\geq$ 75%	Olivine

In Table 5.2, channels 6,7 and 8 were specifically chosen as it is expected that these are the most abundant materials that make up Apophis. This is shown in [54], and the ability to validate this work is crucial for NEO observation, as different deflection techniques largely depend on the composition of the asteroid.

Apophis is relatively small in comparison to other celestial bodies that have been visited during space missions. Additionally, during observation and even more so during deflection, ARMADA will be very close to Apophis with a distance of 1500 and 277 m respectively. This means that accurate mapping and measurements can be made during observation. The camera has been designed around the requirement that the surface should be mapped with a pixel size of 20cm. The specifications of the camera can be found in Table 5.4.

Table 5.3: Optical requirements

Item	**Spec.**	**Units**
Pixel size	25	cm
Resolution	720×720	[-]
Field of view	5.5×5.5	Degrees
Instantaneous field of view	66.7	μrad
Spectral range	$360 - 1041$	nm

Table 5.4: Camera specifications

Item	**Spec.**	**Units**
Mass	8.25	kg
Nominal power consumption	17	W
Bits per pixel	16	bbp

The optical design of the camera should at least be able to fulfil the requirements given in Table 5.3. Table 5.4 shows the mass, power and data rate associated with the camera. These values have been estimated from similar missions discussed earlier in the section.

5.2.2 X-ray spectrometer

X-ray spectroscopy is based on the the different emission spectra of materials. It is based on the fact that solar X-rays and the solar wind interact with Apophis' surface material during the mission lifetime. This application is limited to the observation of the outer surface material layer, to a depth of less than one millimeter. The atoms on the surface, up to 1mm, will interact with, and absorb these X-rays and subsequently become unstable and emit their own X-rays. The process of emitting X-rays is also called fluorescence. Each different element or material has its own characteristic X-ray energy, which is known from analysis in the previous decennial. The spectrometer receives part of these rays and creates a spectral map of the analysed subject, in this case, Apophis. The science behind X-rays will not be further explained in this report as it is not relevant for the mission design. More information about this topic can be found in [59]. This spectrum can then be analysed in order to give more information about the asteroid. It can provide information about the general composition of Apophis during the primary monitoring phase of the mission, or on localised areas when hovering at a closer distance. Furthermore, analysis of the spectrum can give further indication of the abundance of several elements on the surface, which is useful to research the homogeneity of the asteroid. This is mainly interesting in terms of the asteroid history, as finding different materials at different sides of the asteroid can indicate collisions with other objects during its lifetime. Finally, with an accurate enough measurement of the asteroid composition, its class and type can be further identified.

During its close encounter to Earth in 2013, Apophis was studied in more detail and determined to be mainly composed of olivine (65-75%), orthopyroxene (17-27%), and clinopyroxene (3-13%) [54]. It is clear that there is still a lot of uncertainty in these estimates, so further research on Apophis' composition is valuable. These three minerals mainly consist of iron, magnesium and silicate (silicon surrounded by oxygen atoms). In order to detect these elements with the X-ray spectrometer, it needs the ability to receive and process the emission energies of these elements. The respective energies are known and can be found to be ranging from 0.525keV for O-Kα_1 to 7.058keV for Fe-Kβ_1 from [60]. Here, the X-ray lines are identified as follows: a capital Roman letter which represents the shell containing the electron vacancy, a Greek letter indicating the group to which the line belongs, and a number specifying the intensity of the line within the aforementioned group. In Figure 5.1 a graphical representation of the X-ray emission process is presented. For this case, the incident radiation consists of the solar X-rays and solar wind. The emitted X-ray depends on the observed atom and situation. The chosen spectrometer energy range for this mission in order to observe the aforementioned range of energy values is $0.45 - 7.50$keV.

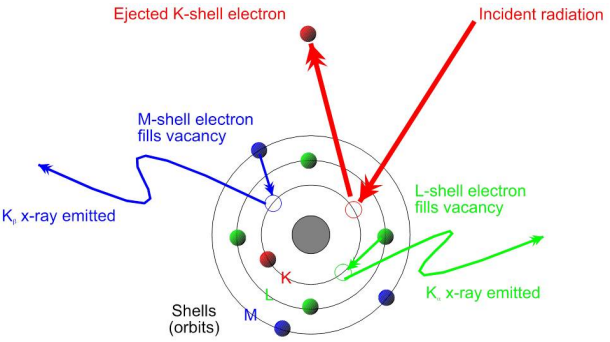

Figure 5.1: X-ray emission by incident radiation [2]

The resolution of a X-ray spectrometer corresponds to the smallest range of energies that the spectrometer can still differentiate. In order to be able to detect two different materials, the resolution of the spectrometer should be smaller than the energy difference of their emitted X-rays. In order to differentiate the Fe-Lα_1 and O-Kα_1 lines with respective energies of 0.525 and 0.705keV, an energy resolution of 180eV is necessary. In order to fulfil this requirement, a resolution of 150eV is chosen.

A main consideration for the use of X-ray spectrometers is that the measurements can be affected by background radiation from space, for example in the form of X-rays or energetic particles [61]. Furthermore, it is important to note that the observed portion of the asteroid should be in sunlight while performing the measurements, otherwise no information can be obtained.

Considering all aforementioned requirements, different X-ray spectrometers from space missions were investigated in order to find the right fit. The REgolith X-Ray Imaging Spectrometer (REXIS) from the OSIRIS-Rex mission was chosen [20]. Regolith points to the outer, rather loose, layer of material on the surface of an object. This sensor had the objective to determine the global elemental

Table 5.5: REXIS X-ray spectrometer specifications [20, 21]

Characteristics	**X-ray spectrometer**
Energy range	$0.3 - 10.0$keV
Energy resolution	130eV@5.9keV
Field of view	$30° \times 30°$
Imaging interval	4s
Operating temperature	$< -60°$C
Size	135mm $\times$ 135mm $\times$ 285mm
Total power	10.8W
Data rate	32000*bps*
Mass	4.4kg

abundance and search for anisotropies in the composition of Bennu. This is exactly what the ARMADA mission requires for its X-ray spectrometer, but for Apophis instead of Bennu. In Table 5.5, the specifications of this sensor can be found. It should be noted that the data rate was not found for this sensor, thus the value in the table is based on reference data from the Selene orbiter X-ray spectrometer [62], which is similar.

5.2.3 Infrared spectrometer

Infrared (IR) spectrometers can be used for different scientific objectives, mostly conducting compositional and thermal measurements of an object. The principle of infrared spectrometers is different from the X-ray equivalent explained in the previous subsection, but also based on the analysis of a certain range of the electromagnetic radiation spectrum. As opposed to the X-ray spectrum, the infrared spectrum is located on the other side of the visible light spectrum, at longer wavelengths of about 1mm to 750nm.
Similarly to the previous instrument, the infrared spectrometer also collects radiation from the Apophis' surface, but in this case, it is in the form of infrared radiation. This kind of radiation is similar to black-body radiation, but is related to the vibration of the molecules, especially the bonds between them. It works as follows: when a molecule changes either its rotational or vibrational state due to a disturbance or the absorption of infrared waves, which is the interesting case for this application, infrared energy or waves will be emitted from the material. The incident infrared energy changes the dipole moment of a molecule which leads to an excitation of its vibrational mode [63]. Every material has its own structure, and thus, its own vibrational modes, so to speak. As each material has this, the infrared radiation emitted from the surface will consist of different wavelengths and energies, creating the so-called (infrared) spectrum in this case. This spectrum is defined based on which kind of molecules were excited. This spectrum can then be analysed and compared to reference data in order to assess the composition of the material. Including a thermal detector in the spectrometer can then be used to obtain thermal information on the surface, by analysing the heating properties of the emitted infrared waves [63]. Together with the tumbling rate determined from the camera and altimeter, and the albedo, the thermal properties can then be used for Yarkovsky estimations.

As mentioned previously, Apophis mainly consists of olivine and pyroxenes according to ground-based measurements. It would thus be interesting to assess the abundance of these materials in Apophis more accurately. This is already being done by the X-ray spectrometer, but in order to have redundancy and provide a way of checking the data acquired by the X-ray spectrometer, which might have errors and false measurements, this sensor will also be incorporated. The second reason for integrating this sensor in the design is the fact that it also provides information about the thermal properties of the target, which is not the case for the other spectrometer.

To obtain the correct measurements, a wavelength range of 850nm to 2100nm is required, as this range contains the expected wavelengths for olivine and pyroxenes [22]. After the consideration of different infrared spectrometers used by other space missions, such as OSIRIS-Rex, ExoMars, Hayabusa etc., the Hayabusa near infrared spectrometer or NIRS-S was chosen, as it fulfils the requirement stated before, and the Hayabusa mission is very similar to the ARMADA mission [22]. This sensor was also used to obtain information about the abundance of olivine and pyroxenes on an asteroid, so it is certainly a relevant reference mission. Some specifications of the NIRS can be found in Table 5.6 and 5.10. In the Hayabusa mission, NIRS-S measurement data is transmitted to the NIRS-E data processing unit, which works together with their X-ray spectrometer. For the ARMADA mission, the data processing unit will also be shared between the infrared and X-ray spectrometer as most processing units are very efficient and can handle several functions.

Table 5.6: NIRS-S near infrared spectrometer specifications [22]

Characteristics	**IR spectrometer**
Spectral range	$850 - 2100$nm
Spectral resolution	26nm
Imaging interval	65.536ms
Field of view	$0.1^\circ \times 0.1^\circ$
Operating temperature	-15°C
Size	$336\text{mm} \times 165\text{mm} \times 100\text{mm}$
(Maximum) power	9.5W
Stand-by power	2.45W
Data rate	13671.875*bps*
Mass	1.534kg

5.2.4 Magnetometer

Magnetometers measure and quantify the magnetic field characteristics of the target object. This can generally be done in two ways: remotely, or through the use of a sample. As the ARMADA mission does not have a landing segment planned, the latter method is not considered. Furthermore a space mining subsystem would be a critical component of the system if a sample is to be taken. The TRL for this technology is quite low, which means that extra cost and time will need to be invested to test and analyse this concepts so as to raise its TRL sufficiently. This is necessary to minimise the risks presented by the use of a new technology. As such, the ARMADA mission will use the former option - remote magnetic field sensing. This report will not go into

much detail about the functioning principles of this sensor, as these can be found in references [64] and [65]. In order to size this sensor, the main parameters need to be identified and then requirements on these can be defined. Firstly, one needs to consider the magnetic field ranges that need to be measured. As Apophis' mass is 14 magnitudes smaller than the Earth's mass, the magnetic field of Apophis will be weaker than the Earth's magnetic field as well. However, since there are uncertainties in both composition and mass distribution, uncertainties in magnetic field cannot be avoided. In order to lessen this uncertainty, the sensor with higher performance may be used, at the expense of extra mass and cost (e.g. a mode with a larger range).
If the cost and mass budgets allow for it, it will be decided that the sensors will be provided with higher performance. This means that the magnetometer is able to register magnetic field values in the order of the magnitude of the Earth's magnetic field (65000 nT). With this in mind, the following ranges are defined, each representing a different functioning mode of the magnetometer: ± 500 nT, ± 2000 nT and ± 65000 nT. It will first be attempted to map the magnetic field in the highest range, then, if the changes are too small to be observable within that large range, a smaller range mode will be used. It is expected, from the relative size and composition of Apophis with respect to the Earth, that the lower range(s) will mainly be used. The largest range will be used to quantify the effects of solar winds, as these will be of a higher order of magnitude than Apophis' natural magnetic field.
Earth observation has shown that minute changes in the order of 1 nT are observed in the magnetic field within a few seconds long time-frame. This means it is desirable to detect a smaller change than this. It is then required that the magnetometer be accurate to within 1% for each specific range, yielding the aforementioned accuracy of under 1 nT for the smallest one. Furthermore, it is required that the noise level of the instrument be smaller than 1 nT.

Another important parameter is the drift, which represents the change in absolute error over time. A requirement on this was set to be ± 2 nT, based on the MAVEN Mars mission [66].
Now, the last two parameters to be set are alignment knowledge and accuracy. Alignment knowledge is the angle between the estimated orientation of the magnetometer and its true orientation, while alignment accuracy refers to the angle between the estimated orientation and the target or desired one. This can be seen in Figure 5.2.
A constraint for this would be a maximum error of under 50 m, as no major differences in magnetic field are expected within this swath size. This yields a maximum total angle of 2.1775 °. This requires the sum of alignment knowledge and accuracy to be under this value. A magnetometer that fulfils all the aforementioned requirements without violating the constraints is the one used in the MAVEN mission [66]. The specifications for this instrument are found in Table 5.7, as stated in [66] and [67].

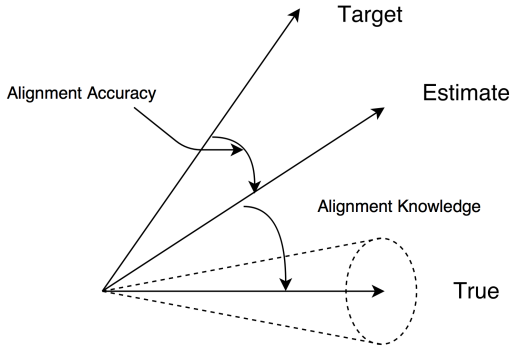

Figure 5.2: Alignment accuracy and alignment knowledge

As the largest range is too big for ARMADA's purposes, a similar magnetometer without the highest range setting would be a perfect candidate. A magnetometer like that is expected to

Table 5.7: MAVEN magnetometer technical specifications

Characteristics	**Magnetometer**
Noise level	< 0.03 nT
Absolute accuracy	± 0.01nT
Ranges	± 512nT, ± 2048nT, ± 65500nT
Drift	± 0.2nTyr^{-1}
Time resolution	1/32
Alignment accuracy	$\pm 0.6°$
Alignment knowledge	$\pm 1.4°$
Radiation tolerance	> 50 krad
Mass	0.39 kg per sensor
Size	12.7cm x 7.6cm x 9.1cm
Average power	6.12 W
Peak power	7.27 W
Data rate	67072 bps
Operational temperature range	-20°C to +60°C
Survival temperature range	-35°C to +70°C

have a lower power consumption and lower mass, however the time needed to design and test such a new instrument is beyond the scope of this project. As such, the MAVEN magnetometer is found to be sufficient for the required performance. It is very important to note that due to interference considerations, the magnetometers need to be mounted as far from the spacecraft body as possible, as any electrical components create a small magnetic field of their own. Thus, it is chosen to mount two magnetometers on the tips of the solar arrays. Finally, as mentioned in Section 5.1, although these sensors are generally employed in investigating more sizable celestial bodies with an iron core, like planets, the fact that there are still uncertainties pertaining to the presence of sizable magnetic fields means it would be useful to the scientific community to confirm or disprove this.

5.2.5 Laser topography mapping

As it is one of the most critical sensors for this missions, the laser altimeter will be used both for observation purposes, as well as for position control during the deflection phase. This is due to its high accuracy and the need to maintain a certain, constant, distance from Apophis at all times. As explained in Section 5.1, identifying craters and gathering more information on the albedo of asteroids is one of the primary scientific objectives. The laser altimeter can help in both regards.
Firstly, the camera can be used to map large areas at once and, once a crater has been identified, the laser can be used to more accurately map said topographical element. Furthermore, the altimeter can also be used to quantify the tumbling rate of Apophis by tracking the movement of certain topographical formations during a set time-frame. This can be done quite accurately with the altimeter, and this will be the very first step of the observation phase.

Secondly, the albedo detected by other sensors can be checked against the values produced by the laser altimeter itself. As the working principle of the altimeter is based on a beam reflecting back off the surface of the asteroid, the albedo will most certainly affect this in a measurable way. The energy of the reflected laser beam received by the sensor will be compared against the expected output energy of the laser, thus giving a measure of the albedo of the asteroid, as elaborated on in [68]. This information can be sent back to the ground station to be compared with similar values from more specialised sensors, like the polarimeter. In terms of requirements, an accuracy better than 20 cm is deemed to be acceptable. Furthermore, it is required that the spot size be smaller than the camera pixel size, namely a diameter smaller than 25 cm. This can be easily achieved by the GALA laser altimeter used in the JUICE mission. The specs of GALA can be found in Table 5.8, based on the definition study report [69].

Table 5.8: GALA altimeter technical specifications

Characteristics	**Laser altimeter**
Laser wavelength	1064 nm
Pulse energy	17 mJ
Pulse length	6 ns
Pulse repetition rate	1 to 50 Hz (variable)
Beam divergence	100 µrad (full cone)
Spot size on surface	13.15 cm (1315 m orbit)
Receiver telescope diameter	0.25 m (F/1 telescope)
Altitude resolution	10 cm (optimal)
Size	NA
Mass	15 kg
Power	52 W
Data rate	7 kbps
Temperature Range	NA

The GALA altimeter satisfies our requirements, whilst not violating any constraints. As such, this will be the chosen instrument for the tasks detailed at the beginning of the chapter. The size, mass, power and data rate of this instrument, as well as the temperature range it can operate in, can also be found in Table 5.8, as stated in its design overview [70]. It is important to note that the actual altimeter volume is not available and is assumed to be 10% of the receiver volume.

5.2.6 Polarimeter

Several difficulties are still found when trying to understand the formation and movement of an asteroid. As mentioned in Section 5.1, several sensors could be included to find more information about NEOs, allowing future deflection missions to be sized with more accuracy. By computing the albedo of the asteroid, much is discovered about it, as it is the characteristic that gives more information about the asteroid's surface composition, texture and history, as mentioned in [71].

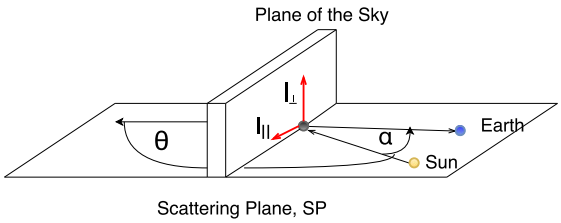

Figure 5.3: Polarimetry

Polarimeters can be used to determine the albedo of the asteroid, due to the fact that small-phase-angle (α) behaviour of NEAs is strongly dependent on the albedo of the asteroid. Thus, by measuring the phase-angle of Apophis, its albedo can be computed using 'the slope-

albedo law', as described in [72]. It is beyond the scope of this report to go into detail on the functioning of a polarimeter and further information can be found in [73] and [74]. Nevertheless, Figure 5.3 gives a general overview on how unpolarized light from the Sun is reflected by the asteroid, which is then measured by the polarimeter, dividing it into two main components, perpendicular ($I_\perp$) and parallel ($I_\parallel$) contributions, which are then used to compute the relevant - aforementioned - asteroid characteristics.
Furthermore, polarimeters have a high applicability, as they offer an excellent technique to derive the albedo characteristics of main belt asteroids and NEOs without being constrained by the size or shape [75]. Thus, the same polarimeter could be used to study other asteroids of interest to the science community. In addition, this system is inherently efficient due to the fact that the validation rate of the phase angle is rapidly performed for these objects, and a polarimetric slope can be obtained in a short period of time. From this slope, the asteroid's albedo can be calculated.
The technical specifications of the polarimeter can be seen in Table 5.9, these values were found in [76]. From this, it can be seen that the major limitation of the polarimeter is the fact that, for accurate measurements, the sensor needs to be placed at an angle of $\pm 90°$. Thus, this pointing accuracy will be taken into account when designing the ADCS, such that the polarimeter is also placed in the optimal position to gather the required data. Furthermore, another disadvantage of polarimeters is that they might contain moving components. These will create internal disturbances that will have to be measured during testing of the components in a latter design phase, however Spex, the chosen instrument, does not contain moving parts. On the other hand, polarimeters have a high accuracy and resolution, which is of extreme importance to accurately obtain measurements from a tumbling asteroid. Finally, having a short measuring time is highly advantageous as measurements can be taken constantly to obtain the different characteristics of Apophis. This allows to check if these properties do indeed vary throughout the asteroid's surface.

Table 5.9: Polarimeter SPEX technical specifications

Characteristics	**Value**
Field of view for each viewing direction	$7° \times 1°$
Relative polarisation accuracy	$0.05 to 0.01$
Spectral resolution for polarisation	$2nm$
Dimensions [cm]	$12 \times 12 \times 6$
Range of temperature control	15-40 °C
Maximum power consumption	2W
Mass	$2kg$

5.3 Mass & Power budget

In the previous section, six sensors are selected. The scientific objectives were already stated in Section 5.1 together with the sensors which can accomplish these objectives. In this section, the total mass and power budgets are given in Table 5.10. It is clear that the scientific payload composes a large part of the total mass of the spacecraft. Mainly the altimeter has a high mass. The power usage is also relatively high, but not all instruments are used at the same time, which mitigates this problem.

Table 5.10: Scientific mission mass and power budget

Instrument	**Mass [kg]**	**Power [W]**
X-ray spectrometer	4.40	10.8
Infrared spectrometer (NIRS)	1.54	9.5
Framing camera	8.20	17
Magnetometer	0.78	14.5
Laser altimeter	15	52
Polarimeter	2	2
Total	31.92	105.8

6. Propulsion & Orbit control

The propulsion system of the spacecraft must provide thrust to the spacecraft during the entire lifetime of the mission. For the ARMADA mission, the relevant thrusting periods are the orbit insertion and the deflection manoeuvre. Because the ΔV required to get into the transfer orbit is provided by the launcher, the propulsion system of the spacecraft does not have to be sized for this phase of the mission. In order to find suitable propulsion systems it will be necessary to perform trade-offs for both the orbit insertion system as well as the system that is active during the deflection.

There are many propulsion systems available on the market, but some of them can be omitted directly and do not have to be considered for the trade-off. In this chapter the requirements for the propulsion system will be stated. Next, the different types of propulsion systems will be elaborated on briefly and some of them will be omitted for the respective mission phases. Additionally, the trade-off between the different systems for both mission phases will be given and explained. After having selected a propulsion system, another trade-off will be performed in order to select a specific model that is available on the market. Finally, the rest of the propulsion system will be sized according to the results found previously.

6.1 Requirements and constraints

For the propulsion and orbit control system several requirements were set. These requirements are listed below in Table 6.1.

Table 6.1: Requirements for the propulsion & orbit control subsystem

Identifier	**Requirement specification**	
ARMADA-P&OC-01	The P&OC subsystem shall be able to provide a ΔV of 420 m/s to the satellite over the entire mission lifetime.	Check
ARMADA-P&OC-02	The P&OC shall be able to provide a vacuum thrust of at least 1084 N.	Check
ARMADA-P&OC-03	The P&OC subsystem shall have no single points of failure.	Check
ARMADA-P&OC-04	The P&OC subsystem shall be able to dispose of leftover propellant at the end of life of the spacecraft.	Check
ARMADA-P&OC-05	The P&OC subsystem shall have a thruster misalignment of less than 0.1 degrees	Inspection

6.2 Thruster type trade-off

There are various types of propulsion systems available on the market, all with their own advantages and disadvantages. These types can be divided into four groups: chemical, electric, advanced propulsion and others. Chemical propulsion systems include: Liquid mono-propellant, liquid bi-propellant, solid propellant and hybrid propellant systems. For a detailed description of each of these systems, references [27, 77, 78, 79] can be consulted. The most important characteristics of chemical propulsion are: high thrust, and moderate to low specific impulse. The electric propulsion system category includes: electrostatic (ion) propulsion, field emission electric propulsion, magneto-plasma dynamic propulsion, arcjet propulsion, resistojet propulsion and pulsed plasma propulsion. For a detailed description of each of these systems the reader is referred to references [80, 81]. Electric propulsion systems are characterised by a high specific impulse, low propellant usage, low thrust and a high power consumption. Advanced propulsion systems include (amongst others): solar sails and thermonuclear propulsion. These systems can have a wide range of characteristics and are mostly experimental. They will not be considered in the trade-off, however they are mentioned here for completeness, following a true systems engineering approach. The "other" group of propulsion systems includes cold gas thrusters. Cold gas thrusters are characterised by a relatively low thrust and a low specific impulse, however they are by far more simple than any of the other propulsion systems mentioned. A detailed description of cold gas thrusters can be found in references [27, 79, 80].

The propulsion system sizing was divided into two parts. A chemical system was used for orbit insertion, orbit maintenance and for attitude control. An electric system was used for hovering during the deflection manoeuvre. The chemical system was then subdivided into two more systems, a system for orbit insertion, and a system for orbit maintenance and attitude control. The sizing methodology for the latter will be given in Chapter 7, the sizing of the former will be explained in this chapter.

Orbit insertion

For orbit insertion a propulsion system must be chosen that is able to provide relatively high thrust values compared to the hovering phase of the mission. As stated before, the advanced propulsion techniques were discarded as most of them are still in experimental stage. Even though nuclear propulsion has been tested extensively, it does not comply with sustainability considerations for the ARMADA mission and is therefore not viable. The electric propulsion options do not provide high enough thrust levels for orbit insertion, which leaves the chemical propulsion and cold gas options for orbit insertion.

For the orbit insertion propulsion system trade-off, criteria that will be taken into account are the specific impulse I_{sp}, thrust, accuracy, and complexity. The thrust and accuracy are the most important criteria because, due to Apophis' low gravitational attraction, the time for orbit insertion is relatively small. For this reason, being able to deliver a high thrust with high accuracy is crucial. The specific impulse is considered to be important as well, because it influences the propellant mass required for the manoeuvre. It is however not as much of a driver as the thrust and accuracy. Finally, complexity is given a weight of 3, as it should be taken into account but it does not influence the mass and performance of the spacecraft as much as the other criteria.

Table 6.2: Propulsion system trade-off for orbit insertion

Propulsion type	I_{sp}	**Thrust**	Accuracy	Complexity	Total
Weight	4	5	5	3	
Cold gas	1	1	5	5	49
Liquid mono-propellant	3	3	5	5	69
Liquid bi-propellant	5	5	5	3	79
Solid propulsion	3	5	1	5	57
Hybrid propulsion	3	4	4	4	64

The grades that can be seen in Table 6.2 were obtained as follows. The specific impulse (I_{sp}) of liquid bi-propellant is better than any of the other systems [80], therefore it scores the highest. Solid, hybrid and liquid mono-propellant all have similar ranges for specific impulse and therefore get a medium score of 3 [80]. Cold gas thrusters have, by far, the lowest specific impulse and therefore score a 1 [80]. For the thrust, liquid bi-propellant and solid propellant get the best score as they both can provide very high thrust levels [80], whilst hybrid propulsion is a mix of these two systems and therefore scores the second highest as it has similar performance [79]. Cold gas propulsion can only provide relatively low thrust levels and therefore scores the lowest [80]. Liquid mono-propellant has thrust levels between those of all the other mentioned systems and therefore scores a 3 [80]. For accuracy, the solid propulsion scores lowest, as solid propulsion systems can not be turned of until all propellant is burned, therefore not being very suitable for high precision orbit insertion burns [80]. All other systems can be controlled and are therefore much more accurate, this is evident in the scores seen in Table 6.2. For complexity, solid propulsion, cold gas propulsion and liquid mono-propellant all score very high. All these systems are relatively simple as they do not require mixing of propellants. Hybrid propulsion scores second highest as it does require mixing of propellants, however it is still less complex than liquid bi-propellant propulsion, which obtained the lowest score.
From Table 6.2 it can be seen that liquid bi-propellant thrusters form the most suitable option for the orbit insertion manoeuvre, therefore liquid bi-propellant thrusters were selected for the orbit insertion manoeuvre.

Hovering

During the hovering phase of the mission a relatively low thrust is required from the propulsion system. Even though the thrust required is rather low, it must continuously thrust for an extended amount of time, i.e. multiple years. Similarly to the orbit insertion, advanced propulsion can be omitted directly due to sustainability and feasibility requirements set for ARMADA. The electric propulsion techniques stand out with respect to the cold gas and chemical options, due to their high specific impulse and thus, low propellant requirement. Additionally, electric propulsion has relatively low thrust capabilities and it can maintain accelerations for a long amount of time which is ideal for the implementation of hovering [82]. From these electric propulsion options, arcjets can be omitted because, as explained previously, the lifetime is not long enough to hover for multiple years.

The criteria that are considered for the hovering propulsion system trade-off are the specific impulse I_{sp}, power, and efficiency. The weight for the specific impulse is the highest (5), because it has a direct effect on the propellant mass that is required for the mission. The power is given a weight of 4 because it has a direct effect on the size of the solar panels, which contributes to the mass. Finally, the efficiency of the propulsion system is given the lowest weight (3) since it does

not directly contribute to mass. It does, however, directly have an effect on power consumption, which relates to the solar panel size. This then leads to an effect on the spacecraft mass.

Table 6.3: Propulsion system trade-off for hovering

Propulsion type	I_{sp}	**Power**	**Efficiency**	**Total**
Weight	5	4	3	
Electrostatic/Ion thrusters	5	4	4	53
Magneto-plasma dynamic thrusters	5	2	3	42
Resistojet	1	5	5	40
Hall effect thrusters	3	4	3	40

The trade-off was performed as follows. It was found that electrostatic thrusters and magneto-plasma dynamic thrusters have the highest specific impulse values available on the market [83], whereas resistojet thrusters have a very low specific impulse and Hall effect thrusters are somewhere in between [81, 80]. Moreover, the power consumption is also quantifiable and was compared based on the appropriate reference literature [81, 80]. Magneto-plasma dynamic thrusters have a high power consumption, whereas resistojet thrusters are very power efficient. Finally, it was found that besides having a low power consumption, resistojet thrusters also have a remarkably high efficiency [81]. Electrostatic propulsion scores a bit lower [80], and magneto-plasma dynamic thrusters and Hall effect thrusters have the lowest efficiency of the thruster types considered in the trade-off [83, 81]. From Table 6.3 it can be seen that, based on the total scores, the electrostatic/ion thrusters are seen as the best option for the deflection manoeuvre, therefore electrostatic/ion thrusters were selected for the deflection manoeuvre.

6.3 Propulsion system sizing methodology

This section will discuss the propulsion system sizing methodology. In order to size the propulsion system, a model was made in MATLAB. Due to the nature of the deflection concept, several parameters such as the total mass of the spacecraft and the deflection distance are closely related to the propulsion system. Therefore the propulsion system sizing also partly determines the deflection distance, launch mass and the power required. The sizing of the propulsion system was split up into two parts. Firstly the chemical propulsion system was sized, which includes the orbit insertion engines, orbit maintenance engines and the thrusters for attitude control. Secondly, the electrical propulsion system which is used for the deflection manoeuvre was sized. Each system is sized using their own program loop, however, since both also depend on each other (e.g. the propellant required for the orbit insertion depends on the propellant mass of the ion thrusters), the program is iterative and both have to be tuned to each other. A graphical representation of the MATLAB tool algorithm is seen in Figure 6.1.

6.3.1 Sizing of the chemical propulsion system

The chemical propulsion system will be used for multiple manoeuvres, the main task to be performed being the orbital insertion at Apophis. Furthermore, the chemical propulsion system will also be used for orbit maintenance and attitude control. Therefore it must function together with the attitude determination and control system (ADCS). For its sizing a MATLAB tool was developed, used both for sizing the chemical and the electrical propulsion system. A block diagram describing the MATLAB tool is shown in Figure 6.1. The tool calculates the total propellant mass required for the chemical propulsion system based on an initial guess which was obtained using the preliminary mass estimate in Chapter 4. With this initial guess, and the specific impulse of the chosen engine, a propellant mass estimate can be made. The engine can be chosen based on the time required for orbit insertion. The orbit insertion time should be less than the time that the spacecraft takes to leave the Hill sphere (or sphere of influence) of Apophis after arrival into this same sphere. The Hill sphere of Apophis is the region around the asteroid where it is gravitationally dominant. Because the method of patched conics is used for the astrodynamic analysis it is assumed that the gravity of only one body is "pulling" on the spacecraft at the same time. For this reason, the spacecraft can only be "captured" by the gravitational pull of the asteroid if it is within the Hill sphere. Therefore it is required that the orbit insertion burn is completed when the spacecraft is within the Hill sphere of Apophis, since, in order to orbit Apophis, the spacecraft needs to be within this sphere. It should be noted that there are more advanced methods which do not require the orbit insertion burn to be performed within the Hill sphere of Apophis [19], however these methods are beyond the scope of this report. The radius of the Hill sphere can be calculated according to equation 6.1 [84].

$$R_H = \left(\frac{m_2}{3(m_1 + m_2)}\right)^{1/3} a \tag{6.1}$$

Where m_2 is the mass of the secondary object, in this case Apophis, and m_1 is the mass of the

primary object, in this case the Sun and a is the semi-major axis of Apophis. After calculating the Hill sphere radius with Equation 6.1, the maximum possible orbital insertion time was calculated using Equation 6.2, where it was assumed that the maximum length of the hyperbolic trajectory upon arrival was twice the Hill sphere radius (this is a conservative estimate).

$$2R_H = \frac{1}{2}at^2 \ , \ dV = at \ \rightarrow t = \frac{4R_H}{\Delta V} \tag{6.2}$$

When the maximum orbital insertion time is known, the required acceleration can also be calculated by taking the second formula given in Equation 6.2. The required thrust force can then be estimated simply by $F = m \cdot a$, where the mass m is assumed to be constant. In reality this is not the case as the mass will decrease as propellant is burned. However, since the maximum mass was substituted for m, this equation gives a conservative estimate.
The propellant mass required for orbit insertion can be calculated by rewriting the Tsiolkovsky equation as is shown in Equation 6.3, where M_0 is the spacecraft starting mass before the orbit insertion burn, ΔV is the ΔV required for orbit insertion and V_e is the specific impulse of the chosen engine.

$$M_p = M_0 - \frac{M0}{e^{(\frac{\Delta V}{V_e})}} \tag{6.3}$$

Once the required propellant mass is known, a safety factor of 1.1 is applied to obtain the final propellant mass [27]. With the propellant mass and maximum orbit insertion time known, the minimum mass flow rate is calculated by dividing the propellant mass by the maximum orbit insertion time. From this, the minimum required thrust was calculated using Equation 6.4, where $\dot{m}$ is the mass flow rate of the engine, and v_e is the exhaust velocity of the engine.

$$T = \dot{m} \cdot v_e \tag{6.4}$$

By assuming an exhaust velocity, a first estimate for the thrust can be made, which can be used to select an existing engine. By substituting the performance parameters of this engine back into Equations 6.4 and 6.3, together with Equation 6.5, the updated orbit insertion time can be calculated.

$$t_{ins} = \frac{M_p}{\dot{m}} \tag{6.5}$$

This process is then repeated until the orbit insertion time is within the maximum allowed value. Furthermore, the propellant consumed is compared to the input value. If the propellant consumed is higher than the total propellant mass, the propellant mass is increased. If the propellant consumed is lower than the total propellant mass allocated for orbit insertion, the starting propellant mass is lowered. This process is repeated until the propellant mass is sufficient and is within a range of 1 kg of the required mass. At the same time, the MATLAB tool is also sizing the electrical propulsion system such that both systems are tuned to each other. This can also be seen visually in Figure 6.1.

Since the propellant mass is known from Equation 6.3, the required tank volume can also be calculated. Two tanks are required, one for the fuel, and one for the oxidiser. The amount of fuel and oxidiser can be calculated from the total propellant mass, if the oxidiser fuel ratio (O/F ratio) is known. The optimum O/F ratio for each fuel combination was calculated using a software package called Rocket Propulsion Analysis v1.2 (RPA). After the O/F ratio is known, the fuel and oxidiser mass can be calculated with Equations 6.6a and 6.6b, respectively.

$$m_f = M_p \cdot \frac{1}{O/F + 1} \tag{6.6a}$$

$$m_o = M_p \cdot \frac{O/F}{O/F + 1} \tag{6.6b}$$

Where O/F is the oxidiser fuel ratio and M_p the total propellant mass. With the fuel and oxidiser mass known the tank volume can be sized using Equation 6.7 [27], where m is the fuel or oxidiser mass, ρ_p is the density of the fuel or oxidiser at the storage pressure and 1.2 is a factor due to tank ullage and safety factors [27].

$$V_t = \frac{m}{\rho_p} \cdot 1.2 \tag{6.7}$$

6.3.2 Sizing of the electrical propulsion system

As was explained in Chapter 4, the ARMADA mission will use a gravity tractor manoeuvre to deflect the asteroid Apophis. For this, active thrusting is required. In this section the sizing of the propulsion system for this deflection manoeuvre will be discussed. In Chapter 4 an approximation for the spacecraft mass required was obtained. However, this approximation assumes an

average spacecraft mass during the entire deflection manoeuvre. In reality this is not the case - as propellant is consumed the mass of the spacecraft decreases. This decrease in mass means that the thrust required to maintain a thrust to weight ratio of one can also be less. To properly size the electrical propulsion system of the spacecraft the MATLAB tool mentioned in Section 6.3.1 was used. The input of the tool is the average spacecraft mass which was determined in Chapter 4, the propellant mass for orbit insertion, and the propellant mass for the deflection manoeuvre. By choosing a propellant type and thruster type, the specific impulse of the propulsion system is known. With these parameters the deflection distance and the mass, power and thrust can be determined as a function of time. This program is implicit, meaning that several iterations are required to converge to a solution.

First, the gravitational force on the spacecraft is calculated using Equation 4.1. For a small time step, this force is assumed to be constant. A thrust force is then calculated using this gravity force and the thruster angle using Equation 6.8, where is F_g is the gravity force, n_{tr} is the amount of thrusters. α_T is the thruster angle which is calculated according to Equation 6.9, where r_{ast} is the radius of Apophis, d is the hovering distance from the asteroids' centre of gravity, α_{exh} is the angular width of the exhaust plume of the thruster and α_{mis} is the maximum allowed thruster misalignment angle, as determined in the propulsion subsystem requirements.

$$T_{req} = \frac{F}{cos(\alpha_T)} \cdot \frac{1}{n_{tr}} \tag{6.8}$$

$$\alpha_T = arcsin(\frac{r_{ast}}{d}) + \frac{\alpha_{exh}}{2} + \alpha_{mis} \tag{6.9}$$

From the required thrust the mass flow rate can be calculated according to Equation 6.10, where n_{tr} is, again, the amount of thrusters, and T_{req} is the required thrust. $V_{e,ion}$ is the exhaust velocity of the ion thrusters, which was calculated using Equation 6.11, where I_{sp} is the specific impulse and g_0 is the standard gravitational acceleration on Earth at sea level.

$$\dot{m}_{ion} = n_{tr} \cdot \frac{T_{req}}{V_{e,ion}} \tag{6.10}$$

$$V_{e,ion} = I_{sp} \cdot g_0 \tag{6.11}$$

With the mass flow rate known, the new mass, after a short time-step dt, can be calculated. This new mass is then used as input to calculate the gravitational force, and this process is repeated in a loop. At the end of the deflection time, the loop is terminated and the masses per time step are summed up to obtain the total propellant mass required for the ion thrusters during deflection. This propellant mass is then multiplied with a safety factor of 1.1 [27] to obtain the final propellant mass required. Next to the mass, the power required to operate the ion thruster at each time step can also be calculated using Equation 6.12 [37]. Here n_{tr} is, again, the amount of thrusters, T_{req} is the required thrust, $V_{e,ion}$ is the exhaust velocity of the ion thrusters and η is the efficiency factor of the ion thruster used.

$$P_{ion} = n_{tr} \cdot \frac{T_{req} \cdot V_{e,ion}}{2 \cdot \eta_{ion}} \tag{6.12}$$

Lastly, the deflection distance was calculated using Equation 4.3. Based on the deflection distance, and the amount of propellant used, a new estimate is made for the mass. This iteration continues until the deflection distance requirement is met, while minimising the ion thruster propellant mass, the orbit insertion propellant mass and the dry mass of the spacecraft. In Figure 6.1 a block diagram is shown, summarising the methodology discussed in this chapter and as used in the MATLAB tool.

6.4 Verification & Validation

In order to make sure that the outputs of the MATLAB program are sound, verification and validation had to be performed. In order to find potential errors, all equations that could be solved analytically were solved for one particular case. Parts of the program that could not be evaluated analytically were verified by changing input parameters and checking if the results correspond to what was expected using theory. For the required power for the ion thrusters in particular, the model was validated by comparing the theoretical results produced by the model to the power curve given in the data sheet provided by the manufacturer.

6.5 Thruster selection

For ARMADA, an existing propulsion system will be chosen. It is possible to design a full propulsion system, but that is beyond the scope of the proposed project. For that reason, the current market must be analysed and appropriate propulsion systems must be chosen.

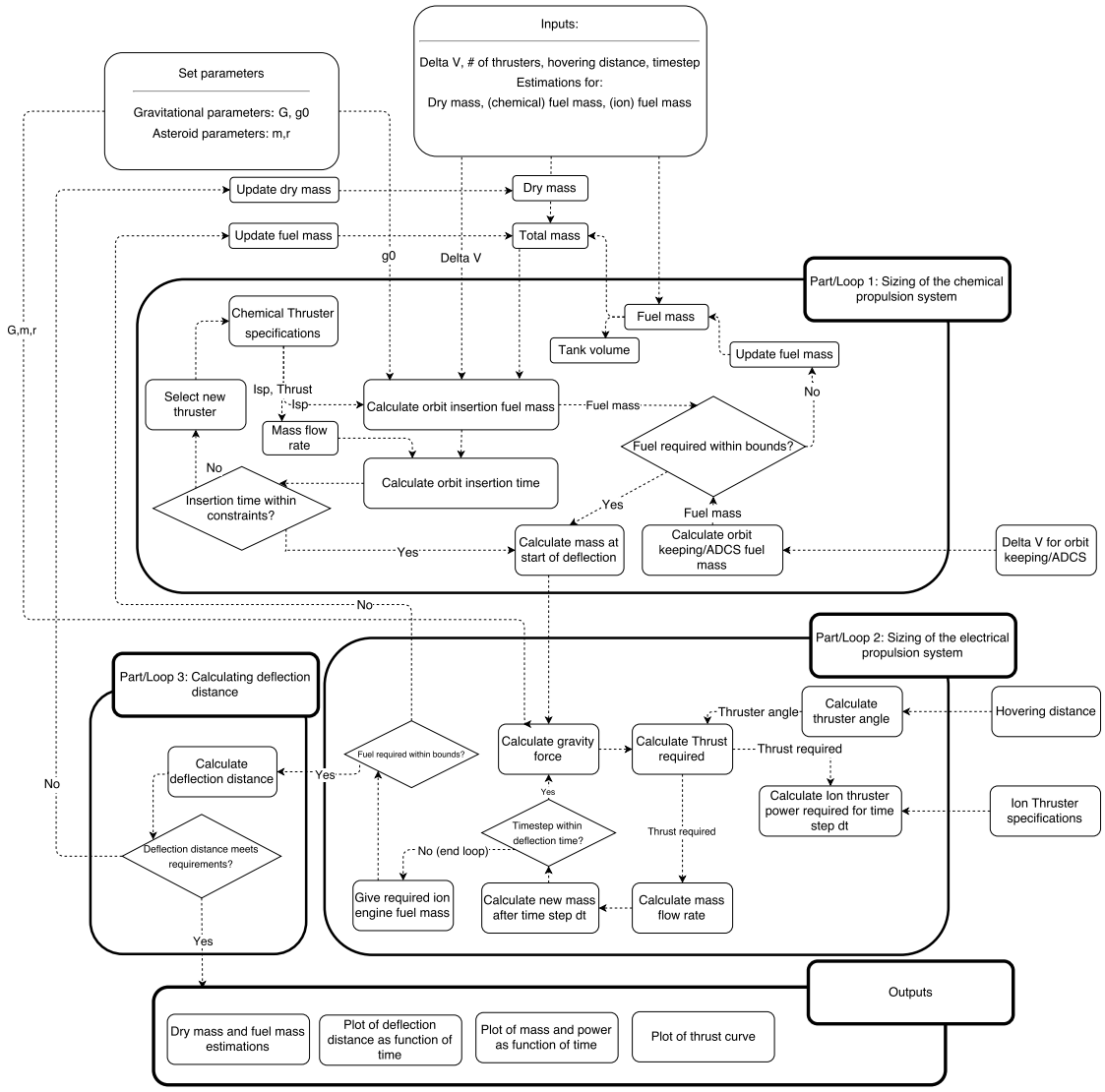

Figure 6.1: Block diagram of the propulsion system sizing MATLAB tool

6.5.1 Thruster selection for the chemical propulsion system

Before thrusters are selected a propellant type had to be selected in order to generate a list of available propulsion systems on the current market. For propellant types, (Monomethyl)hydrazine was selected as the main propellant type, while for oxidisers, dinitrogen tetroxide and so called MON's (Mixed Oxides of Nitrogen) were selected. The main reason for choosing these propellant and oxidiser combinations is that these combinations are hypergolic, which means that the propellant and oxidiser will ignite upon contact. This makes a complex ignition system unnecessary, which makes the system more reliable. Furthermore, these propellant combinations have a relatively high specific impulse and are very common for spacecraft applications [27, 4]. A disadvantage of these propellant oxidiser combinations is the toxicity of the material, therefore precautions should be made to ensure safety during the handling of the propellant.
In order to find appropriate thrusters for orbit insertion, [27] is used to find leading manufacturers in the field of rocket propulsion. Some examples of thrusters are also given in [27]. However, in order to ensure that the most promising thruster is chosen, it is deemed more effective to look at the current market rather than the one of the time when [27] was published. Some of the leading manufacturers are EADS Astrium [4], Aerojet [3], Moog-ISP (formerly known as AMPAC In-Space Propulsion) [85], and Northrop Grumman Space Technology [86]. In Table 6.4 an overview is given of the different thrusters offered by these companies.

Table 6.4: Bipropellant thrusters offered by leading manufacturers

Manufacturer	Engine	Mass (kg)	Propellants	Nominal thrust (N)	I_{sp} (s)
EADS Astrium	4N Thruster	0.65	MMH/N2O4	4	290
	10N Thruster	0.65	MMH/N2O4	10	292
	22N Thruster	0.68	MMH/N2O4	22	300
	200N Thruster	1.9	MMH/MON	216	270
	S400-12	3.6	MMH/N2O4	420	318
	S400-15	4.3	MMH/N2O4	425	321
Aerojet Rocket-Dyne	R-6	0.45	MMH/N2O4	22	290
	R-1E	2.0	MMH/N2O4	100	280
	R-4D	4.0	MMH/N2O4	440	312
	HiPat	5.3	MMH/N2O4	445	323
	R-42	4.53	MMH/N2O4	890	303
	R-40B	6.8	MMH/N2O4	4000	293
Moog-ISP	DST-11H	0.77	N2H4/MON	22	310
	DST-12	0.64	MMH/MON	22	302
	DST-13	0.68	MMH/MON	22	298
	5 lbf	0.80	MMH/MON	22	292
	LTT	0.78	MMH/MON	9	274
Northrop Grumman	TR-308	4.76	N2H4/N2O4	472	322
	TR-312-100MN	6.03	MMH/N2O4	502	325

An important consideration to take into account when selecting the bi-propellant thruster, is the thrust required for orbit insertion. This is a hard constraint, since a thruster that can not provide this amount of thrust can be omitted directly from the thruster options. As discussed in Section 6.3.1 the required thrust is dependent on the Hill sphere of Apophis. The Hill sphere radius can be calculated using Equation 6.1. Since mass estimates of Apophis vary between $2.1 \cdot 10^{10}$ kg [87] and $4.6 \cdot 10^{10}$ kg [50], both values were used to get a worst case scenario and an optimum case scenario. For the remainder of this chapter, the scenario where the mass of Apophis is assumed to be $2.1 \cdot 10^{10}$ kg is called the nominal scenario, whereas the scenario were the mass of Apophis is assumed to be $4.6 \cdot 10^{10}$ kg will be referred to as the worst case scenario. By substituting the relevant parameters into Equation 6.1, the Hill sphere radius was found to be between 21 and 27 km for the nominal case and worst case respectively. With the Hill sphere radius known and the orbit insertion ΔV set equal to 413 m/s, as found in Chapter 3. The maximum orbit insertion time was calculated to be 203.4 seconds, using Equation 6.2. The required acceleration then becomes 2.03 ms^{-2}, and the required thrust for orbit insertion (in the worst case scenario) was found to be 1084 N. Using a similar procedure the maximum orbit insertion time for the nominal case was estimated to be 261 seconds, the required acceleration 1.58 ms^{-2}, and the required thrust 843 N. The thruster was selected based on the worst case scenario, in order to comply with the thrust requirement of 1084 N, it was chosen to cluster two Aerojet Rocketdyne R-42 engines together to perform the orbit insertion burn. This combination has the lowest mass, a relatively high specific impulse and it also complies with the thrust requirement. With the configuration known the orbit insertion time was calculated using Equation 6.5 and was found to be 109 seconds, which is well within the required 203.4 seconds.

Orbit maintenance requires a maximum of about 75 $m\,s^{-1}$ of ΔV per year [27, 88], meaning the required propellant for the orbit maintenance thruster can be relatively low. Using Equation 6.3 it was found that approximately 5 kg of propellant was required for orbit maintenance during the 6 month observation phase. Furthermore the orbit maintenance thrusters will also be used for attitude control as was discussed in Section 6.3.1. Three thrusters will be placed on each of the corners of the spacecraft for full three-axis stabilisation. This means a total of 24 of thrusters are required. The EADS Astrium 10N thruster was selected for orbit maintenance and attitude control because it uses the same propellant and oxidiser as the orbit insertion engines (the Aerojet Rocketdyne R-42), meaning they can use the same propellant tank. Furthermore they are lightweight and meet all the requirements for the attitude control system, as specified in Chapter 7.

6.5.2 Thruster selection for the electrical propulsion system

In order to select the appropriate thruster for the electrical propulsion system, a similar method is followed as for the chemical system. First, an assessment of the market must be made to find leading ion engine manufacturers. As found in [27], some of the leaders in the market are L3 Communications, Qinetiq [5] and Astrium in collaboration with Airbus Defence and Space [89]. An overview of available electrical thrusters is given in Table 6.5.

Table 6.5: Electrical thrusters offered by leading manufacturers

Manufacturer	**Engine**	**Mass** (kg)	**Power** (kW)	**Thrust** (mN)	I_{sp} **(s)**
L3 Communications	2.5cm XIPS 8.0cm XIPS	13.6 2.7	3.4 0.3	124 8	3450 2500
Qinetiq	T5 T6	2.5 8.3	20-825 960-7360	0.6-25 30-230	3500 4000
EADS Astrium & Airbus Defence and Space	RIT 10 EVO RIT μX	1.8 0.440	145-760 50 W	5-25 0.01-3	1900-3200 300-3000

In order to select an appropriate electrical thruster, it is important to first define key constraints that immediately lead to a more narrow design selection space. As explained in Subsection 6.3.2, the required thrust can be calculated immediately. It was found that the thrust that should be provided by one ion thruster lies between 3.2 mN and 9.5 mN (depending on the mass of the spacecraft at a given time). This is computed for a total of 4 thrusters. This constraint directly eliminates all the thruster options but one, namely the Qinetiq T5 Ion Thruster. In order to provide redundancy within the electrical propulsion system, a total of 8 thrusters will be taken on-board.

6.6 Propulsion system sizing results

With the thrusters selected it is possible to give the full subsystem characteristics. This section will contain the most important results from the MATLAB tool discussed in Sections 6.3.1 and 6.3.2. It should be noted that all the results shown here are for a nominal deflection time of 5 years if the mass of Apophis is assumed to be $2.1 \cdot 10^{10}$kg and a nominal deflection time of 6 years if the mass of Apophis is assumed to be $4.6 \cdot 10^{10}$kg.

Using an iterative approach and using the MATLAB tool, it was found that a dry mass of 193 kg was sufficient for a deflection of 11.8 km within 5 years, in case the mass of Apophis is $2.1 \cdot 10^{10}$kg, and within 6 years, in case the mass of Apophis is $4.6 \cdot 10^{10}$kg. For any mass lower than $4.6 \cdot 10^{10}$kg then a deflection is also possible within 6 years with this dry mass.

As discussed in Chapter 3, the required ΔV for orbit insertion is 413 $\mathrm{m\,s^{-1}}$. With this value, the propellant mass required for orbit insertion was calculated to be 78 kg. The propellant for orbit maintenance and attitude control was estimated to be 50 kg, making the total propellant mass 128 kg. Using RPA the optimum O/F ratio for monomethylhydrazine and dinitrogen tetraoxide was calculated to be 2.181 (assuming a chamber pressure of 7.1 bar, which is the chamber pressure used for the R-42 orbit insertion engine). With this ratio the fuel and oxidiser masses were calculated to be 42.13 kg and 91.87 kg respectively, using Equations 6.6a and 6.6b. The pressure inside the tank was assumed to be 15 bar. This pressure was chosen because the orbit maintenance engines and the orbit insertion engines require an inlet pressure between 10 to 23 bar and 6.9 to 29.3 bar respectively, meaning the minimum required pressure would be 10 bar. To accommodate for pressure drops in the feed system, a safety factor of 1.5 was applied making the total pressure inside the tanks 15 bar. Combining these results, the tank volume was calculated to be 0.0578 $\mathrm{m^3}$ for the fuel tank and 0.0766 $\mathrm{m^3}$ for the oxidiser tank using equation 6.7.

Following the procedures in Section 6.3.2, the propellant mass for the electric propulsion system was calculated to be 214 kg. The Xenon propellant is stored at 8.3 MPa, which is the optimum value if a temperature of 300K is assumed [90]. Using Equation 6.7, the tank volume was calculated to be 0.1902$\mathrm{m^3}$. The maximum power required by the ion thrusters was calculated using Equation 6.10 and was found to be 1254 W in the worst case scenario, the minimum power required was found to be 712.2 W. For the nominal case the maximum power required was found to be 572 W and the minimum power was found to be 524.5 W. These values were validated by comparing them with the specifications of the selected thruster. For an efficiency of 52%, it was found that the results from the MATLAB tool correspond exactly to the specifications given on the data sheet for the selected thruster, validating the results of the MATLAB tool. Combining these with the results obtained earlier for the propellant masses, the power required for the ion thrusters and the spacecraft mass as a function of time, during the deflection manoeuvre, were plotted and can be seen in Figure 6.2 for the nominal scenario and in Figure 6.3 for the worst case scenario. From Figures 6.2 and 6.3 it can be seen that the mass and power do not decrease linearly. This is because at the beginning of the deflection manoeuvre the spacecraft is heavier, therefore a higher thrust is required. This, in turn, means that a higher mass flow rate is required, meaning that the mass and power will drop more quickly at the start of the deflection manoeuvre and slower at the end of the deflection manoeuvre.

With the mass known as a function of time, the thrust (as a function of time) is determined using Equations 4.1, 6.8 and 6.9, as well as the methodology described in Section 6.3.2. The

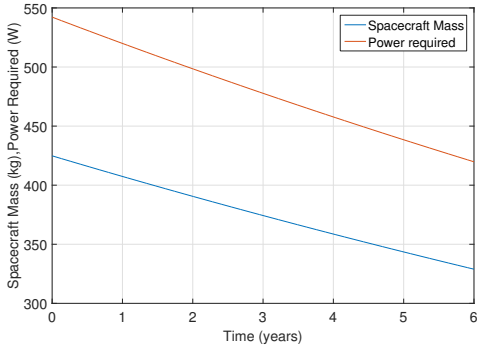

Figure 6.2: Spacecraft mass and ion thruster power as a function of time in the case of a nominal deflection

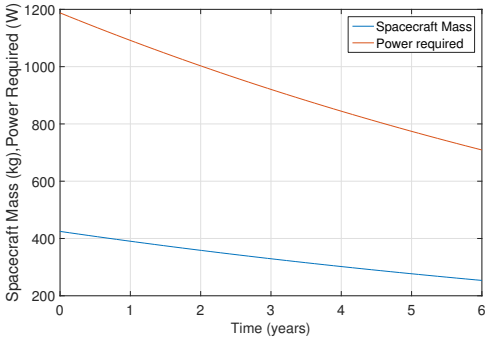

Figure 6.3: Spacecraft mass and ion thruster power as a function of time in the worst case deflection scenario

result is plotted in Figure 6.4 for the nominal case, and in Figure 6.5 for the worst case. It can be seen that the maximum required thrust is 9.5 mN and the minimum required thrust is 5.4 mN in the worst case scenario. In the nominal case the maximum required thrust is 4.34 mN and the minimum is 3.22 mN. These values are well within the operational range of the selected Qinetiq T5 Ion thruster.

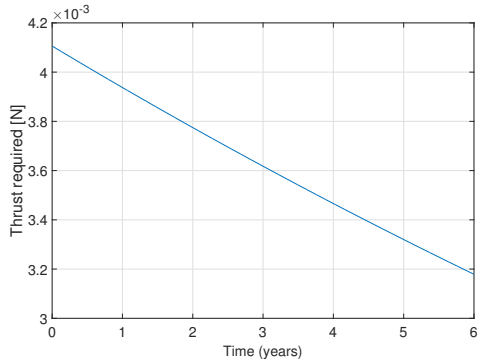

Figure 6.4: Thrust required during deflection (nominal case)

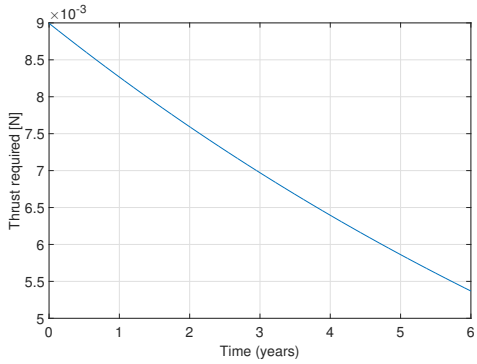

Figure 6.5: Thrust required during deflection (worst case)

With the propellant masses, dry masses, and the thrust known, an updated curve can be produced to show the deflection distance as a function of time. This curve can be seen in Figure 6.6 for the nominal case and in Figure 6.7 for the worst case scenario. It can be seen that in the nominal case the deflection distance is 15.31 km after 6 years, whilst the required deflection distance of 11.8 km is reached after approximately 5 years. In the worst case scenario the deflection distance is 11.804 km after 6 years, meeting the requirement of 11.8 km.

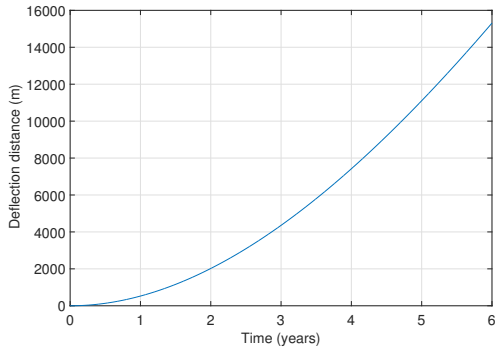

Figure 6.6: Deflection distance as function of time (nominal case)

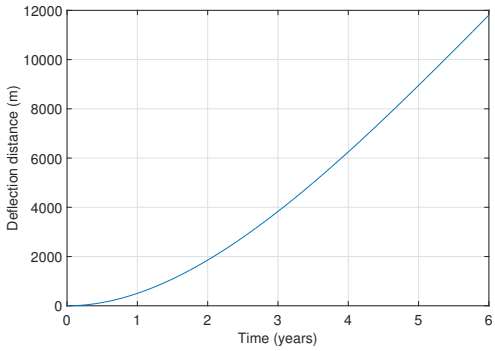

Figure 6.7: Deflection distance as function of time (worst case)

With the deflection distance known, the results for the propulsion system sizing are complete. The most important results of this chapter are summarised below in Table 6.6. The selected engines are shown in Figures 6.8, 6.9 and 6.10.

Table 6.6: Propulsion system sizing results

Parameter			
Launch Mass [kg]	503.5	Orbit insertion time [s]	109
Dry Mass [kg]	212		
Propellant mass (electrical) [kg]	189	Volume Xenon tank [m^3]	0.1680
Propellant mass (chemical) [kg]	102.5		
Oxidiser mass [kg]	*66.16*	Volume Oxidiser tank [m^3]	0.0586
Fuel mass [kg]	*30.34*	Volume Fuel tank [m^3]	0.0442
	Nominal case	**Worst case**	
Maximum power required [W]	542	1187	
Minimum power required [W]	420	709	
Maximum Thrust required [mN]	4.1	9	
Minimum Thrust required [mN]	3.2	5.4	
Deflection distance (6 years) [km]	15.3	11.8	

Figure 6.8: The Aerojet R42 engine used for orbit insertion [3]

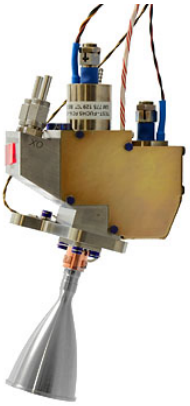

Figure 6.9: The EADS Astrium 10N Bi-propellant engines for orbit keeping and ADCS [4]

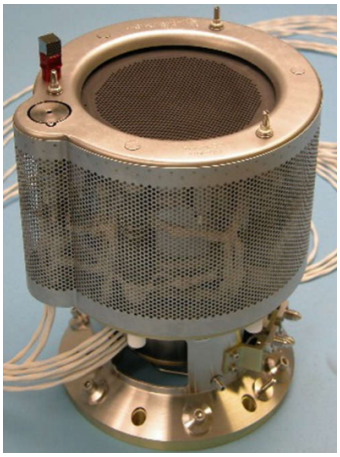

Figure 6.10: The Qinetiq T5 ion thruster [5]

6.7 Propulsion system layout

With all the components of the feed system selected and all the sizing known, the layout of the whole propulsion system can now be completed.

A schematic overview of the feed system for the chemical propulsion system is given in Figure 6.11. Three tanks are used, a fuel tank with monomethylhydrazine (MMH), an oxidiser tank with dinitrogen tetraoxide (N2O4) and a helium tank. This helium tank is optional and may be used in future iterations of the design to increase the performance of the propulsion system by pressurising the fuel and oxidiser tanks. It should be noted that it is also possible to operate the propulsion system without this helium tank, which is how the system operates in the current design iteration. In such a case the system will operate as a blow down system. Furthermore several other components can be seen such as filters, fill and drain valves, pressure transducers, isolation valves, pyro valves and engines. Fill and drain valves are used to fill the tanks at the start of the mission before launch. They can also be used to drain the tanks in case of an emergency or at the end of life of the mission. Filters are used directly downstream of each tank to remove any impurities from the propellants. Impurities can damage engine components or other sensors in the feed system and therefore impurities should be removed from the propellant. Isolation valves can be opened or closed without requiring continuous power [27] and are used to turn engines on or off. An isolation valve is used on each fuel and oxidiser line to supply fuel or oxidiser to the engines. It can also be seen that the EADS Astrium 10N thrusters used for attitude control and orbit maintenance are grouped together in groups of three. However each of these thrusters also have their own isolation valves such that they can be controlled individually. In Figure 6.11 it can also be seen that before the engine inlet of every engine a pressure transducer is placed. This is to measure the pressure at the inlet of the engine to evaluate the engine performance. Lastly it can be seen that before each of the two orbit insertion engines, pyro valves are placed on the oxidiser and fuel lines. These valves are pyrotechnically actuated and can only be used

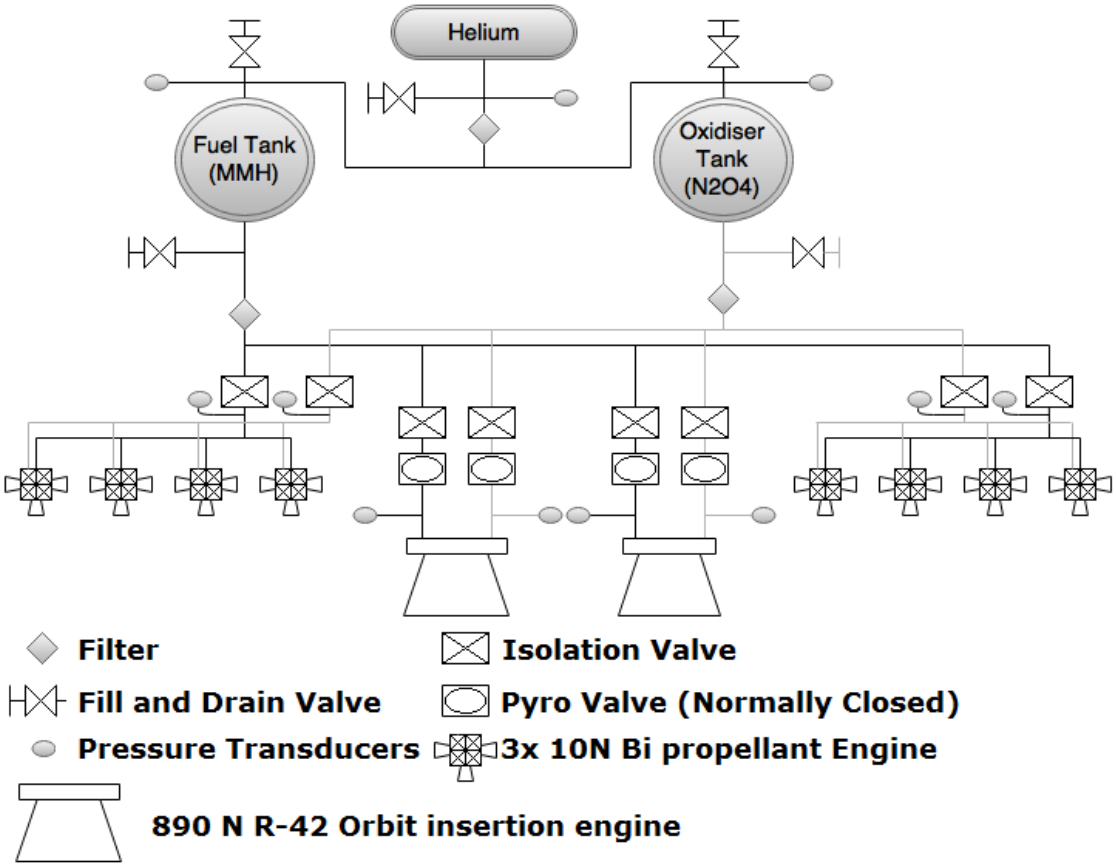

Figure 6.11: Feed system diagram for the chemical propulsion system

once. Their advantage is that they have extremely low leak rates and therefore they are used to ensure safety during ground operations.

7. Attitude Determination and Control System

The Attitude Determination and Control Subsystem (ADCS) is responsible for stabilising and orienting the spacecraft in the desired direction. It is also responsible for counteracting the disturbances present in the space environment within which the spacecraft will operate. In order to be able to meet these two functional requirements, the spacecraft must be equipped with sensors and actuators, which determine the satellite's attitude and contribute to controlling it.

In this section, the internal and external disturbances that the satellite is exposed to are computed. Once the disturbances are quantified, the actuators and sensors are chosen. Finally, the mass and power budget of the ADCS is calculated.

7.1 Introduction

Mission Phases

The requirements for the ADCS are driven by the different phases of the mission and what is to be achieved during these phases. The ADCS will have to meet the different requirements during these phases and will be sized accordingly. Table 7.1 shows which considerations are needed with regards to the ACDS for each mission phase. A description of the individual mission phases can be found in 2.

Requirements

Requirements need to be defined according to the different phases specified in 7.1. During these mission phases, there will be different control and performance requirements that must be met by the ADCS, and the sizing of this system will be based on the requirements that demand the highest performance. This section presents an evaluation of the ADCS requirements that will need to be met according to the aforementioned phases. In Table 7.2, the compliance of the design with the requirements is included. 'Check' indicates the requirement is met. If not, the verification method that should be used to verify the requirement, as given in Section 16.2, is included.

7.2 ADCS sizing method

In this section, the overall method for the ADCS sensor and actuator sizing will be discussed. First of all, the different disturbance torques acting on the spacecraft are obtained in Section 7.2.1, followed by the actuator sizing method in the next section. This method is mainly based on information acquired from [37].

7.2.1 Disturbances

During the mission, various disturbance forces can affect the orientation of the spacecraft by inducing a torque on it. This can come from internal or external sources. Along with the required manoeuvres to be performed using an active control of the ADCS, the actuators must be designed to counteract the torques induced by these disturbances. Certain disturbances can be discounted for ARMADA's mission, such as the torque exerted by the magnetic field, which is considerably large for Earth-orbiting spacecraft, but not abundant for the ARMADA mission orbiting Apophis. Furthermore, as Apophis does not have an atmosphere, there will be no aerodynamic torques.
During mission lifetime, there are also internal torques present, such as torques due to liquid sloshing, thruster misalignment, rotating objects in the spacecraft, thermal shocks and so on. These are extremely difficult to model or compute at this level in the design, as they are mainly dependent on exact layout and structure of the spacecraft. The designers of each of these components, such as the propellant tank, should make sure the induced disturbance torques are limited by taking the right countermeasures. Furthermore, most of these torques are only present for a short time and can be taken care of by an appropriate control loop in the ADCS software. Minimising internal disturbance torques is thus possible, but will require more planning and careful manufacturing, resulting in increased costs.
In order to incorporate some of these internal torques in the actuator sizing method, some parameters used in the equations will be taken as a worst-case scenario [37]. First of all, uncertainties in centre of gravity, which can be around $1 - 3$cm, will be incorporated in such way that the distance between the centre of gravity and action point of disturbance forces have the largest possible distance. Next, thruster misalignment, which can be in the range of $0.1 - 0.5°$, can be taken into account by reducing the effective thrust. Mismatch of thruster outputs can be accounted for by a control loop which compares the actual attitude with the required reference attitude.

Table 7.1: ADCS mission phase considerations

Mission Phase	ADCS considerations
Launch & preparation	None
Transfer	The transfer orbit to Apophis will take 245 days and, during this time, the spacecraft will have to generate power and communicate with Earth. Additionally, payload sensors could be used in this part of the mission for scientific reasons or optical navigation. These activities will require a certain performance in relation to the ADCS, as the payload sensing is the driving requirement with regards to accuracy and jitter for this phase of the mission. The spacecraft might be in a safe or hibernation mode during this phase in order to minimise the power consumption and limit any failures before the actual mission starts.
Injection	Optical navigation will be used in this stage of the mission along with the thrusters used for the actual manoeuvre. The thrusters will have to be oriented precisely in the direction of the desired orbit injection. Some manoeuvres can be necessary in order to acquire the required attitude.
Observation	During observation, the various instruments used for the scientific mission will require a certain pointing accuracy and stability to perform their tasks effectively. This will be derived from the scientific objectives and the corresponding instrument requirements, which can be found in Section 5.1.1. Occasional slew manoeuvres can be required in order to perform certain measurements. Furthermore, the acquired data needs to be sent to Earth and the solar arrays need incident solar radiation.
Deflection	A constant alignment of the ion thrusters is required during deflection to ensure that the asteroid is being deflected in the correct direction and the thrust is not countering this effect by pushing directly on the asteroid. On top of this, the solar cells need to be pointed at the Sun and the antenna needs to be pointed towards the Earth for communication, however the ability to do this at certain times in the mission could be constrained by the deflection requirement. The altimeter still has to be pointed in the nadir direction of Apophis in order to obtain its distance measurements.
End of life	During end of life, the ADCS does not have to perform any special tasks, so this phase is not relevant for this system.

Solar radiation pressure

Light photons from the Sun carry a small amount of momentum ($\approx 1 * 10^{-10}$N m), and when they strike an object, they exert pressure on it. Due to the asymmetry of the spacecraft layout, the centre of mass and solar pressure can be in different locations, leading to a torque when solar pressure is exerted on the satellite body and solar arrays. This phenomenon is complicated to model, however, a good estimate can be made by using Equation 7.1. Here S is the solar constant at the closest distance the spacecraft will be from the Sun, which can be obtained with the inverse squared law from the solar constant at 1 AU which is $S_0 = 1367\text{W m}^{-2}$. c is the speed of light, A_s is the sunlit area, q is the unitless reflectance factor, ψ is the angle of incidence from the sun and Δc is the difference between centres of solar radiation pressure and mass.

$$T_s = \frac{S}{c} A_s (1+q)(\Delta c) cos(\psi) \tag{7.1}$$

The largest solar radiation pressure torque experienced during this mission is when the spacecraft is closest to the Sun. This minimum distance is at perihelion of Apophis at $0.746AU$, the magnitude of this force can be found in Table 7.5.

Gravity-gradient torque

The second disturbance acting on the spacecraft is the gravity-gradient torque. Gravitational attraction is present between any two or more objects of mass. If these bodies are close enough, this attraction will have a considerable value, which is directly proportional to the masses and

Table 7.2: ADCS requirements

Identifier	Requirement	Compliance
ARMADA-ADCS-01	The ADCS shall provide three-axis stabilisation and control during the mission lifetime.	Check
ARMADA-ADCS-02	The ADCS shall have a pointing accuracy of at least 0.05°.	Check
ARMADA-ADCS-03	The ADCS shall be able to counteract all expected disturbance torques.	Check
ARMADA-ADCS-04	The ADCS thrusters shall provide momentum dumping for any internal control wheels once per orbital period of the spacecraft around Apophis.	Check
ARMADA-ADCS-05	The ADCS shall have redundant sensors and actuators.	Check
ARMADA-ADCS-06	The ADCS shall have the ability to perform slew manoeuvres up to 180° in 60 seconds at least twice, along one axis, every week during the observational phase, and once every week during the deflection and transfer phase.	Check
ARMADA-ADCS-07	The ADCS shall incorporate measures to provide a safe mode.	Check
ARMADA-ADCS-08	The ADCS thrusters shall provide a maximum torque of 10N	Check
ARMADA-ADCS-09	The ADCS shall be able to dispose of leftover fuel at the mission end-of-life.	Check
ARMADA-ADCS-10	The ADCS thrusters shall have a misalignment of less than 0.1°	Inspection
ARMADA-ADCS-11	The ADCS shall assure that the solar arrays are pointing at 90 °±5° from the incident solar rays.	Analysis
ARMADA-ADCS-12	The ADCS shall be able to compute its attitude at all times.	Analysis

their separation distance. This gravitational force is also what the gravity tractor concept is based on. Similar to the solar radiation pressure, this gravity force can exert a torque on the spacecraft (due to its asymmetry in centre of mass and gravity). During the spacecraft's operational life, it will get near different celestial bodies, the closest being Apophis and Venus. Every object will exert a gravity-gradient torque on the spacecraft. In order to know which object has the most influence, not only Apophis, but also Venus and the Sun will be taken into account. The torque exerted by Earth is neglected as, during the mission lifetime, the spacecraft is not in the proximity of the Earth, except during the early mission times after launch. These torques only get important in the later mission phases. The approximate gravity-gradient torque T_g can be calculated using Equation 7.2, which is taken from [27]. From this equation it is clear that no torque is present for a symmetric spacecraft where I_z and I_y are equal. The gravity gradient also reduces with distance from the object.

$$T_g = \frac{3\mu}{2R^3} |I_z - I_y| \sin 2\theta \tag{7.2}$$

Here, R is the distance between the centre of the NEO and the spacecraft, μ is the gravitational constant of the celestial body, I_z and I_y are the moments of inertia of the spacecraft around the Z- and Y-axis respectively and θ is the angle between the local vertical and the Z principal axis. It must be noted that this is a simplified expression, as it assumes that the spacecraft's minimum principal axis is in its Z direction [27].

7.2.2 Actuator sizing

After computing the disturbance torques, the different actuators can be sized to counteract these. The actuators which are considered for the ARMADA are reaction wheels and thrusters. Control moment gyroscopes are not taken into account as these have a high degree of complexity compared to the benefit in returns. These are mostly used for high torque applications and require complex control algorithms and momentum exchange for desaturation. This means that they have to be despun when they reach their maximum rotational velocity. This is also the case for momentum and reaction wheels, but these are less complex and still deliver adequate accuracy to the system. Momentum wheels are not considered, as they resist spacecraft control due to their high rotational velocity, which provides gyroscopic stiffness. Of course, this is an advantage for counteracting disturbances, but the disadvantage in control is decisive. Magnetic torquers

are also not considered, as the magnetic field of Apophis, if it even exist, is not known and these are mostly used for Earth orbiting spacecraft. Thus, these are not suitable for interplanetary missions. Furthermore, strong magnetic fields or high currents are necessary to exert torques with these instruments, which also make them less suitable for the ARMADA mission. Finally, they cannot exert a torque along the local field direction, may cause magnetic interference and their torque is sensitive to the position of the spacecraft as stated in [78].

Reaction wheels

Reaction wheels have a zero initial rotational velocity and can rotate in both directions. In this way these can provide control along one axis per wheel. Furthermore, rotating wheels provide gyroscopic stiffness to the system, which is favourable for counteracting disturbances, but unfavourable for control, which was already specified in the introduction of this section. The actual design and configuration of these wheels will be elaborated on in 7.4.1.

In order to size the actual wheels, both disturbance torques and required manoeuvres, such as slewing, have to be taken into account. Then, the wheels need to be sized for the maximum possible torque they have to deliver during the mission time. The disturbance torques are obtained in Section 7.2.1, and should be multiplied by a margin factor, MF, to account for unanticipated disturbance torques, as done in Equation 7.3.

$$T_{RW} = T_D \cdot MF \tag{7.3}$$

During the mission lifetime, different scientific objectives are carried out for which the spacecraft might need to perform slew manoeuvres around different axes. For reaction wheels, the torque required to carry out a slew manoeuvre of θ_{slew} degrees in a maximum time of t_{slew} seconds can be calculated using Equation 7.4, where I is the moment of inertia around the rotation axis.

$$T_{slew} = \frac{4\theta_{slew} I}{t_{slew}^2} \tag{7.4}$$

In addition to sizing for the required torque, the reaction wheels (RW) have to be sized for the amount of momentum they have to store. During the mission, the wheels have to counteract certain disturbances continuously, which leads to increasing rotational speeds and the need for higher momentum storage capabilities. The total momentum storage to counteract the disturbance torque T_D for reaction wheels can be obtained from Equation 7.5.

$$h_{RW} = \frac{0.707 T_D P}{n} \tag{7.5}$$

Here, P is the orbital period of the spacecraft orbiting Apophis. n is either 1 or 4, depending on which disturbance torque, either solar radiation or gravity gradient respectively, is the most influential.

7.2.3 Thruster sizing

In order to size the thrusters, the necessary force to be achieved by this system needs to be quantified. As such, the forces required for various manoeuvres are considered. Firstly, the force due to highest external torques T_D can be calculated using Equation 7.6. Then, the force necessary to perform a certain required slew manoeuvre is obtained in Equation 7.7. Finally, the thrusters should be able to perform momentum dumping for the reaction wheels, governed by Equation 7.8.

$$F_{dist} = \frac{T_D}{L} \tag{7.6}$$

$$F_{slew} = \frac{I\ddot{\theta}_{slew}}{L} \tag{7.7}$$

$$F_{dump} = \frac{h}{L t_{dump}} \tag{7.8}$$

In these equations, L is the corresponding moment arm, I is the mass moment of inertia (corresponding to a certain rotational axis), and $\ddot{\theta}_{slew}$ is the slew acceleration. Furthermore, h is the momentum stored in the reaction wheels and t_{dump} is the time, in seconds, that it takes to dump said momentum.
Now that all forces have been calculated, the thrusters can be sized for the highest disturbance force. This is elaborated on in Section 7.3.
Finally, the required propellant for the thrusters needs to be determined. The main assumption for this computation is that the thrusters will only be used for the big slew manoeuvres and momentum dumping of the wheels. Smaller slew manoeuvres can also be performed using the wheels. Such a manoeuvre consists of two pulses, one to accelerate and one to decelerate. The accelerations only happen for a short amount of time. Momentum dumping only consists of one pulse. Equation 7.9 can be used to estimate the necessary propellant mass M_p.

$$M_p = \frac{I_{total}}{I_{sp} g} \tag{7.9}$$

Here, I_{sp} and g are the thruster specific impulse and gravitational attraction at sea-level, respectively. I_{total} is the total impulse which has to be delivered by the thrusters. This consists of the slew manoeuvre impulses and momentum dumping impulses. The number of impulses was determined considering that it is required to have two slew manoeuvres every week during observation and one per week during the deflection phase. The observational phase is about 10 weeks and the deflection phase can go up to 6 years, which is 312 weeks. As two pulses are required for every slew manoeuvre, a total of $2pulses \times 2week \times 10weeks + 2 \times 1week \times 312weeks = 664$ pulses is required for the complete mission time to perform the slew manoeuvres. The number of momentum dumping pulses can be obtained in the same way, but using one pulse for every wheel, per orbit around Apophis (thus every 95.5 hours) over the complete mission time [37], which is assumed to be seven years. To obtain the total impulse, the number of pulses has to be multiplied by the impulse time. For slew manoeuvres, a time of 3s per pulse is assumed. The pulse time for the momentum dumps can be calculated by rearranging Equation 7.8, and using the design thruster force and reaction wheel maximum momentum storage. Then, these values have to be multiplied by their respective forces, which are calculated in Equations 7.7 and 7.8.

7.2.4 Sensor selection method

In this section the ADCS sensors will be selected. There are two main requirements that need to be taken into account when selecting your sensors: desired spacecraft orientation and the required pointing accuracy. Once these two requirements are set, the ADCS sensors can be chosen from the options shown in Table 7.3.

Table 7.3: ADCS sensors

Sensor	Performance Range	Mass [kg]	Power [W]
Inertial measurement	Gyro drift rate = 0.003° h^{-1}	3 to 25	10 to 200
Sun sensors	Acc. = 0.005 to 3°	0.5 to 2	0 to 3
Star sensors	At. acc. = 1 arcsec to 1 arcmin	2 to 5	5 to 20
Horizon sensors (scanner)	At. acc. = 0.1 ° to 1 ° (LEO)	1 to 4	5 to 10
Horizon sensors (Fixed head)	At. acc. < 0.1 ° to 0.25 °	0.5 to 3.5	0.3 to 5
Magnetometer	At. acc. = 0.5 ° to 3°	0.3 to 1.2	< 1

7.3 Actuator and sensor sizing results

The ADCS system will be designed to counteract the extremes of the disturbances that will be experienced during the mission. A MATLAB model was made using the explained method, and the results are given in this section. All input parameters for Equations 7.3 to 7.8 can be found in Table 7.4 in the same order as they are used in the equations. It must be noted that some of these values are approximations and estimations based on reference data, the set requirements for this system and values obtained by other subsystems. The estimated values include safety margins in order to assure that the ADCS actuators will be able to handle the necessary torques. The verification and validation procedures of the model are also given in this section.

Table 7.4: ADCS input parameters

Parameter	Value	Unit	Parameter	Value	Unit
S	2454	$W\,m^{-2}$	I_z	300	$kg\,m^2$
c	299792458	$m\,s^{-1}$	I_y	300	$kg\,m^2$
A_s	11.6344	m^2	θ	0.01745	rad
q	0.2402	-	MF	1.5	-
Δc	0.3	m	θ_{slew}	π	rad
ϕ	0.19	rad	t_{slew}	60	s
μ_{Venus}	$3.2486 \cdot 10^{14}$	$m^3\,s^{-2}$	P	$3.438 \cdot 10^5$	s
μ_{Sun}	$1.327124 \cdot 10^{20}$	$m^3\,s^{-2}$	I	300	$kg\,m^2$
$\mu_{Apophis}$	1.40154	$m^3\,s^{-2}$	L	0.7474	m
R_{Venus}	$2.41 \cdot 10^{10}$	m	$\ddot{\theta}_{slew}$	0.0175	$rads^{-2}$
R_{Sun}	$1.116 \cdot 10^{11}$	m	t_{dump}	4	s
$R_{Apophis}$	277	m			

Table 7.5 shows the magnitude of the disturbance forces calculated in the model. It should be noted that, due to the symmetric assumption for the mass moment of inertia calculations, all inertia values are equal. To estimate the gravity gradient torque, a moment of inertia difference of $50 kg\,m^2$ was used. It is clear that the gravity-gradient torque of Venus and the Sun can

be neglected with respect to the one from Apophis. This is mainly due to the small distance between the spacecraft and Apophis. The solar pressure gradient is larger than the gravity gradient torque, so this is what the actuators will be sized for.

Table 7.5: Disturbance torques

Disturbance	Value	Unit
Solar radiation pressure	$3.48 \cdot 10^{-5}$	N m
Gravity-gradient Venus	$6.07 \cdot 10^{-17}$	N m
Gravity-gradient Apophis	$1.73 \cdot 10^{-7}$	N m
Gravity-gradient Sun	$2.50 \cdot 10^{-13}$	N m

Table 7.6: Torque, stored momentum and thruster force outputs

Output	Value	Unit
T_{RW}	$5.22 \cdot 10^{-5}$	N m
T_{slew}	1.05	N m
h_{RW}	8.46	N m s
F_{dist}	$4.66 \cdot 10^{-5}$	N
F_{slew}	7.0	N
F_{dump}	6.02	N
M_{prop}	18.20	kg

Furthermore, the values obtained from Equations 7.3 to 7.8, using the input parameters given in Table 7.4, can be found in Table 7.6. It can be seen that the maximum value for the force required is for the slew manoeuvres.

Model verification and validation

The ADCS model is not complicated, as it just incorporates the different functions explained in Section 7.2 and does not have any iterations or loops. For the verification process, standard procedures such as debugging of the code and checking functions through hand calculations are used. All functions were correctly implemented and gave the expected output when using dummy inputs.
After verification the output of the functions was compared to outputs stated in [37], using the same input parameters. The same outputs were acquired, so the validation process was a success. No further verification and/or validation procedures were required as the method is exactly the same as the reference method and the outputs were found to be equal to the reference data, which proves the functionality of the model.

7.4 ADCS sizing assessment and conclusion

7.4.1 Actuator design

In order to design the actual actuators, different considerations have to be taken into account. The basic requirements for the actuators were determined in Sections 7.1 and 7.2 and will be the key factors in the actuator selection. First of all, the reaction wheels will be selected, followed by the thrusters.

Reaction wheels

Reaction wheels can provide torques around one axis per wheel. In order to have three-axis control, this means three reaction wheels are necessary, one for each axis. In case one of the reaction wheels fails, which is plausible, as the mission lifetime is relatively long and reaction wheels can be fragile, four reaction wheels will be used to have no single points of failure as well as fulfil the actuator redundancy requirement. It is important to find the correct configuration of these wheels in such a way that, after the failure of one reaction wheel, the three others can still deliver the required torques around three axes. The solution to this problem is a tetrahedral configuration, illustrated in Figure 7.1. More information on the dynamics of these wheels is not included in this report, as it is outside the scope of this mission phase. More information about this can be found in [6].

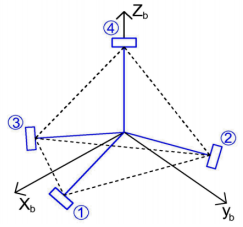

Figure 7.1: Tetrahedral reaction wheel configuration [6]

From Table 7.6, the design parameters for the reaction wheels can be derived. A torque of 1.05N is required, as well as a momentum storage of 8.46N m s. Due to the amount of estimations used, a safety factor of 2 is taken for the preliminary sizing. It is clear that this torque requirement is extremely high as normal reaction wheels can handle torques from $0.01 - 1$N m. Considering this, it was decided to perform all required slewing manoeuvres, except for very small ones, using the thrusters and only use the reaction wheels to counteract disturbance torques. This will increase the required propellant mass, but it will decrease the reaction wheel mass. Different reaction wheels were considered and based on the torque and momentum storage requirement, the W18 reaction wheel unit from MOOG Bradford was selected [23]. Its specifications, per reaction wheel, can be found in Table 7.7. It is clear that these reaction wheels cannot satisfy the torque demand,

but the thrusters are capable enough to create these torques. During safe or hibernation mode, when power needs to be saved, only one wheel can be operated at the time, in order to save power.

Thrusters

For the attitude control, it is required to have three-axes stabilisation or control. This requirement leads the design of the thrusters as enough thrusters should be available for control around three axes. For slew manoeuvres, pure rotations are usually necessary, requiring two thrusters in opposite directions, per axis. In order to spare propellant, it is convenient for the spacecraft to have the ability to rotate in both directions. Otherwise, a 90° rotation in the opposite direction of the thrusters would actually require a 270° rotation, which costs more propellant. This thus leads to four thrusters per axis, which totals twelve. As the ADCS is very important, redundancy is required in order to prevent failures which could have a fatal impact on the mission. This is why 24 thrusters will be used in the design, three on each spacecraft corner.

Table 7.7: Reaction wheel specifications [23]

Parameter	Value	Unit
Momentum storage	18	N m s
Max. torque	0.25	N m
Max. power	29	W
Mass	5	kg
Operational temperature	−15 to 60	°C
Max. operational speed range	4000	RPM

In Table 7.5, the required forces to be delivered by the thrusters are given. The maximum force is 7N. In order to have some contingency, 10N thrusters are used as main ADCS actuators. In Section 6.5.1, different thrusters are given and after consideration, the EADS Astrium 10N thruster was selected to be used in the ADCS as well as for orbit maintenance as explained in Section 6.5.1. The mass of these thrusters is included in the propulsion system mass budget, thus it will not be a part of the ADCS mass budget.

7.4.2 Sensor design

All the sensors given in Table 7.3 were analysed and a final sensor selection was made. It was decided that, for observing and deflecting mission, two kinds of sensors are required. In order to have maximum accuracy and to be able to optimally operate all the payload sensors and point the communication antennas in the desired orientation, star sensors will be used, as they have the best accuracy of all other options and a fine accuracy is required. The spacecraft will be equipped with 6 star sensors and 6 Sun sensors. The Sun sensors can be used for an initial, rather coarse attitude estimate as they are not that accurate. Then the star sensors can be used for more precise measurements.

In addition, when the satellite is in the Sun's proximity, the star sensors might be blinded by the powerful brightness radiated. Because of this, the satellite will also be equipped with Sun sensors. In this way, whenever the Sun blinds the star trackers, the Sun sensors will then be turned on, allowing the system to compute the satellite's attitude. The main reasons for the chosen amount of sensors are redundancy and field of view. When a sensor fails, the ADCS should still be able to determine the spacecraft attitude. Furthermore, one star and one sun sensor will be positioned on each face of the bus in order to supply a broad view and assure enough sensors will always be able to function.

Once the amount of sensors required to ensure mission success is selected, mass and power budgets were computed by selecting existing sensors. More specifications of these systems can be found in [91] and [92]. These can also be seen in Table 7.8. The mass and power given in this table are for ranges of options for each instrument.

Table 7.8: Comparison of considered sensors

Sensor	Accuracy	Mass [kg]	Power [W]
Star sensor (Hydra-M)	0.9 arcsec	1.3	6.8
Star sensor (Hydra-TC)	0.9 arcsec	3.9	8
Star sensor (Hydra CMOS)	0.9 arcsec	1.9	9.8
Sun sensor (nanoSSOC-D60)	< 0.5 °	0.0065	0.115
Sun sensor (SSOC-D60)	< 0.3 °	0.035	0.35
Sun sensor (SSOC-A60)	< 0.3 °	0.025	0.036

The selection of the most optimal star and sun sensors was performed by trading-off the different characteristics of each different component. As it can be seen from Table 7.8, all star sensors have the same accuracy; thus, the sensor with the lowest mass and power consumption will be preferable for the mission. Because of this, the HYDRA-M star sensor was selected. Similarly,

for the sun sensor, it is easy to see that the SSOC-A60 has the same accuracy as the SSOC-D60; however, for the same accuracy, its mass and power consumption are lower. Therefore, the SSOC-A60 was chosen. During safe mode, the Sun sensors are sufficient for attitude determination, which saves power.

7.4.3 ADCS architecture and budgets

In order to give a better overview on the complete ADCS, this section is included. First of all, the architecture, thus, placement of the different components, will be stated followed by the total mass and power budgets.

Architecture

There are four reaction wheels in a tetrahedral configuration. For the torque demands, the placement of these wheels does not matter, so they can be anywhere inside the spacecraft, as long as they are carefully attached so no excessive vibrations can occur. The attachments (bolts etc.) should be sized to withstand the torques created by the wheels. For convenience, one reaction wheel will be aligned with one of the spacecraft body axes. The 24 thrusters will be positioned on the spacecraft corners. Three thrusters aligned with the body axes will be mounted on each corner. The star and Sun sensors are divided over the six faces, one Sun and one star sensor on each face. Their are no exact constraints on their position on the faces, as long as the field of view is maximised, for example by not positioning them in the shadow of another object. Section 13 can be consulted for a more detailed view on the architecture.

Mass & Power budget

In Table 7.9 the total mass and power budget of the ADCS is given. It should again be noted that the thrusters are already included in the propulsion system, thus they will not be taken into account here. Also, the total power budget is higher than the actual operational required power as the four reaction wheels will not be used to their full extent at the same time during the mission. In safe mode, only Sun sensors and one reaction wheel at a time will be used, which leads to a required power of 29.216W during safe mode.

Table 7.9: ADCS mass and power budget

Component	**Mass** [kg]	**Power** [W]	**Amount**	**Total mass** [kg]	**Total power** [W]
Star sensor	1.3	6.8	6	7.8	40.8
Sun sensor	0.025	0.036	6	0.15	0.216
Reaction wheel	5	29	4	20	116
Total				27.95	157.016

7.5 Attitude model

In the previous sections, the ADCS actuators and sensors were determined and sized. Now, an attitude control simulation will be made in order to provide more information on how the spacecraft will act during the mission lifetime, and how it is controlled by the reaction wheels. In order to make this model, different assumptions were made. These are as follows:

- The spacecraft is simulated as a rigid body.
- Gravity gradient and solar pressure torques are neglected. These disturbance torques are both relatively small, as can be seen in Table 7.5, and will thus not be taken into account for this model. However, general disturbance torques will be taken into account, so these continuous torques could be approximated by a step disturbance torque input.
- The principal axes coincide with the body frame axes. This will simplify the inertia matrix according to 7.10. I_{xx}, I_{yy} and I_{zz} are, respectively, the mass moments of inertia around the x-,y- and z-axis.
- The internal control torque is completely supplied by the reaction wheels.
- The rotational and translational equations are completely decoupled, and only the rotational dynamics will be investigated.
- The inertia matrix stays constant during the analysis period. A time derivative of this tensor thus equals zero ($\dot{\mathbf{I}} = 0$).

$$\mathbf{I} = \begin{bmatrix} I_{11} & I_{12} & I_{13} \\ I_{21} & I_{22} & I_{23} \\ I_{31} & I_{32} & I_{33} \end{bmatrix} \approx \begin{bmatrix} I_{11} & 0 & 0 \\ 0 & I_{22} & 0 \\ 0 & 0 & I_{33} \end{bmatrix} = \begin{bmatrix} I_{xx} & 0 & 0 \\ 0 & I_{yy} & 0 \\ 0 & 0 & I_{zz} \end{bmatrix} \tag{7.10}$$

Before any equations of motion can be determined, some reference frames should be defined. In the model, two different reference frames are used, namely a body-fixed and an orbital frame. They are defined as follows:

- **Body-fixed frame (BFF)** - This frame is a right-handed reference frame with x-, y- and z-axis respectively pointed to the left, front and bottom face of the bus. Its centre is in the centre of mass of the spacecraft. Considering this definition, one can notice that this frame always rotates with the spacecraft.
- **Orbital reference frame (ORF)** - This is also a right-handed frame with its origin in the centre of mass of the spacecraft. Its z-axis always points towards the centre of Apophis. The y-axis points towards the Sun and the x-axis makes up the right-handed frame. During the observational phase, when the spacecraft is orbiting Apophis, this axis will be directed along the radial velocity vector of the spacecraft orbit. This reference frame will not rotate with the spacecraft rotation as opposed to the body-fixed frame.

These two reference frames can be transformed into each other using three angles, namely the roll, pitch and yaw angle. For this spacecraft, yaw (ψ), roll (φ) and pitch (θ) are around the z-,y- and x-axis, respectively. It should be noted that both reference frame are the same when these angles are zero. A transformation from the BFF to the ORF can always be defined as a sequence of rotations around the unit axes, also called unit rotations. Using a Z-X-Y or yaw-pitch-roll rotation sequence, the transformation matrix from the ORF to BFF or T_{bO}, results in the final transformation matrix seen in Equation 7.11. Here 'c' and 's' represent cos and sin. Using this matrix, any position vector in the orbital frame can be transformed to its accompanying vector in the body frame. The transformation matrix from the body to orbit frame is just the inverse of this matrix, thus $T_{Ob} = T_{bO}^{-1}$. The rotation matrix is included in this report as it is different from the usual transformation matrix used in aerospace applications.

$$T_{bO} = R_Y(\varphi)R_X(\theta)R_Z(\psi) = \begin{bmatrix} c\varphi c\psi - s\varphi s\theta s\psi & c\varphi s\psi + s\varphi s\theta c\psi & -s\varphi c\theta \\ -c\theta s\psi & c\theta c\psi & s\theta \\ s\varphi c\psi + c\varphi s\theta s\psi & s\varphi s\psi - c\varphi s\theta c\psi & c\varphi c\theta \end{bmatrix} \tag{7.11}$$

The next step in the simulation process is to define the equations of motion (EOM). Then, these equations need to be linearised to get a full set of linearised equations which can be represented in a state-space system. This system can be used as input for MATLAB in order to assess the stability of the system and its reaction to several inputs. In the end, the results will be summarised in Section 7.5.4. The next steps are mainly based on information from [37, 27, 93, 94].

7.5.1 Equations of motion

The EOM consist of both dynamic and kinematic equations, creating a full set of solvable equations. In this section, the derivation of both dynamic and kinematic equations will be given in a concise manner. Not all intermediate steps will be carried out. The main purpose of this section is to give the final EOM. It should be noted that only rotational motion will be taken into account as the main purpose of this method is to simulate the rotational attitude changes during mission lifetime.

Dynamics

The dynamic EOM are based on Euler's moment Equation 7.12. This equation represents the conservation of angular momentum $\mathbf{H}$. Another way to express this is given in Equation 7.13. $\mathbf{T}_D$ is any disturbance torque, ω is the spacecraft rotational velocity vector, $\mathbf{I}$ is the inertia matrix given in 7.10 and $\mathbf{h}$ is the stored angular momentum in any rotating object in the spacecraft, such as the reaction wheels.

$$\dot{\mathbf{H}} = \mathbf{T}_D - \omega \times \mathbf{H} \tag{7.12}$$

$$\mathbf{H} = \mathbf{I}\omega + \mathbf{h} \tag{7.13}$$

Inserting 7.13 in 7.12 and rearranging the terms leads to Equation 7.14. In this step, the assumption of a constant inertial matrix is used to equate the $\dot{\mathbf{I}}\omega$-term to zero. Furthermore, the cross products are rewritten into a linear multiplication using the $\mathbf{S}(\omega)$ matrix, which is given in 7.16. Finally, the rate of change of the angular momentum of the wheels, $\dot{\mathbf{h}}$, equals the total negative control torque $-\mathbf{T}_C$, as the reaction wheels are the only objects which exert an internal control torque. More information on this derivation can be found in [93, 27].

$$\dot{\omega} = \mathbf{I}^{-1}(\mathbf{T}_D - \dot{\mathbf{h}} - \omega \times \mathbf{I}\omega - \omega \times \mathbf{h}) = \mathbf{I}^{-1}(\mathbf{T}_D + \mathbf{T}_C - \mathbf{S}(\omega)\mathbf{I}\omega - \mathbf{S}(\omega)\mathbf{h}) \tag{7.14}$$

$$\dot{\mathbf{h}} = -\mathbf{T}_c \tag{7.15}$$

$$\mathbf{S}(\omega) = \begin{bmatrix} 0 & -\omega_3 & \omega_2 \\ \omega_3 & 0 & -\omega_1 \\ -\omega_2 & \omega_1 & 0 \end{bmatrix} \tag{7.16}$$

Kinematics

It is necessary to define not only the dynamic equations, but also the kinematics of the system. These will also be based on Euler angles. Quaternions can also be used for the kinematics, but, as Euler angles provide a better physical understanding, this method was chosen. It should be noted that Euler angles can give singularity problems in certain cases, but, as only slight disturbances from a initial condition will be studied, this should not pose a problem. For more information about quaternion kinematics, [93] can be consulted. The Euler angle method is mainly based on information from [94].

First of all, the angular rate of the body frame with respect to the orbit frame, Ω_{bO} needs to be derived, which is done in Equation 7.17. This angular rate needs to be expressed in terms of the body frame, so its notation will be Ω^b_{bO}.

$$\Omega_{bO} = \dot{\varphi} y_b + \dot{\theta} x_2 + \dot{\psi} z_1 \tag{7.17}$$

In this equation, y_b, x_2 and z_1 are the rotation axes with b, the body frame, and 1 and 2 the two intermediate frames. Now, x_2 and z_1 need to be expressed in terms of the body frame. This is done by using transformation matrices, obtained in the same way as T_{bO}. After transforming these components, the angular rate with respect to the body frame is given in Equation 7.18.

$$\Omega^b_{bO} = \omega = \begin{pmatrix} \omega_1 \\ \omega_2 \\ \omega_3 \end{pmatrix} = \begin{bmatrix} -\cos\theta\sin\varphi & \cos\varphi & 0 \\ \sin\theta & 0 & 1 \\ \cos\theta\cos\varphi & \sin\varphi & 0 \end{bmatrix} \begin{pmatrix} \dot{\psi} \\ \dot{\theta} \\ \dot{\varphi} \end{pmatrix} \tag{7.18}$$

Inverting this equation leads to the system kinematic relations illustrated in Equation 7.19

$$\Omega^b_{bO} = \begin{pmatrix} \dot{\psi} \\ \dot{\theta} \\ \dot{\varphi} \end{pmatrix} = \frac{1}{\cos\theta} \begin{bmatrix} -\sin\varphi & 0 & \cos\varphi \\ \cos\theta\cos\varphi & 0 & \cos\theta\sin\varphi \\ \sin\theta\sin\varphi & \cos\theta & -\cos\varphi\sin\theta \end{bmatrix} \begin{pmatrix} \omega_1 \\ \omega_2 \\ \omega_3 \end{pmatrix} \tag{7.19}$$

Here, it becomes apparent why Euler angles might be a poor choice in some cases. Due to the $\cos\theta$ term in the denominator, a singularity will form at, for example, $\theta = 90°$. Quaternions or other measures should be taken to avoid this problem if necessary. For the stability analysis, only small deviations will be analysed, as mentioned earlier, so this should not pose a problem for this model.

Reaction wheel dynamics

The previously stated dynamic equations assume a perfect reaction wheel servo, which means the wheel can accelerate infinitely fast. This is, of course, a simplification, as reaction wheels themselves also have inertia and can thus not accelerate at those rates. In order to include the wheel dynamics, a speed control loop can be made around $\dot{\mathbf{h}}$ which will simulate the servo effect of the wheels [93]. The torque on the spacecraft in the Laplace domain is then given in Equation 7.20 where tau_w is the wheel loop time constant. The wheel bandwidth, which will later be used for the control loop, can be defined as $w_b w = \frac{1}{tau_w}$ The Laplace representation is used as it gives insight on the control transfer function.

$$T_c(s) = -\frac{1}{1 + s\tau_w} N_w(s) \tag{7.20}$$

7.5.2 State-space representation

Equations 7.14, 7.20 and 7.19 determine the full set of equations of motion for the system. In order to do a stability analysis and obtain responses of the system to certain inputs, these equations need to represented in state-space form, as presented in 7.21. A state-space requires linear equations, so these three equations need to be linearised in an arbitrary point with respect to the states. Then, the deviation from this initial point can be studied. The state vector $\mathbf{x}$ consists of 9 states: the angular velocities, Euler angles and angular momentum of the wheels. So $\mathbf{x} = [\omega_1, \omega_2, \omega_3, \psi, \theta, \varphi, h_1, h_2, h_3]^T$. The output vector y consists of the angular velocities and Euler angles: $\mathbf{y} = [\omega_1, \omega_2, \omega_3, \psi, \theta, \varphi]^T$.

$$\dot{x}(t) = Ax(t) + B_u T_C(t) + B_d T_D(t) \tag{7.21a}$$

$$y(t) = Cx(t) + Du(t) \tag{7.21b}$$

After linearisation, the different matrices A, B_u, B_d, C and D can be determined and input in MATLAB. B_u and B_d are the control input and disturbance input matrices, respectively. The analysis of the system can be done using control functions from the MATLAB software.
As mentioned in the previous section, wheel dynamics can be included in the model. Doing this

requires to add the wheel state $\dot{\mathbf{h}} = [\dot{h}_1, \dot{h}_2, \dot{h}_3]$ to the state vector, which increases the size of the state-space system. More information can be found in [93].

7.5.3 Attitude control

The method up until now does not contain any actual attitude control. The system is thus still open-loop. In order to include control and create a closed-loop system, a certain reference state should be included in order to calculate a torque demand that will make the actual, measured, state equal to the reference state. The main reason to do this is to make the ADCS more autonomous and able to react to disturbance torques without the need of external commands. For this mission the controller will be based on a reference attitude θ_e and angular velocity ω_e. The control law which incorporates this, is given in Equation 7.22, where T_C is the required control torque of the reaction wheels and K_θ and K_{PD} are two gain matrices [27, 93]. This control law can then be integrated in the state-space system as explained in [93] and will not be elaborated on in this report.

$$T_C = -K_\theta \theta_e - K_{PD}\omega_e \tag{7.22}$$

7.5.4 Results & conclusion

Using MATLAB, different graphs can be made representing the system response to certain disturbances and control torques. The results presented in this section will be kept concise, and only the most important results, which give more information about the system, will be included. In order to estimate the gain matrices, the methods from [93] were used. The wheel bandwidth, which is used to define the gain matrices is taken to be $10.0 rads^{-1}$ as given in [93]. The presented results are mostly qualitative and will not be analysed in too much detail. The figures are included to give a better overview on the dynamics and the motion of the satellite in these cases. In a later design phase, this model can be elaborated on. Next to the presented results, the model can also be used for various simulations, such as torques in several directions or sinusoidal inputs. As no exact design decisions are made from this model, the results are limited to the ones presented below.

Wheel dynamics

In Figure 7.2, a comparison is given between a response due to an input control torque with and without the use of wheel dynamics. It is clear that the response without the wheel dynamics is not realistic, as opposed to the other line, which better represents reality. The final angular velocity of both responses is equal, but the angle, in this case the pitch angle, will lag behind for the case with wheel dynamics, as this response builds up its velocity during the first few seconds as opposed to the other case where the spacecraft directly reaches the final angular velocity.

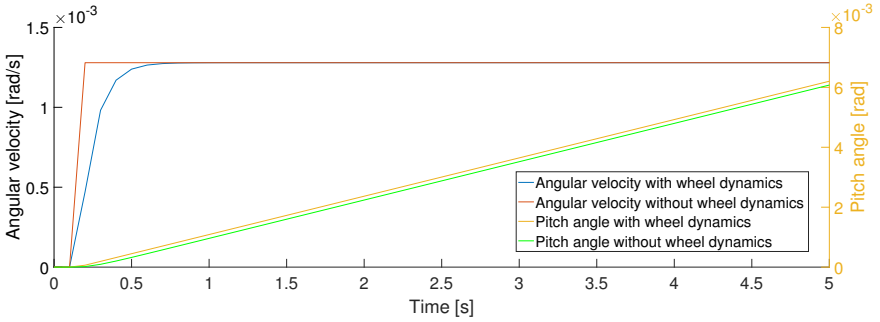

Figure 7.2: System response with and without wheel dynamics

Slew manoeuvre

Performing slew manoeuvres is important during the mission lifetime as it might be required to reorient the spacecraft at certain times. A basic slew manoeuvre works in the following way. First of all, the reaction wheels accelerate, creating a control torque on the spacecraft, which will start to accelerate too. Then, when the required angular velocity is reached, the reaction wheels stop accelerating and keep rotating at this angular velocity for a specific amount of time. Next, when the required rotation is almost reached, the wheels start decelerating again, hereby decelerating the spacecraft. When the spacecraft is stationary again, or when it has reached the required attitude, the wheels stop decelerating and the slew manoeuvre is completed. This is simulated in Figure 7.3 where a slew around the x-axis or pitch axis is represented. The previously mentioned steps can easily be distinguished here.

Disturbance rejection

Finally, in order to give a better view on the implemented control, Figure 7.4 is included. Here, the response to an input control torque is plotted for the closed-loop system. The main objective of the control is to perform disturbance torque rejection. In this case the reference state is equal to the initial state, and from the figure it is clear that the control is functional as the attitude

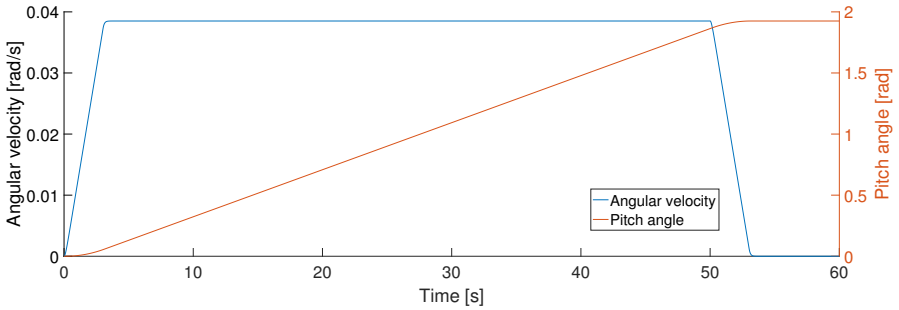

Figure 7.3: Slew manoeuvre simulation

returns to its initial, thus reference, angular velocity after the disturbance. However, the angle does not return to its initial state completely due to an initial reaction of the spacecraft to the torques before the control torques are initiated. An extra control torque will thus be necessary to bring the spacecraft back to its initial state.

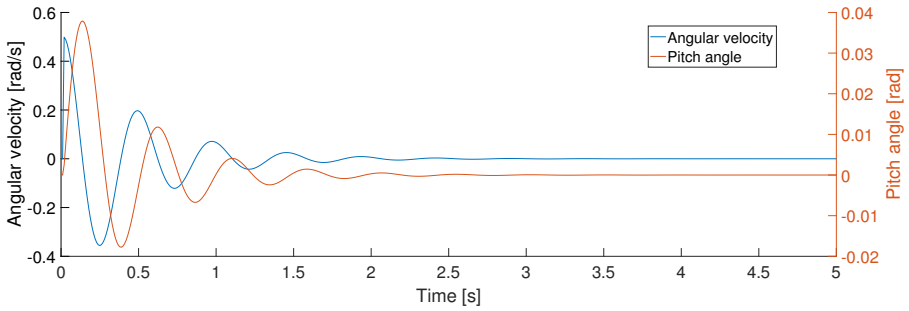

Figure 7.4: Closed-loop response to a continuous disturbance torque

7.5.5 Attitude model verification and validation

This model is mainly based on the use of the equations of motion. If there is a mistake in any of their derivations, a problem can and will occur in the stability analysis. Considering this, these derivations were checked multiple times in order ensure their correctness. These equations were also compared to reference equations, as found in [27, 93, 94]. Different methods of obtaining the kinematics equations were used, all leading to the same equations. Another way to check these equations is to do some hand calculations and see whether the results correspond to expected values.

Once the equations are confirmed to be correct, they are linearised and put in the state-space. Then, this can be inserted in MATLAB in order to perform a stability analysis. Verifying this system can be done in several ways. First of all, zero inputs and initial conditions or other dummy inputs can be used and one can investigate whether the results, thus the responses, correspond with expected results. For example, at zero initial conditions and a step control torque input on one of the axes, a change in angular velocity and angle along this axis will occur. The other parameters along other axes should stay constant. This was found to be the case, as is also visible in Figure 7.2, as only the pitch angle and corresponding pitch angular velocity change after an input torque around this pitch axis. Other tests similar to this were done in order to verify the model. To give an example of a validating hand calculation: using Equation 7.23, the angular velocity due to a certain torque can be obtained, which can then be compared to the result of the model. This was done for different cases along all axes, and the results were always equal to the hand calculation, thus validating the model.

$$T = I\alpha = I\frac{d\omega}{dt} \Leftrightarrow d\omega = \frac{T dt}{I} \tag{7.23}$$

As explained earlier, a singularity can occur at $\theta = 90°$ due to the Euler angle usage. This was also found to be the case in the model. Furthermore, many other sanity checks were conducted in order to further verify the model.

One of the main reason for errors in the model was the reference frame definition. Almost all aerospace applications use the same body reference frame, which is different from the one used in this mission. This led to the lack of reference data usable for validation. It also led to different errors in the model, which were solved during the verification process, as these errors were very prominent in the response analysis.

8. Command & Data Handling

The C&DH system in a spacecraft is equivalent to the human brain; it controls, assesses, monitors and validates all actions going on during the mission. This system has two primary functions; firstly, the system needs to be able to receive data, which will then be validated, decoded and distributed to other satellite's subsystems. Secondly, the C&DH system shall also gather and process all the data obtained during the mission to send it back to Earth or for the On-board Computer (OBC) to be able to use it.

Command messages can originate from three different sources, these being: OBC, uplink transponder and hardline test interface. The commands of each of these sources will then be decoded. The decoding process for the C&DH can be seen in Figure 8.1. Firstly, the arbitration scheme decides which command has the highest priority, and thus needs to be decoded first. Then, the command is validated, decoded, and sent to the system that needs to take the action.

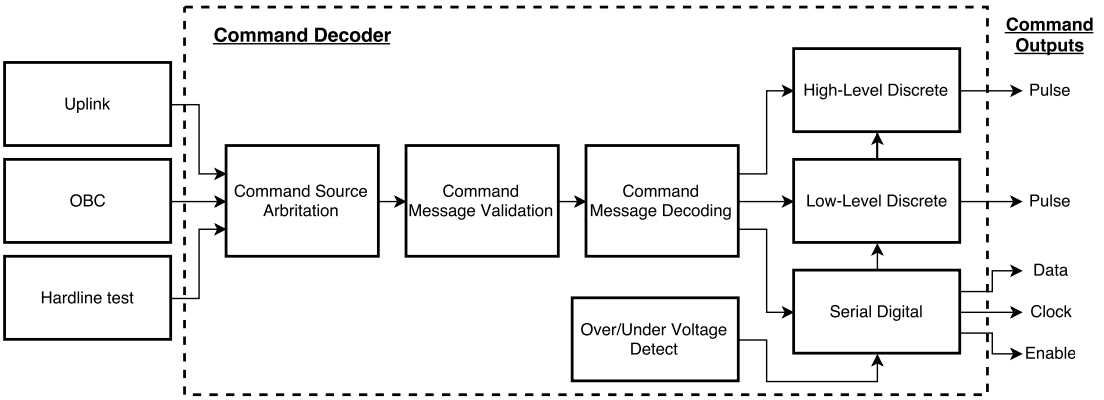

Figure 8.1: C&DH process from received commands to commands' outputs

8.1 C&DH sizing method

The sizing of the C&DH subsystem is carried out in this section in a preliminary way. Detailed is not possible within the given time frame and should be done in a later stage of the design. The output of this process will be an overview of the required hardware to support the mission including estimates of its size, power and mass. The sizing process is mainly based on information from [37] and [27].

System functions

First of all, the main functions which have to be performed by the system are stated in order to find the primary functional requirements for the subsystem. The C&DH system needs to receive and distribute commands to other systems and manages mission data during the mission lifetime.
The communication with the ground segment consists of two parts, namely uplink and downlink. For uplink, all commands and data received from ground needs to be processed and distributed to the correct spacecraft systems or executed directly from the C&DH system. Processing mostly consists of decoding and adapting the received data to the required format. For the downlink, the C&DH gathers all data from the other systems and converts it to the right format for transmitting to Earth via the communication system. The downlink data can contain the following things:

- Orbit or positional data
- Scientific data from the payload sensors
- Status of different systems (housekeeping data)
- Feedback for on-board control

The primary functions of the system are as follows:

- **Command processing** - Commands need to be received and distributed or directly executed by the platform. The main considerations for this function are the number of required output channels, requirements for stored commands in case the spacecraft is not continuously in contact with the ground station and requirements for computer commands or

ADCS functions. If the system itself needs to be able to make decisions and perform computations, for example data processing or running attitude control algorithms, an on-board computer (OBC) is required.

- **Telemetry processing** - The previously mentioned kinds of data need to be processed and send to Earth afterwards. To size the subsystem, it is important to determine the total data rate and amount of data of the system. This is important to know when designing the total required storage space.
- **Time tracking** - The spacecraft might need to keep track of passed time autonomously without input from Earth. This is usually necessary to support different functions of the spacecraft, such as attitude determination and/or control. The main methods to keep time on a spacecraft are computer-maintained counters, hardware timers or GPS receivers, which cannot be used for the ARMADA mission.
- **Computer watchdog** - In order to make sure the on-board computer hardware and software are working as required, a computer watchdog can be used. This is a way of monitoring the computer and detecting possible failures independent of the processor. This is of major importance, as failure of the OBC can lead to catastrophic consequences, such as erroneous attitude control or false formatting or decoding of signals. A watchdog timer, as it is also called, usually works in the following way; countdown timers are used which have to be reset by the OBC before a certain time-out, defined by ground control. If the OBC does not manage this task, the watchdog will carry out a recovery action, which may be resetting the OBC or disabling it until ground control gives a clearance command.
- **ADCS processing** - Usually, the ADCS has its own processing unit, but a part or all of the computational activities can also be carried out by the OBC. This can reduce the total hardware mass of the spacecraft as the OBC contains channels with high current and high accuracy which offer high computational efficiency.

The communication between the different subsystems is illustrated in Figure 8.2.

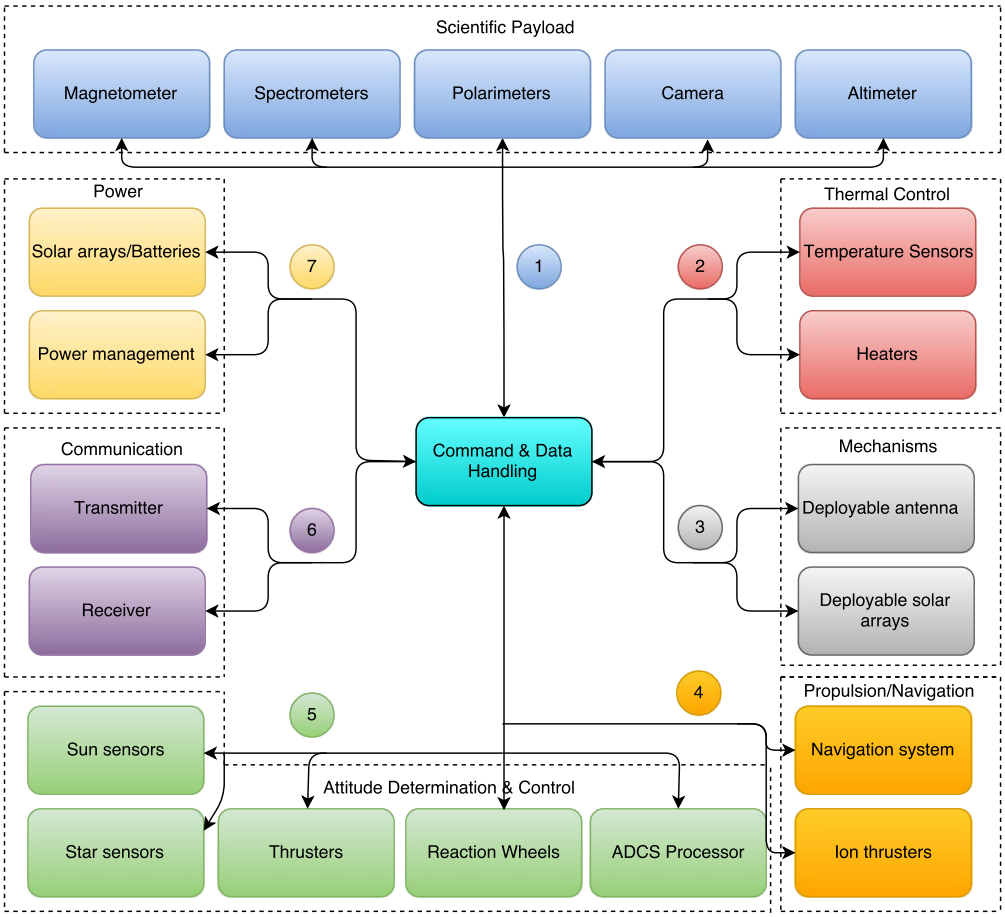

Figure 8.2: Command and data handling communication flow diagram

The numbers on the figure correspond to the order in which the command flow diagrams for specific systems will be presented. Furthermore, it is decided to separate the housekeeping actions

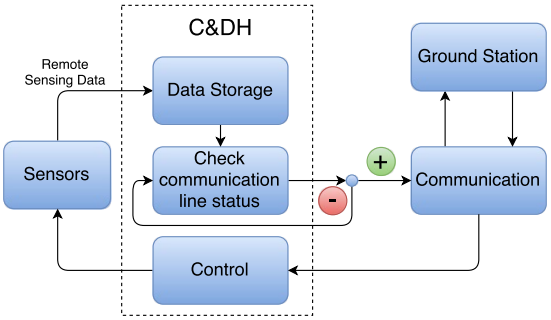

Figure 8.3: Sensors communication flow

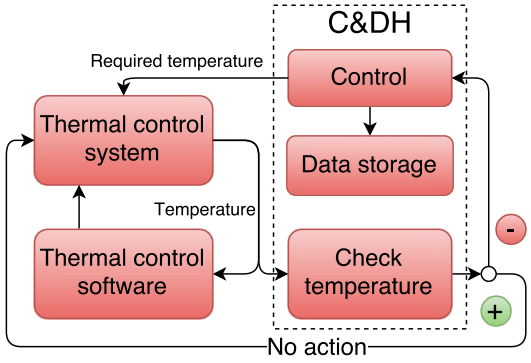

Figure 8.4: Thermal communication flow

from the sensing command and communication line. As such, the observational command line is illustrated in Figure 8.3. It can be seen that the data is first stored, then the communication line is checked to see if data can be transmitted. If it cannot, the system will keep checking until the communication line is free and data can be sent to the ground station. The relevant data will be processed by the ground station, which will then send back a 3D map of Apophis based on data received from ARMADA. It is important to note that all sensors are active at this point and any discrepancy in operational performance needs to be corrected by the C&DH system. The control block will be explained in more detail at the end of this chapter.

Now to define the housekeeping lines - firstly, the thermal command line can be seen in Figure 8.4. The thermal system sends data about the temperatures detected by its sensors from all subsystems. This is fed to the C&DH, which checks this value against its own temperature sensors. If these values differ, the C&DH will need to control this. It is important to note that if a problem arises, the C&DH needs to inform the ground station of this and of the number of stored commands left to deal with this problem. If no problems arise this will also be communicated to the ground station, however, this will be done less frequently.

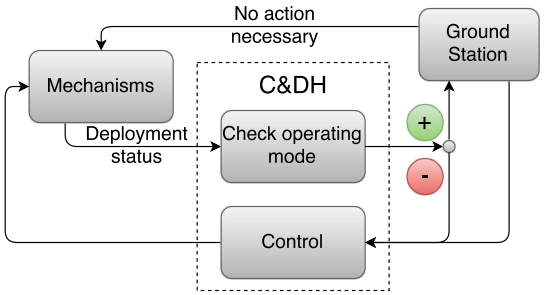

Figure 8.5: Mechanisms communication flow

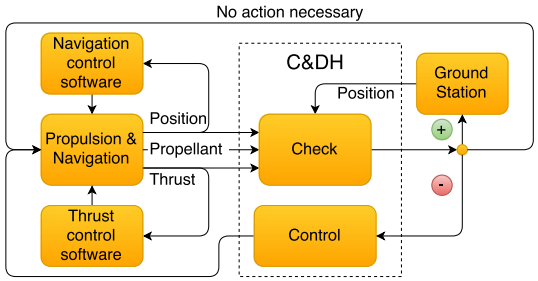

Figure 8.6: Propulsion & navigation communication flow

The next elements to be analysed are the mechanisms. Their interfacing with the C&DH can be seen in Figure 8.5. The deployment status of each mechanism is sent to the C&DH which checks the validity of this based on what operating mode is currently selected (transfer/observation/deflection). This is then controlled if necessary. Similarly to the thermal subsystem, both a problem and an "all OK" signal will be sent back to the ground station, the only difference between them being their sending priority and the frequency with which this information is sent.

The next step is defining the command line between the C&DH and the propulsion & navigation subsystem. This is illustrated in Figure 8.6. This subsystem will send information on remaining propellant mass, thrust level and spacecraft position to the C&DH subsystem. This is then checked against the target position, estimated propellant mass remaining and desired thrust for the particular segment of the mission the spacecraft is currently performing. This is then dealt with in the same way all the previous subsystems have.

Next is the command architecture for the ADCS, which is shown in Figure 8.7. Similarly to the thermal subsystem, the ADCS sends attitude information to the C&DH which checks this against its own data (either from sensors on-board or from the ground station). If a discrepancy is found the necessary action is sent back to the ADCS system, be it a stored command or received from the ground. Furthermore, it is necessary to note that the ADCS, like the thermal subsystem, has a control software that helps avoid attitude discrepancies. The C&DH goes one level further

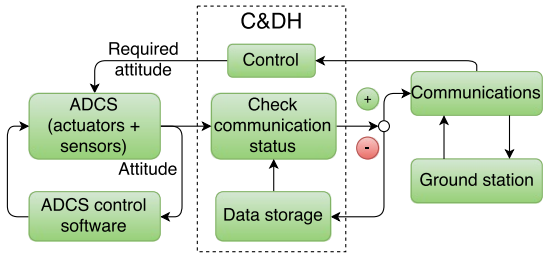

Figure 8.7: ADCS communication flow

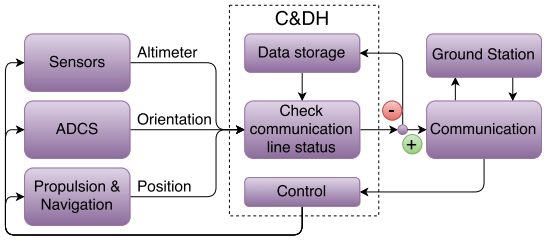

Figure 8.8: Communication flow

and evaluates both the system and this control software, having the choice of commanding either one to evaluate where the problem is.

One of the final subsystems left to be analysed is the communication, for which the command line is illustrated in Figure 8.8. This shows a slightly different case than the previous subsystems. First of all, it can be seen that orientation, position and altimeter data are being constantly communicated throughout the deflection phase. This data will then be sent to ground if the communication line is free, otherwise it will be stored, to be sent at a later time. If any discrepancy arises between the desired parameters and the values detected by the spacecraft, the control block is used to deal with the problem.

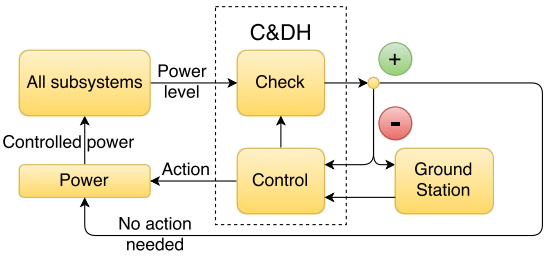

Figure 8.9: Power communication flow

Finally, the last subsystem to be investigated is the power subsystem, evaluated in Figure 8.9. All subsystems will send data on the power level they are currently experiencing. This will be checked against the design values required by each subsystem. If a change in power is needed, the control block will send a command to the power system to lower or increase the power generation to certain subsystems.

The only thing left to be discussed is the control block. This is shown in Figure 8.10. The on-board computer (OBC) will check if there are any stored commands it can use to solve a problem. If there are still available commands that have not been attempted, these will be selected from the data storage and executed. Otherwise, the ground station will be asked for input and the command will come from there.

This effectively describes the architecture of the C&DH, together with the interfaces between this subsystem and all the others inside the spacecraft. Furthermore, the communication done within the system was illustrated through the communication flow diagrams.

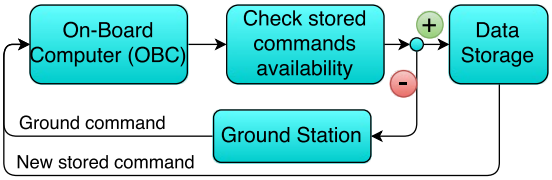

Figure 8.10: Control block

Requirements

The on-board processing requirements can be derived from the missions requirements. For example, the required data storage size can be derived from the extent to which scientific data must be collected from the scientific instruments. It us necessary to identify which subsystem requirements will directly effect the onboard processing. Table 8.2 shows the implications of each other subsystems on the design of the on-board processing and system and the command and data handling in general.

Subsystem complexity

The C&DH subsystem will now be judged in terms of complexity. A more complex system will weight more, cost more and, of course, use more power. In Table 8.1, on the left-hand side one can see the definition of simple, typical and complex C&DH subsystems. The right-hand side shows the requirements for ARMADA's C&DH, in the second to last column, and the required type of system for these requirements and constraints, in the last column.

It can be observed from the data in Table 8.1 that a complex C&DH subsystem is necessary for this particular mission. In Section 8.2, the subsystem weight, power required and size will be correlated with the degree of complexity of the system.

8.2 Results

The mass, power required and size can be determined based on the level of complexity of the system. The values in Table 8.3 for simple, typical and complex systems can be found in [37].

Table 8.3: Mass, power and size estimation for the C&DH subsystem

		Simple	**Typical**	**Complex**	**ARMADA Baseline**
Size [cm^3]	Command only	1500-3000	2000-4000	5000-6000	/
	Telemetry only	1500-3000	4000-6000	9000-10000	/
	Combined systems	2500-6000	6000-9000	13000-15000	13000
Weight [kg]	Command only	1.5-2.5	1.5-3.0	4.0-5.0	/
	Telemetry only	1.5-2.5	2.5-4.0	6.5-7.5	/
	Combined systems	2.75-5.5	4.5-6.5	9.5-10.5	10
Power [W]	Command only	2	2	2	/
	Telemetry only	5-10	10-16	13-20	/
	Combined systems	7-12	13-18	15-25	15

Data storage selection

Now that the general complexity of the system is known, it is time to select a form of data storage. Generally, both processors and data storage devices available commercially need to be significantly enhanced and undergo long-duration testing to prove they can survive the radiation environment of space. In terms of processors, this means a lower frequency can be achieved in space than on Earth. On the other hand, the limit on the amount of data that can be stored is affected by the type of data storage one chooses. This means several types can be compared and traded-off so as to have the best solution tailored to the ARMADA mission profile. In Table 8.4, several different data storage types are compared based on memory capacity, transfer speed, presence of moving parts, cost and resistance to the environment.

Table 8.4: Data storage trade-off

Data Storage Type	**Memory Capacity**	**Transfer speed**	**Moving Parts**	**Cost**
SD card	High	10-12 MB/s	No	Low
Solid State Drive (SSD)	High	1.2 GB/s	No	High
Hard Disk Drive (HDD)	Low	122 MB/s	Yes	Low

It is clear from Table 8.4 that SSD data storage is a better option to take with respect to memory capacity, transfer speed and that it does not include any moving parts. Moving parts have two main drawbacks; they create internal disturbance torques (that will need to be counteracted) and they decrease the reliability of the system. Because of this, the HDD was discarded. Finally, when comparing SD and SSD data storage, cost is the only criterion for which SD card is better suited than an SSD data storage. For the ARMADA mission, cost is not a problem and thus, having a higher capacity and transfer speed will increase the performance of the system and increase the effectiveness of it.
However, "wear-leveling" process is needed for SSD data storage as SSDs cannot write new information without first deleting and then rewriting very large blocks of data at one time. Each time a cell is deleted, the resistance of the transistor increases; increasing resistance leads to an increase in the current required, which may end up being to high for the system to be able to access the data storage [95].

CPU selection

In this section, the CPU that shall be used in the satellite will be selected. In order to be able to make a proper trade-off, a literature study on CPU selection from space missions ranging from Pioneer 10 to Dawn, was carried out.

From this study it was decided that the most suitable CPU system for the ARMADA mission will be one similar to the one used in the Dawn mission. This decision was made as the Dawn and ARMADA missions both have a similar scientific objective, observing an asteroid, and thus, the payload sensors used in both missions are similar (i.e. camera, spectrometer, etc.)[96]. In addition, the CPU used in the Dawn mission, IBM RAD6000, is the state-of-the-art in processing

Table 8.1: CD&H Complexity

Requirement	**System Complexity**			**ARMADA requirements**	**ARMADA complexity**
	Simple	Typical	Complex		
Processing commands:					Typical/complex
CMD rates	50 cmds/s	50 cmds/s	$\geq$ 50 cmds/s	50 cmds/s	
Computer interface	none	Computer or stored cmds	yes	yes	
Stored commands	none	Computer or stored cmds	not needed	necessary	
Number of channels	$<$ 200 channels	300-500 channels	>500 channels	300-500 channels	
Processing of telemetry data:					Complex
TLM rates					
Housekeeping data	500-4kbps	4-64 kbps	64-256 kbps	<20 kbps	
Payload data	none	1-200 kbps	10 kbps - 10 Mbps	92.25 kbps	
Computer interface	none	none	yes	yes	
Number of channels	<200 channels	400-700 channels	>500 channels	>200	
Other:					Typical/complex
Mission time clock	none	included	included	required	
Computer watchdog	none	included if OBC	included	required	
ACS functions	none	none	included		
Bus constraints	Single unit	Single or Multiple units	Integrated or distributed		
Reliability-Class B:				Maximise reliability	
Single String	0.8233	0.7610	0.6983		
Redundant	0.9875	0.9736	0.9496		
Reliability-Class S:				Maximise reliability	
Single String	0.9394	0.9083	0.8285		
Redundant	0.9987	0.9964	0.9829		
Radiation Environment (total dose)	$<$ 2krads	2-50 krads	50K-1Mrads		
Schedule (in months, after order)					
Class B parts	9-12	12-18	18-24	Not applicable	
Class S parts	12-18	20-30	24-36	Under 40 hours	

Table 8.2: Subsystem implications on command and data handling

Subsystem	Implications
Payload	The payload, or more specifically, what is required from the payload will have an effect on the internal data storage of the system. Additionally software will need to be developed to prepare the correct data for downlink.
Power	The command and data handling system will have to distribute the power in the desired way depending on the mission phase. This will often need to be done autonomously and the system will have to identify which systems must take priority in certain situations. Additionally the C&DH system itself will demand power throughout the entire mission duration. The magnitude will vary depending on the mission phase.
ADCS	The ADCS will demand processing power for the interpretation of star and sun sensor results, if the computational power of the ACS processing unit is not sufficient. The OBC will then need to use these to command the spacecraft to obtain the desired attitude. The choice of sensor can also effect the required memory capacity, for example, star trackers identify stars by comparing star patterns against a star catalogue, which can require extensive data and memory sources.
Communication	The amount of anticipated ground commands that will be made can effect the complexity of the system. Storage space required to maintain command lists and sequences will increase as the number of commands increases. The OBC will also have to pack and compress required information for the telemetry stream.
Thermal	The thermal subsystem is active for the entire duration of the mission and will require constant processing power.

units, as it is a 32-bit CPU with the ability to manage its memory [24]. The specifications of this CPU can be seen in Table 8.5. These features were then used to see if the RAD6000 will be able to cope with all the systems in the ARMADA mission. However, to ensure the mission success, the radiation hardness levels of the system were also found in [96]. In this manner, it could be verified if the system will be able to perform under the radiation levels found during its whole operational life.

Table 8.5: RAD6000 key features [24]

Features	Value
Performance	Variable to 35 MIPS
Frequency	Variable up to 33 MHz
Power (max)	13 W at 33 MHz
Power (low)	5 W at 4 MHz
Mass	< 0.8 kg
Size	SEM ES

Table 8.6: Radiation Hardness Levels for RAD6000 CPU [24]

Radiation Level	Value	Units
Total dose	$2x10^{6}$	rads(Si)
Prompt dose upset	$1x10^{9}$	rads(Si)/sec
Survivability	$1x10^{12}$	rads(Si)/sec
Single event upset	$1x10^{-10}$	Upsets/Bit-Day
Neutron Fluence	$1x10^{14}$	$\frac{N}{cm^2}$

Autonomy

Its necessary to mention that, for the system to gain full autonomy, different operational modes are needed for different phases of the mission. These operational modes will dictate what decisions the C&DH can take The ARMADA mission will have three different modes detailed in Table 8.7.

Table 8.7: Operational modes ARMADA

Operational mode	Description
Transfer/Safe Mode	This mode is mainly used during the transfer orbit and injection into Apophis' orbit. This is defined by all the housekeeping elements, in other words, the minimum amount of systems needed to keep the mission on course.
Observation Mode	During observation, aside from the housekeeping functions, the spacecraft will also use its scientific payload. All sensors will be used in cycles defined in more detail in Section 8.3.
Deflection Mode	During deflection, housekeeping functions will be used. Furthermore, the altimeter will be used in cycles in order to effectively maintain hovering distance.

At any point during the mission one of the aforementioned modes is active. Based on what mode is active, the C&DH frequency of communication with ground is affected. The most intensive communication will be done during the observation phase of the mission.

Mission timeline

The final step in the design of the C&DH subsystem is defining the exact time-line of the mission and detailing each phase corresponding to the different modes. In Section 2.2, three phases were defined: transfer, observation and deflection.

During the first stage, only housekeeping functions will be turned on. After launch, when the spacecraft has exited Earth's atmosphere, the solar sails will deploy if the spacecraft is not in eclipse. If it is, this will not happen until the spacecraft has left the eclipsed segment of the journey. At the end of this phase, after 245 days, the spacecraft will be injected into Apophis' orbit, through the use of a manoeuvre lasting approximately 400 seconds.

The second stage is represented by circular orbits around Apophis, at an altitude of 1.5 km. This phase will be separated into three stages. During the first one, the camera will be generating the data necessary to assemble a 3D map of the asteroid. This will be sent to the ground station, where it will be assembled and sent back. In order to make sure the map is as complete as possible, the following approach is used. Firstly, the surface area of Apophis is calculated based on a constant radius assumption. Due to the uncertainty in shape and to account for the slow rotation of the NEO (namely 263 hour period), a safety margin of 1.5 is used for this area. The next step is calculating the area seen by the camera in one 720x720 image, with a 20 cm x 20 cm pixel size. Dividing the calculated area with the safety margin by this area yields the number of pictures necessary, namely 32. Due to the fact that the asteroid is tumbling with a period of 30.5 hours, in order to maximise the mapping done, a safety factor of 2 is chosen for the number of pictures, so as to reduce the uncertainties in the 3D map to be produced. This yields a total of 64 pictures for the full mapping process. As mentioned in Subsection 5.2.1, the camera is equipped with 8 different filters. As such, each measurement will have 8 pictures, not one. This yields a total of 512 pictures necessary for this phase of the mission. The rate at which these pictures will be taken is calculated based on a 10% overlap in pictures with a spacecraft orbital velocity of 0.0274 $\mathrm{m\,s^{-1}}$. This yields a total time of 28.41 days for this stage of the mission. Using a communication duty cycle of 2 hours per day, this yields a data rate of 20.77 kbps. The total amount of data produced is 506.4 MB, which can be stored in the internal memory of the camera before being transmitted.

The second stage of this phase is characterised by the use of X-ray and Infrared Spectrometers, together with the magnetometers and polarimeter, in order to investigate the albedo, magnetic properties, as well as mass composition and distribution of Apophis. It is necessary to note that, since the previously mentioned uncertainties pertaining to Apophis' actual surface area and tumbling rate have not been mitigated, the same amount of time is needed for this stage of the mission. It is important to note that, the sensors will not be taking continuous measurements for 28.41 days. The different measurements will be in increments of 5 cm travelled over the surface of the NEO. With the current orbital speed, this makes the measurement frequency 14.8 seconds, with 1 second of actual measurements. This means the scientific measurements will represent 6.45% of the 28.41 days. With this in mind, the total data rate needed to transfer this information to the ground station is 92.25 kbps with a duty cycle for transmission of 2 hours per day and the total amount of data produced is 2.1903 GB.

At the beginning of the third stage of the observation phase, the 3D map assembled by the ground station should have been sent back to the spacecraft. This means that the uncertainties related to tumbling and area have been resolved. Due to this the safety factor of 2 can now be dropped. This means that for the last leg the time-frame defined is half the time needed for the two previous observation legs, namely 14.205 days. In this final stage of observation, craters will be investigated in more detail and their surface characteristics mapped in more detail using the laser altimeter. The exact number of craters to be investigated is currently unknown, however, it is expected that the total amount of data produced during this phase is less than 100 kbps and

that the most data-intensive phase is the second one. This is validated through the fact that the laser has a relatively low data rate compared to the magnetometer, for example. Furthermore, small regions need to be mapped so, the amount of measurements needed for this purpose, will be relatively low. It is expected that the data storage has been cleared by the beginning of this phase to make room for the 3D map and crater measurements. In this case, the memory capacity is found to be sufficient for this final stage.
The final phase of the mission is the actual deflection of the NEO. During this period, the spacecraft will be hovering at a distance of 277.5 m from Apophis. The altimeter will be taking measurements with a 1 cm accuracy during this time. This data will be used in correlation with the 3D map to maintain the correct altitude. This data will not need to be sent to ground under normal circumstances. It is used by the C&DH subsystem for housekeeping purposes. The duty cycle for communication will still be 2 hours per day, however, since this full time is not needed for spacecraft status update, a large part of this duty cycle is kept as emergency reserve in case critical information needs to be communicated to ground.

8.3 Conclusion

The Command and Data Handling subsystem is the nervous system of the spacecraft and thus, it is the main responsible of all the mission's housekeeping. Due to this, it is essential to minutely design this system to meet all the requirements. The CPU and data storage were selected by using the set requirements as the trade-off criteria between different system choices. The driving requirements for the C&DH subsystem were on the data rates, both housekeeping and maximum, the components necessary, number of channels required and maximum number of commands per second.
Furthermore, from these requirements a literature study was then carried out to discover the different CPUs that were able to fully meet all the set constraints. It was found that IBN RAD6000 processor, which was, in fact, also used in the Dawn mission, was the processing unit which will better perform under the mission's extreme conditions. The IBN RAD600 will be capable of doing all the required housekeeping actions, it will also process and decode all the given or generated commands, and to distribute these commands to each respective subsystem. The specifications of the RAD6000 can be found in Table 8.5 and in [96].

The next step was sizing and selecting the data storage. Data storage main requirement was to be able to store all data generated by the scientific sensors and to safe the commands that cannot be immediately sent to the ground station. After doing a trade-off between the three main types of data storage (SD, SSD and HDD), it was selected that an SSD data storage will fully comply with all the requirements of the mission. Whereas, SD cards don't have enough transfer data speed, and HDD have a low memory capacity to handle all the data gathered by the scientific payload, plus, includes moving parts which greatly reduce the reliability of the system.
Finally, having selected the CPU, data storage and established the communication links between all subsystems and the CPU, the general C&DH architecture was chosen. As the CPU selected was the same processor used in the Dawn mission, and taking into account that both missions have shared objectives and subsystem components, it was decided that the final C&DH architecture of the ARMADA mission will be represented by the Dawn architecture [96]. The data lines with their respective data rates are illustrated in Figure 8.11.

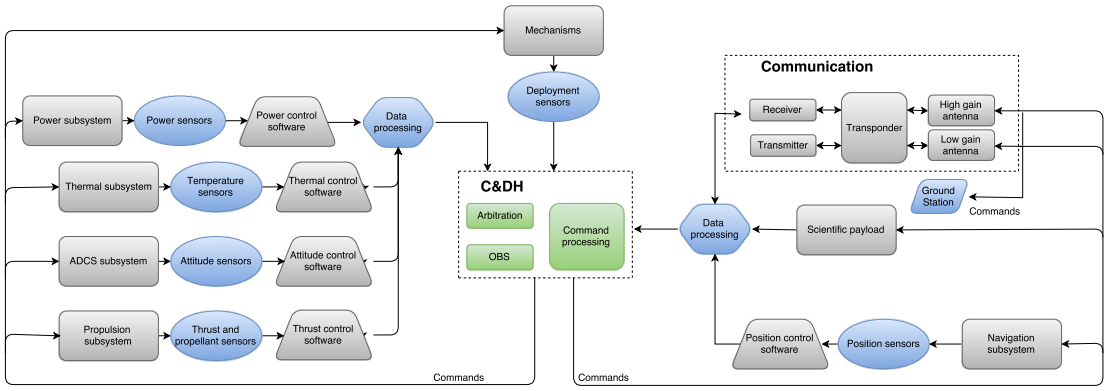

Figure 8.11: Data Handling block diagram

It is necessary to note that the housekeeping data was assumed to be similar to that of the DAWN mission [97]. Furthermore, with a 50 kbps achievable transmission rate, and taking into account the mission timeline, as specified in 8.2, all the necessary scientific data can be sent and processed by the ground segment before the deflection phase starts (namely, the data acquired by the camera), leaving enough space to also send relevant housekeeping information.

Table 8.8: Command & data handling system requirements

Identifier	Requirement	Compliance
ARMADA-C&DH-01	The C&DH system shall contain an on-board computer.	Check
ARMADA-C&DH-02	The C&DH system shall be able to process received commands.	Check
ARMADA-C&DH-03	The C&DH system shall be able to execute received commands.	Check
ARMADA-C&DH-04	The C&DH system shall be able to distribute commands to their target subsystem.	Check
ARMADA-C&DH-05	The C&DH shall allow interfacing between the payload sensors and propulsion to autonomously control its altitude and attitude with respect to Apophis.	Check
ARMADA-C&DH-06	The spacecraft subsystem components shall have compatible interfaces for data links.	Inspect
ARMADA-C&DH-07	The size of the data storage shall allow for a 20% free space for use during the mission.	Check
ARMADA-C&DH-08	The C&DH system shall perform its function over a lifetime of 8 years.	Analyse/Test
ARMADA-C&DH-09	The C&DH system shall be operational within 3.5 years.	Check
ARMADA-C&DH-10	The C&DH subsystem shall have a data storage capacity of 8 GB.	Check
ARMADA-C&DH-11	The C&DH system shall be able to autonomously control power distribution throughout the spacecraft depending on mission phase, prioritising power to the correct subsystems during eclipse or downtime.	Analyse/Test
ARMADA-C&DH-12	The command and data handling system shall continuously monitor the thermal environment and autonomously send commands to the thermal subsystem if required.	Analyse/Test
ARMADA-C&DH-13	The C&DH system shall provide space for command storage.	Check
ARMADA-C&DH-14	The C&DH system shall transform up- and downlink data to the required format.	Check
ARMADA-C&DH-15	The C&DH shall have a command rate of at least $50 cmds s^{-1}$.	Check
ARMADA-C&DH-16	The C&DH shall have a number of channels in the 300-500 range.	Check
ARMADA-C&DH-17	The C&DH system shall provide time tracking during the mission.	Check
ARMADA-C&DH-18	The C&DH system shall contain a computer watchdog.	Check
ARMADA-C&DH-19	The C&DH system shall provide support to the ADCS processing unit when necessary.	Check
ARMADA-C&DH-20	The C&DH system shall be able to monitor the status of all the critical components.	Analyse/Test
ARMADA-C&DH-21	The C&DH system shall provide subsystem status updates to the Earth control segment.	Check
ARMADA-C&DH-22	The C&DH system shall perform both pre-programmed tasks and tasks sent from mission operations.	Check
ARMADA-C&DH-23	The C&DH system shall have a maximum housekeeping data rate of $20 kbps$.	Check
ARMADA-C&DH-24	The C&DH system shall have a maximum data rate of 100 $Mbps$.	Check

9. Communications

The telemetry, tracking and command (TT&C) or communications subsystem is responsible for providing a direct connection with the ground system, in order to communicate with the spacecraft. The different functions to be performed are sending acquired data, receiving commands, and providing the means for tracking the spacecraft. All three functions are performed actively using a transponder, that simultaneously receives and transmits data from and to an antenna. The design of the subsystem includes selecting components that meet the needed specifications, and the sizing of the antenna. In this chapter, the approach to designing this subsystem is described, as well as the results. The first step is defining the requirements and constraints seen in Section 9.1, which was already done for the baseline report. A block diagram, showing the different top-level components in this subsystem was made to identify the component interfaces, concluding the section. A preliminary link budget analysis was done in the mid-term report, and will be continued in this report in Sections 9.2, 9.3, 9.4 and 9.5. A selection of components is done mainly based on reference missions, as described in Section 9.6. The sizing of the antenna is performed in Section 9.7, while the integration in the spacecraft is considered in Section 9.8. The concluding remarks and the mass and power budgets of the communication system are shown in 9.9.

9.1 Requirements and constraints

The requirements on communications from the baseline report are illustrated in Table 9.1.

Table 9.1: Requirements for the communications subsystem

Identifier	Requirement specification	Compliance
ARMADA-COMM-01	The communications subsystem shall be able to convert acquired data to a transmittable format.	Check
ARMADA-COMM-02	The communications subsystem shall be able to transmit acquired data to the ground segment.	Check
ARMADA-COMM-03	The communications subsystem shall be able to receive data from the ground segment.	Check
ARMADA-COMM-04	The spacecraft shall send and receive data using frequencies in either the S-, X-, or Ka-bands.	Check
ARMADA-COMM-05	The spacecraft and ground segment's antenna polarisation difference shall not account for more than 10 % in signal loss.	Analysis
ARMADA-COMM-06	The spacecraft downlink shall have a data rate of 50000 bits per second.	Check
ARMADA-COMM-07	The spacecraft uplink shall have a data rate of 25000 bits per second.	Check
ARMADA-COMM-08	The link budget shall be closed for a signal-to-noise ratio (SNR) of 10.53 dB.	Check
ARMADA-COMM-09	The communications subsystem shall be operative for the entire duration of the mission life time.	Check
ARMADA-COMM-10	The communications subsystem components shall be flight-proven.	Check
ARMADA-COMM-11	The communications subsystem shall be tracked using radiometric tracking.	Check

There are certain constraints on this subsystem. Firstly, the signals have to be compatible with the ground system, in this case the Deep Space Network. This means that the frequency and modulation type are constrained, as well as the transmission periods and scheduling. The antenna has to be integrated in the spacecraft, which has certain implications on its type and size. Furthermore, in case the primary antenna is not functioning correctly, or the spacecraft has lost its attitude control, a secondary low gain antenna is necessary to maintain communication with the spacecraft. There are limits on the transmission power. This is due to the generated heat in the transmitting components, but also due to their limited power specifications. The visibility of the spacecraft, together with the positioning and pointing of the antenna, has to be taken into account. To accomplish a communication, the ground system compatibility is an important input. This will first be considered, after which a link budget for both the downlink as well as the uplink is made, characterising the hardware needed on board. In the mid-term

report, the ground system characteristics were defined to a certain extend, this will be briefly discussed in Section 9.2 and further expanded on.

9.2 Telemetry and Command of the spacecraft

In this section, the uplink and downlink between the spacecraft and the ground system are considered. To establish a link budget, the following assumptions are made on the communication links.

- **No eclipses or unavailable ground station** - It is assumed that the duty cycle of transmitting and receiving can always be achieved, but a margin is set to account for disturbances that delay the next transmitting time, resulting in higher channel capacity needed.
- **Any frequency allocation provided by the DSN can be used** - The current missions will, in reality, occupy many of the available frequencies, but for the design this is not taken into account. This is to not spend time on researching availability, but rather on the actual design. It will have negligible effect on the design results, because the available frequencies lie in close range within the frequency bands.
- **Atmospheric attenuation is constant** - In reality, different frequencies and different elevation of the spacecraft will result in different atmospheric attenuation, but an assumed value is taken instead. This value will be chosen such that the actual attenuation is lower, to prevent the design from under-performing, thus not affecting performance.

The main requirement on the communication links is the amount of data to be sent in a specified time. The channel capacity of the link can be calculated using Shannon's equation [98], seen in Equation 9.1, where the maximum channel capacity C_{ch} is given in bits per second, as a function of the bandwidth, B, and the carrier-to-noise ratio (CNR), or $^C/_N$. The actual capacity of the channel is constrained by the actual spectral efficiency, which is determined by the modulation type. The needed capacity of the channel for downlink is dependent on the downlink duty cycle and the average generated data. The capacity of the uplink is dependent on the uplink duty cycle, and the average command size.

$$C_{ch} = B \ \log_2\left(\frac{C}{N} + 1\right) \tag{9.1}$$

The carrier-to-noise ratio can be calculated using Equation 9.2 from [98], with P_{TX} for transmitted power, G_{AT} the transmitter antenna gain, G_{AR}, receiving antenna gain, L_{FS} the free space loss, L_{atm}, atmospheric loss, k_b the Boltzmann constant, T_{sys} for receiving system temperature, and ,B, bandwidth. G_A and L_{FS} can be calculated using Equation 9.3, where A_E is the antenna effective area, $\lambda = \frac{c}{f}$ is the wavelength, a function of the speed of light c and the frequency f. However, internal circuit inefficiency should also be taken into account, thus a loss factor is subtracted from the CNR.

$$\left(\frac{C}{N}\right)_{dB} = (P_{TX})_{dB} + (G_{AT})_{dB} + (G_{AR})_{dB} - (L_{FS})_{dB} - (L_{atm})_{dB} - (k_b)_{dB} - (T_{sys})_{dB} - B_{dB} \tag{9.2}$$

The transmitted power can be expressed in effective isotropic radiated power (EIRP), which is the product of the transmitted signal power P_{Tx} and the transmitting antenna power gain G_{AT}. As electromagnetic waves are transmitted over an angle, the signal will spread over a larger area, where the signal power per unit area is proportional to the inverse of the square of the distance d covered. Hence a free space loss L_{FS} is taken into account. The budget must close for the worst case, which is the maximum distance possible within the mission [27]. This is calculated using the model described in Chapter 3 to be 2.0996 AU, and occurs on the 24th of August, 2024, at 1221 days from the departure date.

$$G_A = \frac{A_e}{A_{iso}} = \frac{4\pi A_e}{\lambda^2}, \qquad L_{FS} = \left(\frac{4\pi d}{\lambda}\right)^2 \tag{9.3}$$

Atmospheric attenuation, L_{atm}, is dependent on the frequency in which the communication is operated, as the different gases in the atmosphere absorb radiation at certain frequencies. For an X-band frequency of 8.5 GHz, the zenith attenuation (elevation of 90°) is only 0.05 dB [78]. However, for lower elevations, it is assumed to be much higher. For a minimum elevation of 5°, a conservative value of 3 dB is taken, thus half the signal power that enters the atmosphere reaches the ground station.
The noise can be modelled using the system temperature T_{sys}. This is not the total physical temperature, although related to it, as it represents the noise generated in the system. From the DSN, the system temperature is given as a ratio with the gain, $^G/_T$. For the spacecraft receiver, the temperature can be determined for the antenna, transponder and cabling. However,

a conservative value of 500 K is used for the budgets. The noise power can be found using Equation 9.4 with k_b the Boltzmann constant and B the bandwidth of the signal [98]. The bandwidth is selected on the basis of the calculated CNR from a link budget based on the required channel capacity. For the DSN, it is selectable for a bandwidth of 1 kHz – 2 MHz [25].

$$N = k_b T_{sys} B \tag{9.4}$$

For signal quality, the signal-to-noise ratio (SNR) is of interest to calculate the bit error rate (BER). The calculation of the SNR is done using 9.5, where R is the data rate.

$$\frac{E_b}{N_0} = \frac{C}{N} \cdot \frac{B}{R} \tag{9.5}$$

9.3 Tracking the spacecraft

Tracking of the spacecraft can be done using frequency comparison between received signals at ground and a reference generated frequency. The shift in frequency is a function of relative velocity between the transmitter and receiver, and this effect is called the Doppler effect. Tracking can be done in multiple approaches. The one-way approach consists of the spacecraft generating a downlink signal using an on-board oscillator. This signal is transmitted to the ground station, where the difference is measured between the received signal and a local oscillator generating a signal with the same frequency as the on-board oscillator. The two-way approach consists of the ground system generating an uplink signal and sending it to the spacecraft, which tracks the phase of the received signals and returns a phase coherent downlink signal. Finally, the three-way approach consists of two ground systems, of which one has a two-way tracking mode with the spacecraft, and the other only receives the downlink signal. This is done during a switch between ground stations [26]. As the two-way approach gives the most accurate results, this will be used for the tracking of the spacecraft.
For effective tracking with the DSN, a certain transponder turnaround ratio should be used. This means that the phase of the downlink signal should be coherent to the received uplink signal. As the spacecraft will have both uplink and downlink communication in the X-band, the turnaround ratio recommended by the DSN is 880/749 [26]. This means that, for every frequency chosen for downlink, an uplink frequency is set as well, in order to track the spacecraft.

9.4 Chosen characteristics

In this section, the choices and considerations of frequency band, polarisation, modulation, spectral efficiency, data quality and bandwidth will be elaborated on.

Frequency

In the mid-term report [46], three different frequency bands were considered for communication, as they were supported by the DSN: the S-, X- and Ka-band. The latter is only available using the 34m beam wave guide (BWG) antenna, while the S- and X-band are available for all ground system antennas [25]. In addition, the X-band is generally used for deep space missions, thus it is a conservative choice [27]. As the free space loss is a function of wavelength, which is smaller for higher frequencies, there is a combination that is preferred - see Table 9.2. The free space loss values in the table are calculated using Equation 9.3, the others are provided by the DSN [25].

Table 9.2: Comparison of the different frequency bands using different antennas

Specification	**S-band**	**X-band**	**Ka-band**
Average downlink frequency	2250 MHz	8450 MHz	32000 MHz
G/T 34 meter BWG antenna	40.8 dBK^{-1}	54.2 dBK^{-1}	61.1 dBK^{-1}
G/T 70 meter antenna	49.8 dBK^{-1}	61.5 dBK^{-1}	(not supported)
Free space loss, d = 2.0996 AU	-269.45 dB	-280.89 dB	-292.51 dB
Combination using 34 meter BWG antenna	-228.65 dB	-226.69 dB	-231.41 dB
Combination using 70 meter antenna	-219.65 dB	-219.39 dB	(not supported)

When communicating in the X-band, the highest values are achieved independent of the antenna used, thus it is found to be the best frequency band for the communication downlink. As the frequency should have a certain turnaround ratio, the uplink is also assigned to the X-band, as allocated by the DSN. There are 35 different channels with frequencies between 7147 and 7189 MHz for uplink, and between 8400-8446 MHz for downlink [26].

Polarisation

Considering the antenna polarisation, either right- or left-handed circular polarisation shall be used, in order to be compatible with the ground station [25]. This does not further affect the design, although a polarisation mismatch must be taken into account.

Modulation

The digital modulation, or Phase Shift Keying (PSK), type to be used for both downlink and uplink must be supported by the DSN. For downlink three digital phase modulation types are compatible. The types are called Binary PSK (BPSK), Quadrature PSK (QPSK), and Offset Quadrature PSK (OQPSK). PSK is based on phase modulation, a technique in which digital information is coded in the phase of the carrier wave. The choice of which to use lies in a trade-off between the spectral efficiency and the cost, as will be explained here [98]. For uplink commands radiation, the used modulation by DSN is BPSK [25]. BPSK has two possible phases, that are half a period apart. This implies that one phase holds the value '0', while the other holds the value '1'. A transmitted symbol holds one bit. BPSK, QPSK and OQPSK are cases of M-ary phase-shift keying (MPSK), where M is the amount of different phases, and $M = 4$ for the mentioned types. Thus both have four possible phases, all separated by a quarter period. This means that every phase can hold one of four values, thus one symbol contains two bits. The difference is that OQPSK implements a delay in one of the phases, resulting in a maximum phase shift of a quarter period or 90°, in contrast to the maximum phase shift of half a period or 180°for both BPSK and QPSK.

Spectral efficiency

The largest difference in the considered types of modulation is the spectral efficiency of the signal, seen in Equation 9.6, where $M = 2^l$ is the number of phases, R is the bit rate, and B_T is the null-to-null bandwidth. The spectral efficiency defines the amount of bits per second that can be sent, per hertz of bandwidth. Thus, the spectral efficiency of QPSK and OQPSK is generally twice that of BPSK [37], or 1.0 and 0.5, respectively. The maximum possible efficiency η_{max} is found from Shannon's equation, by dividing the channel capacity by the bandwidth. The spectral efficiency can not exceed the maximum efficiency, otherwise large errors will occur [98].

$$\eta = \frac{R}{B_T} = \frac{l}{2}, \qquad \eta < \eta_{max} = \log_2\left(1 + \frac{S}{N}\right) \tag{9.6}$$

Data quality

The other critical factor to take into account is the detection of the signal. All types considered require coherent detection, which implies that the receiver needs a reference signal equal in phase to the received signal. For optimal reception, the bit-error-rate (BER) must be considered. It is defined as the probability an error occurs, or P_e, when receiving a certain amount of bits. This error comes from noise along the path and in the receiver. Generally, the BER is dependent on the signal-to-noise ratio (SNR) or energy-per-bit to noise ratio, or E_b/N_0. An acceptable amount of BER is usually in the order of 10^{-6} [27, 98]. The noise is assumed to be additive white Gaussian noise, which has an even power distribution over frequency and can be added to the signal power for the received power. The probability of error P_e can then be expressed in terms of the Gaussian distribution function $Q(z)$ defined in Equation 9.7 [98], and plotted in Figure 9.1.

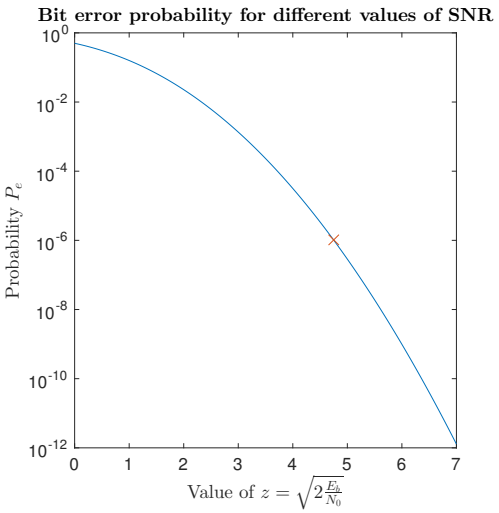

Figure 9.1: Probability of an error for different values of z, which is a function of the SNR. The selected value for the BER is marked.

$$Q(z) \equiv \frac{1}{\sqrt{2\pi}} \int_z^\infty e^{-\lambda^2/2} d\lambda \tag{9.7}$$

For BPSK, QPSK and OQPSK, $P_e = Q\left(\sqrt{2\left(\frac{E_b}{N_0}\right)}\right)$ [98]. The needed signal-to-noise ratio is calculated from 9.7 for a BER of 10^{-6}. This was found to require a value of SNR of 10.53 dB, by selecting the value of z from Figure 9.1. The bandwidths are, however, not the same, as a BPSK signal contains one bit per symbol, where the QPSK signals contain two bits per symbol. In terms of bandwidth, the latter needs only half of that of BPSK [98, 99]. It is therefore preferred to use QPSK for downlink communication, as the bandwidth influences the signal-to-noise ratio for a

selected data rate from the channel capacity.

Conclusion

The choice lies therefore in the mass and power usage of considered transponders to transmit and receive the signals. The design is thus based mainly on the transmitted power, the antenna sizing, the transponder to be used and the bandwidth. In the mid-term report, it was found that the downlink budget closes for bandwidths in the order of 50 kHz. Although the bandwidth is thus slightly constrained by the DSN regulations, the bandwidth has a large influence on the noise generated in the receiving circuit. At all times, the bandwidth should be sized according to the need, and preferably minimised. Furthermore, the transmitter power is constrained by the thermal control and the electrical power available. Finally, the antenna sizing for the gain should take into account that the antenna must be integrated in the spacecraft, and, in addition, it should also be deployable. This constrains the size of the antenna.

9.5 Link budgets

The input values for the link budget are in Table 9.3. The received gain by the deep space network is given by [25], the maximum EIRP of 115.8 dBW at a transmitted power of 20kW for the 70 meter receiver resulted in the transmitting antenna gain [25].

Table 9.3: Inputs for the link budget [25, 26, 27]

Constants and constraints	**Value**	**Unit**	**Ground system**	**Value**	**Unit**
c	$3.00 \cdot 10^{8}$	$\mathrm{m\,s^{-1}}$			
k_b	$1.38065 \cdot 10^{-23}$	$\mathrm{m^2\,kg\,s^{-2}\,K^{-1}}$	Diameter	70	m
BER	$1.00 \cdot 10^{-6}$	$\mathrm{s^{-1}}$	A_{eff}	2892.81	m
d_{max}	$3.15 \cdot 10^{11}$	m	G_{AR}	$2.88 \cdot 10^{7}$	-
R_{avg}	4166.67	bit/s	P_{TX}	20000	W
Duty cycle	0.08		G_{AT}	$1.99 \cdot 10^{7}$	-
L_{polar}	0.9	-	T_{sys}	20.4	K
L_{atm}	0.5	-	Loss factor	0.9	-
Design parameters			**Spacecraft system**		
Spectrum section	X-Band	-	Loss factor	0.9	-
f	8.45	GHz	T_{sys}	500	K
λ	$3.55 \cdot 10^{-2}$	m	P_{TX}	20	W
Modulation	BPSK	QPSK	G_A Primary	10000.0	-
η_{sp}	0.5	1	G_A Secondary	10	-

In Table 9.6 the complete link budget is shown. The basic method of obtaining this budget was as follows. The EIRP was set to 53 dBW. For example, this could be realised using an antenna with 40 dBi, and transmitting power of 20 W. All other inputs come from mission and ground system requirements, or are assumed from other reference missions. As the actual channel capacity is dependent on bandwidth only, and the data is chosen to be as high as this capacity, only the bandwidth was varied to obtain a SNR of at least 10.53 dB. This bandwidth was then used to compute the maximum and actual channel capacity, and thus the data rate. However, for the secondary antenna, the actual data rate was chosen to be different than the actual channel capacity, to ensure a SNR of 10.53. There is, however, no required data rate for the downlink using the secondary antenna, but it should be as high as possible.
The bandwidths used for downlink are found to be 50 kHz for the primary antenna, and 300 Hz for the secondary one. As for uplink, 50 kHz is found for receiving with the primary antenna, and 3000 Hz for receiving with the secondary one. This link budget is made for the worst case distance, however, during the mission, the spacecraft will mostly be at a closer distance to Earth. As this analysis shows that the budget closes for the worst case scenario, the transmitter power could be adjusted to the distance. In addition, if the transponder allows for it, the transmitted bit rate used can be increased for smaller distances, as both the CNR and SNR increase. The uplink budget is shown for maximum transmitter power. However, as the CNR and SNR are rather large, and, in addition, the transmitter power is too large, the latter may be decreased with more than a factor of 10, if necessary. However, for the uplink speed, using the secondary antenna, this results in lower data rates than budgeted. Although the communication link should allow for sending acquired data to the ground, the connection speed is constrained by the limits set on the antenna and transmitting components. If higher data rates than the presented rates are desired, this can be achieved by increasing antenna size or transmitted power, but this will influence the whole design as the mass and power are increased. The data rate of 50000 bits per

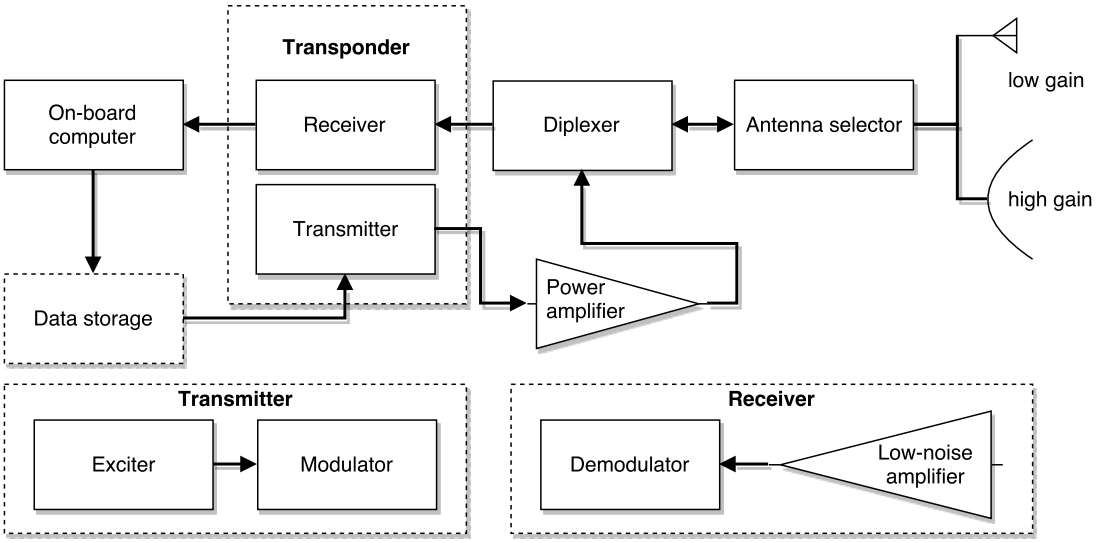

Figure 9.2: Layout of the communications subsystem

second is sufficient to transmit the acquired data back in time.

9.6 Subsystem components selection

The general layout of the subsystem is shown in Figure 9.2. It implies that for the on-board system, three main components must be selected: The transponder, the diplexer, and the power amplifier.

Transponder

The following transponders are considered for the design. They have the required turnaround ratio of 880/740 and receive and transmit in the selected frequency ranges in the X-band. The first is the General Dynamics Small Deep Space Transponder (DST), of which a couple are used in the successful NASA Dawn mission to the asteroids Vesta and Ceres [30]. The output power of this transponder should be amplified to match the set power of 20 Watts. In addition, a diplexer must be selected [28]. The second is the X/X Deep Space Transponder from Thales Alenia Space. This transponder includes a diplexer. This company also provides a transponder for ESA's planned BepiColombo mission to Mercury [29].
The selection of the transponder is thus based on the comparison seen in Table 9.4. Considerable differences lie in the transmitter power usage and output power, and in the transmitter modulation types. The General Dynamics DST needs an extra power amplifier as the output power is much lower. The Thales Alenia DST is lighter overall, as the General Dynamics DST will need a complementary power amplifier and diplexer. Both support BPSK as transmitted modulation type, however the General Dynamics DST is in favour due to the option for QPSK, which was found to be preferred over BPSK. The Thales Alenia DST has an option for Gaussian Minimum Shift Keying (GMSK), but it is not known if this type is supported by the DSN. Concluding, although the Thales Alenia DST is a lighter solution, the General dynamics Small DST is chosen for having the option of QPSK, and being flight-proven.

Table 9.4: Characteristics of the considered Deep Space Transponders [28, 29]

Characteristic	**Unit**	**General Dynamics**	**Thales Alenia**
Mass	kg	3.2	3.3
Size	mm^3	180 x 170 x 110	258 x 148 x 195
Receiver power usage	W	12.5	14
Transmitter power usage	W	3.3	38
Output power	dBm	23.5 ± 2.5	up to 37.8
Operating temperature range	°C	-40 to +60	-20 to +60
Transmitter modulation	-	BPSK (up to 15 Mbps) & QPSK (up to 30 Mbps)	BPSK (up to 512 kbps) & GMSK (up to 10 Mbps)

Power amplifier

From the output, the power must still be amplified, as the maximum output power is 26 dBm or 0.4 Watt. This can be done using two types of amplifiers: Travelling wave tube amplifiers

(TWTA) and Solid State Power Amplifiers (SSPA). SSPAs are mainly efficient at lower power levels in X-band frequencies or less, for output powers of about 15 Watts. TWTAs are more effective at higher power levels, and have a higher overall efficiency, but are heavier [27]. Generally, an SSPA is more suitable for the lower power output, despite its low efficiency. The considered power amplifier is the X-Band Solid State Power Amplifier from General Dynamics. This amplifier comes in combination with the Small DST from the same company. It is capable of delivering a maximum of 17 Watts of output power. However, it has a high input power, about 60 Watts nominal. The total power will then be set to be 75.8 W [32]. For future design phases, a different amplifier could be chosen to decrease power. For instance, the TWTA that was used in the Dawn mission could also be an option, but this unit has an even higher power usage [30]. In addition, the SSPA used in the NEAR mission has a lower input power of 34 W, but also a low output power of 5 W [31]. In case no suitable solution is found, the amplifier could be a custom design to maximise efficiency.

Diplexer

General Dynamics also provides diplexers to be used in this configuration. These are suitable for the required circular polarisation and frequency ranges [33]. An estimate of the diplexer mass is based on reference missions. The Dawn mission used diplexers with a mass of 0.6 kg [30], the NEAR mission used diplexers with a mass of 0.1 kg [31]. A conservative value is found to be 0.5 kg.

9.7 Antenna sizing

The communication subsystem will be equipped with one main high-gain antenna, and one type of secondary antenna that will be used in case the first antenna encounters any functional problem. The next step is to size each of these components and make a trade-off between the different secondary antenna options, to see which one complies best with the mission requirements.
There are two main parameters to size for an antenna: the gain and the half power beam-width (HPBW). Once these two parameters have been sized, the rest of the antenna can be tailored. The gain of an antenna is described in Equation 9.3.

$$G = \eta \left(\frac{\pi D f}{c} \right)^2 \tag{9.8}$$

Where, G is the antenna gain, η is the antenna efficiency, D, the antenna diameter, f, the frequency used and c, the speed of light. The efficiency of the antenna is composed of several efficiencies, such as radiation efficiency due to ohmic losses, aperture taper efficiency, and spillover [100]. However, for the sizing of the antennas, a typical efficiency value for each antenna type was found in [37]. The results of the antenna gain for the main and secondary antennas can be found in Figure 9.3.

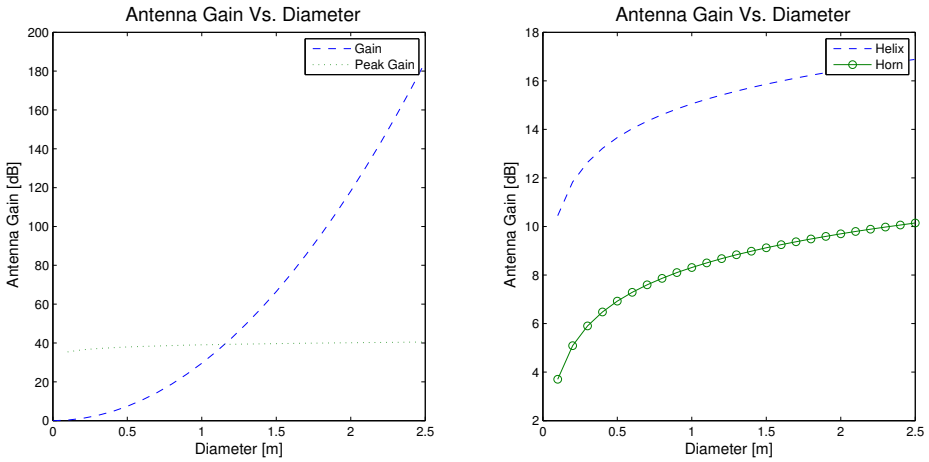

Figure 9.3: On the left the main antenna gain, on the right figure, the gain of both a helix and horn antenna for each diameter

From the figure it can be seen that the peak gain and average gain of the main antenna have an intersection point. The main antenna will be sized for this point and thus, shall have a gain of $42.88dB$ with a diameter of 1.2m. On the other hand, it can also be seen that the helix antenna has a higher gain than the horn antenna for the same diameter. Nevertheless, the secondary antenna is required to have a gain of $10dB$. From Figure 9.3 it can be seen that the range of gain of the helix antenna is always above the required and thus, the component would be over-designed. Due to this, the horn antenna will be selected. For a horn antenna to have a gain of $10dB$ the required diameter will be 0.2m.

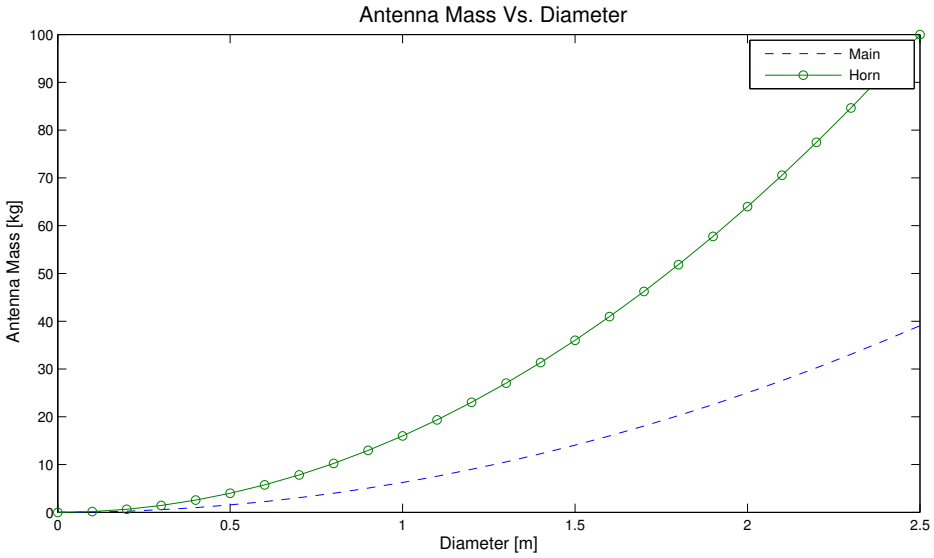

Figure 9.4: Primary and secondary antenna's mass

The next step is to compute the area for each antenna type, and to estimate the relative mass. Since the area of a parabolic antenna is directly proportional to the diameter squared, and the horn antenna is proportional to the product of the diameter and width of the horn, the areas of each antenna were calculated and, from it, the masses could be computed. The mass of each antenna type can be seen in Figure 9.4.
Correlating the diameter required to achieve the necessary gain for the mission with Figure 9.4, the masses are calculated to be 6.7858kg and 0.640kg for the primary and secondary antennas, respectively. Finally, the last parameter to compute for both antennas is the HPBW. This value will serve as a reference to know the amount of power that is lost by a misalignment in the antenna. The results are illustrated in Figure 9.6. In order to clarify the final design of the horn antenna, Figure 9.5 was added. The height of the horn antenna was determined to be 0.311m and the diameter was sized to be 0.2m.

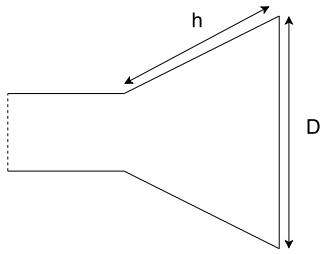

Figure 9.5: Horn size parameters

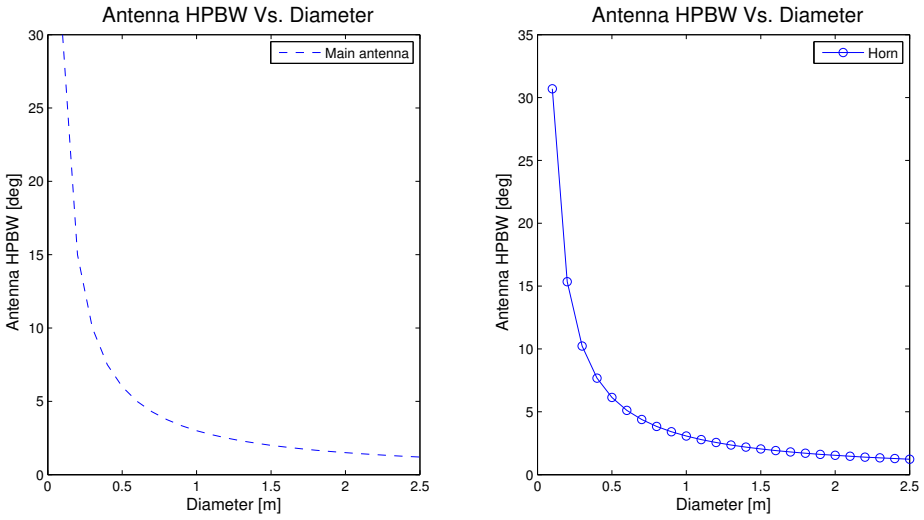

Figure 9.6: On the left, primary antenna's HPBW for different diameter values, and on the right, secondary antenna's HPBW for varying diameter

9.8 Integration into spacecraft

Now that the components are selected and sized, they should be integrated in the spacecraft. During launch, the antenna should be secured to the spacecraft, and, after separation, it should be deployed and positioned such that it can be pointed towards the ground system. The attachment, the deployment mechanism, and a pointing mechanism should thus be selected to allow for communications. From other missions, it follows that there are several ways to implement this. The Rosetta spacecraft uses two mechanisms: The Hold-down and Release Mechanisms (HRM) and the Antenna Pointing Mechanism (APM) [101]. As the names indicate, the HRM is used for keeping the antenna into place during launch, and deploy it after separation. The APM is then used to point the antenna over two rotational axes. The Dawn spacecraft used a fixed antenna, meaning it must be pointed using attitude control [30]. Also, the NEAR spacecraft used a fixed antenna, as the trajectory allowed for this [31]. For the ARMADA mission, there are several demands on the attitude of the spacecraft from the payload sensors, solar arrays, and thrusters. This means that, in order to increase communication window opportunity, an APM is used to turn and point at different angles about, at least, one axis. An example is the pointing mechanism from RUAG designed for a mission called SILEX. RUAG provided the pointing mechanisms for the Rosetta mission. This mechanism weighs 9 kg, and is able rotate the antenna over one axis. It uses less than 6 W of power [34]. Before launch, the dish should take the minimum amount of space possible. After launch, the dish must be deployed. To achieve this, the deployment mechanisms of RUAG could be used. The deployment mechanism for large appendages is a non-reversible system that provides rigidity and high position accuracy. The mass is only 1.5 kg [34]. As for positioning, the high gain antenna will be placed on top of the spacecraft in launch configuration, as this location allows for the space needed as well as the loads to be carried. The low gain antennas are positioned such that they are pointing in different directions along the axis. This is done to increase the covered angles relative to the spacecraft and, thus, the probability of picking up a signal, in case the attitude control fails and the spacecraft is tumbling.

9.9 Conclusion

As the components are now selected from the requirements that followed from the Deep Space Network needs, a final mass and power budget can be given, seen in Table 9.5, where also the operational temperature range (OTR) is given. For redundancy, two of the selected components will be used, which is common practice in spacecraft, as seen in reference missions [30, 31]. For the antennas, only one high gain antenna is used, while three low gain antennas are implemented with different orientations. The cabling is an estimate from [27].

Table 9.5: Communication subsystem mass and power budget [27, 30, 31, 28, 29, 32, 33, 34]

Component	**Quantity**	**Mass [kg]**	**Power [W]**	**OTR [°C]**
Transponder	2	3.2	15.8	-40 to 60
Power amplifier	2	1.37	60	-40 to 60
Diplexer	2	0.5	-	-
High gain antenna including waveguides, feed, etc.	1	6.7858	-	
Pointing mechanism	1	9	<6	-
Deployment mechanism	1	1.5		-30 to 50
Low gain antenna	3	0.64	-	
Cabling	-	5	-	
Total		34.35	75.8 to 81.8	

Table 9.6: Link budget when using the primary or the secondary antenna

Downlink budget	**Primary**	**Secondary**	**Unit**
Transmitting circuit loss	-0.46	-0.46	dB
Transmitting power	13.01	13.0	dBW
Transmitting antenna gain	40.00	10.00	dBi
Free space loss	-280.9	-280.9	dB
Atmospheric loss	-3.0	-3.0	dB
polarisation loss	-0.46	-0.46	dB
Receiving circuit loss	-0.46	-0.46	dB
Receiving antenna gain	74.6	74.6	dBi
System temperature	-13.1	-13.1	dBK
Boltzmann's constant	228.6	228.6	dBW/(K.Hz)
Bandwidth	-47.0	-24.8	dBHz
Total CNR	10.8	3.0	dB
Required channel capacity	50000	-	-
Maximum spectral efficiency	3.701	1.59	-
Maximum channel capacity	185031.1	475.6	bps
Actual spectral efficiency	1	1	-
Actual channel capacity	50000	300	bps
Selected bitrate	50000	52	bps
Total SNR	10.79	10.62	dB
Required SNR	10.53	10.53	dB
Margin	0.262	0.09	dB
Uplink budget	**Primary**	**Secondary**	**Unit**
Transmitting circuit loss	-0.458	-0.458	dB
Transmitting power	43.0	43.0	dBW
Transmitting antenna gain	73.0	73.0	dBi
Atmospheric loss	-3.01	-3.01	dB
Free space loss	-280.94	-280.94	dB
polarisation loss	-0.46	-0.46	dB
Receiving antenna gain	40.0	10.0	dBi
Receiving circuit loss	-0.458	-0.458	dB
System temperature	-26.99	-26.99	dBK
Boltzmann's constant	228.6	228.6	dBW/(K.Hz)
Bandwidth	-47.0	-34.8	dBHz
Total CNR	25.3	7.5	dB
Maximum spectral efficiency	8.41	2.73	-
Maximum channel capacity	420310.7	136544.7	bps
Actual spectral efficiency	0.5	0.5	-
Actual channel capacity	25000	1500	bps
Selected bitrate	25000	1500	bps
Total SNR	28.30	10.52	dB
Required SNR	10.53	10.53	dB
Margin	17.77	-0.01	dB

10. Thermal Control System

The thermal control system is tasked with maintaining the temperatures of all internal and external components within their operational temperature range. This must be true, not only for all phases of the mission, but also for the worst case scenario combinations of orientation and thermal load.

10.1 Requirements

First, the temperature requirements of all of these components can be found in Table 10.1.

Table 10.1: Spacecraft components characteristics heat dissipated

Components	Mass (kg)	Temperature range (K)	Power usage (W)
Battery	16.5	263 to 323	700
Camera	8.25	173 to 213	17
Diplexer (2x)	0.6	233 to 358	17
Infrared spectrometer	1.534	173 to 258	19.5
Laser	15	288 to 313	52
Magnetometer (2x)	0.39	253 to 333	6.12
Polarimeter	2	288 to 313	2
Power amplifier (2x)	3.2	233 to 333	15.8
RAD6000 (CPU)	0.8	248 to 378	13
Reaction wheel (4x)	5	259 to 333	20
Transponder (2x)	1.37	233 to 333	60
X-Ray Spectrometer	4.4	173 to 213	10.8

10.2 Method

In this section, a description of the modelling approach used to size the thermal control subsystem is given. The design methodology is then explained in terms of the passive and active temperature control.

10.2.1 Modelling approach

For the modelling method, it was decided to use a finite element spacial representation, discretising the spacecraft as nodal elements connected by conductive and/or radiative paths. This can be seen in Figure 10.1, which shows the conductive paths between components, as well the heat radiated in and out of the system.
Of course, this diagram shows all the possible incidences of heat from the Sun, whereas the model only simulates solar fluxes based on spacecraft orientation. This means, for example, that in the average case, only the front face, solar arrays, antenna and magnetometers will be irradiated by the Sun.

As for the determination of the internal heat flows, the temperature, mass and specific heat capacity of each node has to be defined, in order to set a starting point for the model. Using these initial temperatures, the heat flows between the nodes are then determined by the conductive and radiative paths between them using a finite difference approach.

The conductive paths are defined by the Fourier law [102], where the conducted heat flow is given by:

$$Q_{cond} = Ak\frac{(T_A - TB)}{l} \tag{10.1}$$

Where A is the cross-sectional area of the conductive path, k is the conductivity of the path, $T_A - TB$, the temperature difference across the path and l, the length of the path. This form of the Fourier law is a simplification of the differential form, which is made in order to discretise the computations in time as well. As such, the above equation is used to set a constant heat flow between two elements for a set temperature at a certain time step. These heat flows are then used to determine the temperatures of the nodes at the next time step, iterating repeatedly for the full timeframe.

As for the radiative paths, these are based on the Stefan-Boltzmann law, with the radiated heat

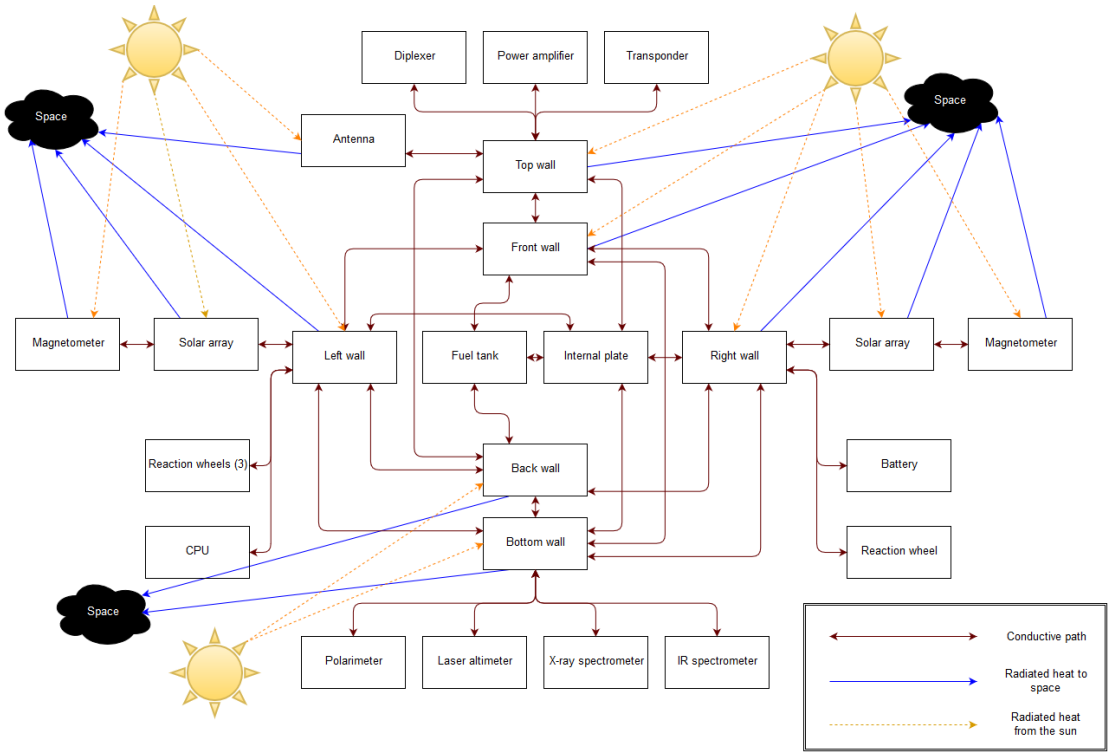

Figure 10.1: Spacecraft conductive and radiative paths

flow given by Equation 10.2.

$$Q_{rad} = A\epsilon\sigma(T_A^4 - TB^4) \tag{10.2}$$

Where ϵ is the emissivity of the radiating surface and σ is the Stefan Boltzmann constant, equal to $5.67 \cdot 10^{-8}$. In contrast to the conductive paths, the radiative paths are much more relevant to the external thermal control than the internal heat flows. For example, these paths were used to determine the losses due to radiation into space, which, in the thermal model, are the only heat sinks of the system. Indeed, apart from this externally radiated heat, all other heat flows and transfers will remain within the spacecraft, between the different internal components. So ultimately, the overall heat balance of the satellite will occur for a total conducted and radiated heat equal to the total radiated heat out of the external components (satellite walls, solar arrays, antenna, etc.)

As for how the properties at the nodes are updated, this is done using the relationship between an input of heat energy into a material and the corresponding change in temperature, as shown in Equation 10.3.

$$H_{in} = mc_p\Delta T \tag{10.3}$$

Which follows from the definition of the specific heat of a material (amount of energy required to change 1kg of mass by 1K). This can be derived with respect to time to yield Equation 10.4.

$$\frac{\delta(H_{in})}{\delta(t)} = Q_{in} = mc_p\frac{\delta(T)}{\delta(t)} \tag{10.4}$$

As such, the change in temperature at a node between two time steps can be found by taking the total heat flow generated, as well as conducted and radiated heat from the node at the previous time step, thus obtaining the derivative of temperature. From this temperature derivative, as well as the size of the time step, the temperature change is computed.

10.2.2 Passive control

The passive thermal control is charged with dissipating or conserving the heat energy of temperature sensitive subsystems, without requiring any power. This is done through the use of thermal surface finishes, insulation and radiators.

In order for the thermal control subsystem to use the least amount of power over the whole mission, the passive control of the spacecraft design is sized to handle the average thermal load during deflection. Yet, for the design of a proper passive thermal control it is also important to consider the worst case scenarios, as an improper passive control sizing would lead to too much power required in extreme cases. Another important consideration is that, as previously

mentioned, the satellite's stable temperature is entirely dependent on the heat balance of the spacecraft. This heat balance, being between the internally produced heat, solar radiation heat and the outgoing radiation from the external surfaces, is mainly influenced by the absorptivity and emissivity of the spacecraft's exterior.

As such, the first consideration of this passive control is modifying the emissivity and absorptivity of the spacecraft's external surfaces. This usually translates in the use of white paints or Multi Layer Insulation to minimise absorbed heat [103]. Yet, because of the degradation of surface finish paints, which leads to an increase of paint used at beginning of life and thus a colder spacecraft temperature, the use of multi layer insulation was found to be a more desirable option.

In the case of the ARMADA mission, the satellite will be oriented in the same position relative to the Sun throughout the deflection portion of the mission (with the front wall Sun pointing and the bottom, or sensor wall, asteroid pointing). This means that one side of the spacecraft will be hotter than the rest for most of the mission, except for cases such as eclipses and required rotations of the spacecraft. This was considered in the placement of the internal components with regard to each component's operational temperature range.

As such, the methodology for the sizing of the external insulation is to make sure the stable temperature of each wall is within the operational temperature range of all its attached components. By doing so, minimal insulation will need to be applied to these components as heat transfer to and from the walls will only help to stabilise them.

On top of this, a black coating is also applied to "hot" components in order to maximise their absorptivity. As such, once the type of coating to be used on the external walls and internal components is determined, the conductive and radiative paths to these components can be sized for the desired stable temperature of each component (as each wall is assumed to have a single temperature, whereas the attached components have various required temperatures).

Finally, the last consideration of the passive thermal control system is the use of external radiators to dissipate heat either from particularly hot components, or from components requiring a very low stable temperature. This is the case of the X-ray spectrometer and framing camera, which both require an operational temperature of less than -60° Celsius. They thus both come with their own external radiators to help maintain this temperature ([21], [56]).

10.2.3 Active control

The active control of the spacecraft can now be designed for the worst case scenario thermal loads. This is done by inputting the heat profile under extreme conditions into the thermal model to check if any of the internal components violate their operational temperature range. If so, an active heating or cooling component is added to that region. In the case where various components require heating, several combinations of heaters are simulated by the MATLAB model, which then optimises for minimum power consumption. In the case where cooling is required, a choice is made between the use of active radiators, louvers, coolant pipes or thermoelectric coolers.

Of course, the operational temperature range is not the only thermal requirement that needs to be met. For some components, the experienced temperature gradient can be detrimental to their functioning and as such, must be checked for. In order to do so, the initial temperatures must be appropriately defined, as they govern how rapidly heat will be transferred to and from the spacecraft, and thus, how rapidly the internal temperatures will change. In order to accurately determine the temperature response at each phase of the mission, the stable temperature of the previous phase are used as initial temperature for the next one. As for the launch phase, it is assumed the components start at room temperature.

10.3 Results

As mentioned in the previous section, the first step of the thermal sizing is to size the passive thermal control from the average thermal load during deflection. Using the model for the solar flux throughout the mission, used also in the power subsystem sizing, the average solar flux was determined to be 1627 W/m^2. Inputting this value into the thermal model, we find that, because the components have no insulation, they stabilise at the wall temperatures, which can be found in Figure 10.2. This is especially problematic for the bottom panel, which holds the components with the lowest maximum operational temperature.

As can be seen, the temperatures of the magnetometers, as well as both spectrometers are outside of their bounds. For the magnetometers, this is due to the fact that the solar array that they are attached to reaches very high temperatures. This can be solved with either of two methods, either wrap or paint the magnetometers with a high emissivity material or insulate their attachment to the solar array. With a combination of basotect foam (with a conductivity

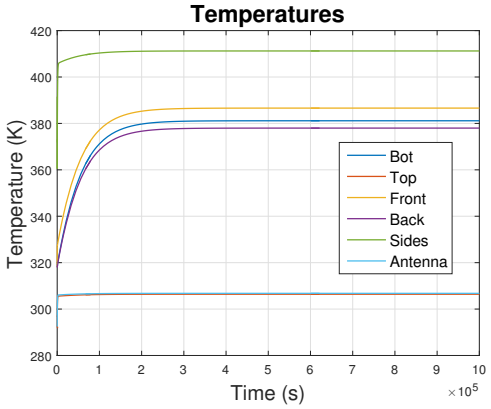

Figure 10.2: External spacecraft temperatures without passive control

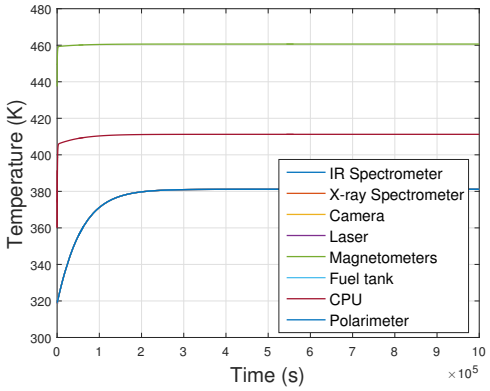

Figure 10.3: Spacecraft component temperatures without passive control

of 0.035 $\mathrm{W\,m^{-1}\,K}$ [104]), and a white paint coating (Z93 with an absorptance of 0.17 and an emissivity of 0.87 [105]), the operational temperature is maintained within its required range.

As for the spectrometers and camera, they all suffer from the fact that the bottom wall is far above their operational maximum. Again, two approaches are combined to mitigate this problem, first, the exterior wall of the spacecraft can be covered in MLI to reduce its absorptivity as well as increasing its emissivity from 0.2 for bare Aluminium, to 0.85. Additionally, the path between the wall and spectrometers can be insulated with basotect foam to reduce the heat flow from the wall. Although this suffices for the IR spectrometer, the X-ray spectrometer and camera can only be brought within their operational temperature range through the use of radiators. Using the thermal model, an external surface area of 0.08 and 0.04 $\mathrm{m^2}$ for the X-ray spectrometer and camera respectively, is found to be sufficient to keep them below their operational minimum.

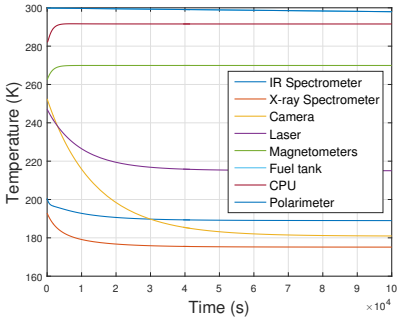

Figure 10.4: Spacecraft component temperatures after passive control

Although this is sufficient for the average case, it was found that only sizing for the average case leads to the passive control being too inefficient in dealing with extreme cases. Of course, designing the passive control for the hot case will lead to increased active control in the cold case and vice versa. Because active cooling is less efficient than active heating, it was therefore chosen to size the passive system for minimum cooling in the hot case. This involves insulating the interface between components and the wall they are attached to in order to control how much heat is dissipated to or from the component. The application of this thermal control method isn't always straightforward though, as applying too little insulation can lead to excessive heat loss in the cold case, while too much insulation can cause the components to overheat from their own internally generated heat. This is especially true of high heat dissipation components such as the battery and power amplifier, which constantly give off high amounts of heat energy. Insulation is also useful in minimising the loss of heat from components that do not actually have any internal sources of heat, such as the fuel tank (which also has a high minimum temperature). To minimise the power consumption of the thermal control system, the thicknesses of the interface insulation layers were sized for minimum hot case power. Having applied all of these passive thermal control methods to the spacecraft, Figure 10.4 is obtained.

10.3.1 Hot case

Now that all of the components meet their required temperature range for the average case, the active thermal control can be sized for the worst case scenario thermal loads. These can occur during launch and orbit perihelion for worst case hot, and eclipse for worst case cold. First, the thermal response of the launch is determined using the heat flux given in the Soyuz user manual [40], shown in Figure 10.5. This thermal load is evenly distributed across all of the spacecraft's external surfaces and gives the responses shown in Figures 10.6.

As can be seen, thanks to the insulation of the internal components, despite the increase in temperature in all of them, none have the time to go over their operational limit in the time in takes

for the aerothermal flux to dissipate and the spacecraft to stabilise under space environment conditions. And though the battery's temperature increases due to internal heat dissipation while the CPU's temperature drops from the radiated heat to space, they both stay within their temperature ranges. It is also important to mention that although most of the sensors are outside their operational temperature range during launch, it is assumed that they can survive at room temperature as long as they are turned off, which will be the case until the observation phase of the mission.

Moving on to the next hot case, we input the perihelion thermal load of 2454 $\mathrm{W\,m^{-2}}$ into the thermal model and change the orientation of the spacecraft so that the sensor side is Sun facing. Although this is extremely unlikely, as the sensors will be pointing to Apophis during the whole deflection phase, it is not impossible for this to happen. And because the sensors are the most sensitive to high temperatures, it must be taken into account. We find that the camera, reaction wheels and both Spectrometers are now above their operational temperature range, whereas the power amplifier, transponder and diplexer are below their operational minimum, as depicted in Figure 10.8. The hot components are clearly due to the sensor panel now being Sun facing, combined with the components' low maximum temperatures, as for the cold components, their low temperatures are due to the drop in the antenna temperature, which through its connection to the top wall, also decreases the top wall's component temperatures. As for the reason why the antenna's temperature drops, this is due to the fact that it is usually illuminated by the Sun, and thus coated with high emissivity paint (Z93 white paint [105]) to prevent excessive heating through irradiation. Although this is beneficial under the average case, it causes enough heat loss for the top wall components to go over their operational limit.

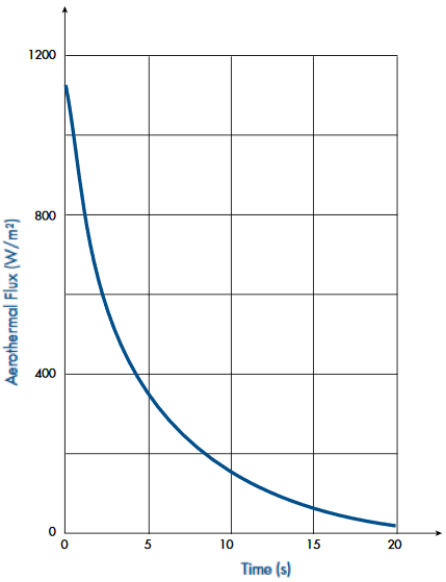

Figure 10.5: Aerothermal flux after fairing jettisoning

Moving on to the selection of the active cooling of components, we look at the three main methods previously mentioned: increasing the radiated heat through the use of louvers and active radiators, transferring heat within the spacecraft through mass flow using coolant pipes to conduct it away from the material and the use of the Peltier effect to create a temperature difference through thermoelectric coolers. Because this particular hot case is an extreme condition that is unlikely to happen during the actual mission, the use of thermoelectric coolers would be preferable to any other active component, but unfortunately, for cooling values exceeding 10 W (as is the case for the sensors in the hot case), these devices become increasingly inefficient and are thus not a viable option on their own. Attention must thus be given to the dynamic options. For louvers, it can be noted that, although they provide high increases in radiated heat, they are not easy to use for precision thermal control of individual components as they will increase the heat rejected from the spacecraft's interior as a whole. As for the fluid pumps, they are efficient in transferring heat within the spacecraft, but do not actually reject it externally, which can lead to hot spots around the pipes. As such, active radiators are chosen as the preferred active control method as they combine the high dissipated heat through radiation found in louvers, as well as the effective and controllable heat flow of fluid pipes. The mass of these radiative surface can then be determined from a reference maximum density of 8 $\mathrm{kg\,m^{-2}}$ [106].

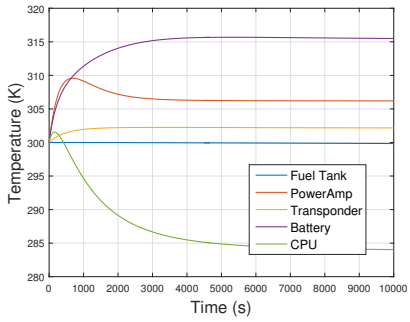

Figure 10.6: Internal thermal response under aerothermal flux

Having accounted for the hot components in the spacecraft, attention must now be given to the cold ones. Although these components will also be checked against the cold case to check their maximum required power rating, it is predicted that they will require heating for that case as well. As such, the placement of heaters on these components can have uses in both the extreme hot and cold cases. As for the type of heating to be used, patch heaters are found to be the most viable option due to their high efficiency, low mass and low complexity (especially compared to heat pipes). Indeed, a single solid state thermal controller, equipped with a patch heater and temperature sensor can weigh as little as 30 grams at a power rating of up to 100 W with an

efficiency of 98 % [103]. To determine the amount of heat to be added or removed from each component, two iterative schemes were used. The first consisted in continuously incrementing the heat flow out of a component that was above its temperature range until it met its requirement, then moving on to the next component. The second scheme involved incrementing the heat flow out of each component before incrementing it again. This second scheme was found to produce lower values than the first and was therefore used for the determination of the required powers. A diagram showing the program flow of this particular scheme can be found in Figure 10.7.

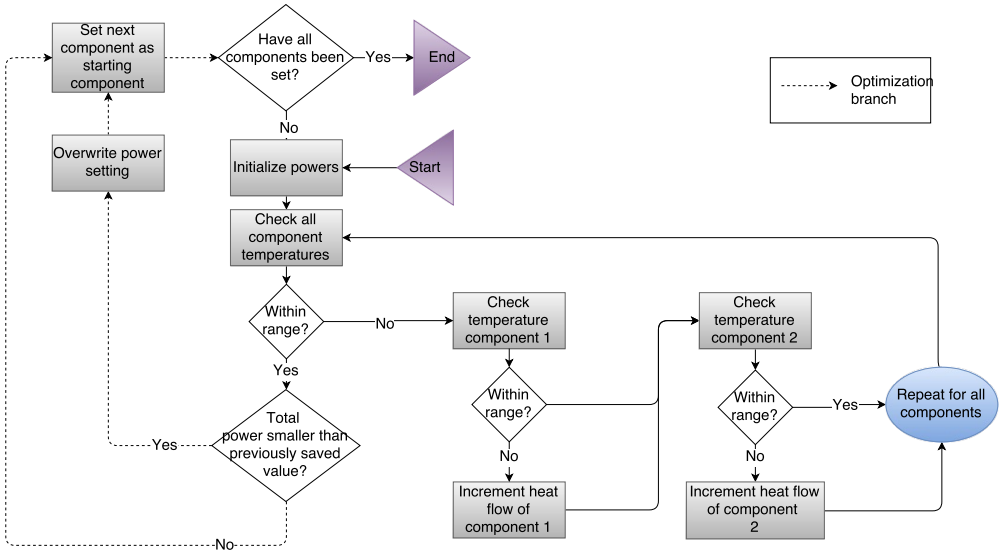

Figure 10.7: Power determination scheme

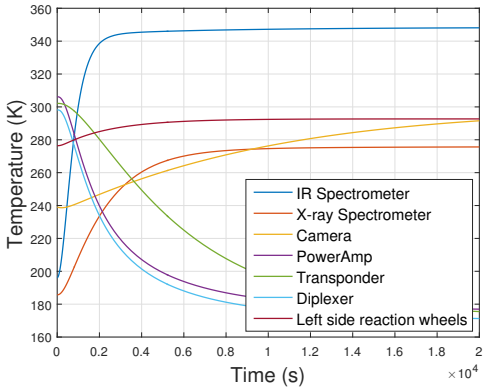

Figure 10.8: Thermal response at perihelion with sensor side sun facing

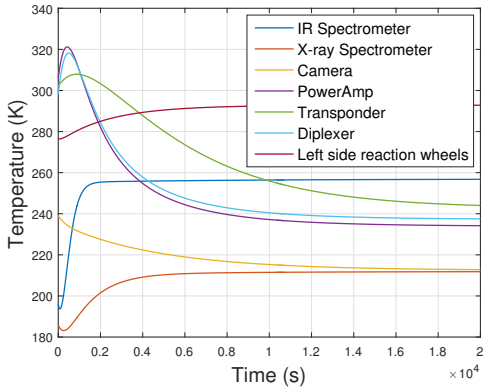

Figure 10.9: Thermal response at perihelion after active cooling implementation

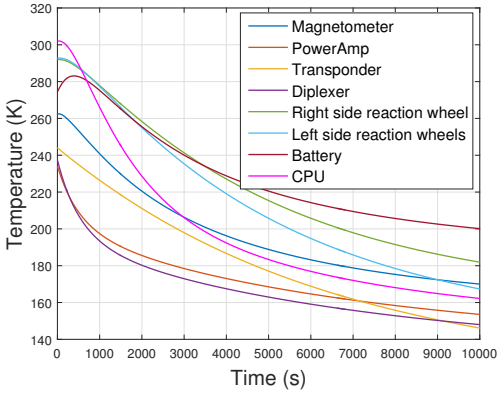

Figure 10.10: Thermal response in eclipse

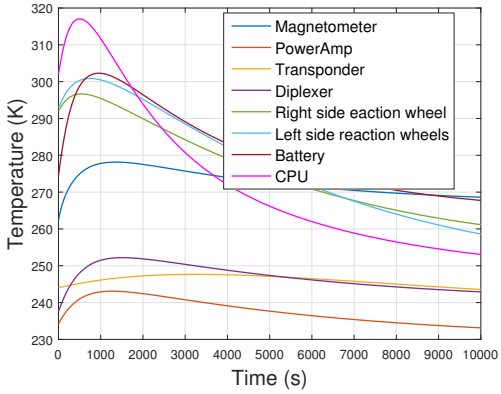

Figure 10.11: Thermal response in eclipse with active thermal control

Using this method, a combination of 21 W on the power amplifier, 11 W on the diplexers and 9 W on the transponder is found to be needed for the components to meet their temperature requirement. With an efficiency of 98% this yields a total power consumption during worst hot case of 42 W. This yields Figure 10.9.

10.3.2 Cold case

Finally, having sized the active control for the hot case, as well as the power they require for the hot case, the transition to the cold case can now be investigated. As previously mentioned, the initial temperatures of the cold case model are taken to be the final temperatures of the hot case (in order to check for worst case temperature gradients). Without any external source of heat, the magnetometers, power amplifier, transponder, diplexer, reaction wheels, battery and CPU quickly fall short of their operational temperature limit (found on Table 10.1), as can be seen on Figure 10.10. The design is iterated for different powers of the heaters and find the lowest total power consumption at the power ratings shown on Table 10.2, with a total cold case power consumption of 315.5 W. Comparing this to the hot case value of 42 W, it is clear the cold case power required will be the maximum possible power required in all mission phases (as eclipses will be the same in all phases). This configuration yields the response shown on Figure 10.11.

Table 10.2: Heating power required for spacecraft components active thermal control

Components	**Power (W)**
RAD6000 (CPU)	18.4
Magnetometer (2x)	4.1
Transponder	14.3
Battery	120.4
Diplexer	15.3
Power amplifier	28.6
Right side reaction wheel	24.5
Left side reaction wheels (3x)	28.6

10.4 Conclusion

Having now sized for the worst case hot and cold scenarios, the heaters and coolers are therefore able to handle any thermal load in this range. Additionally, having found the amount of heaters and coolers as well as their location, the actual mission thermal load can be applied to obtain the total thermal control subsystem power consumption throughout the whole mission.

Testing for the thermal profiles at perihelion under standard orientation (sensor side is asteroid facing), we find that, although the passive control was sufficient to maintain the components within their operational temperature ranges, the battery, power amplifier and transponder are now above their operational maximums and thus require cooling. The transponder and power amplifier can both be cooled with a low amount of heat removed (3 and 9 W respectively) and thus thermoelectric coolers can be used.

This is not the case for the battery because of the excessive internally generated heat which cannot be dissipated by conduction to the side walls, and must thus be expelled externally. This can be done with no excess mass added by converting a portion of the back wall to a passive radiator. Using the thermal model, a surface area of 0.07 m^2 with an emissivity of 0.9 (Z93 white paint) is found to be the minimum surface area for the battery to meet its operational temperature range at perihelion. This configuration is then tested at aphelion, where it is found all temperatures are within range and, thus, a nominal maximum power consumption (using a thermoelectric cooler efficiency of 10% from reference in [103]) of 120 W is obtained. All of the previously mentioned control methods can be found in Table 10.3.

It must be noted that a layer of betacloth insulation, which was chosen for its high absorptivity compared to other insulation materials (0.45 as shown in [103]), was added to the fuel tank along with two patch heaters (including one for redundancy), despite its temperature staying within range for all modelled cases. This is because although the model was rigorously checked, due to the lack of experimental data to validate it, some unexpected circumstances can occur during the actual mission, and, as the fuel tank is a mission critical component, it must be accounted for regardless of the model results. This is the case for the solar arrays and antenna as well, which although not breaching their operational temperature limits, are still equipped with high emissivity paint (Z93 white paint) to maintain their temperatures well within bounds.

10.5 Model verification

For the verification of the program, several measures were taken to ensure the reliability of results. These measures can be separated into different phases, starting with a qualitative check, then a unit check, function check and validation of the model.

The qualitative check is a simple way of eliminating errors in the definition of the model. This is done by critically assessing the outputs of the model as well as of its subfunctions to determine if they make sense with regards to the expected output. This obviously requires a good

Table 10.3: Spacecraft components passive and active control

Components	Control method	Control type	Mass (g)
Antenna	Z-93 white paint	Passive	-
Battery	Wall radiator	Passive	-
-	Patch heaters (2x)	Active	60
Diplexers (2x)	Basotect foam	Passive	1.32
-	Patch heaters (4x)	Active	120
External walls	Teflon, backed MLI	Passive	67
Framing camera	Basotect foam	Passive	0.70
-	Wall radiator	Passive	-
-	Deployable radiator	Active	0.56
Fuel tank	Beta cloth MLI	Passive	100
-	Patch heaters (2x)	Active	60
Infrared Spectrometer	Thermoelectric cooler	Passive	30
-	Wall radiator	Passive	-
-	Deployable radiator	Active	1128
Magnetometer (2x)	Basotect foam	Passive	0.08
-	Patch heaters (4x)	Active	120
Power amplifiers (2x)	Patch heaters (4x)	Active	120
-	Thermoelectric coolers (4x)	Active	120
RAD6000 (CPU)	Basotect foam	Passive	0.36
-	Black paint	Passive	-
-	Patch heaters (2x)	Passive	60
Reaction wheels (4x)	Basotect foam	Active	9.29
-	Patch heaters (8x)	Active	240
Solar array	Z93 white paint	Passive	-
Transponders (2x)	Basotect foam	Passive	0.12
-	Thermoelectric coolers (4x)	Active	120
-	Patch heaters (4x)	Active	120
X-Ray Spectrometer	Wall radiator	Passive	-
-	Deployable radiator	Active	1240
Total	-	-	4325

understanding of the underlying principles that define the model, which means that an extensive literature study must be performed beforehand. In order to increase the effectiveness of this method, outputs of individual nodes were analysed as soon as those nodes were implemented in the model. Doing so prevents errors from accumulating in the program, at which point they would become increasingly hard to find. An example of a sanity check for the thermal model was obtaining different temperature responses for the left and right solar arrays when the satellite was supposed to be modelled as a symmetrical structure. This led to finding an improperly defined conductive path between the spacecraft walls.

The unit check consists in verifying the consistency of units across all functions. This means that every function within the model must be checked to make sure the input variables are the same type and in the same order of magnitude as the equations using it. To make this easier, it was decided all values would be given in SI units, unless a specific equation requires a different form of input. Also, because most of the values used and determined by the thermal model range from 10^{-4} to 10^{4}, all inputs and outputs are used in base unit form (distances in metres, power in watts, etc), greatly reducing the risk of obtaining magnitude errors.

For the function test, the individual functions, such as the radiative and conductive paths, were tested for reference thermal values to verify that they behaved as expected. This was done by calculating the expected output of the function and comparing it to its actual output. By doing so, it was found, for example, that the radiated heat to space was considerably lower than its predicted value. The reason for this was found to be that certain components had their initial temperature overwritten by the program for high values of radiated heat. These temperatures were therefore defined as high priority elements to prevent them from being overwritten.

11. Electrical Power System

The electrical power subsystem is in charge of generating, regulating and distributing power to all subsystems. This makes it a critical aspect of the design, as it is necessary for other critical subsystems like the ADCS or Communication subsystem to function properly. Considering the different functions of the power subsystem, it can be further broken down into a primary power system, a secondary power system and a power regulation interface. In this chapter, first the requirements for the power system will be listed. Afterwards, the power system architecture and the related design choices will be addressed. Thereafter, the power system modelling of the spacecraft will be discussed. This section will discuss the solar flux environment, the power demand throughout the mission and finally the sizing of the power subsystem.

11.1 Requirements

Table 11.1: Requirements on the electrical power system

ARMADA-POWER-01	The spacecraft shall be able to store energy.	Check
ARMADA-POWER-02	The Electrical Power System shall not have any single point of failure.	Analysis
ARMADA-POWER-03	The spacecraft shall generate power.	Check
ARMADA-POWER-04	The Electrical Power System shall provide power to all other subsystems.	Check
ARMADA-POWER-05	The Electrical Power System shall be able to provide a peak power of 2318 Watts at beginning of life.	Check
ARMADA-POWER-06	The Electrical Power System shall be able to provide a peak power of 2308 Watts at beginning of deflection.	Check
ARMADA-POWER-07	The Electrical Power System shall be able to provide an end of life power of 1706 Watts.	Check
ARMADA-POWER-08	The battery shall have a cycle life of 2506 cycles.	Analysis
ARMADA-POWER-09	The battery shall have a total beginning of life capacity of 1222 Watt-hours.	Check
ARMADA-POWER-10	The battery shall be able to provide a peak power of 235 Watts at beginning of life.	Check
ARMADA-POWER-11	The Electrical Power System shall include a redundant power source.	Check

11.2 Power system architecture

The power system of a spacecraft comprises several components each having a specific function. First of all, the power system needs to generate the power required for the operation of the spacecraft. A primary power system must be sized for the generation of this required power and a secondary power system might be needed to complement the system in order to meet all power requirements throughout the entire mission. Besides that, the secondary power system needs to be able to take over all power loads for a short period of time when the primary power system fails. Secondly, the power system needs to be able to store energy in order to account for peak power demands or temporary limited power generation. Thirdly, the power generation needs to be regulated and controlled. When the primary power system is not generating enough power the secondary power system must be activated and when the power system is generating too much power the excess power needs to be dissipated to avoid overheating. Finally, the generated power needs to be distributed over the spacecraft.

11.2.1 Power system energy source

The first step in the design process of the power subsystem is selecting the type of power generation for the primary and secondary power system. The main drivers for the selection of the type of power generation are the power level and the mission duration. Figure 11.1 shows the optimum type of power generation over mission duration and power level. An initial estimation of the power budget and mission duration of the ARMADA mission, as specified in the Mid-term report [46], show that the 'Solar PV-battery' power system is the most feasible system for the ARMADA mission. A Solar PV-battery power system means that the primary power generation system will be solar arrays generating electrical power from solar radiation and that the secondary power system will be rechargeable batteries [7]. The power management unit then needs to regulate the charging and discharging of the batteries to complement the power generated by the solar panels.

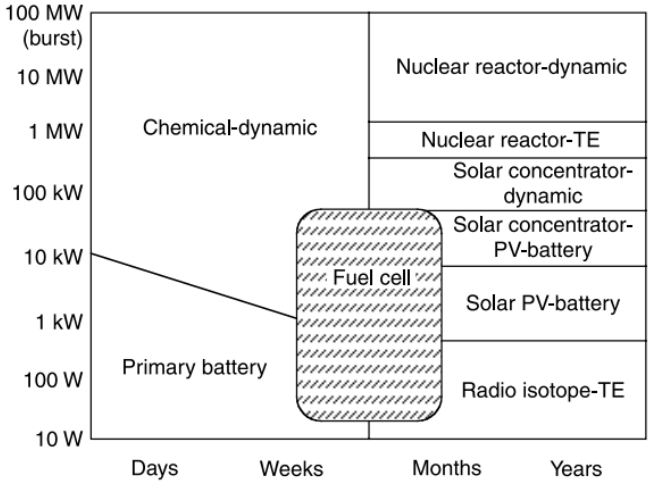

Figure 11.1: Power system energy source selection [7]

11.2.2 Solar PV-Battery system architecture

As described above, the Solar PV-Battery system generates power using solar panels, stores part of it in a battery and discharges the battery when required. Since the solar array voltage, battery charge and discharge voltages and subsystem operating voltages all are different, voltage regulators are included in the power system to account for these inherent differences and for voltage level fluctuations due to degradation and temperature changes. Besides that, changing power demands throughout the mission require a power system that regulates the power that is provided. The regulation of the power system can be done in various ways. The main kinds of regulation systems for Solar PV-Battery power systems will be discussed in this section and finally one of them will be selected.

The main choice in the selection of the power control system architecture is the choice between a 'Direct Energy Transfer (DET)' or a 'Peak Power Tracker (PPT)' system architecture. In a DET power system the power generated by the solar arrays is provided to the subsystems directly, while in a PPT system the solar array output voltage is controlled such that the voltage is always set on the operating point where output power is highest. DET power systems can be further divided into 'Fully Regulated Bus (FRB)' and 'Sun-Regulated Bus (SRB)' power systems. The main difference between these two systems is that the 'Sun-Regulated Bus' system has no battery discharge converter in its 'Power Regulator Unit (PRU)' [7], so the voltage output of the battery is not regulated in an SRB system. However, the charge and discharge rates are of course regulated.

In Chapter 4.9 of the book 'Spacecraft Power Systems' these three different power system architecture types are compared and their efficiencies analysed. There it is stated that peak power tracking power systems are efficient for small spacecraft in low or irregular orbits with a power requirement of less than 500 W [7]. However, the ARMADA mission will be interplanetary and as can be seen in Section 11.3.2 the power demand will exceed 1000 W which means that having a Direct Energy Transfer power system on the spacecraft is considered to be more feasible [7]. Besides that, peak power tracking is mostly efficient for LEO satellites coping with large periods of eclipses or for satellites coping with high variation in solar incidence angle. During the ARMADA mission however it is presumed that the spacecraft will not encounter any eclipses and the incidence angle of the sun on the solar panels will not exceed 11 degrees.

So the choice comes down to a direct energy transfer system either sun regulated or fully regulated. The sun regulated system is the simplest power system and is the most efficient for small load and solar input variations. The fully regulated system on the other hand thrives in regulating the voltage levels throughout the mission and is therefore more efficient when the power loads vary a lot during the mission. The ARMADA mission has several different mission phases each with specific power requirements. Three observation phases are distinguished with different payload sensors active in each of them and besides that, the deflection phase demands an active ion engine with a high power requirement. Moreover, as the mass of the spacecraft is decreasing over the deflection due to the expelling of propellant the power required to power the ion engine decreases over time. Since big variations in spacecraft bus voltage level is not beneficial for the subsystems powered by the system, for the ARMADA mission the fully regulated power system is considered to be the most feasible option for the ARMADA spacecraft.

11.2.3 Electrical block diagram

In Figure 11.2 the electrical layout of the power subsystem can be seen. This is a typical layout for a fully regulated power system. The PRU regulates the amount of power that is generated by the battery in order to complement the power generated by the solar array panels. Afterwards the voltage level is compared to a set reference voltage, which will be the spacecraft bus voltage as specified in the next subsection. The information obtained during the voltage verification will then be communicated to the 'Mode controller' which will command the PRU and shunts to make adjustments accordingly. The 'Power Distribution Unit' then distributes the current flowing towards each separate power load. Finally, at each subsystem a voltage converter is included in the design, such that the voltage at each subsystem is at their specific operational required voltage level.

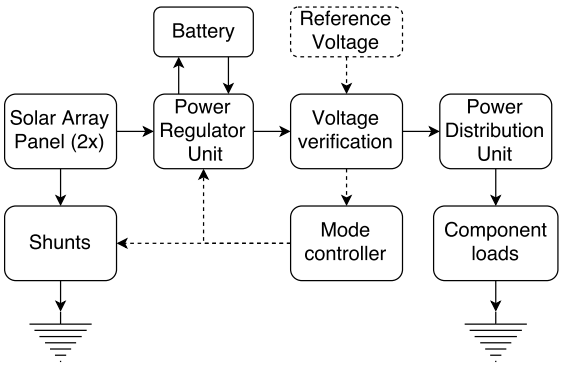

Figure 11.2: Electrical block diagram fully regulated power system [7]

11.2.4 Spacecraft bus voltage

The voltage induced by the power system on the rest of the spacecraft is called the spacecraft bus voltage. The spacecraft electrical circuit can be modelled as having the power system as the power source and having each power load modelled as a resistance connected in parallel. Since the voltage over parallel connected resistances is equal, the voltages acting over the subsystems are basically the same. However, electrical cables transporting the electrical current to the subsystems causes power losses dependant on their length. The bigger the spacecraft, the longer the electrical cables and therefore the higher the cable losses. Due to this fact, in big spacecraft a high bus voltage is needed to compensate for the cable losses. Another determining factor is the power level required of the spacecraft. Power is the product of current and voltage, so for the same power level a higher bus voltage results in less current running through the cables and thus less cable power loss. These effects can be seen in Figure 11.3, which shows the optimal bus voltage over power level. An obvious trend can be noticed between increasing power levels and increasing optimal bus voltages. Besides that, it can be seen that the International Space Station (ISS) requires a higher bus voltage than the spacecraft LM7000 and BSS702, manufactured by Lockheed Martin and Boeing respectively, because of the fact that the ISS is bigger and therefore has higher cable losses. Since the power demand level of the ARMADA spacecraft will be between 1 and 2 kW and since the size of the spacecraft will be similar to Boeing's BSS601 spacecraft, a bus voltage of 50 V has been chosen [107].

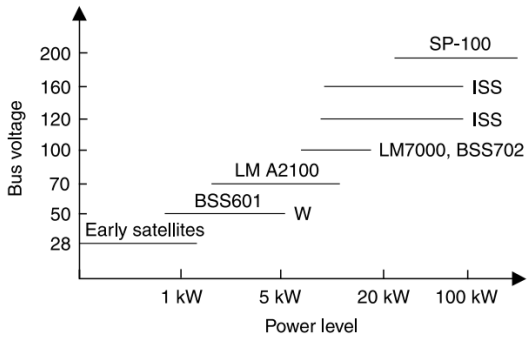

Figure 11.3: Bus voltage selection [7]

11.2.5 PV cell selection

The solar panels consist of a number of 'Photovoltaic Cells' connected in series and parallel configuration in order to meet the required voltage and current levels. For the selection of the type of PV cells efficiency, mass and resistivity to radiation are taken into account. Since efficiency is considered to be the most important criterion in the selection process an initial selection of PV cell types has been made only upon that criterion. In Table 11.2 the efficiencies for various types of PV cells can be found.
From Table 11.2, it can easily be concluded that multi-junction PV cells are the most feasible in terms of energy conversion efficiency. They use multiple layers of different material in order to capture as much as possible of the solar spectrum radiating on the cell. These cells are being increasingly used in the space-

Table 11.2: Efficiency of various types of solar cells [35]

Solar Cell Type	**Efficiency** (%)
Mono-Crystalline Si	24.7
Multi- Crystalline Si	20.3
Amorphous Si	10.1
HIT cell	23.0
GaAs cell	26.1
InP cell	21.9
Multi junction cell	40.8
CdTe	16.5
CIGS	19.9
CulnS2	12.5
DSSC	11.1
Organic solar cell	6.1

craft industry due to being highly efficient and still
cost effective [7]. Therefore, the PV cells will be a multi-junction type of PV cell. The European leader in the development and production of these multi-junction PV cells is called AZUR Space. AZUR Space offers six different PV cell options varying in type or size and these are all analysed and compared to each other in order to select the most favourable one. The characteristics of these seven types of PV cells can be found on the website of AZUR Space [36]. The criteria for the selection are chosen to be efficiency, mass and resistivity to radiation. The efficiency of the solar cells is evaluated at both beginning of life (BOL) and after being subject to $1 \cdot 10^{15}$ MeV of radiation to assess the resistivity to radiation per solar cell. In Table 11.3 the characteristics of the solar cells can be seen. From these characteristics it has been concluded that the extra thin '30% Triple Junction GaAs type TJ Solar Cell 3G30C - Advanced' is the most favourable PV cell for the ARMADA spacecraft.

Table 11.3: Photovoltaic cell characteristics [36]

	Efficiency @ BOL (%)	**Efficiency @** $1 \cdot 10^{15}$ MeV (%)	**Mass** (mg/cm^2)
30% Triple Junction GaAs			
(40x80 mm) Type TJ Solar Cell 3G30C - Advanced	29.5	26.5	86
(40x80 mm) Type TJ Solar Cell 3G30C - Advanced (Extra Thin: 80 μm)	29.5	26.5	50
(80x80 mm) Type TJ Solar Cell 3G30C - Advanced	29.4	26.5	86
(120x60 mm) Type TJ Solar Cell 3G30C - Advanced	29.4	26.5	130
28 % Triple Junction GaAs			
(40x80 mm) Type TJ Solar Cell 3G28C	28	24.5	86
Silicon Solar Space Cell			
(74x32 mm) Type S 32	16.9	0.74	32

11.2.6 Battery selection

A crucial part of the design of the secondary power system, the battery, is selecting the electrochemistry of the battery. In this section five different chemicals are compared on various aspects to select the most feasible chemical composition of the battery. The considered chemicals are NiCd, NiH2, NiMH, Li-ion and Lithium-polymer. The characteristics of these chemicals regarding their performance in space applications are found in the book 'Spacecraft Power Systems' [7].

Table 11.4: Battery chemicals specifications [7]

Type	**Specific Energy** (Wh/kg)	**Specific Power** (W/kg)	**Energy Density** (Wh/l)	**Power Density** (Wh/l)	**Cycle life** (100% **DoD cycles**)	**Relative Cost** ($/kWh)	**Remarks**
NiCd	40-50	150-200	50-100	300-500	1000-2000	1500	Memory Effect
NiH2	45-65	150-200	35-50	200-300	2000-4000	1500	
NiMH	50-70	150-200	140-180	300-500	1000-2000	2000	Temperature Sensitive
Li-ion	90-150	200-220	150-250	400-500	500-1000	3000	New technology
Lithium-polymer	100-200	>200	150-300	>400	500-1000	>3000	Still in development

Based on the characteristics as shown in Table 11.4 a trade-off has been performed. The criteria for the trade-off are specific energy, specific power, energy density, power density, reliability and costs. Both cycle life and additional remarks are taken into consideration in the reliability criterion. The criteria are considered to be of equal importance, and the scores range from 1 to 5. Lithium-polymer is not taken into account in the trade-off since this type of battery is still in development and not yet used in space. Table 11.5 shows the trade-off that has been performed for

the selection of the battery cell chemistry. Nickel Cadmium (NiCd) and Nickel Hydrogen (NiH2) batteries are the most commonly used batteries in space applications. However, the battery of the ARMADA spacecraft will need to have a high capacity to be able to be a redundant power source during deflection. Therefore, because of the performance in specific energy and energy density a Nickel Metal Hydride (NiMH) battery has been found to be the most feasible option. Important to note is that Nickel Metal Hydride batteries are temperature sensitive, so therefore need to be constantly kept within its operational temperature range of -10 to 50 degrees Celsius [7].

Table 11.5: Battery chemistry trade-off [7]

Type	Specific Energy	Specific Power	Energy Density	Power Density	Cost	Reliability	Total Score
NiCd	1	3	2	3	5	4	18
NiH2	2	3	1	2	5	5	18
NiMH	3	3	4	3	4	4	21
Li-ion	4	4	4	4	2	2	20

11.3 Power system model

The primary and secondary power systems must be sized using the power consumption from other subsystems, the incident power and through various constraints employed in order to model the system itself. In this section, the model, the sizing and the verification and validation of the system will be discussed.

11.3.1 Solar Flux environment

The power generated by the solar panels, the primary power system, is dependent on the solar radiation incoming perpendicularly on the solar panels, the area of the solar panels and the efficiency of the PV cells within the panels. Therefore the solar flux on the spacecraft must be analysed. Since the solar flux varies with the distance to the Sun, first the distance between the spacecraft to the Sun throughout the mission has been analysed. Thereafter, the angle between the velocity vector of the spacecraft and the direction from the spacecraft to the Sun has been plotted to finally calculate the effective solar flux throughout the mission.

Distance to sun

In Chapter 3 the astrodynamics related to the ARMADA mission are specified. There it can be seen that the transfer trajectory towards Apophis is similar to Apophis' orbit. Also during observation and deflection the spacecraft will follow the orbit of Apophis around the Sun. Therefore, for the assessment of the solar flux throughout the mission it has been assumed that the spacecraft follows the orbit of Apophis. This means that the distance of the spacecraft to the Sun can be calculated using Kepler's first law with the orbital properties of Apophis.

Incidence angle

The incidence angle is the angle the solar rays make with the solar panels. This is an important consideration in the solar flux environment model since the more the solar panels are angled with respect to the incident solar flux, the less effective the solar cells in the panels are. The incidence angle throughout one orbit around the Sun is calculated by first calculating the flight path angle γ with Equation 11.1 and then subtracting 90 degrees from it [1]. Figure 11.4 shows the context of the variables in Equation 11.1.

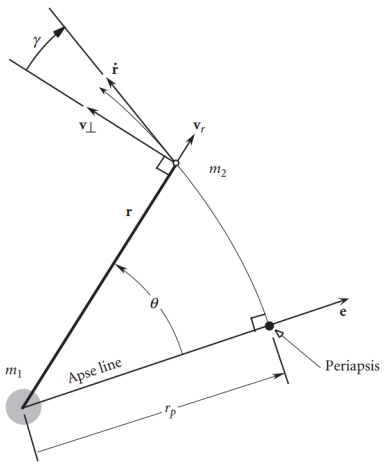

Figure 11.4: Flight path angle (γ) [1]

$$\tan\gamma = \frac{e\sin\theta}{1+e\cos\theta} \tag{11.1}$$

Effective solar flux

The effective solar flux throughout the mission is mainly important to address the minimum solar flux for the sizing of the solar arrays. Besides that, the maximum effective solar flux will be discussed in the sizing of the shunts. The effective solar flux is the solar flux coming in per-

pendicularly to the solar panels. First the 'real' solar flux has been plotted over one orbit using the inverse square law taking the solar flux at one AU as a reference. Afterwards, the real solar flux has been multiplied with the cosine of the incidence angle over the whole orbit to come to the effective solar flux plot. Figure 11.5 and Figure 11.6 show the effective solar flux plot and the percentage difference between the 'real' and effective solar flux respectively. This difference has been plotted to check whether it would be beneficial to rotate the solar arrays in order to increase their effectivity. However, since the maximum percentage loss is below 2 percent, it has been decided not to rotate the solar arrays throughout the deflection such that the ADCS does not need to counteract the moments induced by the rotation of the arrays.

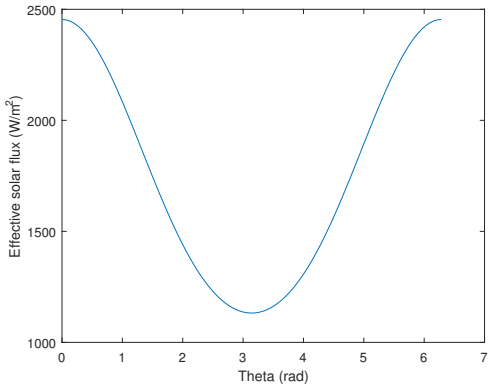

Figure 11.5: The effective solar flux as a function of true anomaly

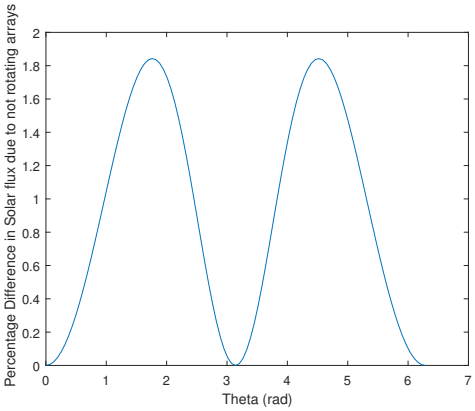

Figure 11.6: The solar flux percentage loss due to fixed solar arrays as a function of true anomaly

11.3.2 Power demand

The power system shall provide the necessary power to all subsystems inside the spacecraft throughout the mission lifetime. Since the mission comprises several phases, the spacecraft will have various operating modes each with different power demands. That is why in this section the power demand throughout the mission will be analysed. The power demand profile will then be used to select and size the power system architecture. The following nine phases are considered: 1. Launch, 2. Deployment, 3. Transfer, 4. Orbit insertion, 5. Observation phase 1: 3D mapping, 6. Observation phase 2: Asteroid properties, 7. Observation phase 3: Crater investigation, 8. Deflection and 9. End of life.

During the launch phase only a few of the subsystems will be operating. The spacecraft will be hibernating and just needs to power the subsystems necessary for housekeeping of the spacecraft. The subsystems that will be active are the thermal, C&DH and power subsystem. After the launch is completed, the solar panels and antenna will be deployed and the rest of the subsystems will be activated. After everything is deployed the transfer can be initiated and the spacecraft will start communicating with a transponder to Earth. When the spacecraft arrives at Apophis the spacecraft will go into orbit around Apophis perpendicular to its orbital plane such that the solar panels will be facing the Sun. The propulsion subsystem will be activated for orbit insertion. Then, during the orbiting phase the payload will be activated and the asteroid observed. Three different observation phases can be distinguished and during each of them different payload sensors will be activated, some of them continuously and others periodically operating. After the observation phase, the spacecraft will position itself along track of Apophis' orbit, turn on the ion engines and hover in front of the asteroid until the asteroid is fully deflected. Since the mass of the spacecraft will be decreasing over deflection phase also the power consumption of the ion engines and thus the power required during deflection will decrease over time. Finally, when the deflection mission has been succeeded, the spacecraft will be shut down. In Table 11.6 the power demand during all mission phases are presented. The power demand profile is used to assess the maximum power required for the sizing of the power subsystem.

Table 11.6: Power demand range per mission phase in Watts

Subsystem	**1**	**2**	**3**	**4**	**5**	**6**	**7**	**8**
Duration	1600 seconds	600 seconds	245 days	116 seconds	28.41 days	28.41 days	14.205 days	5-6 years
Power	3-11	19-82	3-113	37-131	3-116	3-120	3-123	145-361
Thermal	0-42	0-316	0-316	0-316	0-316	0-316	0-316	0-316
C&DH	15	15	15	15	15	15	15	15
Mechanisms	0	80	0	0	0	0	0	0
TT&C Duty Cycle	0	0	76 8.33%	76 100%	76 8.33%	76 8.33%	76 8.33%	76 8.33%
ADCS	0	0	0-157	0-157	0-157	0-157	0-157	0-157
Propulsion	0	0	0	92	0	0	0	0
Ion Thrusters	0	0	0	0	0	0	0	709-1187
Camera Duty Cycle	0	0	0	0	17 0.31%	0	0	0
Laser Altimeter	0	0	0	0	0	0	52 20%	52 2.74%
X-ray Spectrometer Duty Cycle	0	0	0	0	0	10.8 6.76%	0	0
IR Spectrometer Duty Cycle	0	0	0	0	0	9.5 6.76%	0	0
Magnetometer Duty Cycle	0	0	0	0	0	14.5 6.76%	0	0
Polarimeter Duty Cycle	0	0	0	0	0	2.0 6.76%	0	0
Total	18-68	114-493	18-677	220-787	18-697	18-721	18-739	869-2164

11.3.3 Solar array sizing

Based on the solar flux environment, the power demand profile and the power system characteristics, the solar arrays have been sized. For the sizing of the solar arrays two design points are chosen. One of them is at beginning of the deflection while the other is at end of deflection. At beginning of deflection the power required is maximum since the ion engines are just turned on and the spacecraft has not yet expelled a significant amount of mass. However, degradation of the solar cells is also an important factor which needs to be taken into account. Therefore, the power required is also evaluated at end of deflection. Both power requirements at these design points are then translated to beginning of life required powers using the solar array degradation coefficient (D_{cell}). Important to note is that the solar array does not only need to power all the subsystems (P_{req}), but also needs to be able to provide enough power to charge the battery (P_{charge}). The battery is not only a redundant power source but is also used for powering the camera, the altimeter and the TT&C subsystem. Therefore, the battery needs to be charged by the solar array in between the battery discharge periods. Other factors contributing to the minimum power required to be generated at beginning of life include cable loss (F_{path}), 'inherent degradation' (D_{Inher}) and besides these a reliability margin (F_{rel}) has been included. Inherent degradation comprises both solar cell degradation due to manufacturing and due to temperature increase of the solar panel. Finally, with the required power to be generated at beginning of life, the minimum solar flux input (S_{in})) and the cell efficiency (E_{cell}) the minimum required solar area (A_{req}) has been calculated. The parameters required for the solar array sizing are aggregated from references [7, 37, 27, 36, 38, 39]. Equation 11.2 shows the equation used for the calculation of the required solar array area. Most of the parameters in the equation are specified above. Not yet discussed was F_{pow}, which is a multiplying factor to account for the power usage of the power system itself. Table 11.7 presents all the values of the parameters used in the solar array sizing model and the sources where they have been found.

$$A_{req} = \frac{(P_{req} + P_{charge}) \cdot F_{pow} \cdot F_{rel} \cdot F_{path}}{(D_{cell})^t \cdot D_{Inher} \cdot S_{in} \cdot E_{cell}} \tag{11.2}$$

Table 11.7: Solar sizing input parameters [7, 37, 27, 36, 38, 39]

Parameter	Value	Source
PV Cell efficiency	0.29%	[36]
PV Cell voltage (maximum power)	2.4 V	[36]
PV Cell current (maximum power)	0.5 A	[36]
PV Cell dimensions	40 x 80 mm	[36]
PV Cell degradation (per year)	0.5%	[27]
Inherent degradation (total)	28 %	[27]
Cable loss factor	1.05	[37]
Reliability margin	1.1	[7]
Round-trip efficiency	0.8%	[39]
PV Cell specific mass	50 mg/cm^2	[36]
PV Cell cost (per cell)	€250	M. Preissner, AZUR Space

Using the characteristics of the PV cell as specified in Subsection 11.2.5 the dimensions of the solar panels have been calculated. For the calculation of the length and width of the panels the solar arrays are modelled as a constant voltage source. The number of cells connected in series and parallel are calculated with the required current and the spacecraft bus voltage. With that and the PV cell properties a new solar panel area has been computed and compared to the previously calculated minimum required solar panel area. Afterwards, the number of PV cells in series and parallel has been scaled upwards such that also the requirement for minimum solar panel area for solar input flux was met. As a last step, the configuration of the PV cells on the solar panels and with that the dimensions of the panels had to be determined. The two solar panels were both divided in three smaller rectangular panels such that they could be rotated individually for greater freedom in tailoring the power generation. The length and width of each of the six small panels (2 times 3) are designed such that over the width of the panels the PV cells are connected in parallel, while over the length of the panel the PV cells are connected in series.

Now the layout of the solar panels is fully determined, the mass and cost of the panels can be calculated. The specific mass of the PV cells was found on the website of AZUR Space [36]. For the cost of the PV cells M. Preissner, Sales Assistant at AZUR Space, was approached. M. Preissner could give us a price indication per PV cell which was further used in the cost estimation of the solar array. In Table 11.8 the results of the solar panel sizing can be seen.

Table 11.8: Solar array sizing results

Parameter	Result
Solar panel area (2 panels) (m^2)	10.0
Number of PV cells in series (per panel)	23
Number of PV cells in parallel (per panel)	71
Panel length (per panel) (m)	5.63
Panel width (per panel) (m)	0.89
Solar panel mass (2 panels) (kg)	5.02
Solar array cost ($)	783,900

11.3.4 Battery sizing

The secondary power system on the ARMADA spacecraft will be a battery. The battery is used for providing power to the camera, the altimeter and to the TT&C subsystem, since these cause peaks in the power demand and do not need constant power provision. Additionally, the battery is in charge of deploying the solar panels and the antenna and activating the subsystems after launch. Furthermore, the battery is used as a redundant power source for when the solar panels cannot generate enough power. In eclipse for example, the solar panels will not be able to generate any power and the battery will take over. The amount of time the battery needs to be able to power the spacecraft is set to be 12 hours. During that time the spacecraft will be in safe mode, which means that only the crucial subsystems will be operating. The subsystems still active in safe mode are the C&DH, thermal, power and ADC subsystem.

Table 11.9: Battery sizing input parameters

Parameter	Value	Source
Battery discharge efficiency	0.9%	[37]
Battery capacity degradation (total)	20%	[108]
Depth of Discharge limit	10%	[109]
Cable loss factor	1.05	[37]
Reliability margin	1.1	[7]
Battery characteristics	See Table 11.4	[7]

Again two design points are considered for the sizing of the battery. The maximum required capacity and power of the battery are evaluated for meeting the redundancy requirement of 12 hours and to be able to power the transponder and altimeter during deflection. Both these design points are again considered at end of deflection and then translated back to beginning of life design requirements by taking into account the degradation of the battery (D_{cap}). Other considerations are the limit on 'Depth of Discharge' (L_{DoD}), the discharge efficiency (E_{dc}), the cable loss (F_{path}) and again a reliability margin (F_{rel}) has been included. After calculating the capacity and power required the mass, volume and cost of the battery has been determined using the characteristics of the battery as specified in Subsection 11.2.6. The parameters used in the battery sizing model are aggregated from references [7, 37, 110, 109, 108] and can be seen in Table 11.9. Equations 11.3 and 11.4 show the method of calculating the required capacity and power for the battery respectively. P_{ttc} and P_{DC} denote the power required and the duty cycle of the TT&C respectively. T_{cycle} is the operational cycle time of the battery, while T_{redun} denotes the time the battery needs to be able to power the whole spacecraft for redundancy. In Table 11.10 the results of the battery sizing can be seen.

$$C_{req} = \frac{(P_{ttc} \cdot DC_{ttc} \cdot T_{cycle} + P_{req} \cdot T_{redun}) \cdot F_{pow} \cdot F_{path} \cdot F_{rel}}{L_{DoD} \cdot E_{dc} \cdot D_{cap}} \tag{11.3}$$

$$P_{req} = \frac{P_{req} \cdot F_{pow} \cdot F_{path} \cdot F_{rel}}{E_{dc}} \tag{11.4}$$

Table 11.10: Battery sizing results

Parameter	Result
Capacity required at beginning of life	1344 W h
Power required at beginning of life	258.7 W
Number of charge cycles	2506
Depth of Discharge per normal cycle	16.2 %
Battery mass	19.2 kg
Battery volume	7.91 dm^3
Battery cost	2688 $

11.3.5 Power management sizing

The power management unit of the power system consists of power regulators, power converters, power distribution cables and a power control unit. The shunts are possibly the most important power regulators. They are in charge of dissipating all the excess power absorbed by the solar arrays. In the power demand profile as shown in Subsection 11.3.2 it can be seen that the required power varies a lot. The solar arrays are sized for the maximum required power. Therefore, before the deflection phase and the activation of the ion engines the solar arrays will produce a lot more power than necessary. However, to minimise the amount of excess power it has been decided to not point the solar arrays directly to the Sun before the ion engines are activated. It has been calculated that the solar arrays can be angled by 66 degrees to still be able to power the spacecraft for orbit insertion, which is the most demanding phase before the ion engines are activated. The mass of the power management system is estimated based on Figure 21-6 of Space Mission Engineering: The New SMAD [27]. The results are shown in Table 11.11.

Table 11.11: Power management sizing results

Parameter	Result
Effective solar area required before deflection	4.00m^2
Solar panel incidence before deflection	66 °
Maximum shunted power	5852 W
Power regulation and control mass	3.79 kg
Power distribution mass	1.17 kg
Power regulation and control cost	169,000 $
Power distribution cost	67,500 $

11.3.6 Verification of MATLAB model

The power control subsystem model has been verified in several ways. First of all, sanity checks have been performed continuously throughout the construction of the model. Furthermore, unit tests have been performed for each step of the model. Finally, the outcomes of the model have been validated by comparing them to the sizes and masses of the power system of similar missions.

The unit tests consisted of both analytical calculations and of checking the effect of changing input variables on the outputs. Firstly, the solar flux variation model was verified by performing analytical calculations by hand and by varying the semi-major axis and the eccentricity of the orbit. As was expected, an increase of the semi-major axis resulted in a decrease in solar flux. An increase in eccentricity not only resulted in a greater variation in solar flux, but also in a higher percentage solar flux loss when not rotating the solar panels. This is caused by the fact that a higher eccentricity at the same semi-major axis results in a periapsis closer to and an apoapsis further away from the Sun. That also makes the angle between the velocity vector of the spacecraft and the direction to the Sun bigger, resulting in less effective solar arrays.

As for the sizing of the solar arrays, conservative efficiencies and degradation factors are used and a reliability margin has been included in order to make sure the solar arrays will be capable of providing the required power necessary to successfully perform the mission. Higher efficiencies and lower margins resulted in a smaller required solar array. Additionally, significantly lower PV cell voltages and currents result in bigger solar panels. Finally, the solar array size, mass and cost have been compared to those of other spacecraft with similar missions. For example, the size of the solar arrays of the Rosetta orbiter is 64 m^2 and output 850 W power at 3.4 AU and 395 W at 5.25 AU [111]. This corresponds with a solar efficiency of just 12 percent, while the solar array of the ARMADA spacecraft will have a beginning of life efficiency of 21 percent (taking into account solar cell efficiency and inherent degradation). However, the moment the Rosetta orbiter comes to distances such as 3.4 AU and 5.25 AU, it will have been degrading for some time, which could explain the lower efficiency at these points.

For the verification of the battery sizing a similar procedure has been followed. It has been shown that higher battery discharge efficiencies, lower degradation and higher depth of discharge limits result in a smaller and lighter battery. Furthermore, the longer the required period the battery needs to be able to power the whole spacecraft for redundancy the bigger and heavier the battery will be. For the verification of the power management unit it has been shown that bigger solar arrays and batteries result in heavier regulators and distribution units.

12. Spacecraft Structure

The spacecraft structure is crucial to the design. Its job is to protect the payload and other subsystems from the launch and mission loads and also from external effects such as radiation. In this chapter, the material choice, the sizing and the design considerations of the structure will be discussed in detail.

12.1 Requirements

The requirements are shown below with a check to display whether requirements have been met.

Table 12.1: Requirements for the spacecraft structure

Identifier	Requirement specification	Compliance
ARMADA-SB-01	The space bus shall be able to withstand the maximum longitudinal launch loads of 4.3g.	Check
ARMADA-SB-02	The space bus shall be able to withstand the maximum lateral launch loads of 1.8g.	Check
ARMADA-SB-03	The space bus shall be used as a means to protect the inner subsystems from external radiation.	Check
ARMADA-SB-04	The space bus shall be able to house all subsystems.	Check
ARMADA-SB-05	The space bus shall be able to withstand shock loads during launch and the mission.	Test
ARMADA-SB-06	The deviation of the centre of gravity of the satellite from the longitudinal axis shall not be greater than 0.015 m.	Check
ARMADA-SB-07	The space bus shall have a mass below 70 kg.	Check
ARMADA-SB-08	The space bus shall be able to damp all oscillatory responses to dynamic loads.	Check

Note that requirement 6 is based on the launcher requirements from the manual [40] and requirement 7 is based on the preliminary required dry mass budget.

12.2 Material Selection

The material selection process is crucial in the design of a spacecraft. The spacecraft must be able to withstand structural, acoustic, shock and thermal loads. Moreover, the spacecraft must also be shielded from radiation and high velocity impacts of small debris over the course of the whole mission. In this section, the material for the main structural components will be selected using a trade-off procedure.

12.2.1 Considered Materials

In order to be able to perform a proper trade-off, an initial selection of materials has been made. For the initial selection between material types, the structural requirements are the critical criteria. During launch of the spacecraft the spacecraft experiences huge accelerations and vibrational loads which have to be taken in by the structure. The two types of materials capable of doing so are metals and composites.

For several reasons, the choice has come down to the use of metal alloys for the spacecraft structure. Firstly, the application of composites in spacecraft is relatively new, resulting in a lack of data regarding the use of composites. Moreover, metal alloys have been used for decades, which is why they are preferred over composites in terms of uncertainty and therefore risk [112]. Additionally, the manufacturing of composites is still a costly and time-consuming process. Delays need to be minimised as the gravity tractor concept takes several years to deflect the asteroid in the first place.

Composite materials are less resistant to environmental degradation [112]. They also show high outgassing rates, which increases internal pressure and endangers electrical components within the spacecraft [113]. Finally, the main advantage of using composites in spacecraft design is their low density and therefore lower weight. However, the gravity tractor concept demands a certain weight of the spacecraft and therefore for this specific mission minimising the structural weight of the spacecraft is less of a concern.

The leading source for determining which metal alloys should be considered for the material selection is chosen to be the book 'Spacecraft Structures' of J.Wijker [114]. J. Wijker gained his

structural knowledge at Dutch Space B.V., formerly Fokker space B.V., where he worked over a period of 35 years. Furthermore, he has been professor at the Faculty of Aerospace Engineering, lecturing the Master course 'Spacecraft Structures'. That is why this source has been considered to be valuable and chosen to be leading in the material selection and potentially in further stages of the structural analysis. In the chapter on material selection, five metal alloys are considered to be the most favourable for spacecraft structures: Magnesium alloys, Aluminium alloys, Titanium alloys, Beryllium alloys, and steel alloys. The characteristics of these alloys will be further examined in the trade-off process, and finally one specific alloys will be selected.

12.2.2 Trade-off criteria and weights

The criteria for the trade-off procedure are based on the functionality of the structural components. Firstly, the main purpose behind the structural subsystem is to be able to carry the loads effectively. Therefore, strength and stiffness were selected as criteria for the trade-off. Secondly, the structure must be capable of mitigating environmental threats to the spacecraft subsystems, which is the reasoning behind having radiation resistance and corrosion resistance as criteria. Thirdly, the thermal conductivity is crucial for preventing the propagation of heat throughout the structure. Finally, the mass and costs of the structure should be minimised, so that a higher portion of the respective budgets can be allocated to the payload, thermal, power and communication subsystems. In Table 12.2 the criteria with their associated weights can be seen. A division in propellant tank and spacecraft bus structure has been made, since the criteria will have different weights based on their respective functionality.

The main load carrier of the spacecraft structure will be the propellant tank. That is why strength and stiffness have been given high weights (w.r.t the outer structure) in the trade-off for the tank. However, stiffness is considered to be more important than strength for the spacecraft bus since stiffness is crucial in resisting not only structural but also vibrational loads. The outer structure must be able to carry vibrational loads, which is why stiffness is rated higher for the bus criteria. Mass is considered to be the most important criterion for the spacecraft structure. The more mass saved in structure the more mass is available for other purposes such as bringing additional payloads.

The tank will experience only secondary radiation coming from the spacecraft bus structure and the environment in the spacecraft bus will not be corrosive. Therefore, the weights for these criteria are the lowest for the tank. Thermal conductivity is considered to be of less importance for both the tank and the spacecraft bus structure. The outer structure must protect the inner structure and components from radiation and other degradation effects, which is why corrosion and radiation resistivity are weighted higher than thermal conductivity. Bad conductive performance of the structure can be compensated by the thermal control system by adding insulation for example. Finally, the cost criterion has been given a medium weight. An initial cost estimation, as presented in the Mid-Term Report [46], has shown that the costs of the spacecraft will be well within the budget. However, this cost estimation was a very rough approximation so still caution must be taken to make sure that the the budget will not be exceeded.

Table 12.2: Weights of criteria for material selection

Criteria	Tank	Bus
1. Strength	4	2
2. Stiffness	4	3
3. Mass	5	5
4. Radiation resistivity	1	3
5. Corrosion resistivity	1	3
6. Thermal conductivity	2	2
7. Costs	3	3

12.2.3 Material Trade-off

The scores of the materials for each criteria range from 1 to 5, 1 referring to bad and 5 to excellent performance. High strength and high stiffness properties are preferred. Also, the material shall be as resistant as possible to radiation and corrosion. On the other hand, the lesser conductive materials are preferred since for the thermal control of the system it is necessary that the heat pipes have superior conductive properties in order to direct the heat in the desired direction. Finally, lower mass and costs are favourable to keep the system within the budgets.

First a trade-off between the different types of alloys is performed for both the propellant tank and the spacecraft bus structure. As can be seen in Table 12.3 aluminium alloys are chosen to be the most favourable material for the spacecraft structure and titanium alloys to be most favourable for the propellant tank. J. Wijker mentions just one titanium alloy in the material selection chapter [114], namely Ti6Al-4V. Therefore this is the alloy selected as the material for the propellant tank. However, four aluminium alloys are considered for the material selection of the spacecraft bus structure and compared to each other in Table 12.4. For that trade-off the same criteria and weights are used as for the initial trade-off of the spacecraft bus structure. In

the end the aluminium alloy 2024-T36 was chosen to be used for the spacecraft bus structure. The scores for the structural properties, strength, stiffness and mass, are based on Table 13.1 of 'Spacecraft Structures' [114]. The conductivity properties are found on the website of 'Aerospace Specification Metals, Inc.' [115] and in references [116, 117]. The scores for resistivity to radiation and corrosion are based on references [114, 118]. The cost of the materials are estimated based on current exchange prices [119].

Table 12.3: Material selection (TWS = Total Weighted Score)

	1	2	3	4	5	6	7	TWS Propellant Tank	TWS spacecraft bus
Aluminium alloys	3	3	5	4	4	2	5	76	83
Magnesium alloys	2	2	5	1	1	3	4	61	59
Titanium alloys	5	4	3	4	3	5	3	77	77
Steel alloys	5	5	1	4	4	4	5	76	77
Beryllium alloys	3	5	5	2	2	1	1	66	63

Table 12.4: Spacecraft bus alloy selection with Total Weighted Score(TWS)

Aluminium alloy	1	2	3	4	5	6	7	TWS spacecraft bus
2014-T6	3	3	2	3	3	2	3	56
2024-T36	4	3	3	3	3	5	3	69
6061-T6	1	2	5	3	3	1	3	62
7075-T6	5	3	2	3	3	4	3	64

12.3 Structural Analysis

The structural analysis and sizing of the satellite bus and internal structure will be addressed in the section. For the mission, it is crucial that the spacecraft can carry the loads during launch and the mission; this includes the force loads, the vibrational and acoustic loads and the shock loads. All of these need to be taken into account in order to design the structure adequately for the mission.

Table 12.5: Launcher Requirements

Parameter	Unit	**Value**
Longitudinal Natural Frequency	Hz	35
Lateral Natural Frequency	Hz	15
Longitudinal Load	$m\,s^{-2}$	4.3g
Lateral Load	$m\,s^{-2}$	1.8g
Maximum payload fairing volume	m^3	36.35

12.3.1 Launcher Constraints

The selected launcher is the Soyuz, which has certain requirements regarding the structural integrity of the spacecraft bus, see Table 12.5. The mission phase that generally exerts the greatest loads on the spacecraft is the launch phase. For this reason, the spacecraft will be sized for the launch loads.

12.3.2 Sizing The Structure

The structure of the spacecraft shall be sized using the structural loads (the accelerations on the spacecraft during launch); in particular for bending, compression loads and shear loads. The sized structure will then be checked to see whether it meets vibrational requirements (natural frequencies, sinusoidal loads, random vibrations etc). The structure itself will be modelled as a beam containing a propellant tank and a set of panels, the latter of which function as ribs, in order to provide greater resistance against shear and bending loads. This is seen in Figure 12.1 below:

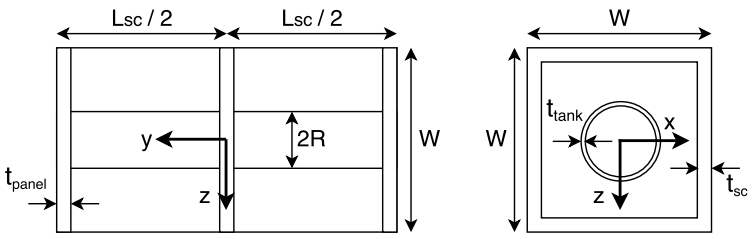

Figure 12.1: An overview of the spacecraft bus

On the right is the front view and on the left is the side view of the spacecraft bus. The propellant tank is the cylindrical component in the centre, the outer structure is the rectangular

beam, and the panels in the centre of the side are the ribs. The idea behind the design is that the propellant tank will carry the bulk of compression, shear and bending loads. Because it is made of Titanium, which has greater strength and stiffness than Aluminium (which makes up the rest of the structure), this is possible even with a lower moment of inertia and volume (see later sections for clarification). The model itself will be designed in MATLAB.

12.3.3 Modelling the Structure

A certain set of initial sizes are assumed for the spacecraft. The main unknowns are the thicknesses of the panels, the outer structure beam and the propellant tank (t_{panel}, t_{sc} and t_{tank} respectively). However, based on the volume constraints of the launcher and mass constraints (the total dry mass of the spacecraft should be 195kg), and assuming that the spacecraft is a cube, together with the propellant parameters (in order to size the tanks), the initial parameters are shown in Table 12.6. Since the spacecraft is modelled as a beam, the free body diagram is shown in Figure 12.2, where the lateral load is modelled as a distributed load.

Table 12.6: Initial Parameters for Sizing

Parameter	Unit	**Value**
V_{sc}	m^3	13.36
w	m	2.3728
L_{sc}	m	2.3728
Total Propellant Volume	m^3	0.31765
Total Propellant Tank Pressure	Pa	$9.8 \cdot 10^6$
Propellant Tank Radius	m^3	0.2064
Propellant Tank Length	m	2.3728

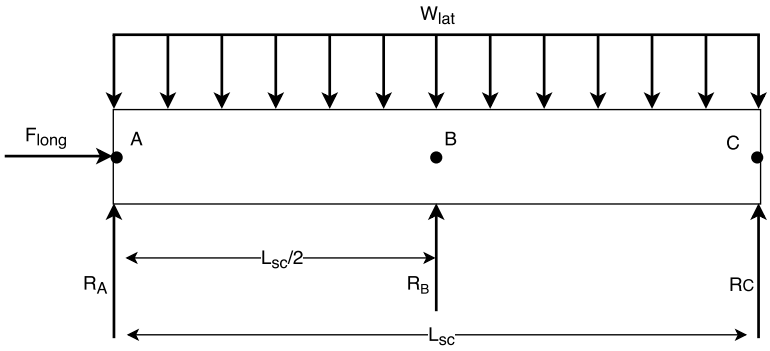

Figure 12.2: Free body diagram of launch phase

Where L_{sc} is the length of the spacecraft, w_{lat} is the distributed lateral load, F_{long} is the longitudinal load, and the reaction forces at A, B and C are R_a, R_b and R_c, respectively. Note that the accelerations given in the launcher requirements take into account the gravity. The axes are based on the reference frames outlined in previous sections. This is a statically indeterminate problem. Therefore, using methods from Mechanics of Materials by R.C. Hibbeler [120], the reaction forces and the longitudinal loads (F_{ab} and F_{bc}, respectively) were found to be:

$$F_{long} = F_{ab} = F_{bc} \tag{12.1}$$

F_{ab} is the load in member AB, whilst F_{bs} is the load in member BC.

$$R_a = R_c = 0.1875 \cdot w_{lat} \cdot L_{sc}, \qquad R_b = 0.625 \cdot w_{lat} \cdot L_{sc} \tag{12.2}$$

Based on the above, the structure is loaded (along its length) as shown in Figures 12.3 and 12.4.

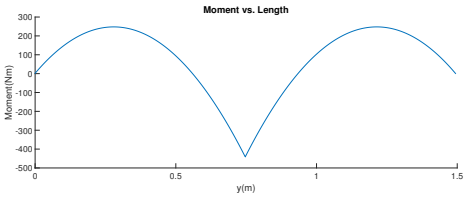

Figure 12.3: Moment vs. length along structure

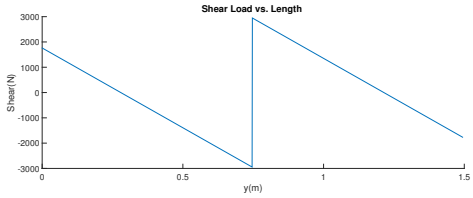

Figure 12.4: Shear vs. length along structure

Once the reaction forces are found, the stress analysis can begin. The assumptions for the structural model are listed below:

- As seen in the free body diagram, the structure will be modelled as a beam with a simple support at the middle and at the ends. This means that the critical buckling load will be lower and the moments along the beam will be higher, providing a worst case scenario (this is crucial during the preliminary design of a structure).

- The propellant tank and the outer skins will carry bending, shear and buckling loads. This means that these components will be designed for this.
- The ribs will carry the lateral compression loads and the bending loads along the structure. This will ensure the structural rigidity required for the spacecraft structure. It will also provide a high resistance against torsion.
- The cross section of the beam will be assumed to have strain compatibility.
- The cross section of the beam will be assumed to have radius of curvature compatibility.

Because the structure is made up different materials, the usual methods cannot be applied straight away. In order to size for bending stresses, buckling and shear, one needs to determine the portion of the load that is transferred to each respective material. This can be determined through strain compatibility and radius of curvature compatibility. For strain compatibility for multi-material beams under compressive loads [120]:

$$\delta = \frac{F_1 \cdot L}{E_1 \cdot A_1} = \frac{F_2 \cdot L}{E_2 \cdot A_2} = \frac{F \cdot L}{E_1 \cdot A_1 + E_2 \cdot A_2} \tag{12.3}$$

Where F_1, is the force on material 1, E_1 is the E-Modulus of material 1, A_1 is the cross sectional area of material 1, F is the total compressive force on the structure, L is the length of the beam, F_2 is the force on material 2 and so on and so forth. From this, taking the tank (index:tank) and the outer structure of the spacecraft (index:sc) as an example, the portion of compressive loads attributed to each section are shown as follows (Note that F_{total} is the total load on the structure):

$$F_{tank} = \frac{E_{tank} \cdot A_{tank}}{E_{tank} \cdot A_{tank} + E_{sc} \cdot A_{sc}} \cdot F_{total} \tag{12.4}$$

$$F_{sc} = \frac{E_{sc} \cdot A_{sc}}{E_{sc} \cdot A_{sc} + E_{tank} \cdot A_{tank}} \cdot F_{total} \tag{12.5}$$

This in turn means that (assuming the beam is simply supported at the centre), the critical buckling load for the outer structure and tank becomes:

$$P_{cr_{sc}} = \frac{(\pi^2) \cdot E_{sc} \cdot I_{sc}}{(L_{sc}/2)^2} \tag{12.6}$$

$$P_{cr_{tank}} = \frac{(\pi^2) \cdot E_{tank} \cdot I_{tank}}{(L_{sc}/2)^2} \tag{12.7}$$

This in turn means that the normal stresses caused by the compressive loads ($\sigma = Force/Area$) are as follows:

$$\sigma_{compr_{tank}} = \frac{E_{tank} \cdot A_{tank}}{E_{tank} \cdot A_{tank} + E_{sc} \cdot A_{sc}} \cdot \frac{F_{total}}{A_{tank}} \tag{12.8}$$

$$\sigma_{comp_{sc}} = \frac{E_{sc} \cdot A_{sc}}{E_{sc} \cdot A_{sc} + E_{tank} \cdot A_{tank}} \cdot \frac{F_{total}}{A_{sc}} \tag{12.9}$$

For bending and shear loads, a similar issue arises in the case where cross sections have different materials. In this case, one assumes the same radius of curvature of both beams, according to the Massachusetts Institute of Technology [121]. For a cross section of two materials, the radius of curvature is as follows:

$$\frac{1}{R} = \frac{M_{total}}{E_1 I_1 + E_2 I_2} \tag{12.10}$$

Where M_{total} is the total moment load on the structure, R is the radius of curvature, E is the E-modulus and I is the area moment of inertia. The indexes 1 and 2 represent materials 1 and 2, respectively. Since the propellant tank is inside the outer structure of the beam (which represents the spacecraft), and has the same centroid as the outer structure (see Figure 12.1), the radii of curvature of both components coincide. Since both components have the same radii of curvature, Equation 12.11 is obtained.

$$\frac{1}{R} = \frac{M_{total}}{E_1 I_1 + E_2 I_2} = \frac{M_1}{E_1 I_1} = \frac{M_2}{E_2 I_2} \tag{12.11}$$

Where M_1 and M_2 are the portions of the moment load on each structure with materials 1 and 2, respectively. Note that the above would not apply if the propellant tank was not exactly in the centre of the outer structure, as the radii of curvature would have to be different. Based on the above, both the normal stresses due to bending, and the shear stresses due to shear loads (as

the latter is directly derived from the former), can be determined for differing materials. The bending equations for the tank and the outer structure are shown below:

$$\sigma_{bending_{tank}} = \frac{E_{tank}I_{tank}}{E_{tank}I_{tank} + E_{sc}I_{sc}} \cdot \frac{M_{total}z_{tank}}{E_{tank}I_{tank}} \tag{12.12}$$

$$\sigma_{bending_{sc}} = \frac{E_{sc}I_{sc}}{E_{tank}I_{tank} + E_{sc}I_{sc}} \cdot \frac{M_{total}z_{sc}}{E_{sc}I_{sc}} \tag{12.13}$$

The shear flow equations for the the tank and the outer structure are shown below:

$$q_{shear_{tank}} = \frac{E_{tank}I_{tank}}{E_{tank}I_{tank} + E_{sc}I_{sc}} \cdot \frac{S_{total}}{I_{tank}} \cdot \int_0^s t_{tank}z_{tank}ds \tag{12.14}$$

$$q_{shear_{sc}} = \frac{E_{sc}I_{sc}}{E_{tank}I_{tank} + E_{sc}I_{sc}} \cdot \frac{S_{total}}{I_{sc}} \cdot \int_0^s t_{sc}z_{sc}ds \tag{12.15}$$

In order to ensure that the structure will not fail, the normal and shear stresses will be compared to the yield and shear strength of the respective material. Using equations 12.8 and 12.12, the total yield stresses in the tank induced by the loads are as follows:

$$\sigma_{total} = \sigma_{bending_{tank}} + \sigma_{compr_{tank}} + \frac{pR}{2t_{tank}} \tag{12.16}$$

The final term in the equation is the internal longitudinal stress of the tank, induced by the pressure forces from the propellant. The maximum yield stresses are compared to the yield stress of the material of the propellant tank. If the load induced stresses are larger than the yield stress, then the structure has failed. The structure will be sized to avoid this.
Similarly, the shear stresses in the tank are compared to the shear strength of Titanium (the tank material). The shear stresses are simply as follows:

$$\tau_{total} = \frac{q_{tank}}{t_{tank}} \tag{12.17}$$

For the outer structure, the equations are for the most part, the same, except they use equations 12.9, 12.13 and 12.15 for the stresses. However, they do not contain the tank pressure components.
The rib panels are placed at the pin supports (see Figure 12.2) are sized according to the compressive reaction loads. The idea is that they provide extra support against bending loads, but more importantly, manage to prevent the lateral loads from causing lateral buckling. These are assumed to be simply supported and are calculated according to:

$$P_{cr_{panel}} = \frac{(\pi^2)E_{panel}I_{panel}}{w^2} \tag{12.18}$$

The above formulae are put into MATLAB, and are iterated for various ranges of thicknesses for the panels, the outer structure and the propellant tank. The resulting stresses are then compared to the shear and yield strength of each component's respective material. If the resulting stresses are smaller than the yield and shear strength, the corresponding thicknesses are then chosen and minimised in order to reduce the weight of the structure as much as possible. A simplified flowchart for the structural MATLAB code is shown in Figure 12.5.

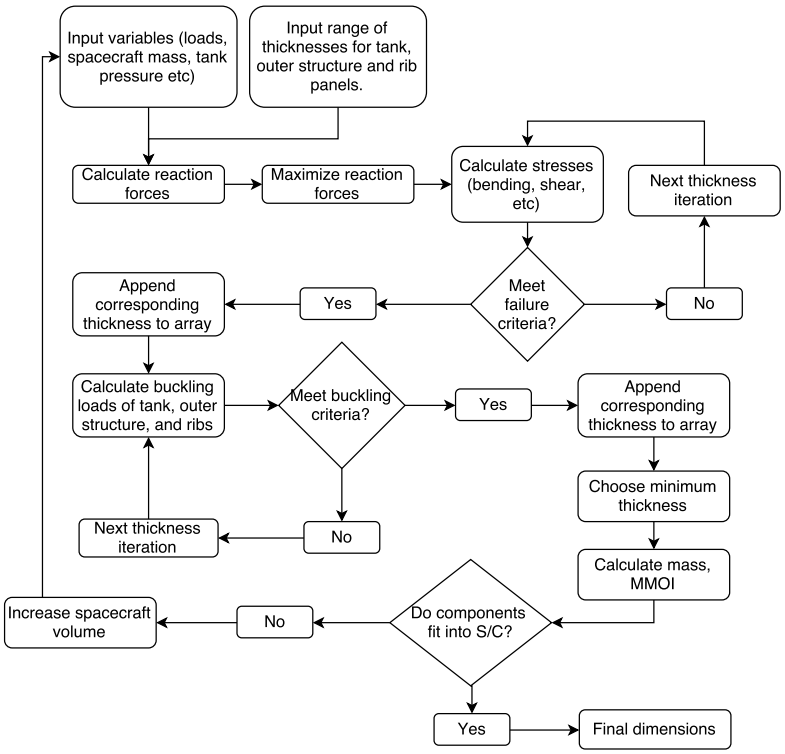

Figure 12.5: Flowchart For Structural MATLAB Model

12.3.4 Results of Structural Analysis

After iterating for a lower mass whilst maintaining structural integrity, the final dimensions of the spacecraft bus are shown in Table 12.7.

Table 12.7: Final Parameters of Spacecraft Bus

Parameter	**Unit**	**Value**
V_{sc}	m^3	3.34
w	m	1.4948
L_{sc}	m	1.4948
Total Propellant Volume	m^3	0.31765
Total Propellant Tank Pressure	Pa	$9.8 \cdot 10^6$
Propellant Tank Radius	m^3	0.2601
Propellant Tank Length	m	1.4948
Rib Thickness	m	$5 \cdot 10^-4$
Tank Thickness	m	0.002
Outer Structure Thickness	m	$5 \cdot 10^-4$
Total Spacecraft Bus Mass	kg	43.2218
MMOI x	$kg\,m^2$	16.8388
MMOI y	$kg\,m^2$	12.7940
MMOI z	$kg\,m^2$	16.8388

The above values are reasonable, considering the mass fraction of the structure. The mass fraction of the structure relative to the total dry mass is 0.2217, which is similar to remote sensing satellites; the latter of which have a structural mass fraction of 0.19 [37]. The Von Mises stress distribution along the tank cross section (at the point of maximum moment and shear i.e. at $L_{sc}/2$) is plotted in Figure 12.6 in terms of θ, which is zero at the bottom of the propellant tank, and 180 at the top:

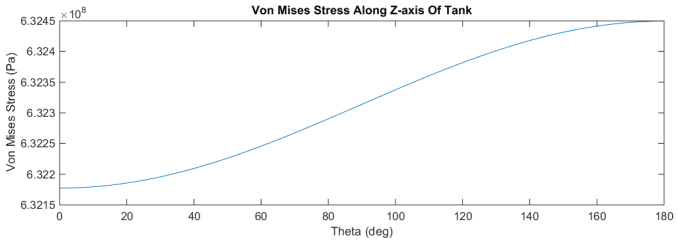

Figure 12.6: Von Mises stresses vs. z-axis of propellant tank

Similarly, the Von Mises stresses along the z axis of the cross section of the outer structure are shown in Figure 12.7 :

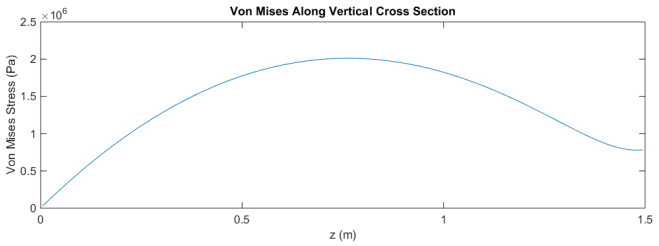

Figure 12.7: Von Mises stresses vs. z-axis of outer strcutre

Note that the increase in stress towards the end of the z-axis of the cross section is caused by the normal stresses, which increase linearly across the z-axis; this is due to the stresses induced by the bending moment. Note that the Von Mises stresses never surpass the Von Mises failure criterion, which for the tank (Titanium) and outer structure (Aluminium) are as follows:

$$\sigma_{VonMises_{Ti}} = \sqrt{(}\sigma^2_{yield_{Ti}} + 3\tau_{fail_{Ti}}) = 1.7174 \cdot 10^9 \tag{12.19}$$

$$\sigma_{VonMises_{Al}} = \sqrt{(}\sigma^2_{yield_{Al}} + 3\tau_{fail_{Al}}) = 5.6836 \cdot 10^8 \tag{12.20}$$

The Von Mises stresses on the structure are lower than the failure Von Mises stresses of the respective materials of the components. Initially, this suggests that the structure is significantly over-designed. However, whilst reducing the thicknesses of the components would indeed make it such that the Von Mises stresses are higher in the face of bending, shear and compressive loads (i.e. less over-designed), it also means that the buckling requirements will not be met. The buckling requirements for the structure are the main constraints in the launch case, as longitudinal compression loads are generally the highest. This is why the Von Mises stresses are relatively low. However, by decreasing the thickness a small amount, the buckling requirements are not met.

12.4 Vibrational Analysis

For the vibrational analysis, the shock loads, the random vibrations and sinusoidal loads will be considered. The idea behind this is that the structure itself will be discretised as a spring mass-damper model. It will then be converted into a state space matrix, so that the response of the system can be calculated with respect to the input loads mentioned above. Depending on whether the responses meet the prescribed qualification loads mentioned in the launcher manual [40], the structure will be re-sized. If there is no need to re-size the structure, based on the responses to vibrational loads, then of course the dimensions of the model will remain the same. In this section, the vibrational model and the corresponding results will be discussed. As for the structural part, the MATLAB model also iterates between various thickness ranges of the components, ensuring that the structure meets vibrational load requirements.

12.4.1 The spring mass-damper model

The structure will be discretised into a single degree of freedom spring mass-damper system as shown in Figure 12.8. On the left is the lateral load model, whilst on the right the longitudinal model is displayed.
The equations of motion are then as follows:

$$m\ddot{x} = -k_{long}x - c_{lat}\dot{x} + u \tag{12.21}$$

$$m\ddot{y} = -k_{lat}y - c_{lat}\dot{y} + u \tag{12.22}$$

Where m is the spacecraft bus mass, k is the stiffness, c is the damping coefficient, u is the input, x is the longitudinal displacement and y is the lateral displacement. The outputs required are the resulting accelerations of the structure; this is due to the fact that qualification responses to vibrational loads are given in accelerations [122]. Subsequently, the equations of motion are converted into a state-space system of matrices, in order to calculate the responses to the load inputs in MATLAB. Although the state-space systems have been found, the stiffness and damping coefficients are still unknown. However, it is known that:

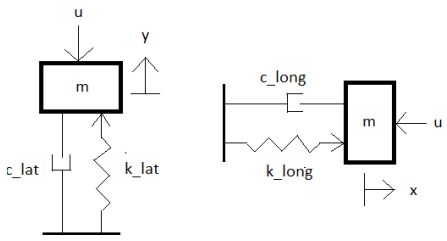

Figure 12.8: Lateral Model (left) and Longitudinal Model (right)

$$\omega_{nat} = 2\pi \cdot f_{nat} = \sqrt{\frac{k}{m}} \tag{12.23}$$

The natural frequency can be calculated using formulae from Space Mission Analysis & Design [37] assuming a simple beam, these equations are as follows:

$$f_{nat_{longitudinal}} = 0.25\sqrt{\frac{E_{tank}A_{tank} + E_{outersc}A_{outersc}}{m \cdot L_{sc}}} \tag{12.24}$$

$$f_{nat_{lateral}} = 0.56\sqrt{\frac{E_{tank}I_{tank} + E_{outersc}I_{outersc}}{m \cdot L_{sc}^3}} \tag{12.25}$$

Based on the above, the stiffness can be calculated according to equation 12.23. The damping coefficient for a second order system is also as follows:

$$c = DR \cdot 2\sqrt{mk} \tag{12.26}$$

Where c is the damping coefficient, DR is the damping ratio, m is the spacecraft mass and k is the stiffness. According to J.Wijker [114], a damping ratio of 0.05 is generally assumed; the damping coefficient can then be calculated as all values are known.
The sizing for these vibrational loads has been carried out in MATLAB; the simplified flowchart for the code is shown in Figure 12.9.

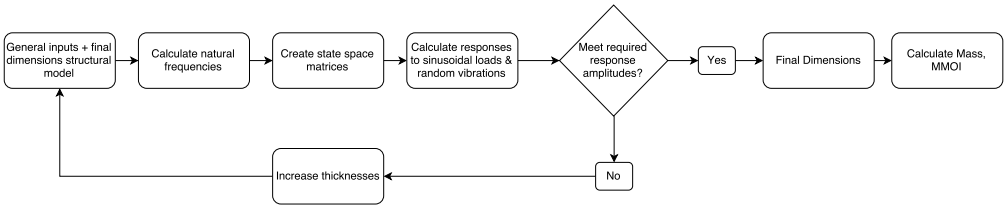

Figure 12.9: Flowchart for vibrational MATLAB model

12.4.2 Responses to sinusoidal loads

The sinusoidal loads have been modelled as shown in the equation below:

$$m\ddot{x} + k_{long}x + c_{lat}\dot{x} = A_{ext}sin(2\pi * f_{ext}t) \tag{12.27}$$

Where A_{ext} is the excitation amplitude of the sinusoidal loads and f_{ext} is the excitation frequency. By modelling the state space systems and applying the lsim command in MATLAB, the acceleration response can be plotted. For example, for a sinusoidal load input to the system with an acceleration of 0.3 g's at 100Hz, the response curve is plotted (shown in Figure 12.10. Note that the figure is zoomed in as the original plot is unclear (due to high frequency oscillations).

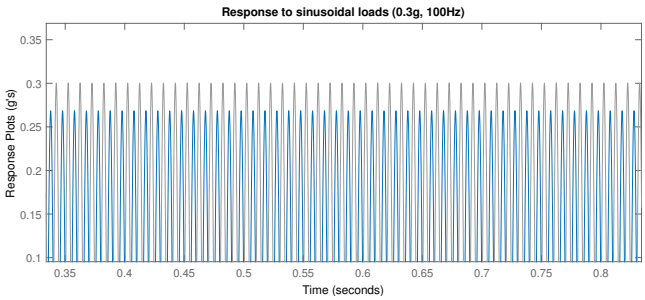

Figure 12.10: Spacecraft response to sinusoidal input

The darker lines are the response, whilst the lighter lines are the input function. As can be observed, the response lines have a lower amplitude than the input sinusoids. In the case of the sinusoidal loads, this means that requirements have been met in this case.
In order for the spacecraft to meet the qualification requirements of the launcher, the response of the spacecraft bus to the lateral and longitudinal sinusoidal loads must meet the required amplitudes. In Table 12.8, the response amplitudes of the structure to the range of sinusoidal inputs are displayed. The required responses and the inputs are based on the Soyuz launcher manual [40]. Note that the dimensions of the structure are the same as displayed in Table 12.7. The MATLAB code tests the structure with the above-mentioned dimensions and with higher thicknesses in order to determine whether the dimensions produced by the structural analysis model are sufficient for the sinusoidal loads.

Table 12.8: Sinusoidal requirements and results

f [Hz]	**Input Amplitude [g]**		**Maximum Required Response [g]**		**Spacecraft Bus Response [g]**	
	Long.	Lat.	Long.	Lat.	Long.	Lat.
5	0.4	0.4	0.4	0.4	0.0000	0.0005
10	0.5	0.6	0.5	0.6	0.0001	0.0029
20	0.8	0.6	0.8	0.6	0.0004	0.0117
30	0.8	0.4	0.8	0.4	0.0008	0.0179
40	0.5	0.4	0.5	0.4	0.0009	0.0330
60	0.5	0.3	0.5	0.3	0.0020	0.0619
100	0.3	0.3	0.3	0.3	0.0034	0.2683

As seen in Table 12.8, the structure meets the launcher requirements, meaning that for this case, resizing is not required.

12.4.3 Responses to random vibrations

The random vibrations have been modelled in a similar manner to the sinusoidal loads. The random loads model the sinusoidal loads during three flight stages; each have the same frequency variation, but different input acceleration amplitudes. The 1st stage has an input amplitude of 4.94 g's, the 2nd stage has an input amplitude of 3.31 g's and the 3rd stage has an input amplitude of 1.63 g's [40]. Note that the amplitude in this case is the RMS value. In this case, the input signal becomes:

$$x_{input} = \sqrt{2} G_{rms} sin(2\pi * f_{input} * t) \tag{12.28}$$

Where G_{rms} is the RMS input amplitude (as shown above), and f_{input} is the input frequency in Hertz. According to the launcher manual, the required response acceleration for qualification is a maximum of 7.5 g's [40]. The response for an input RMS of 4.94 g's at a frequency of 2000Hz is shown in Figure 12.11. Note that the response curve is zoomed in for clarity.

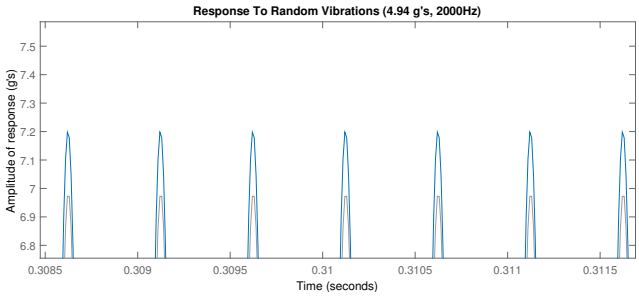

Figure 12.11: Spacecraft response to random vibrations(4.94g's,2000Hz

As can be observed, the peak values for the steady state response reach 7.2 g's, which is still below the qualification loads. Since this is the worst case random load, the structure has been sized sufficiently for these loads.

12.4.4 Responses to shock loads

The shock loads themselves are modelled according to the parameters given in the launcher manual [40]. The parameters are shown in Figure 12.12.

Flight Event	Frequency (Hz)		
	100–1000	1000–2000	2000–5000
	SRS, Shock Response Spectra (Q = 10) (g)		
Fairing & stages separations	15–350	350	350–200

Table 3.2.7a - Shock response spectra at Fairing and stages separations

Figure 12.12: Shock Loads vs. Frequency

Shock loads generally occur during the separation of the stages. According to Figure 12.12, there are three frequency ranges, which correspond to different ranges of input loads. From this information, a shock response diagram can be created; these diagrams show the response of the spacecraft (in g's) to shock loads at all three frequency ranges. However, whilst shock response diagrams are useful in their own right, there are no requirements provided so as to allow one to determine whether the spacecraft meets shock load requirements; this can only be done through testing. However, a basic analysis can be carried out based on plotting responses at the three frequency ranges. The shock itself is modelled as a sinusoidal load lasting 0.005 seconds. Seeing as shocks are essentially impulses, this is a reasonable input signal time; even a worst case estimate. The shock response plot is shown in Figure 12.13. According to Figure 12.13, the response accelerations are far too high, even reaching 2000 g's, suggesting that the structure needs resizing for these loads. However, this needs to be looked into in more detail. At a frequency of 1000Hz and an input acceleration of 350 g's, the response plot is shown in Figure 12.14.

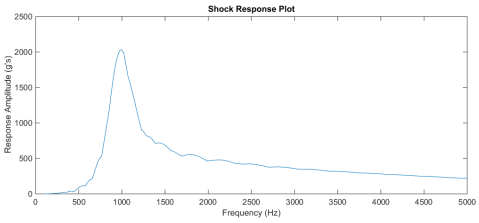

Figure 12.13: Shock Response Plot

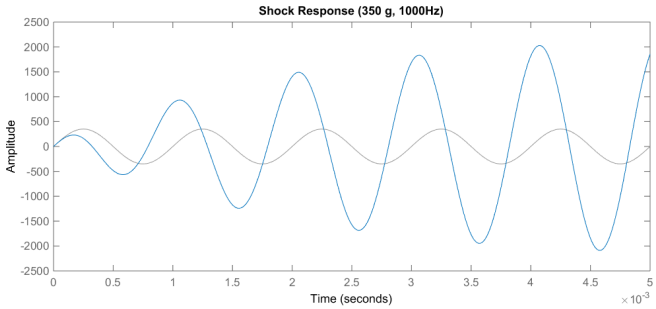

Figure 12.14: Shock Response At 350g's, 1000Hz

As can be observed, the response is under-damped. This implies that the damping coefficient for the system is too low, which means that a highly efficient shock absorber system needs to be

designed and sized in order to allow the spacecraft to carry such loads. However, this is outside of the scope of the DSE, and will be carried out in the post-DSE phase. Moreover, the exact requirements for suitable shock load acceptance during testing for the launcher being used for the mission are not known. Shocks are usually sized for through testing; in the current design phase, this is not possible.

12.5 Radiation

Another important consideration for the design of the structure is the radiation damage to certain (electrical) components. Since radiation analysis is mainly based on stochastic simulation and the project has a set schedule, this was not done directly, instead a toolbox was used to quantify the radiation sources and their effects for the ARMADA mission. The name of this toolbox is SPENVIS and it was designed and is currently used by ESA engineers.

Orbit generator tool

The first step when using SPENVIS is defining the orbital characteristics. An orbit generation tool is used for this. It requires as input the mission duration, start date and orbit type. It is necessary to note that the orbits defined follow three Keplerian laws:

- Orbit is an ellipse with Earth at one of its foci.
- Radius vector of the satellite with respect to the Earth, as origin, sweeps over equal areas in equal time.
- Ratio of squares of periods of 2 satellites is equal to the ratio of cubes of semi-major axes of their orbits.

For the ARMADA mission, the closest fit in terms of orbit type is the near Earth planetary orbit option. Although this simulates a circular orbit at 90000 km altitude, this is considered to be a good approximation of deep space and interplanetary missions mainly due to the fact that, at that altitude, the only sources of radiation are long-term and short-term solar particle fluxes, as well as cosmic rays. The start date chosen was the 21/04/2021 and the duration used was 2677 days. It is necessary to note that for this particular orbit type, the duration does not affect the results that much as the models are only dependent on spacecraft trajectory not actual location. Furthermore, the orbital radius can be varied to simulate a different celestial body than Earth. Using the average radius of Apophis' orbit, the orbit coordinates were defined.

Radiation sources

Using these, different radiation sources can be added to the system. As stated previously, the most relevant radiation sources for the ARMADA mission are long-term and short-term solar fluxes, as well as galactic cosmic rays (GCR). The Van Allen belt radiation is discounted due to the fact that the ARMADA spacecraft will pass through the belt relatively fast, preventing sufficient electrons and protons from getting trapped inside the system, directly affecting it. The long-term solar particle fluences can be simulated by four models: King, JPL, Rosenqvist et al and ESP. The one chosen for this mission is the ESP model, which has one of the biggest data sets for solar events. It was mainly chosen on the basis of the fact that, for predicting incomplete data sets, it uses the maximum entropy principle, which is a significant improvement from lognormal distributions or power laws, on which the other models are based. Furthermore, this model is coupled with the PSYCHIC model which predicts the contribution of heavy ions to the fluences. The inputs for this model are the prediction period (or mission length), ion range to be considered, as well as confidence level for the model. The same mission length as input in the orbit generator is used in this model. The ion range chosen was from H to U, thus considering all ions, with a confidence level of 95%. The outputs of this model are energy levels, fluxe levels, as well as attenuation along the orbit for this source.
For the short-term solar particle fluxes, three models exist: CREME 86, CREME 96 and Xapsos et al. All three are based on particle measurements near Earth, at energy levels relevant for Single Event Effects (SEE). After trying each one, the worst-case scenario was chosen, given by the CREME 86 model, with peak worst-case flare flux and worst-case composition mode selected. This model received as input the ion ranges to be considered and output the solar flux spectra and attenuation factor along the orbit for this particular source.
The final source, galactic cosmic ray, or GCR particles can be simulated using four models: ISO 15390, CREME 86, CREME 96 (Solar Minimum) and Nymmik et al. The chosen model for ARMADA is ISO 15390, as it is the international standard for estimating the impact of this particular source. It takes as input the ion ranges to be evaluated and, in the case of both ISO 15390 and Nymmik et al, the epoch in which the modelling should be done. The ion range is

chosen to be, as for all the previous sources, from H to U, whilst the epoch chosen is the mission epoch, defined in the orbit generator tool. The outputs will be the proton and electron fluxes.

Total ionising dose analysis

Using all these sources, for an input thickness, the total ionising dose can be calculated, using one of two models: SHIELDOSE and SHIELDOSE 2. Both determine the absorbed dose as a function of depth in Aluminium shielding material of the spacecraft, given the values from the radiation sources, quantifying the fluences into total ionising dose. This is based on Equation 12.29.

$$Dose = 1.6 \cdot 10^8 \cdot \frac{dE}{dx} \cdot Phi \tag{12.29}$$

Where $\frac{dE}{dx}$ is the electron stopping power and Phi is the incident fluence. The models deal with simple geometries and take as input the shielding and target material, as well as a thickness of the shielding and geometry type. SHIELDOSE 2 was used since it has a better treatment of proton nuclear interactions. In this case, the shielding is Aluminium and the target material is Silicon - most commonly used in electrical components. This can be duplicated several times or a range of thicknesses can be input. Grouping the results into a text file makes it ready for MATLAB to plot. A MATLAB code is used to read the total ionising doses (TIDs) for specific thicknesses, with two types of geometry, and plot this. The geometry types chosen are Aluminium finite thickness slabs and centre of Aluminium spheres. Furthermore, the program allows for inputting of the radiation tolerances of critical instruments like the sensors, or the CPU. Using this information, the tolerances are plotted against the TID for all thicknesses, ranging from 0.0001 to 20 mm, as can be seen in Figure 12.15.

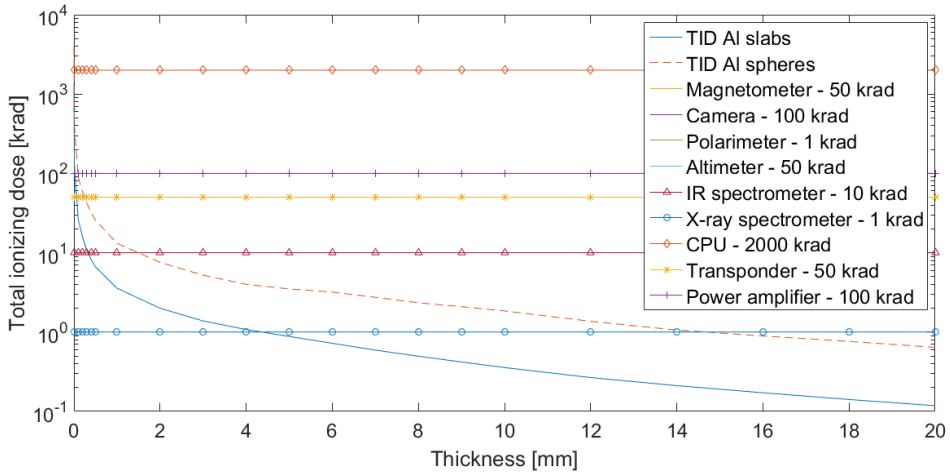

Figure 12.15: Total ionising doses vs shielding thickness, including instrument radiation tolerances

It is important to note that there are two curves for the total ionising dose. This is due to the fact that two shielding methods can be used, namely using Aluminium finite slabs, or at the centre of Aluminium spheres. It can be seen that a slab or box design is better in terms of radiation protection than a sphere, as it requires a lesser thickness for the same total ionising dose, and it is easier to manufacture. As such, the ARMADA mission will be using this type of shielding.
Furthermore, the intersections of the total ionising dose curves with the various instruments represents the minimum required thickness for that specific instrument to survive the full mission time. It is clear that the CPU needs almost no shielding, because its tolerance is 2000 krad, whilst at 0.0001 mm the TID is 1358 krad. For most of the instruments, namely the magnetometers, altimeter and transponders a 0.1 mm thick Aluminium wall is sufficient to enable their survival for the whole mission time. The camera and power amplifiers will require an even lower thickness of 0.05 mm. The IR spectrometer requires only 0.5 mm shielding, which coincides with the structural walls of the spacecraft. Lastly, the most prone instruments to radiation damage are the X-ray spectrometer and polarimeter, which require a thickness of 4.1 mm. Requiring separation walls corresponding to this thickness will be sufficient to ensure the survival of these final two instruments, as the structural walls provide sufficient shielding for the rest of the electrical components.

12.6 Verification of the model

The verification process has been performed continuously throughout the creation of the model. Qualitative checks have been performed during the construction of the model. For example, the

formula for the stiffness k (Equation 12.23) was initially written incorrectly in the MATLAB code and was later fixed. Unit tests have also been carried out by changing input values and checking the affect on output values. For example, the mass was changed to zero; this resulted in zero loads. Similarly, full system checks have been performed, where the failure stresses were changed to zero; this resulted in no possible thicknesses of spacecraft bus components being produced by the program, suggesting that it is working correctly. The unit tests are shown in Table 12.9:

Table 12.9: Unit Tests For Spacecraft Bus

Input Parameter	**Input Value**	**Output Parameter**	**Output Value**
Spacecraft Mass	0	Lateral Load	0
Spacecraft Mass	0	Longitudinal Load	0
Fuel Volume	0	Tank Volume	0
Fuel Volume	0	Tank Radius	0

System tests are shown in Table 12.10:

Table 12.10: System Tests For Spacecraft Bus

Input Parameter	**Input Value**	**Output Parameter**	**Output Value**
Tank Pressure	0	Tank Thickness	1mm
Titanium Yield Strength	0	Tank Thickness	NO VALUE
Aluminium Yield Strength	0	Tank Thickness	NO VALUE
Aluminium Yield Strength	0	Outer Structure Thickness	NO VALUE
Buckling Load	0	Tank Thickness	NO VALUE

The above suggests that the structural analysis model has been verified.

13. Spacecraft configuration

After the specification and sizing of the subsystems, the configuration of the spacecraft can be designed. The positions of some instruments are dictated by their requirements or geometrical restraints, whereas others are free to move around. This chapter will outline the design process which led to the final configuration of the spacecraft, which can be seen in Figures 13.5 to 13.9.

13.1 Configuration determination

It was decided to optimise the internal layout of the spacecraft. The Soyuz rocket will be used for launch, and this comes with a requirement that the center of gravity of the spacecraft must stay within a distance of d$\leq$ 15mm from the launchers longitudinal axis [122]. Additionally, each instrument inside the spacecraft dissipates a certain amount of heat which is to be minimised over the satellite panels. This is so that "hot spots" are not created, putting less strain on the thermal control subsystem. In other words, one would like to reduce the temperature gradients throughout the spacecraft. This optimisation has to be done in accordance with the various subsystem layout requirements. An example of these is the fact that all the scientific instruments must be placed on the panel that should be pointing at Apophis.

Method and code description

The following method was used to determine the internal layout of the spacecraft, the process flow diagram can be seen in Figure 13.1:

1. The spacecraft was split up into six panels which represent the rectangular shape of the spacecraft. The panels are then split up into meshes, which relate to the smallest dimension of part that will be placed on that panel.

2. The instruments geometry is then also simplified into blocks. With each block in the instrument having the same dimensions as the panel mesh. A schematic of the system can be seen in Figure 13.3, where the coloured blocks represent an instrument placed on the satellite panel and where the panel is represented by the entire grid.

3. First, the code finds every possible position that each shape can have individually on the mesh and assigns the coordinates to an array. Then the code checks the arrays of each instrument against each other to obtain all configurations that the instruments can have on that panel without instruments overlapping and saves these coordinates to a final array. This array contains all possible configurations of the instruments on a certain panel without overlap.

4. Now that all the configurations have been found the centre of gravity requirement can be fulfilled. The code runs through the array of all possible configurations and calculates the centre of gravity, it then only saves the configurations whose centre of gravity lie within 15mm of the longitudinal axis of the launcher.

5. The final step is to optimise for heat distribution on the panel. The idea is to make the heat dissipation as uniform as possible over the entire panel. The configurations that lie within the centre of gravity are put into the objective function 13.4

   This function is derived from Equations 13.1 to 13.4. The configuration that yields the lowest value of $H_{influence}$, while still in accordance with set requirements, such as the predefined position of the engines, will be chosen as the configuration for that panel.

13.1.1 Heat optimisation

The method used to find the configuration with the most uniform heat distribution is derived from formulae 13.1 to 13.4.
Again, we consider the mesh created for implementation in MATLAB. In equation 13.1, D represents a simplified form of the influence of an instrument's heat dissipation on each of the panel cells. If one assumes that the instruments heat dissipation comes from a point heat source then its influence on the rest of the panels is seen in Figure 13.2.

$$D_{i,j,k} = \frac{P_{i,k}}{r^2_{i,j,k}} \tag{13.1}$$

Where the piece of equipment, the satellite panel, and the cell number are denoted by the subscripts i,j and k respectively and r is the distance from the centre of a cell to the centre of gravity of an instrument. This is depicted in Figure 13.2. The influence on each cell on the grid is the sum of the influence of each instrument on that cell and can be calculated using Equation 13.2.

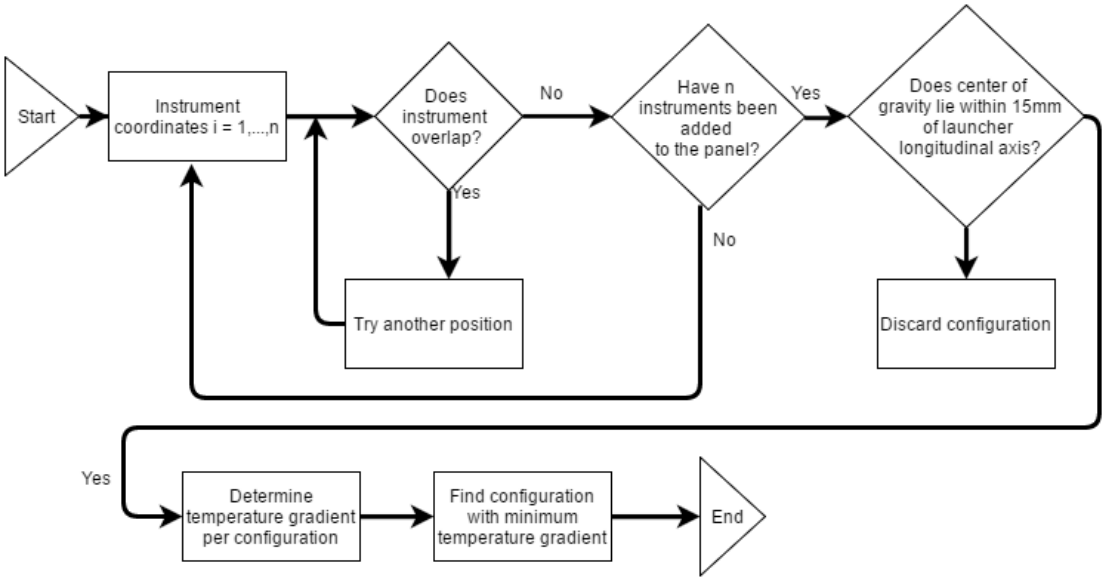

Figure 13.1: Configuration process flow diagram

$$D_{j,k} = \sum_{i=1}^{N} D_{i,j,k} \tag{13.2}$$

The average value of the influence of the instruments heat dissipation over all the cells is given by Equation 13.3.

$$\bar{D} = \frac{\sum_{j=1}^{N_{cells}} D_{j,k}}{N_{cells,k}} \tag{13.3}$$

An indicator of the dissipated heat for each cell, along with the average over the entire panel has now been acquired. By plugging in all coordinates from the configurations that meet the centre of gravity requirement into Equation 13.4, one obtains a value, H, that indicates how uniformly the heat is spread out over the panel.

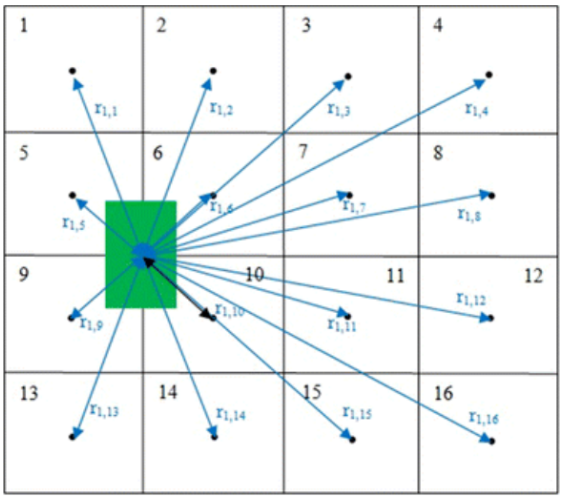

Figure 13.2: Instrument influence on mesh

$$H_{influence} = \sqrt{\frac{\sum_{j=1}^{N_{cells}} (D_{j,k} - \bar{D}_{j,k})^2}{N_{cells,k}}} \tag{13.4}$$

The configuration with the lowest value of $H_{influence}$, that still abides with the requirements of the other instruments and panels will be chosen as the configuration for that panel.
Its necessary to mention that when combining the panels to obtain the final integrated internal layout, compromise will have to be made to ensure that requirements are met and instruments do not collide when considering the configurations in 3D.

Results

This subsection present the results of an optimisation of a panel, the panel containing the scientific instruments will be used as an example. It was chosen to optimise this panel first and use it as a baseline for the rest of the spacecraft, because this panel had the requirement that all scientific instruments be on it. This will be the side of the spacecraft that faces Apophis when any scientific measurements are made. As discussed, the size of the instruments have been simplified into blocks, of the same size as the blocks in the panel mesh. The table provides the colour of that instrument in figures 13.3 and 13.4. Along with the mass, which is related to the centre of gravity requirement, the heat dissipation, relating to the heat optimisation and the block size, which is related to the mesh representation of the panel. The heat dissipation was based on an assumption of 80% efficiency for all the instruments and the assumption that all power lost was in the form of heat.
The total amount of configurations before optimisation was 400000, so it was decided to first run the configurations with 4 instruments only through the gravity requirement, then add the fifth instrument, then finally run the configurations with 5 instruments through the gravity requirement again. There were 526 configurations that met the centre of gravity requirement,

Table 13.1: Scientific instrument characteristics

Scientific Instrument	Colour in Figure 13.3	Mass [kg]	Power Dissipation [W]	Block size
Framing Camera	Blue	10	3.4	5 x 4
Polarimeter	Red	5	0.4	2 x 1
Laser Altimeter	Green	12	10.4	2 x 2
X-Ray spectrometer	Brown	4.4	2.2	2 x 2
Infrared spectrometer	Yellow	1.5	1.9	3 x 3

and of these, the configuration that spreads out heat dissipation as uniformly as possible, or has the lowest temperature gradients across the panel, can be seen in figure 13.3. This configuration partly validates the optimisation as it makes sense for the inputted requirements. This panel was optimised about the centre of the i axis in the figure. The heaviest two instruments which are the framing camera and laser altimeter, lie along the centre of the i axis. While the highest heat dissipating instrument, the laser altimeter, is not touching another instrument. Additionally the the polarimeter and the infrared spectrometer, which are the lowest dissipating instrument are allowed by the program to lie next to each other. A comparison of the outputted configuration and its implementation in the cad model can be seen in figures 13.3 and 13.4.

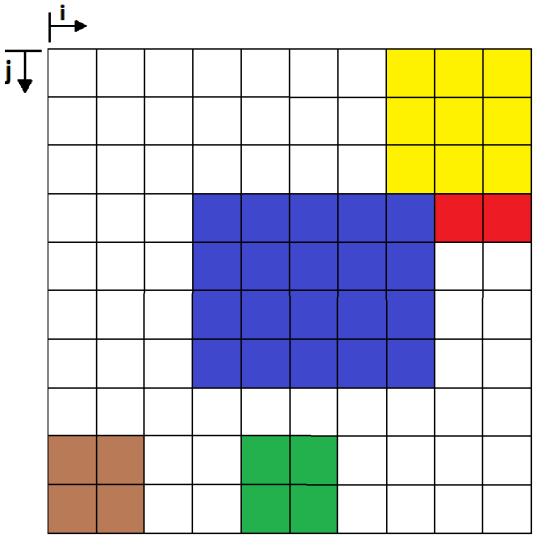

Figure 13.3: Mesh view of scientific instrument panel

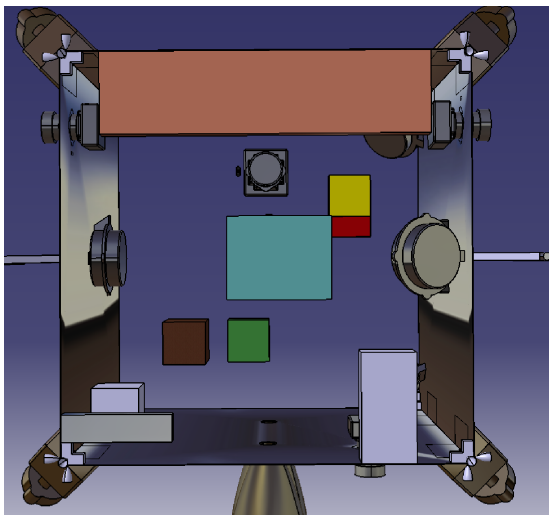

Figure 13.4: CAD view of scientific instrument panel

The remaining panels of the spacecraft were built up in a similar way, that is, the placement of instruments that had freedom of position were optimised.

13.2 Spacecraft layout

This section presents the layout of the spacecraft, including figures showing notable features of the spacecraft. Figure 13.5 shows the full spacecraft as designed in Catia, a render of the full spacecraft can also be seen on the front cover of this report. As discussed, many features of the spacecraft had little design freedom with respect to where they could be placed. In figure 13.7 the configuration of the crafts three different engines can be seen. Firstly, the insertion engines, shown in green in figure 13.7, had two sides of the craft where they could be placed, as they had to be in line with the fuel tank, which can be seen by the circle between the two insertion engines. The fuel tanks' position inside the spacecraft can be seen in 13.8, the tank has been placed from panel to panel as it has been designed to take the high loads that will be seen during take-off. It is possible that additional fuel tanks will be placed around the craft in the future, however, for now, the equivalent volume of all the space needed for fuel has been incorporated into the one tank. The ion thrusters which are coloured red in figure 13.7, have been placed at the corners with an angle to the spacecraft to ensure that the exhaust plumes do not hit the asteroid. It was favourable to have them as high on the spacecraft's z axis as possible, which is the top of figure 13.7, this was for stability reasons. Their final position has been chosen to meet the center of gravity requirement. The final engines were the ADCS thrusters which have been

placed on each corner of the craft. Figure 13.6 shows the reaction wheels, in red, in a tetrahedral configuration. The reaction wheels had to be placed in a tetrahedral configuration, however they were free to be placed anywhere in the spacecraft. They were placed on these panels due to free space, and it was favourable for the center of gravity.

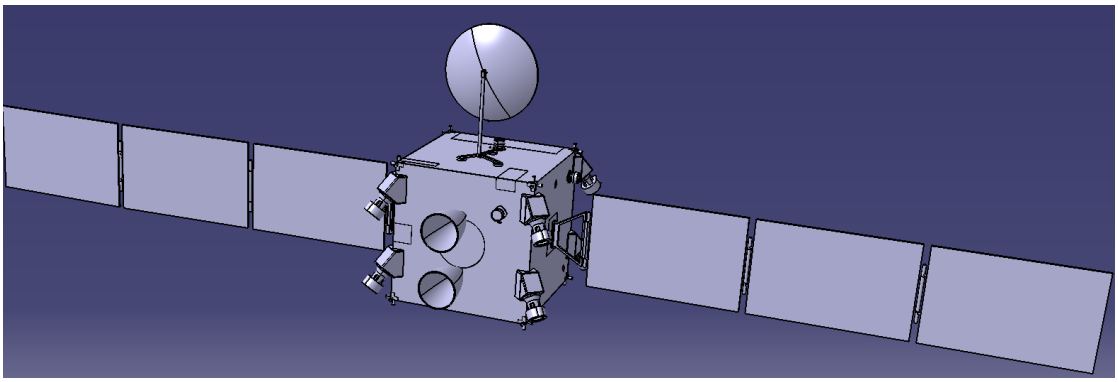

Figure 13.5: Full spacecraft CAD model

The battery, depicted in yellow in figure 13.8, is the highest heat dissipating device and the optimisation has simply placed it as far as possible from any other instrument. After all instruments, both inside and outside the craft, had been positioned the center of gravity requirement has been met and it lies 7.2 mm from the longitudinal axis of the Soyuz rocket. It is necessary to mention that the initial structural design has yielded a $1.5m^3$ craft. As can be seen in the figures, there is a considerable amount of empty space inside the spacecraft. With sufficient time, further iterations would be performed to reduce the size, using the same technique for the configuration determination.

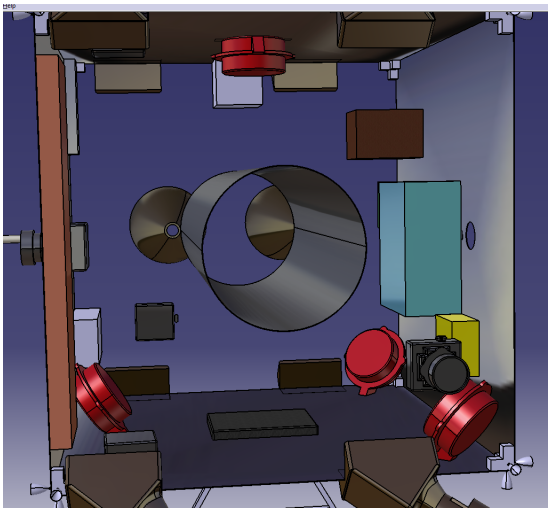

Figure 13.6: Reaction wheel configuration

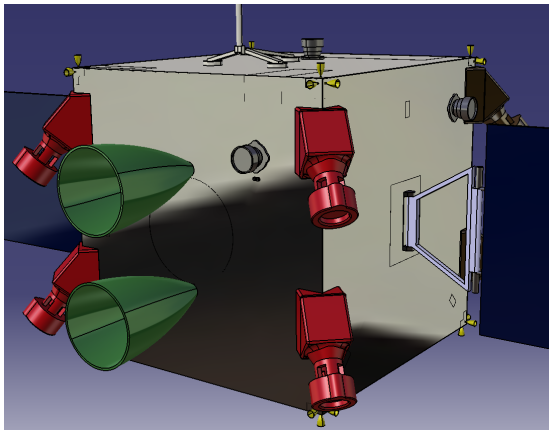

Figure 13.7: Spacecraft engine configuration

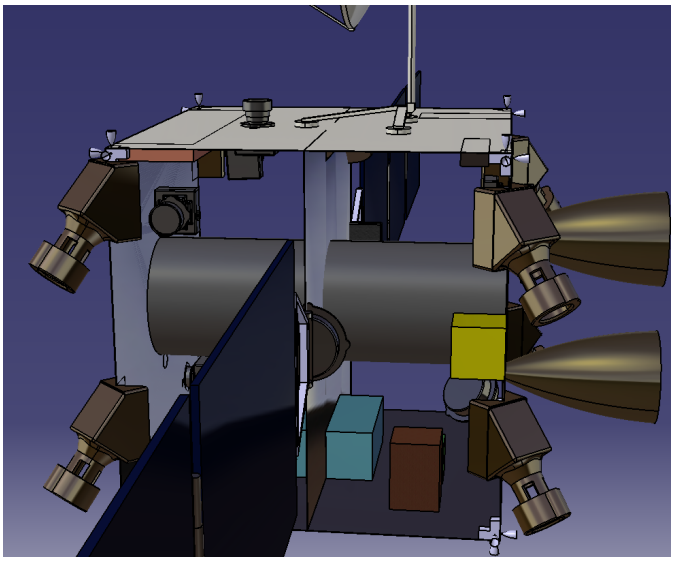

Figure 13.8: Spacecraft interior

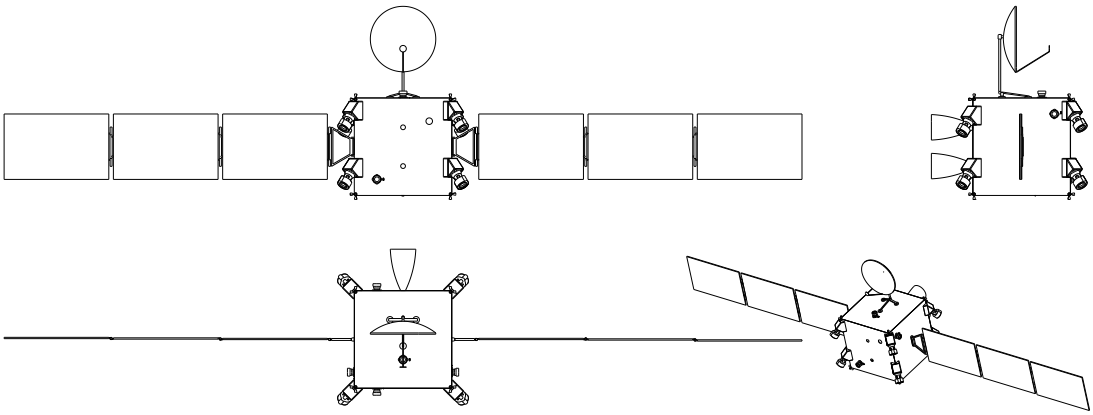

Figure 13.9: The spacecraft seen from different views

14. Design analysis

This chapter will give an overview of the analysis and modification of the design for risks, reliability, availability, maintainability, safety, sustainability, sensitivity, its compliance to the set requirements and finally the final resource allocation.

14.1 Risk management

In the design, the risks for each functional phase will be considered. For the first phase, the risks of all activities prior to launch will be considered. For all consequent phases, the risks will be identified and assessed for severity of consequences and probability. The measures taken in the design to mitigate the risks are also detailed. In this report, the technical risks posed to the mission as described in Chapter 2 are considered, as well as technical risks that may occur before the mission starts. In addition, there are several risks present in the organisation of the design execution. As discussed in the mid-term report, the risks can be divided based on two characteristics: the likelihood that it occurs, and the effect or consequences it has on the mission if it were to occur. These are both characterised by four levels. The likelihood ranges from low to moderate, high, or very high. The effect ranges from low to moderate, high, or catastrophic. The risk equation is illustrated in Equation 14.1, where R is the risk, P is the probability or likelihood, and C is the consequence or effect.

$$R = P \cdot C \tag{14.1}$$

During all design phases of the spacecraft, every foreseeable event that influences the chance of mission success must be considered. This can be shown with the different risks plotted on a risk map, see Figure 14.1. The risks will be elaborated on afterwards.

Likelihood	**Very high**				
	High		T3	T5, T10	O6
	Moderate			T1, T2, T4, T6, O2	T9, T11, O1
	Low			04, O5	T7, T8, T12
		Low	**Moderate**	**High**	**Catastrophic**
		Effect			

Figure 14.1: Risk map showing risks before mitigation

External technical risks in pre-launch activities

Several external risks are present in the necessary activities to manufacture the spacecraft and prepare for launch. These can be listed as following.

- **T1. Manufacturing errors** - During the manufacturing of the components, undetected errors might occur. The highest risks arise from human intervention, in the case components are not made by computer-controlled machinery. The likelihood of occurrence is moderate, while the consequences may seriously affect performance and are thus considered high. The risk can be mitigated by extensive testing, and applying redundancy. The likelihood of occurrence is then considered low, with moderate effects on the spacecraft if it occurs.
- **T2. Impurities in used materials** - Although the materials used can be scanned and checked thoroughly, impurities at critical spots could still be present. This risk is considered to be as likely as risk T1 of manufacturing errors, with equal consequences. The risk can be mitigated by extensive testing, and applying redundancy. As for risk T1, this risk is mitigated to low likelihood and moderate effect.
- **T3. Transporting to launcher** - As components are sometimes produced in a different location from where assembly takes place, and these may, in turn, be far away from the launcher assembly, these transport distances may pose a risk to sensitive equipment. The effect on the mission is considered moderate, the likelihood is considered high. The risk can be mitigated by either minimising the transport costs, or investing in safe method to transport the components. If this is implemented properly, both the likelihood and effect will be low.
- **T4. Extreme weather conditions** - If an optimal launch date is selected, it may be the case that unforeseen extreme weather conditions will delay the launch. This may be very costly, but in addition could also lead to less optimal transfer trajectories, which, in turn, leads to effectively decreasing the safety margins in propellant. Although extreme

weather may be forecast in advance, the likelihood is moderate but the effect is high if it occurs. A proper planning and analysis of the launch site, as well as proper investigation of alternate launch dates can decrease both the likelihood and the effects, mitigating the risk to a moderate likelihood with low effects.

External technical risks in post-launch activities

After launch, the first phases are critical for mission success. For instance, all stage separations, system boot up activities, and mechanical deployments must be performed correctly in order to continue. In addition, the environment of space is harsh and poses several threats to the mission. The following list elaborates on the identified risks for this mission phase.

- **T5. Shock damage** - During launch and separation events, shocks can be more severe than initially expected. If such a shock were to damage a critical component, the mission success may be compromised. In addition, sensitive cabling attachments may detach due to this. Both the consequences and the probability of occurrence are high. Designing the components to endure higher shocks than projected, i.e. using a high safety factor will highly decrease the likelihood of such an event, rendering it to low. Properly implemented redundancy further reduces the effect to be moderate.
- **T6. Radiation damage** - After leaving Earth, the spacecraft is no longer protected by the atmosphere and magnetic field. Radiation from the Sun and from cosmic background can result in errors in electrical equipment, which may be damaged or not functioning properly. The consequence is considered high, the likelihood is moderate. However, by properly shielding the components, the likelihood of damage by radiation will be decreased to low. With sufficient redundancy, the effect will be moderate.
- **T7. Collision with space debris** - Although space is vast and generally empty, there is natural occurring or man-made small space debris that may hit the spacecraft. Especially smaller debris, with high relative velocity, pose a significant threat to the spacecraft since they generally cannot be detected. The likelihood of this happening may be low, but the consequences are catastrophic if critical components are damaged. Proper shielding of the spacecraft will decrease the effect of collisions to moderate, effectively mitigating the risk.
- **T8. Extreme solar events** - In addition to general radiation, sometimes highly energetic solar flares or winds are expelled by the Sun. The intensity of such events is so high that it may damage electrical equipment or induce large errors in software. Although this is assumed to be of low likelihood, the effects can be catastrophic. The only feasible measure to mitigate this risk is using extra radiation shielding, rendering the effect moderate.

Internal technical risks

In addition to the external risks, internally there are certain foreseeable events that may lead to unwanted situations.

- **T9. Component failure** - If a certain component fails, it cannot be repaired or replaced. As many components are vital for mission success, this internal risk is considered to have catastrophic consequences. It is assumed to be moderately likely. However, with sufficient redundancy, the likelihood of all redundant components failing is low. Furthermore, the effect is low, as another component can take over when a failure occurs.
- **T10. Short circuit** - As some of the components used are rather sensitive to changes in current and voltage, this means that sudden changes in power supplied may result in short circuits, damaging the components. If the power system is not properly designed, this risk is highly likely and the effects are also high. However, with effective power design, the likelihood of a short circuit occurring is low, with moderate effects.
- **T11. Malfunction of deployment mechanisms** - If the deployment mechanisms fail due to any external risks like manufacturing errors, this affects the whole mission. The likelihood of these malfunctions is moderate, and the effect is catastrophic as either no power is available, or no communications. Extensive testing and redundant systems can mitigate this risk to have moderate effects and low probability.
- **T12. Software malfunction** - As the spacecraft is autonomous, every function and action is pre-programmed. As it is quite difficult to update the software, any bugs present in the programs may result in malfunctions. The likelihood is considered moderate, but the effect may be catastrophic. However, with proper code verification and validation, and the option of sending and implementing updates, the likelihood and effect of this happening can be reduced to low.

Organisational risks

Apart from mistakes and events in the design and realisation, the organisation of the whole project poses several risks on the design.

- **O1. Delays** - In the event that an activity takes more time than scheduled, the next events will be delayed. If the schedule is poorly managed, one delay will cause a chain reaction. As delays usually bring high additional costs, a properly maintained schedule minimise the cost. The effects of delays can be severe, even catastrophic, with moderate likelihood of occurrence. However, if effective planning and a procedure for early detection of delays and time management is implemented, the likelihood and effects can be mitigated to low.
- **O2. Ineffective or absent communication** - As many different companies produce different components of the spacecraft, it is of utmost importance that the communication between the organisation and these companies is effective and efficient. Failing to do so may, in turn, result in delays, unforeseen circumstances, or even loss of contracts. This risk is therefore considered to be moderately likely, with high consequences. However, if procedures are developed for efficient communication and effort is put into collaborating with the intermediate companies, the likelihood and effect of this risk is considered low.
- **O3. Losing investors** - If a stakeholder or investor of the project is not satisfied by the progress, they may cease to have interest and cancel their investments. Although this has a moderate likelihood, it may have a high effect on the mission, as budgets need to be re-evaluated. As with risk O2, this risk can be mitigated by constantly keeping the investor updated, as well as keeping sufficiently high margins in the budget.
- **O4. Legal issues** - In case of the accidental use of a patented idea or product, the company responsible may be sued by the patent holder. This may mean delay or high costs, which effectively decreases the safety margins in the budget. Although these accidents have low likelihood, the effects can be high. However, proper research into the selected concepts and designs can mitigate the probability to low.
- **O5. Political issues** - As spacecraft missions tend to encompass international collaboration of companies and agencies, this may pose a risk in case relations between countries deteriorate, and collaboration becomes difficult. As this can seriously influence the design possibilities in terms of component selection, for example, the effects are high, but the likelihood is low. However, researching this issue in advance can mitigate the effects to be low, as then only small details may result in problems.
- **O6. Competitors** - The ideas and designs of the project are subject to the interest of companies and agencies, as will be seen in the market analysis in Section 16.5. However, competitors may be favoured if the design is not properly presented or performed. The result of losing the assignment to another design team is catastrophic for the mission, and has a high probability if not taken into account. However, if a proper market analysis is performed, the chances of unforeseen competitors appearing will decrease, thus decreasing the likelihood of this occurring to low. If, in addition, collaboration with competing organisations is established, the effect of this risk is nullified and the competitors become assets instead.

The mitigation measures taken lead to a new risk map after mitigation, shown in Figure 14.2

Likelihood	**Very high**				
	High				
	Moderate	T4, T5			
	Low	T3, T9, T12, O1, O2, O3, 05, O6	T1, T2, T6, T7, T8, T10 T11	O4	
		Low	**Moderate**	**High**	**Catastrophic**
		Effect			

Figure 14.2: Risk map showing risks risks after mitigation

14.2 Reliablility, Availability, Maintainability & Safety

The Reliability, Availability, Maintainability, and Safety (RAMS) analysis presented in this report is based on similar missions and knowledge gained through the design of the gravity tractor and its associated characteristics. RAMS is a method used to determine in which areas failures are likely to occur, and centres around the prevention of failure, as well as the reduction of the

consequences of failure. For clarity, the exact definitions with which the RAMS of the system will be evaluated are as follows:

- **Reliability** - *Reliability is a measure of a system's ability to perform the specific task it has been assigned for a specific period of time.*
- **Availability** - *Availability is a measure of a system's ability to remain in a functioning state. For non-repairable systems this is simply the reliability.*
- **Maintainability** - *Maintainability is related to the ease and speed with which maintenance can be performed on an item or equipment.*
- **Safety** - *Safety is the reduction of unacceptable risk to life, limb and health.*

14.2.1 Reliability

Reliability is the process of estimating the system RAMS by assuming failure rates for each component in the system. This process offers a quantitative measure of the extent to which each individual component meets the required mission objectives. By doing so, different components can be compared to see which one increases the probability of the system to be able to perform all the necessary actions throughout its operational life.

The elementary expression for the reliability, R, of a single component, as a function of its operational time is the following:

$$R = e^{-\lambda t} \tag{14.2}$$

However, the most common way of computing the reliability of a system is by using the Weibull distribution [123]. This approach assumes that the relationship between the failure rate (λ) and time (t) can be described by three parameters: shape (β), location (γ) and scale (η) parameters. The elementary equation for the Weibull distribution can be seen below.

$$R = e^{-(\alpha t)^{\beta}} \tag{14.3}$$

Then, assuming that all the subsystems are stacked in series, the following relation to describe the reliability of the whole system was found. This assumption is the worse-case scenario as assuming that all subsystems are in series means that if even one of them fails, the general system will also fail to meet its objectives.

$$R_{a-n} = R_a \cdot R_b, ..., R_n \tag{14.4}$$

When estimating for the reliability of the system, three case scenarios can be observed: increasing, decreasing or constant failure rate. This is controlled by the shape parameter. Thus, by plotting the three possible solutions one can check whether or not the system complies with the requirements. These results can be seen in Figure 14.3. On the same figure, it can also be seen the reliability of the whole system depending on the probability of failure of each subsystem. It was obtained from [124], the failure rates of each subsystem which were then used to compute the reliability of the whole system, this curve main purpose is to be used as reference to see which subsystems have a higher chance of failing, and thus, redundant components should be added.

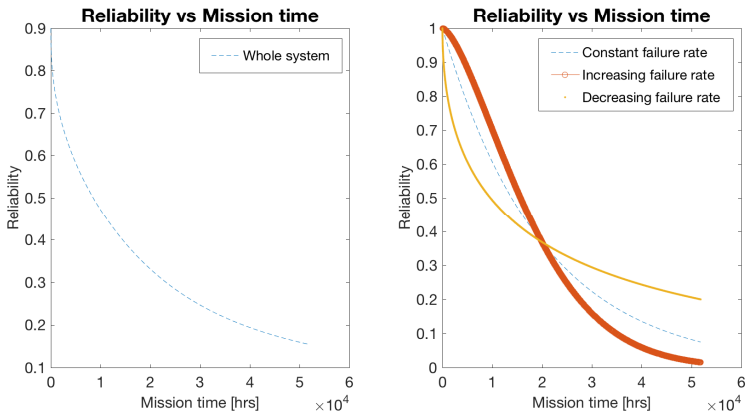

Figure 14.3: Three different failure rates of the ARMADA mission.

14.2.2 Availability

Availability, A, can be thought of as the proportion of the total time that the vehicle is operational [27], quantified in equation 14.5.

$$A = \frac{t_{operational}}{t_{total}} \tag{14.5}$$

The ARMADA mission aims at reducing eclipse times to the bare minimum, thus maximising availability. The type of orbit chosen was traded off with communication in mind, so, barring the transfer, the ARMADA spacecraft will be available to users from the ground for the full duration of the mission.

Redundancies will be incorporated for any (sub)systems or parts that have single points of failure. This will increase availability, in the case of redundancy in communication, as well as the overall reliability of the system.

14.2.3 Maintainability

Maintainability refers to the ease, cost, accuracy and safety related to maintaining a system. For most space missions, physical maintenance is not possible, albeit not unheard of. This is mostly due to the fact that a large amount of space missions are unmanned, thus a physical action is almost impossible to produce. It is important to note that if redundant systems have been installed, it is possible for the spacecraft to automatically recover from failure by switching to the redundant system, or this can be done by means of a ground station issuing commands to the control module of the spacecraft.
Even though physical maintenance activities are unlikely for the ARMADA mission, other types, applicable to this particular scenario, can be implemented. These are separated into three categories and each is explained in more detail, giving an overview of what specific actions make each of them up.

Ground station maintenance

- Maintain operational ground station procedures, databases and documentation.
- Provide ground station support to operations during critical mission phases, before and after launch.
- Report on ground station and associated systems performance.
- Plan and schedule testing, validation and implementation phases.
- Provide support to new programs in terms of definition, integration and development.
- Analyse obsolescence and evolution of ground station systems.

Orbit maintenance

- Maintain required position and attitude.
- Control position and attitude.
- Maintain required power and temperature levels.
- Control power and temperature levels.

Software updates

- Analyse obsolescence and evolution of software.
- Plan, schedule and implement necessary updates.
- Create and store a back-up of the old system before update.
- Test/analyse and validate software updates.

In addition, there are three main measures to quantify the maintainability actions required for the system. These three methods are Mean Time to Repair (MTTR), Mean Time to Failure (MTTF) and Mean Time between Failures (MTBF). To have a clear view of the difference between these three techniques, Figure 14.4 can be found below.

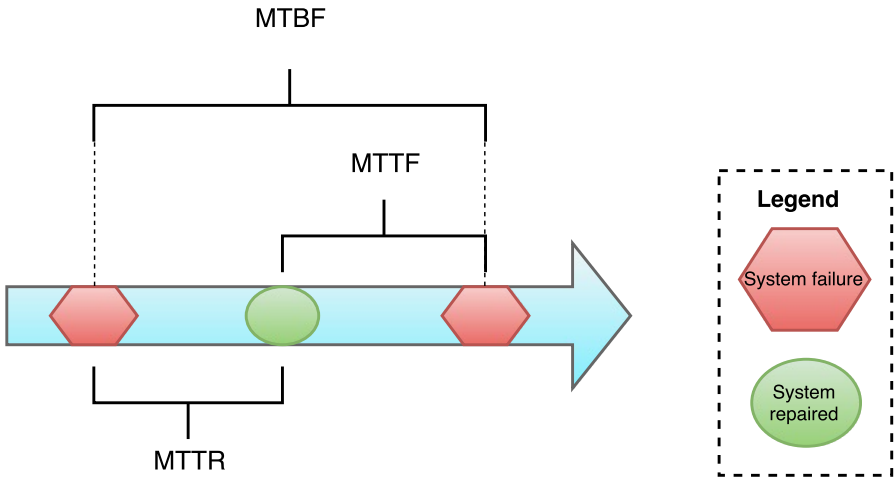

Figure 14.4: Three different maintainability measures of the failures in the system and how they are dealt with.

The next step is to quantify the three different maintainability methods. For this, the formula of each technique will be required.

$$MTBF = \frac{1}{FR_1 + FR_2 + ... + FR_n} \tag{14.6}$$

$$MTTR = \frac{\text{total maintenance time}}{\text{number of repairs}} \tag{14.7}$$

$$MTTF = \int_0^\infty R(t)dt \tag{14.8}$$

The actual values for each method will be computed in a later design phase when all the parameters can be quantified without adding major uncertainties.

14.2.4 Safety

Safety is strongly linked to risk mitigation as the main objective of safety is to ensure the absence of unacceptable levels of risks which could threaten the mission. Due to this, careful monitoring and constant checks need to be done throughout the product's life cycle. The design can be divided into three main phases, these being: development and fabrication, integrating and test and operations. Following, a list of all the possible actions that can be taken during each phase to reduce the likelihood and effect of the system risks will be given.

Development and fabrication

- Monitor developing and manufacturing activities to ensure that development meets mitigation requirements.

Integration and test

- Once the whole system is integrated, assessing tests should be carried out to see if the system is able to perform as expected without any point of failure. Then, the results obtained can be verified by re-testing the system and checking if it behaves in a similar manner as the one observed previously. In this way, the major system risks can be effectively mitigated.

Operational life

- Data obtained during operational life can be reviewed by the ground station to see if there are any on-orbit anomalies that endanger the mission. If so, priority commands can be sent to the spacecraft in order to reduce or terminate the unanticipated risks.

14.3 Sustainable development

Sustainable development is the philosophy of implementing sustainable approaches to engineering through the use of renewable energy, as well as the minimisation of the mission's environmental impact. Sustainability is thus not only concerned during the design phase, but for the following mission phase as well. This section is divided into two subsections, first the sustainable approach with respect to the design process is explained, afterwards the implementation of sustainable development over the entire mission life time is discussed.

14.3.1 Design implemented sustainable approach

During the design phase, sustainability has been a consideration for the major trade-offs between different design options. Although it was not always the driving criteria, it was certainly considered for all major trade-offs and thus contributed to the following design decisions:

Avoid using RTGs

The final decision regarding the use of radioisotope thermoelectric generators (RTGs) was based on a trade-off between the different design options, such as solar panels and fuel cells, which considered sustainability both within, and without its own criterion. Within the sustainability criterion itself, the design focused on how renewable the power sources were, whilst some other aspects of sustainability were taken into account for different criteria. For example, when scoring the different power sources in terms of risk, a lower score was given to the use of RTGs than the other options, because of the added risk of releasing nuclear isotopes in the atmosphere in case of a failed launch.

Use of solar panels

Contrary to the RTGs, solar panels as an energy source greatly benefited from being scored on sustainability. This is obviously because they do not use any fuel to generate their energy (contrary to RTGs and fuel cells) but also because the duration of the mission is so long that any other power source would end up requiring a large amount of fuel and thus, the effect of using non renewable energy will considerably increase.

Use of ion thrusters

During the design of the propulsion system for the deflection phase of the mission, various options were looked at, ranging from the use of cold gas to electric propulsion implementations. During the selection process, priority was given to the properties of the different options (specific impulse, complexity, etc.). As such, the choice of using ion engines was not driven by sustainability considerations, yet these are still worth mentioning. Indeed, for such a deflection mission where a constant thrust is required over a long mission time, the choice of propulsion system will considerably affect the total consumption of non-renewable fuels. Therefore, due to the ion thrusters' low fuel consumption, this system has a great advantage over the other options in terms of minimising use of resources.

Gravity tractor

The gravity tractor was chosen as the deflection method for several reasons, including its low complexity, low risk and high reliability, but also because of its sustainability. This is, of course, considered in the sustainability criteria. It is though worth mentioning that the mass and power budget, which were given the highest weight, also have an effect on the sustainability of the mission. For mass, this is due to the extra fuel required to escape the Earth's gravitational field as well as maintaining a constant distance to Apophis during deflection. For power, this translates into added required fuel, either indirectly through an increase in mass, or directly in the case of non renewable power sources. This is to highlight the fact that even though sustainability was evaluated directly as a criterion in the trade-off, it was also accounted for in all criteria likely to affect it.

14.3.2 Mission implemented sustainable approach

Sustainability can be applied both in system design, as well as during the mission. The latter refers to implementation of sustainable approaches throughout production, assembly, testing and operational life.

Manufacturing

To make sure that sustainability is taken into account during manufacturing, the philosophy of lean manufacturing will be followed. Lean manufacturing involves taking a systematic approach within the manufacturing process to ensure the elimination of waste. By doing so, the stress on the environment will be kept at a minimum.

Transportation

In order to have a clear overview of the sustainability of any process, one must not only look at the process itself, but all steps required to achieve this process. For the ARMADA mission, this means looking beyond just manufacturing and assembly, at the transportation of the parts themselves. This is simply because a considerable portion of the carbon footprint of any production process is due to the transportation of components from different manufacturing companies. As such, when choosing manufacturers for the different spacecraft components, proximity to the planned location of assembly will be an important consideration.

Ground station operations and logistics

After launch, a group of engineers will be tasked with ground operations and logistics during the whole mission time. As such, this aspect of the mission must also be analysed and planned with sustainability in mind. This can be done by reducing the use of resources or increasing the amount of recycling. As such, the facilities can be accommodated to include low intensity water faucets, low wattage light bulbs, recycled paper cups, sheets and towels. All waste produced by ARMADA mission staff must be sorted for recycling.

No creation of space debris in Earth orbit

The ARMADA team will, in collaboration with the launch service provider, assure that no new space debris is created in orbit around the Earth in order to not make the problem of space debris any worse. However, it is likely that the upper stage of the launch vehicle and the spacecraft itself will remain in orbit around the sun after they have completed their useful life. This is not a problem as the problem of space debris is only relevant for orbits around Earth. Any space debris created in orbit around the Sun is insignificant in comparison to the scale of the solar system, therefore it is not customary to remove or salvage spacecraft and boosters that are on a heliocentric trajectory.

14.4 Sensitivity Analysis

In this section, the influences of changing the major design parameters are investigated. Furthermore, the effect of changes in parameters associated with the target asteroid Apophis on the mission are investigated. For example, if Apophis turns out to be twice as heavy as estimated through Earth based observations, how will the deflection distance be affected? These uncertainties are evaluated quantitatively to estimate the robustness of the design and to ensure mission success even if design parameters change during a later phase of the design process.

The most important design parameters for the gravity tractor were identified to be the mass of the spacecraft and the power required for the ion thrusters. These design parameters are dependent on multiple uncertain characteristics of the target asteroid, such as the mass and diameter. In Table 14.1 the change in launch mass and maximum power required for the ion thrusters is given for a change in deflection time and a change in hovering distance. Furthermore the effect of the uncertainty in Apophis' Mass and Diameter are taken into consideration, for an increase and decrease in mass of Apophis of 10% and an increase and decrease in diameter of Apophis of 10% the optimum spacecraft mass and power are calculated. However, even if the spacecraft mass is not changed, deflection is still possible, however, the deflection distance will change. This is shown in the fourth column of Table 14.1. Furthermore, after some options an (X) sign is placed. This means that, in this scenario, the mission time must be shortened. This is however not a problem, as discussed in Chapter 6, a worst case scenario for the mass of Apophis and a nominal case was considered during the design process. As such, the spacecraft is able to perform the mission even in the worst case scenario. All values in Table 14.1 assume a worst case scenario. Therefore it is more likely that the spacecraft will over-perform instead of under-perform. Furthermore in Table 14.1 the parameters ΔX and $M_{s/c}$ are mentioned - these are the deflection distance and spacecraft mass at launch respectively.

Table 14.1: Sensitivity of mass and power for different mission parameters (reference time is 6 years)

Change in parameter	**Change in mass**	**Change in power**	**Deflection distance**
Deflection time			
+10%	-12%	-13%	
-10%	+17%	+17%	
Hovering distance			
+10%	+5%	-24%	
-10%	+5%	+62%	
Mass of Apophis	**(Constant ΔX)**	**(Constant ΔX)**	**($M_{s/c}$ constant)**
+10%	+5%	+15%	-5% (X)
-10%	-4%	-14%	-5%
Diameter Apophis			
+10%	+11%	-8%	-10%
-10%	-9%	+12%	+10% (X)

As can be seen in Table 14.1 the mass and power decrease for an increase in deflection time, and increase for a reduction in deflection time. The reason is that, if the deflection distance stays constant but the time is increased, the required gravitational force to deflect the asteroid will be smaller. Therefore the overall spacecraft mass can be lower. With a reduction in mass, the

thrust required by the ion engines also becomes less, therefore decreasing the required power.

From Table 14.1 it can also be seen that the power is most dependent on the hovering distance, when decreasing the hovering distance of 1.5 asteroid radii by 10% the power increases with 62%. If the hovering distance is increased with 10 % then the power decreases with nearly 24%. The spacecraft mass however increases both with an increase and decrease in hovering distance. This is because the current hovering distance (1.5 times the asteroid radius) is an optimum hovering distance, for which the spacecraft mass is minimal.
In case the mass of Apophis is not as expected the spacecraft mass and power also change accordingly. For an increase in the mass of Apophis the spacecraft mass and power would increase, for a decrease in the mass of Apophis the spacecraft mass and power decrease. However the mass of Apophis is unknown until the spacecraft arrives and can accurately measure it. Since the spacecraft design can no longer be changed after it arrives at Apophis, the spacecraft was designed to be able to deflect Apophis assuming a wide range of values for the mass estimation of Apophis. Because of this it makes more sense to take into account the difference in deflection distance, instead of the change in mass and power. It can be seen that for an increase in mass of Apophis the deflection distance is decreased. This makes sense; it takes more energy to "tow" a heavier asteroid. It can also be seen that in case of a 10% mass increase the required deflection distance can not be met as the spacecraft runs out of propellant before the whole deflection is performed. However, it should be noted that the values in Table 14.1 are for the worst case scenario so this is not likely to happen. Furthermore the required deflection distance includes a safety factor of two, so even if the deflection distance is decreased by 5% the deflection distance would still be sufficient in a real life scenario.
The final case presented in Table 14.1 is a change in the diameter of Apophis. In this case an increase in diameter corresponds to an increase in mass and a decrease in power. A decrease in diameter corresponds to a decrease in mass and an increase in power. Again, the spacecraft mass and power can not be changed after launch, therefore it makes more sense to look at the variation in deflection distance. In Table 14.1 it can be seen that the deflection distance decreases for an increase in diameter, on the other hand the deflection distance increases for a decrease in diameter. The Table also shows an (X) for a 10% decrease in diameter of Apophis, meaning that the 6 year deflection time can not be achieved. However this is not a problem, because the performance of the gravity tractor is actually better when the diameter is decreased the mission is performed in a shorter time frame, and therefore the full 6 years allocated for the deflection manoeuvre are not required.

14.5 Compliance & Feasibility

A crucial part of spacecraft design involves checking whether the requirements of each subsystem, and the top-level requirements, are met. The compliance matrices allow one to make a simple check to determine whether the requirements are met. In this section, the top-level compliance matrix is given. No matrices for each subsystem are included in this section, but the compliance with their requirements will be stated in each subsystem chapter. Table 14.2 shows the compliance matrix for the top-level requirements. If a certain requirement is met, a 'check' will be inserted. If not, the verification method (inspection, test, analysis or demonstration) as given in Section 16.2 is given.
As can be seen, all requirements but one are met by the current design. The design can be further analysed and tested in order to assure this requirement is met.

Table 14.2: Compliance matrix for top-level requirements

Identifier	Requirement	Compliance
ARMADA-SYS-CON-1.1	The risk posed by the asteroid to be studied shall be considered for a time frame of 100 years.	Check
ARMADA-SYS-CON-1.2	The operational lifetime of the mission shall be no more than 30 years after launch.	Check
ARMADA-SYS-CON-1.3	The time required to launch the satellite shall be less than 10 years.	Check
ARMADA-SYS-CON-2.1	The total mission cost shall not exceed 1 billion euros.	Check
ARMADA-SYS-CON-3.1	The system shall not violate any (inter)national space regulations.	Check
ARMADA-SYS-CON-4.1	The system shall not increase the amount of space debris in Earth orbit.	Check
ARMADA-SYS-CON-4.2	No radioactive isotopes shall be released into the atmosphere during launch.	Check
ARMADA-SYS-CON-5.1	The system shall have no single points of failure.	T/A
ARMADA-SYS-CON-5.2	The system shall have a safe mode.	Check
ARMADA-SYS-CON-5.3	The system shall not increase the risk of an asteroid colliding with the Earth.	Check
ARMADA-SYS-TECH-1.1.1	The mission shall use an existing launcher.	Check
ARMADA-SYS-TECH-1.1.2	An existing launch facility shall be used.	Check
ARMADA-SYS-TECH-1.2.1	The launch trajectory shall not pose a threat to civilisation.	Check
ARMADA-SYS-TECH-1.2.3	The launcher shall have a fundamental frequency lower than the fundamental frequency of the spacecraft.	Check
ARMADA-SYS-TECH-1.3.1	The ground segment shall receive data sent from the spacecraft.	Check
ARMADA-SYS-TECH-1.3.2	The ground segment shall transmit data to the space segment.	Check
ARMADA-SYS-TECH-2.1.1	The spacecraft shall be able to provide a maximum power of 2100 W until end of life.	Check
ARMADA-SYS-TECH-2.2.1	The spacecraft shall be able to keep the temperature between 173 and 378 Kelvin as required by its components.	Check
ARMADA-SYS-TECH-2.3.1	The spacecraft shall actively maintain its orbit as required by the payload.	Check
ARMADA-SYS-TECH-2.4.1	The spacecraft shall provide axis stabilisation according to the needs of the payload.	Check
ARMADA-SYS-TECH-2.5.1	The spacecraft shall operate autonomously.	Check
ARMADA-SYS-TECH-2.5.2	The spacecraft shall have the ability to communicate with Earth during its lifetime.	Check
ARMADA-SYS-TECH-3.1.1	The system shall be able to monitor the asteroid.	Check
ARMADA-SYS-TECH-3.2.1	The system shall reduce the risk of a NEO impacting Earth.	Check
ARMADA-SYS-TECH-3.2.2	The system shall be innovative with respect to other existing missions.	Check
ARMADA-SYS-TECH-4.1.1	The structure shall support all load cases during launch, orbit insertion and operating life.	Check
ARMADA-SYS-TECH-4.2.1	The system shall use existing technologies and materials for the spacecraft design.	Check
ARMADA-SYS-TECH-4.3.1	The space segment of the system shall be designed as a satellite.	Check
ARMADA-SYS-TECH-5.1.1	The leftover propellant shall be expelled at end-of-life.	Check

15. Resource Allocation

This chapter treats the allocation of resources such as mass and power for the ARMADA mission. Furthermore, a cost estimation is performed, the results of which will be discussed in the last subsection of this chapter.

15.1 Mission budgets

In this section the mass and power budgets are summarised and can be seen in Table 15.1. It should, however, be noted that, for the power budget many instruments or components will not be used at the same time. It should also be noted that the power values listed in Table 15.1 are the maximum power values required for each system. Therefore the total power value seen in Table 15.1 is much higher than the peak power actually required during the mission. The ΔV budget was shown in Chapter 3

Table 15.1: Spacecraft Mass Budget

Component	Mass (kg)	Power (W)
Dry mass	**225.7**	-
Scientific Payload	**31.96**	**97.42**
Framing Camera	*8.25*	*17*
Polarimeter	*2*	*2*
Magnetometers	*0.78*	*6.12*
Laser Altimeter	*15*	*52*
X-ray spectrometer	*4.4*	*10.8*
Infrared spectrometer	*1.534*	*9.5*
Propulsion	**44.66**	**1279**
Chemical system	*24.66*	*92*
Electrical system	*20*	*1187*
Attitude Determination and Control System	**27.95**	**157.02**
Command & Data Handling	**10**	**15**
Telemetry and Communication	**34.35**	**76**
Thermal Control	**4.325**	**316**
Power Control	**29.2**	**361**
Structures and Mechanisms	**43.22**	**80**
Propellant mass	**333**	-
Propellant mass (electrical)	*222*	-
Propellant mass (chemical)	*111*	-
Total	**559**	**2381**

It can be seen from Table 15.1 that the dry mass is close to, but slightly higher than the mass estimates made in Chapters 6. The propellant masses have been updated to account for this accordingly making the total mass slightly higher, this should not cause any problems as it is still within the range of masses that the launch vehicle can launch into the selected orbit as can be seen in Section 3.5. It should be noted that the mass budget given in this section is only an estimate and that it is likely that the mass budget will change again during future iterations of the design.

15.2 Cost estimation

In this section the cost estimation process is explained in detail. Firstly, the basic fundamentals of cost estimation are presented. Next, the chosen cost estimation method is elaborated on. Finally, a summary of the mission costs is presented in a schematic manner.

15.2.1 Cost estimation fundamentals

In the space industry, maximising performance and minimising weight has always been a primary consideration. Pushing these boundaries, however, has always been a major concern, as it increases cost substantially. Nowadays, minimising cost has become one of the most, if not the most, important concerns considering spacecraft design [125]. For that reason, it is of extreme importance to provide a cost estimation in the early design stage. An additional benefit of having a meaningful preliminary cost estimation is that it gives an overview of the cost for different design parameters. This, in turn, leads to more incentive to find cost-effective solutions

to satisfy the mission requirements.

Before performing a cost estimation, the significant cost contributions to the system must be well defined. Moreover, the components that make up the total cost must cover research, development, testing and evaluation, as well as production and operations [37]. Using Cost Estimation Relations (CERs) the individual cost contributions may be computed and, finally, summed to find the total. It is also considered to be the norm to provide a so-called Standard Error of Estimate (SEE) along with these relations. The relations used to predict costs are always based on statistical data [27]. The SEE provides an estimate of how well the CER fits the data used to develop it. The SEE is defined in Equation 15.1.

$$SEE_{\%} = \sqrt{\frac{1}{n-p}\sum_{i-1}^{n}\left(\frac{y_i - f(x_i)}{f(x_i)}\right)^2} \tag{15.1}$$

Where $f(x_i)$ is the forecast value, and y_i is the value obtained from the reference data. Also, n is the number of pairs of data points and p is the number of parameters in the CER. The SEE for each subsystem CER is given in [27]. In general, one can distinguish between three phases which constitute significant components of the cost [27]:

- **Development**: includes the design, analysis, and testing of hardware and software elements. These are usually considered as non-recurring costs (i.e: prototype approach which does not produce a flight unit).
- **Production**: related to the manufacturing and assembly of flight units, as well as their launch.
- **Operation**: these costs include any on-going operations and maintenance related activities, spacecraft replacement units, and software tests. In the case of unmanned missions a majority of these costs are taken up by the ground station.

There is a large number of cost estimation models available within the aerospace industry, but not all of them can be used for every mission. Firstly, a distinction is made between publicly available and private models. Publicly available models are normally developed by government agencies or government-funded research centres and universities. They may also be provided by private companies that provide their services to licensed users. Private models are generally developed by contractors for their personal use, and can not be used by external parties. Another distinction within cost estimation models can be made between general purpose and special purpose models. Special purpose models are desired for cost estimations, as they provide more meaningful and accurate predictions for specific kinds of missions and spacecraft. General models can also be used, but, in order to be accurate, they need to be calibrated and modified to fit personal requirements.

15.2.2 Cost estimation ARMADA

In order to provide a cost estimation for ARMADA, the Unmanned Space Vehicle Cost Model version 8 (USCM8) is used. As explained in [27], USCM8 is a cost model based on statistical regression techniques from 44 satellites. A distinction is made between non-recurring costs (design and development, manufacturing, model testing) and recurring costs (fabrication, manufacturing, integration, assembly, and testing of hardware). Note that for the payload no accurate cost estimation relations exist, as they vary too much in terms of specifications [27]. Also, for the power subsystem a cost estimation was peformed by contacting the manufacturer directly. An overview of the cost estimation relations, as well as their driving parameters is shown in Tables 15.2 and 15.3.

Table 15.2: Non-recurring cost estimation relations for ARMADA

Subsystem	**CER (FY2010 K$)**	**Driving parameter**
Structures & Thermal Control	$Y = 110.2X1$	X1 = S/C Weight (kg)
ADCS	$Y = 324X1^{0.684}$	X1 = ADCS Weight (kg)
Propulsion	$Y = 20.0X1^{0.485}$	X1 = Total RCS tank volume (cm^3)
Communications	26916	Based on statistical data X2 = Nr of channels
Integration & Assembly	$Y = 0.195X1$	X1 = Spacecraft bus and payload costs
Program costs	$Y = 0.414X1$	X1 = Space vehicle + IA&T costs
Ground equipment	$Y = 0.421X1^{0.907} \cdot 2.244^{X2}$	X1 = S/C bus non-recurring costs X2 = 1 (non-comm sats)

Table 15.3: Recurring cost estimation relations for ARMADA

Subsystem	**CER (FY2010 K$)**	**Driving parameter**
Structures & Thermal Control	$Y = 22.6X1$	X1 = S/C Weight (kg)
ADCS	$Y = 795X1^{0.593}$	X1 = ADCS Weight (kg)
Propulsion	$Y = 29X1 + 0.024X2$	X1 = Thruster mass X2 = Burn-time (s)
Communications	$Y = 883.7X1^{0.491} * 1.13^{X2}$	X1 = Communications subsystem Weight (kg) X2 = 0 (no GTO)
Integration & Assembly	$Y = 0.124X1$	X1 = Spacecraft bus and payload costs
Program costs	$Y = 0.320X1$	X1 = Space vehicle + IA&T costs
Launch operations & orbital support	$Y = 5850$	Based on statistical data

The masses from the mass budget in Table 15.1 can be filled in to obtain the estimated costs. For payload, command and data handling, and power system, cost estimations were obtained from literature. For the other subsystems, the USCM8 model was used. The final cost results are shown in Table 15.4.

Table 15.4: Cost estimations for ARMADA

Subsystem	**Recurring (FY2010 K$)**	**Non-recurring (FY2010 K$)**	**Total costs**
Structures & Thermal	976	4762	5740
ADCS	5729	3161	8890
Propulsion	1279	8620	9897
Power	-	1120	1120
Communications	4991	26916	31907
Integration & Assembly	4307	6774	11081
Program costs	13284	17186	30471
Ground equipment	-	12411	12411
Launch operations & orbital support	5850	-	5850
Payload	-	240000	240000
Command & Data Handling	-	300	300
Launcher cost		45000	45000
Total spacecraft costs			417590

As can be seen from Table 15.4, the final cost of the mission is estimated to be around $417.6 million, which is well below the budget constraint of $1000 million.

16. Future Activities

16.1 Project Design & Development Logic

As this final report represents an early design, the post-DSE activities must be planned to have an overview of the many tasks that are to be executed in the following phases. The planning will be based on the methods described by the European Cooperation for Space Standardization (ECSS) Space Project Management [126]. The seven phases are described below, with a mention of which phases the DSE encompasses.

- **Phase 0: Mission Analysis/Needs Identification** - As the name states, in this phase the mission is identified and characterised, and expressed in terms of needs and performance. Furthermore, its constraints within the physical and operational environment are identified. The project management should be assessed. Possible concepts should be identified, while also researching any previous work in the field. Generally, this is done during the DSE in the project plan and baseline report.
- **Phase A: Feasibility** - The technical and economic details of the needs should be critically explored. The functionality of the mission is described and completed with the exploration of different concepts for feasibility. Their constraints, such as time, cost, organisation, operation, implementation, production and disposal are evaluated, and the margins are assessed. Generally, during the DSE this is done partly in the baseline report, but mostly in the mid-term report.
- **Phase B: Preliminary Definition** - In this phase, by understanding the feasibility, the final concept is selected together with the solutions to the imposed technical issues. Implications of 'make or buy' decisions on product can be assessed. The requirements set on the design are reviewed. In addition, various factors of the design are evaluated, such as risks, production, reliability and safety, amongst others. This is partly done during the DSE in the mid-term report, and mostly in the final report.
- **Phase C: Detailed Definition** - This first post-DSE phase goes into the detailed study of the selected solution in phase B. The production of representative elements helps in defining the system and component requirements as well as specifications in more detail, whilst definitive 'make or buy' decisions are made for these components. In addition, verification and validation methods are applied to assess the technology to be used.
- **Phase D: Production/Ground Qualification Testing** - The components and systems in the design are defined and qualified fully, and can be produced and tested, allowing experimental data to be compared to the theoretical findings of previous phases. The confirmation and qualification of the procedures, methods, production and verification allows for the actual realisation of the design. This phase is closely linked to the previous one, and activities within these phases are generally not separately performed.
- **Phase E: Utilisation** - This phase contains the launch and testing in space. Afterwards it can be operated, aiming to perform all mission tasks that the system is designed for.
- **Phase F: Disposal** - This phase completes the mission by covering all events from utilisation until the end-of-life of the system.

The project design and development will thus be focused on the four phases C to F.

16.1.1 Detail definition

The preliminary definition given in this report must be continued in order to derive the necessary details on all subsystems and their components. The phase starts after the DSE on the first of July, 2016. This phase is planned to take two years, until June, 2018. The planning is shown by means of a Gantt chart in Figure 16.1. Engineers of all the fields relevant to the design are needed to investigate in detail what the final requirements and specifications of components are, and whether they are to be bought or designed. Planned activities include the production of accurate models, a detailed analysis of the environment, defining an accurate resource allocation and layout of the entire system, an accurate selection of materials and parts within the custom designed components, the production and assembly methods of the parts, determining the test setup for the qualification procedures, arranging the purchase of components from companies, and the organisation and scheduling of Phase D.

16.1.2 Production/Ground Qualification

The production and qualification procedures phase is planned to start on the first of July, 2018. The phase continues for about 32 months, until three months before launch, on the first of February, 2021. This is visualised using another Gantt chart, as seen in Figure 16.2. Planned

activities include performing tests and experiments for parts of the design and models, the actual production, assembly of the components and systems, extensive testing of all used components, and testing systems for correct integration, transportation, and assembly to launcher.

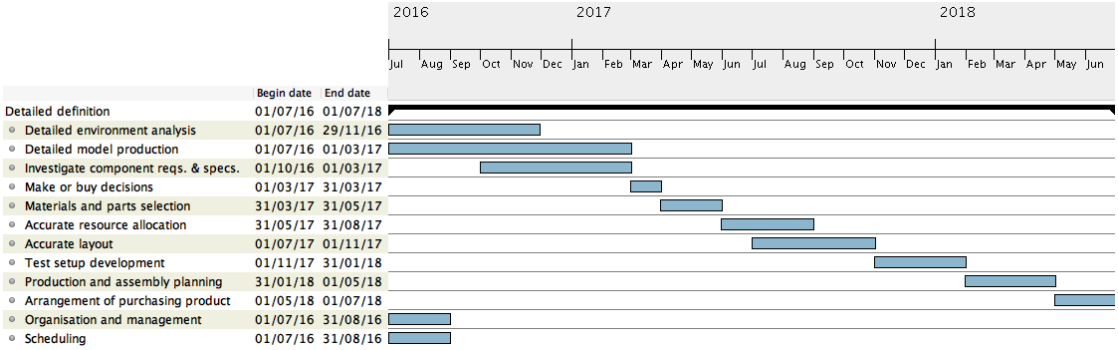

Figure 16.1: Gantt chart for Phase C

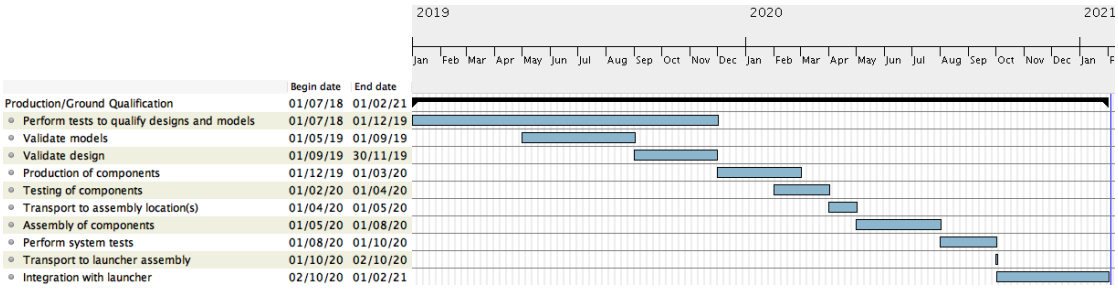

Figure 16.2: Gantt chart for Phase D

Now only Phases E and F, utilisation and disposal, need to be elaborated upon.

16.1.3 Utilisation

This phase starts at the end of the previous phase and continues for seven years after launch, until around May, 2028. Activities are the preparation for launch, and the rest is described in the mission timeline found in Chapter 2.

16.1.4 Disposal

Although the exact moment of end of life is not determined, it is estimated to be in 2028. The spacecraft lifetime should be estimated, and the options for disposal should be researched during phase C.

16.2 Verification & Validation

Throughout the design process of any product or system, verification and validation procedures (V&V) have to be applied in order to assure that the product will work as required and that the right system was developed. These two aspects can be defined as follows according to NASA [127]:

- **Verification** - Proof of compliance with design solution specifications and descriptive documents.
- **Validation** - Proof that the product accomplishes the intended purpose based on stakeholder expectations.

This is of utmost importance as poor V&V can lead to disastrous consequences for the mission or even total failure. An example is the space shuttle Columbia disaster. During re-entry, the thermal tiles on the spacecraft were damaged due to debris, which led to the explosion of the spacecraft. With a more thorough V&V procedure, this disaster could possibly have been prevented.

V&V procedures can be split up in several steps, all of which have to be carried out before the product, in this mission's case the ARMADA spacecraft, can be certified to be launched. In Figure 16.3, the verification and validation process over the mission design timeline is given. It is clear that V&V is carried out throughout the complete design process up to the actual start of mission operations.
In the figure, five different V&V steps in chronological order can be defined:

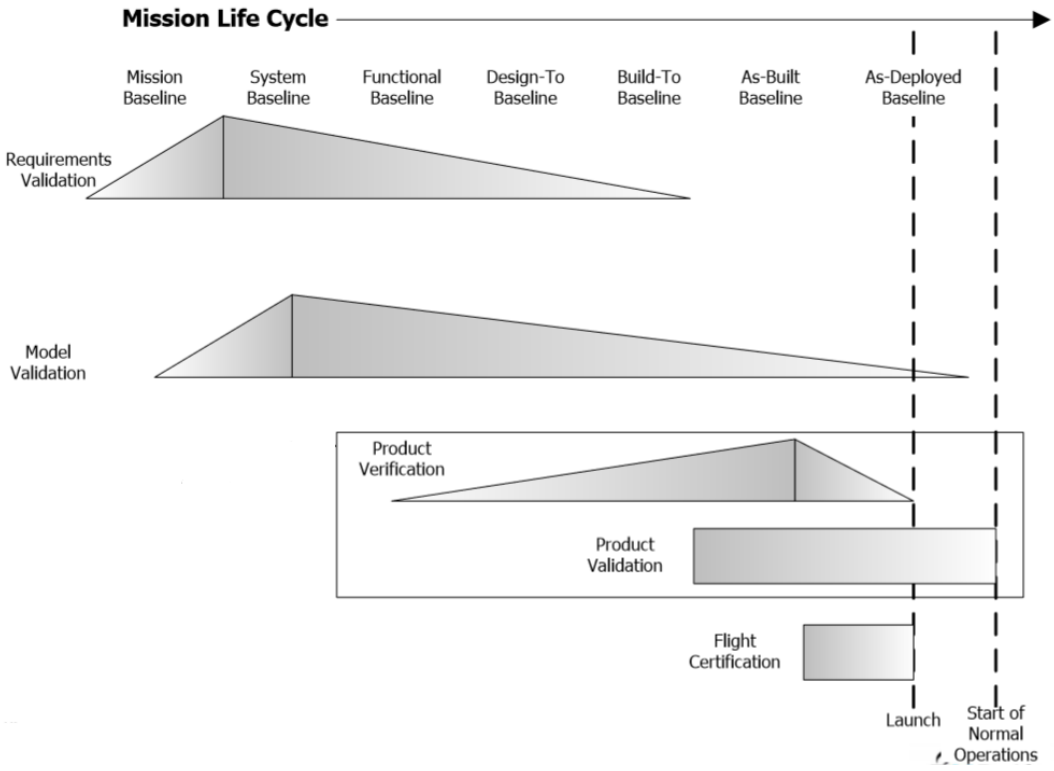

Figure 16.3: Verification and validation process time line [8]

- **Requirements validation** - During the early design phase, a lot of system and subsystem requirements are defined. Requirements have to follow certain rules in order to be valid. Thus, all requirements have to be validated in order to assure that these requirements are actually stated in the correct way. One could define this step as analysing whether these are the right requirements.
- **Model validation (and verification)** - Certain components of the design need a model which computes different outputs and gives more information about the system behaviour. These models need to be assessed in order to prove their correctness. First of all, they have to be verified using different tests, either unit or system tests, and then the complete model can be validated using reference data or other methods to compare the results with.
- **Product verification** - In this step, it is assessed whether the product meets the set requirements. Every requirement has to be investigated, and if one is not satisfied, countermeasures have to be taken in order to mitigate this problem.
- **Product validation** - After product verification it is still necessary to see if the right product was actually built. In other words, it has to be investigated if the product does as was intended by the customer and that it fulfils its purpose.
- **(Flight) certification** - In the end, the complete product needs to be certified before it can be used. After this step, in case of the ARMADA mission, the product is ready to be launched.

In the following sections, each of these steps will be elaborated on to give a better overview of the complete V&V process. It should be noted that the first two steps are already incorporated in the design up to this point. The other steps give more information about the future activities in the design process.

16.2.1 Requirements validation

All requirements have to satisfy certain guidelines in order to be VALID. These are as follows:

- **Verifiable** - The requirement has to be made in such a way that it can, in the end, be verified. Mainly, this means that the requirement should be objective and preferably include a quantitative value which can be checked at the end, or during the design process.
- **Achievable** - Impossible requirements are not useful for the design. The design team should have the available resources in order to satisfy all requirements.

- **Logical** - All requirements have to be posed in such way that they are easy to understand and do not include any possible misunderstandings.
- **Integral** - The requirements have to be complete and include all information necessary in order to actually design the mission for said requirement. Units should be included when requiring a quantitative value and the requirement should not compose of several design targets.
- **Definite** - Requirements have to be unambiguous, thus meaning they should be clear about the objective and not pose any chance of hesitation or misunderstanding regarding what exactly is expected.

These rules were used when generating the requirements.

16.2.2 Model verification and validation

All models used for the design of the ARMADA mission were properly verified and validated, meaning they were tested and compared to available reference data. First of all, unit tests are used in order to sort out minor bugs in the coding. Dummy input data can be used for this and hand calculations can help to verify the different blocks of the code. Next, a system test can be done meaning the final output is checked and some sanity checks can be done in order to assess the validity of the model. The software, MATLAB or Python, can also help by identifying errors in the code. This concludes the verification phase. Then, validation consists of checking the different outputs and comparing them with reference data and results of other models and/or methods. Model validation basically means developing evidence that the models represent reality as accurately as required. During these procedures, there will be discrepancies between the expected and acquired results, so these should be addressed. Discrepancies or differences in output values mostly originate from making simplifying assumptions or using an incomplete method. Next to comparison with reference data, analysis of the model and experience are also methods which are use for model validation.

16.2.3 Product verification

During and after the design process, the product has to be verified, meaning all requirements have to be checked and met by the design. Not all requirements can be assessed in the same way, so different verification methods need to be used. These methods are as follows:

- **Inspection (I)** - This is the most straightforward and simple method, which is mostly used for quantitative requirements concerning sizes or physical parameters of the design. As the name says, inspection consists of inspecting the design or product and see if the requirement is met.
- **Analysis or simulation (A)** - Compliance with the requirements can also be proven by a thorough analysis of the system, mostly done by simulating the system through a mathematical model.
- **Demonstration/review of design/similarity (D)** - Proving compliance with requirements during operation of a test product is called demonstration. Reconsidering the design or comparing it with similar products can also be used.
- **Test (T)** - A model of the product can be tested in representative conditions to show its compliance with requirements.

For each requirement, these methods should be considered and the best one should be used. Testing is mostly the most accurate way, but can not always be used if the operating conditions cannot be simulated properly during the test. Inspection can only be used for physical parameters and a limited range of other requirements. Analysis requires a lot of work as a representative model has to be created. Using assumptions for this model can already limit the representativity of the model. In Table 16.1, some examples of verification methods used for certain requirements are given. Not all requirements are analysed in this table, as the method for the other requirements can be obtained in the same way as presented here.

16.2.4 Product validation

After the product verification, a validation procedure needs to be applied to ensure the right product was built, so that it can actually execute all its intended functions. During these procedures, extensive testing is performed. Tests such as mission scenario tests, which demonstrate that the flight hard- and software can actually work as intended under representative conditions, are often conducted. Stress testing is done and an operation readiness test, which assesses the operation of the ground segment, is also performed.

Table 16.1: Requirement verification method examples

Requirement	Method	Reasoning
ARMADA-SM-06	A	Creating a simulation, is the only viable method to verify the compliance of the product, in this case the spacecraft, and especially the focal camera, with this requirement. Inspection cannot be used, neither demonstration or testing, as these require replication of the flight conditions, which is not fully possible.
ARMADA-SM-09	I/D/T	The energy range for which an X-ray spectrometer checks is a specification of said spectrometer, thus it can just be checked by inspection whether a certain X-ray spectrometer can fulfil the requirement. Demonstration can also be used as the spectrometer functionality can easily be demonstrated. A test can also be used to check the functionality in representative conditions. The choice in method to be used will be guided by safety and cost considerations.
ARMADA-P&OC-07	I	During production, this can be measured by inspection of the product. No other methods are necessary as this is a physical characteristic of the spacecraft.
ARMADA-ADCS-07	A	Making a model is the only way to check this requirement. Inspection will not give any information and testing or demonstration are not possible as the exact conditions of orbiting in a low gravity environment, as can be found around Apophis, cannot be replicated on ground.

16.2.5 Flight certification

In the end, before the spacecraft can be launched, it has to be certified. This is often done by a specialised engineer or group of engineers. During this process, it is mainly assessed whether the mission, consisting of the spacecraft and all other segments, meets all regulations and safety standards imposed by (inter)national laws.

16.3 Production

The production plan or Manufacturing, Assembly and Integration (MIA) plan is a flow chart which gives insight on all the different activities that need to be done to design, and finally manufacture the ARMADA spacecraft. Due to this, all the different stages during design will be presented with the sub-tasks that compose each of them. The whole production plan, from project planning to production, of the ARMADA mission can be seen in Figure 16.4.

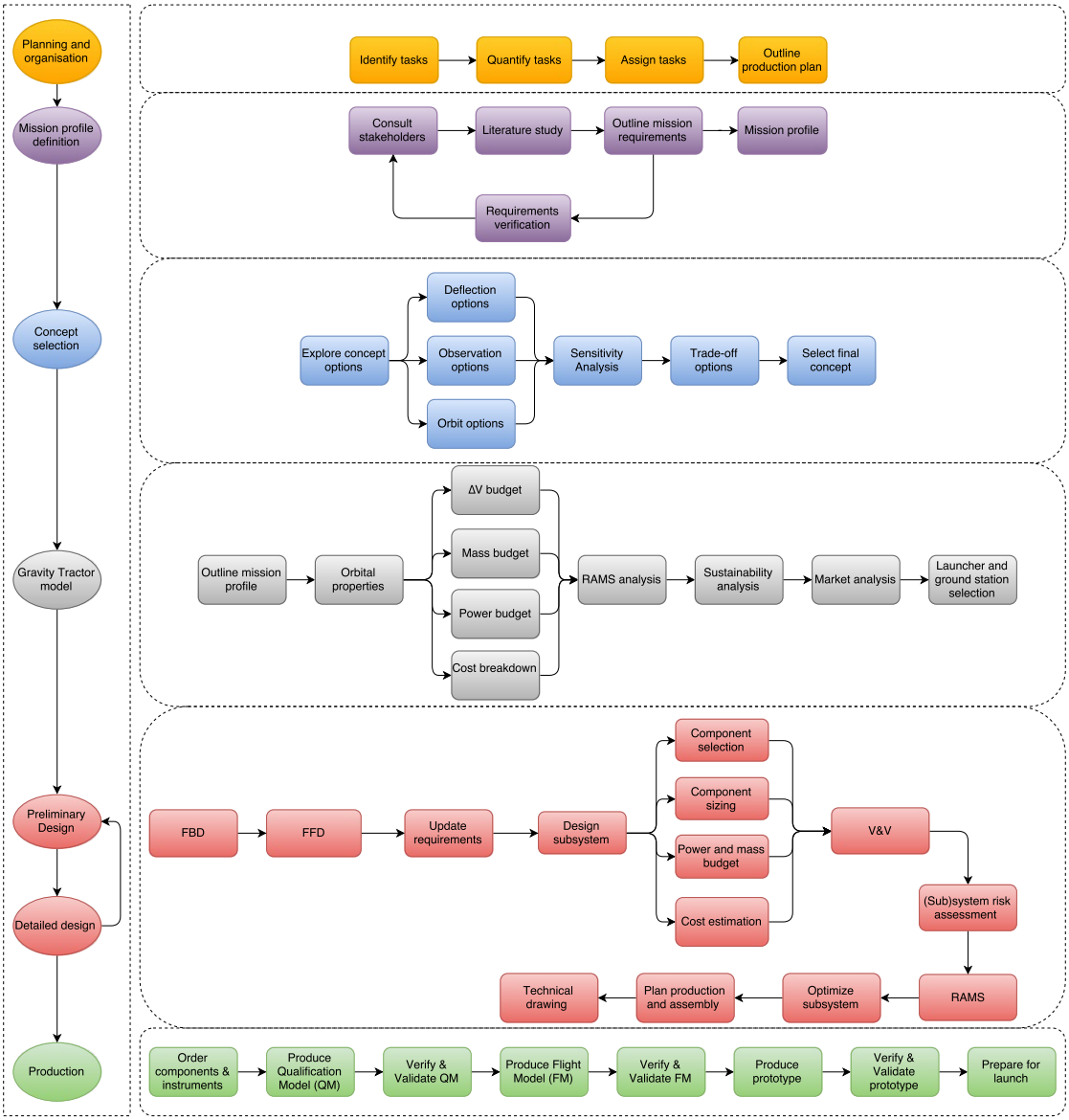

Figure 16.4: ARMADA mission production plan.

As can be seen, the first stage is all about planning and detailing a mission profile, as well as setting top-level requirements. Then concept selection begins, which ended with the Mid-term review (MTR) where the gravity tractor was chosen from nine different concepts. This payload choice was then investigated in more detail and subsystem design began. Iterations are necessary from preliminary to more detailed design so as to respect all constraints, whilst meeting the specified requirements. In future stages, the design will be optimised in the detailed design phase and the production stages will begin, characterised by regular testing phases. This will be followed by assembly and further testing, finally leading up to launch.

16.4 Operations and logistics

After the spacecraft has been designed, produced and assembled, it begins its operational life. The spacecraft shall be launched into space, where it will be monitored from the ground. If the commands stored on the on-board computer are found to be insufficient, the ground station has the possibility of issuing high priority commands. In this section the logistics and operational characteristics of the mission shall be elaborated upon.

Launch logistics

The launch of the spacecraft will be outsourced to a launch service provider. As such, only the transportation to the launcher shall be assessed within the logistics of the launch segment. All operational costs for this segment are assumed to be included in the launcher costs, as can be found in Section 3.5. Table 16.2 gives a short overview of the launch service providers and launch sites corresponding to each considered launcher. It is assumed that the spacecraft will be tested before launch at ESTEC in Noordwijk, the Netherlands, since the closest ESA testing facility is located there. The logistics behind the design up until, and including the testing phase are

presented in the production plan, in Section 16.3. After the spacecraft is tested in Noordwijk. it will be shipped to the launch site by air.

Table 16.2: Launch service provider and launch site [40, 12, 13, 14, 15]

Launcher	Launch Service Provider	Launch site
Ariane 5	Arianespace	Kourou, French Guiana
Atlas V (551)	United Launch Alliance	Cape Canaveral
Delta IV Heavy	United Launch Alliance	Cape Canaveral
Falcon 9	SpaceX	Cape Canaveral
Soyuz (Fregat)	Arianespace	Kourou, French Guiana
Vega	Arianespace	Kourou, French Guiana

Ground segment operations

To support the spacecraft operations, the spacecraft is communicating with the ground station. This segment provides all the installations, personnel and other facilities to enable communication with the ARMADA spacecraft. The ground station selected for this mission is the Deep Space Network. The costs of using this service can be computed using Equation 16.1 and is given in weighted aperture fee AF, per hour of use. The contact dependent hourly rate RB in fiscal year (FY) 2010 was \$1057 per hour [25]. The aperture weighting AW is dependent on the different stations used. A single 34 meter station has an AW of 1, while the 70 meter station has an AW of 4 [25]. Finally, the number of contacts per calendar week FC also contribute to the cost. For example, when using a single 34 meter station for 7 days a week, 2 hours a day, this would amount to a cost of 1.235 million dollars per year, the cost necessary for the ARMADA scenario. For the same operating time but the 70 meter station, this amount is four times more expensive, however this value is still under 5 million dollars per year. It is necessary to note that the 70 meter antenna is preferable only in the extreme communication cases, where the separation distance between the ground station and the spacecraft is at a maximum, whilst the smaller antenna can be used when the separation distance decreases.

$$AF = RB[AW(0.9 + FC/10)] \tag{16.1}$$

The operations defined in the ground segment are elaborated on in Table 16.3.
When the scientific and system data is received, it must be used for monitoring the spacecraft. This means that a mission operations and control segment is needed which can be located anywhere, but should be available at all times. This requires models of the spacecraft to compute the conditions of the spacecraft, the operation monitoring personnel, and the planning of the mission. When looking at reference missions, such as the Rosetta mission, the personnel can be divided into several teams. A Mission Control team is responsible for data processing to control the mission. A Data Disposition team is positioned to convert and distribute the raw data, whilst a Mission Planning team handles command requests and plans or schedules of the spacecraft and payload. A Flight Dynamics team will support and determine or predict the orbit, trajectory, and manoeuvres necessary during the mission and monitor the actual performance of the spacecraft when engaging in these manoeuvres. Finally, the Spacecraft Simulation team supports procedure validation and training of operators for upcoming mission phases [128].

16.5 Market Analysis

In order to properly set up a mission, it is important to assess what is currently being done on the market. The dynamics of the market can be studied by means of a market analysis. In this section, the market analysis begins by identifying the potential customers for the mission. Note that customers are defined as stakeholders that may fund the mission. Next, the potential competitors are identified and the relevance of the mission is elaborated upon. Finally, a SWOT analysis is developed which highlights the strengths, weaknesses, opportunities, and threats of the mission.

16.5.1 Potential customers

Since the mission is purely scientific, the stakeholders funding the mission can be seen as customers. Multiple stakeholders can be defined for this mission, ranging from space agencies to governments and military organisations. Since this mission aims at demonstrating new technology, it is assumed that governments and military organisations will not have a high degree of interest in this project. In terms of space agencies, the following potential customers were identified: ESA, NASA, JAXA, DLR, CNES and Roscosmos. Out of these potential customers, ESA is considered to be the most likely candidate, due to the fact that this mission is based in Europe and due to its past experience and budget. NASA and JAXA are also considered likely candidates for providing either additional funding or for collaboration efforts, due to their experience and budget. DLR, CNES and Roscosmos are considered as secondary customers; funding small parts of the mission, or contributing to certain subsystems or payloads. In the following

section the motivation for each customer is discussed, going into more detail for the most likely customers.

ESA
ESA has studied several concepts to deflect asteroids. Among these are the Marco Polo and the Don Quijote spacecraft. In 2005 the Don Quijote spacecraft was selected by the Near-Earth Object Mission Advisory Panel (NEOMAP) as the most favourable mission for deflecting an asteroid [129]. One of the possible targets for the Don Quijote spacecraft was 99942 Apophis [129], the same target as ARMADA. The Don Quijote mission was, however, cancelled in 2005 and the budget was allocated to the joint ESA-NASA AIDA mission. ESA's involvement in this mission shows that ESA is interested in finding methods to change the orbits of asteroids. Furthermore, ESA has shown interest in deflecting 99942 Apophis, calling for proposals for an asteroid deflection mission during 99942 Apophis' close flyby of Earth in 2029 [130]. ARMADA fits this call for proposals. ESA has an annual budget of approximately €5.25 billion (FY2016), of which only a part goes into funding the sectors this mission fits into. Namely, €192.8 million is allocated for robotic exploration, €12.9 million is allocated for space situational awareness and €507.9 million is allocated for scientific research [130].

NASA
NASA already has a history regarding missions to asteroids. For example, in 2001 NASA landed the NEAR Shoemaker spacecraft on the Asteroid Eros after a successful mission. NASA is also currently working on several missions which include asteroids in one way or another. One of these is the Asteroid Redirect Mission (ARM) [131] which aims to capture an asteroid and move it to cislunar space in the early 2020s. Therefore, demonstrating technology to deflect an asteroid might be interesting to NASA. Furthermore, NASA is currently working together with ESA on the Asteroid Impact & Deflection Assessment Mission (AIDA), which will attempt to change the orbit of an asteroid by a kinetic impact [132]. NASA's involvement in the AIDA mission shows that it is interested in finding methods to change the orbits of asteroids. Finally, NASA has a department of planetary defense which tracks asteroids for potential impacts with Earth. Therefore, ARMADA might be of interest for this department. NASA has an annual budget of approximately $19 billion (FY2017), of which $50 million is allocated to NEO observation and over $1.5 billion is allocated to planetary science [133]. With a maximum mission cost of 1 billion euros over the entire mission time, ARMADA could be accommodated by the NASA budget.

JAXA
JAXA has a lot of experience studying asteroids. In 2005 they landed the Hayabusa spacecraft on asteroid 25143 Itokawa and collected samples which were returned to Earth in 2010 [134]. In 2014 Hayabusa 2 was launched to asteroid 162173 Ryugu [135]. Furthermore JAXA is working on the Hayabusa Mk. 2 which is planned to launch in 2018. For the Hayabusa Mk. 2 mission deflection of an asteroid is considered [135]. JAXA has also expressed interest in international collaboration on an asteroid mission [135]. Due to JAXA's previous experience and interests in asteroid missions they are considered as a potential customer for ARMADA.

DLR, CNES and Roscosmos
DLR, CNES and Roscosmos are considered as secondary customers. They are not likely to fund the entire mission by themselves but can be considered to fund part of the mission or contribute in the design of certain subsystems. DLR for example funded part of the Rosetta mission, CNES funded part of the Hayabusa mission and Roscosmos expressed interest in NASA's Asteroid Redirect Mission.

16.5.2 Potential Competitors
In order to evaluate the place of the ARMADA mission on the market it is important to study the potential competitors. This section will discuss some of the competitors of the ARMADA mission.
The competitors can be divided into several categories. First there are direct competitors in the form of similar missions. Secondly, there are indirect competitors. Indirect competitors consist of missions that do not have similar objectives. Even though these missions do not compete directly with the ARMADA mission, they can compete indirectly since only a limited budget is available to space agencies. Identifying all the potential indirect competitors is beyond the scope of this report, however it is important to take them into account. The remainder of this section will focus on some examples of direct competitors of the ARMADA mission. It should be noted that this is not a complete list, but only serves to show what potential competition for the ARMADA mission could look like.

Asteroid Impact & Deflection Assessment Mission One of the main competitors of the ARMADA mission is the joint ESA-NASA AIDA mission. The AIDA mission aims to deflect an asteroid by a kinetic impact in 2022 [132]. The market advantage that ARMADA has over the AIDA mission, however, is that the ARMADA mission will demonstrate a different new technology. Furthermore the ARMADA mission also uses only one spacecraft instead of the

proposed two spacecraft that the AIDA mission will use. This means that the ARMADA mission is less complex and can be achieved for a lower cost.

Hayabusa Mk.2 Another competitor of the ARMADA mission is the Hayabusa Mk.2. The Hayabusa Mk.2 aims to collect materials from an asteroid and return them to Earth to be studied. A secondary objective is to try to change the orbit of the asteroid [135]. The market advantage that ARMADA has over the Hayabusa Mk.2 mission is that the ARMADA mission is specifically designed for asteroid deflection. Therefore the ARMADA mission is probably more suited to deflect an asteroid. Furthermore, the characteristics derived from sample studying are also evaluated in the observation phase of the ARMADA mission. As such, the scientific objectives have a multitude of common elements.

Asteroid Redirect Mission NASA aims to capture a small asteroid and move it to cislunar space in the early 2020s [131]. Even though the ARM mission seems similar to the ARMADA mission the two have some differences. The ARM mission will only capture a very small asteroid (roughly 4 meters in diameter) [131], while the ARMADA will be designed for a larger asteroid. The ARMADA will therefore demonstrate a different technique for deflecting asteroids which is also suitable for larger asteroids.

16.5.3 Mission relevance

Space missions tend to be fairly costly, and there must always be a valid reason to spend resources on a mission. This is especially the case when a number of missions is available for a funding party to choose from. In general the mission with the most scientific value will be chosen. For that reason, it is important to clearly define the main reasons for the relevance of ARMADA. These are listed below:

- **Gain more insight on composition of Apophis** - The composition of Apophis has been studied before, but not to the extent of what ARMADA will be able to do while orbiting Apophis.
- **Gain more insight on size of Apophis** - Similar to the point of the composition, there are estimates available on Apophis' size. During the mission this size can be determined more accurately.
- **Gain more insight on the orbit of Apophis** - As Apophis is one of the NEOs tracked by the JPL system, there is data available on its orbit. However, uncertainties still exist regarding this and Apophis' tumbling rate. A quantification of the elements influencing the orbit, such as albedo and tumbling rate will greatly improve the reliability of future deflection missions.
- **Demonstrate technology** - No asteroid has ever successfully been deflected in the past. Deflecting an asteroid during the ARMADA mission will prove that humans can indeed deflect NEOs if necessary.

The first three points regarding the scientific value of studying Apophis are of particular interest when looking at the future. In order to get a better picture of how the ARMADA mission can contribute to the international scientific community several experts were approached, such as Dr. Imke de Pater and Dr. Daphne Stam. Prof. Dr. Imke de Pater is a planetary scientist and professor at the University of California Berkley. Dr. Daphne Stam is a planetary scientist and associate professor at Delft University of Technology. After consulting prof. Dr. Imke de Pater it was found that there is some interest within the scientific community when it comes to asteroid mining. Knowing more about the physical characteristics of asteroids directly affects the possibilities of mining asteroids in the future. Dr. Imke de Pater also said that demonstrating the technology to deflect an asteroid might be of interest for companies that want to mine asteroids. By bringing an asteroid in an easier to reach orbit (for example in an orbit around the Moon) it may become much easier to mine such an asteroid. Therefore, ARMADA provides valuable data for future missions to asteroids and for companies that are interested in mining asteroids. Furthermore Dr. Daphne Stam was contacted. According to her there is a particular interest in studying Apophis' composition and orbital parameters, as well as craters present on the NEO. This is also possible by the means of the ARMADA mission.
It can be concluded that performing the ARMADA mission can be motivated, as it provides a significant amount of information to the scientific community, whilst also demonstrating technology relevant to the safety of humanity.

16.5.4 SWOT analysis

The strengths, weaknesses, opportunities, and threats of the mission can be assessed in a SWOT analysis. The SWOT analysis results are shown schematically in Figure 16.5. Additionally, the main points in the SWOT diagram are explained more elaborately.

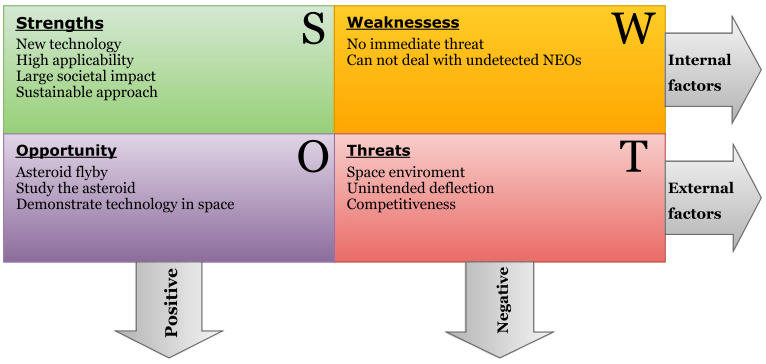

Figure 16.5: SWOT analysis scheme

Strengths

- **New technology** - Demonstrating a new technology for asteroid deflection is the main feature of the mission. It opens up a new set of possibilities that may be relevant whenever an asteroid poses a threat to mankind.
- **High applicability** - In terms of physical characteristics (size and properties) there is a large number of NEOs similar to Apophis [42]. If Apophis can be deflected correctly, the method may be used for similarly sized asteroids in the future.
- **Large societal impact** - The mission will provide a solution for a problem that may lead to serious consequences for society if no solution is found.
- **Sustainable approach** - It is of significant importance to take sustainability into account in the design, since it has an effect on future generations of the human race.

Weaknesses

- **No immediate threat** - There is no immediate threat of the asteroid colliding with the Earth. Probabilities of impact are small so there is no direct necessity for a deflection mission to be set up.
- **Can not deal with undetected NEOs** - In order for the mission to work, there must be sufficient information about the target NEO. The mission itself does not focus on detecting NEOs and gaining information about them, so some prior knowledge about the NEO must be available.

Opportunities

- **Study the asteroid** - Because the spacecraft will be orbiting Apophis for an extended period of time, there is an opportunity to gain more insight on the physical characteristics of the asteroid, which may have scientific purpose.
- **Improve accuracy of remote sensing techniques** - There are multiple ways of remotely measuring characteristics of asteroids however, due to the fact that these are Earth based, there will be a measure of uncertainty. The data that ARMADA will produce can then be used to increase the accuracy of these techniques, effectively contributing to the reliability of future deflection missions.

Threats

- **Space environment** - Since the space environment can be unpredictable at times, it may pose a threat to the effective execution of the mission.
- **Competitiveness** - For a space mission like this one it is not necessary to have different options on the market. Therefore, if there are multiple available missions and only one will be chosen, there is a high level of competitiveness related to the development.

Table 16.3: Ground station operations

Operations	**Description**
Pre-launch preparation	This includes all the testing, verification and validation activities related to the final certification of the spacecraft.
Initiate mission	The start of the mission will need to be scheduled, signalled, controlled and monitored.
Data retrieval	The ground station will receive the scientific payload data generated by the ARMADA spacecraft. Furthermore, the planned status reports and emergency housekeeping signals are also received and interpreted by the ground station.
Data management	This includes transmitting the scientific payload data to an outsourced data processing company and back, as well as distributing it to the relevant scientific community.
Data processing	This includes processing the camera images into a 3D map of Apophis, as well as organising and validating the asteroid properties and crater data. The 3D map will be sent back to the ground station for use during deflection.
Transmit commands	If an emergency signal is received from the spacecraft or the housekeeping data indicates a need for action that the onboard computer is not programmed to anticipate, the required command is sent from the ground station.
Energy control	This is applicable to both ground station and spacecraft, as it refers to minimising the energy loss through avoiding the constant use of unnecessary subsystems. For the spacecraft, this is solved through the definition of different operational modes, whilst for the ground station, the use of green equipment with low power modes is a valid option.
Waste control	Waste in any form should be minimised. This can refer to switching from physical documents to digital databases, as well as avoiding duplicated work.
Equipment upkeep	The ground station equipment needs to be maintained. Furthermore, the maintenance will be planned, scheduled and executed by the ground station operators or associated staff.
Software updates	This refers to checking the obsolescence and evolution of software being used both by the spacecraft and the ground segment. If an update is necessary, the availability of memory space needs to be evaluated before this action is scheduled and executed.
Documentation management	In order to reduce uncertainties related to future asteroid deflection missions, the ARMADA mission will be documented extensively. This information will be distributed to the relevant scientific community, in order to help reduce the risk of an NEO impacting the Earth in the future.
Ground station maintenance	This pertains to all operations related to maintaining specific performance of the ground station, including, but not restricted to human resource management, interfacing with other companies and maintaining facilities.

17. Conclusion and recommendations

The aim of this report was to document the design process between the mid-term and final review, and to give an overview on the progress made in the mission design. A final, but still preliminary, design for the ARMADA mission is given in this report, including subsystem design and an overall mission analysis, which consists of risk management, RAMS analysis, sustainable development, sensitivity analysis of the design and the compliance matrix, which will state whether the ARMADA mission meets its requirements. Then, as this is still preliminary design, several future activities, such as further planning of the design, testing, verification and validation procedures, as well as production, operations and logistics and a market analysis, are elaborated on to examine any further work that still needs to be implemented in a later design phase.

The design of each subsystem yielded certain results. Based on the astrodynamics calculations, the total ΔV of the transfer was found to be 4.8238 km/s. The selected launcher is the Soyuz (Fregat), as it is the cheapest option for the current spacecraft mass estimate of 559 kg. The required deflection distance for the gravity tractor was found to be 11.8km, with a corresponding deflection time of 5-6 years (depending on nominal or worst case estimations of the mass of Apophis). In order to meet the mission requirements, the observation time was restricted to 0.5 years and based on this, the scientific instruments were selected. In the end, the selected instruments consist of a framing camera, an X-ray and infrared spectrometer, two magnetometers, a laser altimeter, and a polarimeter. These were chosen due to uncertainties in the mission and also to find out more information about the asteroid, based on the information required by the scientific community for research.

The orbit insertion propulsion system was chosen to be a liquid bi-propellant system whilst the hovering propulsion system consists of ion thrusters. For the C&DH system, the CPU chosen is the RAD6000, with an SSD data storage system. The communications subsystem consists of two transponders, two power amplifiers, a high gain parabolic antenna and a 3 low gain horn antennas. These were selected based on required communication times and distances from the ground station on Earth. The thermal control system was sized according to the required component temperature ranges, using a combination of passive and active control. Passive control systems include Teflon, Beta cloth, Basotect foam, and passive radiators. On the other hand, active control consists of thermoelectric coolers, deployable radiators and patch heaters. The power system consists of a multi-junction solar array (sized to $10.0m^2$) and a battery with a capacity of 1344 Wh. Finally, the structural bus was sized to have a final mass of 43.2kg, an outer thickness of 0.5mm and a propellant tank thickness of 2mm, leading to a spacecraft volume of $3.34m^3$. Taking into account all subsystems and the propellant masses, the launch mass of the spacecraft was found to be 559 kg.

As the ARMADA mission design is still in an early phase, some recommendations can be made to improve the design in the future. First of all, every model used can be elaborated on and treated in more detail to get an even better overview on the design conditions and constraints. Next, it would be interesting to have a look at shorter mission times and optimise the design for time, mass and other important parameters. During transfer, a barbecue mode could be implemented, which basically means the spacecraft is continuously rotating in order to make the thermal control more efficient. More detail could be put in the instrument and component selection, for all subsystems as well as for the scientific payload. There might be more suitable components available in terms of mass, power and other specifications, which were not found due to time constraints. For the orbit insertion, the ARMADA uses two thrusters, which could possibly be reduced to only one. This can be investigated in a later design phase. As the total cost of the mission is still under the budget, the spacecraft could be given extra functions. A good example would be implementing a way to actually gather a sample of the asteroid for further analysis and examination. The scientific community is extremely interested in actual samples, so this could be an interesting opportunity for further design.

Bibliography

[1] H. Curtis, *Orbital Mechanics for Engineering Students, Second Edition.* Elsevier Butterworth-Heinemann, Oxford, United Kingdom, 2010.

[2] "Handheld XRF: How it works," Bruker Corporation, https://www.bruker.com/products/x-ray-diffraction-and-elemental-analysis/handheld-xrf/how-xrf-works.html.

[3] "Bipropellant Rocket Engines," Aerojet, Cited 06-06-2016 from: https://www.rocket.com/files/aerojet/documents/Capabilities/PDFs/Bipropellant%20Data%20Sheets.pdf.

[4] "Spacecraft Propulsion," Airbus Defense and Space, EADS, Cited 06-06-2016 from: http://www.space-propulsion.com/home-lam.html.

[5] J. Huddleson, "QinetiQ Electric Propulsion Technology & Capability," Qinetic Ltd, November 2014, http://espace-ftp.cborg.info/epic_2014/d2_s10_5_QinetiQ_Space_EP_Technology_EPIC.pdf.

[6] I. Kök, "Comparison and Analysis of Attitude Control Systems of a Satellite Using Reaction Wheel Actuators," Cited 07-06-2016 from: https://pure.ltu.se/ws/files/41443450/LTU-EX-2012-41440533.pdf.

[7] M. R. Patel, *Spacecraft Power Systems.* CRC Press, 2005.

[8] W.J.Larson *et al.*, " Applied Space Systems Engineering (ASSE)," 2009.

[9] R. Baalke, "99942 Apophis (2004 MN4)," Jet Propulsion Laboratiru, National Aeronautics and Space Administration, Cited 2-06-2016 from: http://ssd.jpl.nasa.gov/sbdb.cgi?sstr=99942;orb=1.

[10] D. R. Williams, "Planetary Fact Sheet - Metric," National Aeronautics and Space Administration, Cited 2-06-2016 from: http://nssdc.gsfc.nasa.gov/planetary/factsheet/.

[11] United Launch Alliance, "Delta IV payload planners guide, 2007," Cited 14-06-2016 from: https://www.apsu.edu/sites/apsu.edu/files/astronomy/DeltaIVPayloadPlannersGuide 2007.pdf.

[12] E. Perez, "Vega User's Manual Issue 4 Revision 0," April 2014, Cited 13-05-2016 from: http://www.arianespace.com/wp-content/uploads/2015/09/Vega-Users-Manual_Issue-04_April-2014.pdf.

[13] E. Perez, "Ariane 5 User's Manual Issue 5 Revision 1," July 2011, Cited 12-05-2016 from: http://www.arianespace.com/wp-content/uploads/2015/09/Ariane5_users_manual_Issue5 _July2011.pdf.

[14] P. Blau, "Delta IV Heavy," Spaceflight101, 2016, Cited 13-05-2016 from: http://spaceflight101.com/spacerockets/delta-iv-heavy/.

[15] ESA, "ESA Previous launches," April 2016, Cited 13-05-2016 from: http://www.esa.int/Our_Activities/Launchers/Previous_launches.

[16] P. B. de Selding, "Vega Expected to be Price-competitive with Russian Rockets," January 2012, Cited 13-05-2016 from: http://spacenews.com/vega-expected-be-price-competitive-russian-rockets/.

[17] "Ariane 5 ECA," Spaceflight101, 2016, Cited 13-05-2016 from: http://spaceflight101.com/spacerockets/ariane-5-eca/.

[18] G. Krebs, "Soyuz-FG (11A511U-FG)," 2016, Cited 13-05-2016 from: http://space.skyrocket.de/doc_lau_det/soyuz-fg.htm.

[19] R. Biesbroek, *Lunar and Interplanetary Trajectories.* Springer Praxis, Noordwijk, The Netherlands, 2016.

[20] B. Allen *et al.*, "The REgolith X-Ray Imaging Spectrometer (REXIS) for OSIRIS-REx: Identifying Regional Elemental Enrichment on Asteroid," *Veritas*, June 2009, doi:10.1117/12.2041715.

[21] M. Jones, M. Chodas, M. J. Smith, and R. A. Mastersona, "Engineering design of the regolith x-ray imaging spectrometer (rexis) instrument: An osiris-rex student collaboration," *SPIE*, vol. 9144, 2014, doi: 10.1117/12.2056903.

[22] M. Abe *et al.*, "Characteristics and current status of near infrared spectrometer for Hayabusa mission," Cited 07-06-2016 from: http://www.lpi.usra.edu/meetings/lpsc2004/pdf/1724.pdf.

[23] M. Bradford, "Reaction Wheel Unit," 2014, http://bradford-space.com/userfiles/SCC_Heerle_Reaction%20Wheel%20Unit%20LR(1).pdf.

[24] L. Martin, "Rad6000 radiation hardened 32-bit processor," https://www.power.org/download_file.php?file=7733.

[25] J. Berner, "Deep Space Network Services Catalog," December 2014, DSN No. 820-100, Rev. F, Issue Date: JPL D-19002. Cited 12-05-2016 from: https://deepspace.jpl.nasa.gov/files/dsn/820-100%20F.pdf.

[26] D. K. Shin, "DSN Telecommunications Link Design Handbook: Frequency and Channel Assignments ," December 2014, DSN No. 810-005, Rev. E, part 201, Rev. C. Cited 12-05-2016 from: http://deepspace.jpl.nasa.gov/dsndocs/810-005/201/201C.pdf.

[27] W. J. Larson, J. R. Wertz, and J. J. Puschell, *Space Mission Engineering: The New SMAD*. Microcosm Press, Hawthorne, CA, United States of America, 2011.

[28] E. Stiller, "Small Deep-Space Transponder (SDST)," General Dynamics Advanced Information Systems, Cited 10-06-2016 from: https://gdmissionsystems.com/wp-content/uploads/2015/07/SDST_-_DS5-813-12.pdf.

[29] "Deep Space and Secure Transponders," Thales Alenia Space, 2012, Cited 10-06-2016 from: https://www.thalesgroup.com/sites/default/files/asset/document/Deep_Space_Secure_Transponders.pdf.

[30] J. Taylor, "Descanso design and performance summary series article 13: Dawn telecommunications," Jet Propulsion Laboratory, California Institute of Technology, August 2009, retrieved from: http://descanso.jpl.nasa.gov/DPSummary/090924dawn-FinalCorrex–update5G.pdf.

[31] R. S. Bokulic, M. K. E. Flaherty, J. R. Jensen, and T. R. McKnight, "The NEAR Spacecraft RF Telecommunications System," *Johns Hopkins Apl. Technical Digest*, vol. 19, no. 2, 1998, Available from: http://www.jhuapl.edu/techdigest/TD/td1902/bokulic.pdf.

[32] J. Verderame, "X-Band Solid-State Power Amplifier," General Dynamics Advanced Information Systems, Cited 11-06-2016 from: https://gdmissionsystems.com/wp-content/uploads/2015/07/17b-SSPA_Datasheet.pdf.

[33] "RF products - Diplexers," General Dynamics Advanced Information Systems, Cited 11-06-2016 from: http://www.gdsatcom.com/rfproducts_diplexers.php.

[34] "Satellite Mechanisms," RUAG Space, Cited 15-06-2016 from: http://www.ruag.com/space/products/satellite-structures-mechanisms-mechanical-equipment/satellite-mechanisms/.

[35] M. K. et al., "A Review: Comparative Studies on different generation solar cells technology," 2014, Cited 12-06-2016 from: http://benjapan.org/ICEAB/proceedingsICEAB14/i14%20p33.pdf.

[36] "Space Solar Cells," AZUR Space, Cited 12-06-2016 from: http://www.azurspace.com/index.php/en/products/products-space/space-solar-cells.

[37] W. J. Larson and J. R. Wertz, *Space Mission Analysis and Design*. Microcosm Press and Kluwer Academic Publishers, 1999.

[38] M. M., "An Overview of Solar Cell Technology," Stanford University, 2011, https://gcep.stanford.edu/pdfs/2wh9Q1Alh3q2zMOQRKD4MQ/MikeMcGehee_ SolarEnergy101.pdf.

[39] e. a. Corrigan D., "Nickel-Metal Hydride Batteries For ZEV-Range Hybrid Electric Vehicles," Ovonic Battery Company, http://www.rdrop.com/ev/hybrid.pdf.

[40] Arianespace, "Soyuz User's Manual Issue 2 Revision 0," March 2012, Cited 18-05-2016 from: http://www.arianespace.com/wp-content/uploads/2015/09/Soyuz-Users-Manual-March-2012.pdf.

[41] O. P. Popova *et al.*, "Chelyabinsk airburst, damage assessment, meteorite recovery, and characterization," *Science*, vol. 342, pp. 1069–1073, 2013.

[42] P. Chodas and R. Baalke, "Near Earth object program," National Aeronautics and Space Administration, Cited 8-05-2016 from: http://neo.jpl.nasa.gov/.

[43] M. van Amerongen *et al.*, "ARMADA - Baseline Review," Delft University of Technology, April 2016.

[44] E. J. O. Schrama, *Lecture notes on Planetary sciences and Satellite Data processing.* Delft University of Technology, Faculty of Aerospace Engineering, 2016.

[45] R. H. Gooding, "Procedure for the solution of lambert's orbital boundary-value problem," *Celestial Mechanics and Dynamical Astronomy*, vol. 48, pp. 145–165, 1990, doi:10.1007/BF00049511.

[46] M. F. van Amerongen *et al.*, "ARMADA - Mid-Term Review," Delft University of Technology, April 2016.

[47] E. T. Lu and S. G. Love, "Gravitational tractor for towing asteroids," *Nature*, vol. 438, pp. 177–178, November 2005, doi:10.1038/438177a.

[48] G. Mengali and A. A. Quarta, "Rapid Solar Sail Rendezvous Missions to Asteroid 99942 Apophis," *Journal of Spacecraft and Rockets*, vol. 46, no. 1, pp. 134–140, January-February 2009, doi: 10.2514/1.37141.

[49] D. Izzo and A. Rathke, "The asteroid deflection formula for Earth quasi co-orbiting asteroids," European Space Agency, Tech. Rep., 2006, aDFECA06, the Advanced Concepts Team, 2006, Cited 11-5-2016 from: http://www.esa.int/gsp/ACT/doc/MAD/pub/ACT-TNT-MAD-ADFECA06.pdf.

[50] B. Wie, "Dynamics and Control of Gravity tractor spacecraft for asteroid deflection," *Journal of Guidance, Control, and Dynamics*, vol. 31, no. 5, pp. 121–142, September 2008, doi:10.2514/1.32735.

[51] M. Krolikowska, G. Sitarski, and A. M. Soltan, "How selection and weighting of astronomic observations influence the the impact probability Asteroid (99942) Apophis case." *Monthly Notices of the Royal Astronomical Society*, vol. 399, pp. 1964–1976, November 2009, doi:10.1111/j.1365-2966.2009.15276.x.

[52] "Predicting Apophis' Earth Encounters in 2029 and 2036," NASA, Cited 23-05-2016 from: http://neo.jpl.nasa.gov/apophis/.

[53] P. Pravec *et al.*, "The tumbling spin state of (99942) apophis," *Icarus*, vol. 233, pp. 48–60, January 2014, doi:10.1016/j.icarus.2014.01.026.

[54] R. P. Binzel *et al.*, "Spectral properties and composition of potentially hazardous Asteroid (99942) Apophis," *Icarus*, vol. 200, no. 2, pp. 480–485, April 2009, doi:10.1016/j.icarus.2008.11.028.

[55] B. Zellner and D. J. Tholen, "The eight-color asteroid survey: Results for 589 minor planets," *Icarus*, vol. 61, pp. 355–416, November 1984, doi:10.1016/0019-1035(85)90133-2.

[56] H.Sierks *et al.*, "The dawn framing camera," *Space Science Reviews*, vol. 163, pp. 263–327, February 2011, doi:10.1007/s11214-011-9745-4 .

[57] M. Ishiguro *et al.*, "The hayabusa spacecraft asteroid multi-band imaging camera (amica)," *Icarus*, vol. 207, pp. 714–731, January 2010, doi:10.1016/j.icarus.2009.12.035 .

[58] H. U. Keller *et al.*, "Osiris-the scientific camera on-board rosetta," *Space science reviews*, vol. 128, pp. 433–506, November 2006, doi:10.1007/s11214-006-9128-4 .

[59] B. K. Agarwal, *X-ray spectroscopy - An introduction.* Springer-Verlag Berlin Heidelberg GmbH, 1991.

[60] L. B. N. Laboratory, "X-ray Data Booklet," Cited 30-05-2016 from: http://xdb.lbl.gov/.

[61] T. Okada *et al.*, "X-ray Fluorescence Spectrometry of Asteroid Itokawa by Hayabusa," pp. 1338–1341, June 2006, doi:10.1126/science.1125731.

[62] K. Shirai *et al.*, "Instrumentation and performance evaluation of the xrs on selene orbiter," *Earth Planets Space*, vol. 60, p. 277–281, April 2008, https://www.terrapub.co.jp/journals/EPS/pdf/2008/6004/60040277.pdf.

[63] C. P. S. Hsu, "Infrared Spectroscopy," Cited 07-06-2016 from: http://fp.okstate.edu/nanotech/Assignments/Readings/Char_Intro/reading%201.2%20ir-hsu.pdf.

[64] W. S. Goree and M. Fuller, "Magnetometers Using RF-Driven Squids and Their Applications in Rock Magnetism and Paleomagnetism," *Journal of Guidance, Control, and Dynamics*, vol. 14, no. 4, pp. 591–608, November 1976, doi10.1029/RG014i004p00591.

[65] M. D. Michelena, "Small Magnetic Sensors for Space Applications," *Sensors*, vol. 9, pp. 2271–2288, 2009, doi:10.3390/s90402271.

[66] D. Sheppard, "MAVEN Magnetometer Description and Interface Specification," NASA MAVEN-MAG-SPEC-0015, Revision D, November 2012, ftp://apollo.ssl.berkeley.edu/pub/MAVEN/Instruments/MAG/MAVEN-MAG-SPEC-0015%20Rev%20D%2009Nov2012.pdf.

[67] "MAVEN Magnetometer Description and Interface Specification," NASA Press Kit, November 2013, http://mars.nasa.gov/files/resources/MAVEN_PressKit_Final.pdf.

[68] D. Smith *et al.*, "The Lunar Orbiter Laser Altimeter Investigation on the Lunar Reconnaissance Orbiter Mission," 2008, Cited 18-06-2016 from: http://lunar.gsfc.nasa.gov/lola/images/smith_lola_ssr09.pdf.

[69] M. Dougherty *et al.*, "JUICE: exploring the emergence of habitable worlds around gas giants," ESA/SRE(2014)1, December 2011, Cited 7-06-2016 from:Dominic Dirkx.

[70] K. Lingenauber, *et al.*, "JUICE: exploring the emergence of habitable worlds around gas giants," International Workshop on Instrumentation for Planetary Missions, November 2014, Cited 7-06-2016 from:http://elib.dlr.de/94264/1/JUICE%20GALA%20-%20Design%20Overview%20v04.pdf.

[71] K. Muinonen, J. Piironen, Y. G. Shkuratov, A. Ovcharenko, and B. E. Clark, *Asteroid III*. University of Arizona Press, 2002.

[72] A. Cellino and S. Bagnulo, "Spectro-polarimetry as a potentially powerful tool for asteroid studies," INAF- Osservatorio Astrofisico di Torino, 2013.

[73] A. D. Bacher, "Polarimeter," University of California, Los Angeles. Cited 30-05-2016 from: http://www.chem.ucla.edu/ bacher/General/30BL/tips/Polarimetry.html.

[74] F. A. Carey, *Organic Chemistry, fourth edition*. The McGraw-Hill Companies, 2000.

[75] K. Optronic, "High-Speed Polarimeter Series – the fastest polarimeter worldwide," Cited 30-05-2016 from: http://www.kruess.com/laboratory/products/polarimeters.

[76] J. Rietjens, F. Snik *et al.*, "SPEX: The Spectropolarimeter For Planetary Exploration," October 2010, ftp://ftp.osupytheas.fr/pub/svives/ICSO/Papers/Session%207b/FCXNL-10A02-1983748-4-Rietjens_ICSO_Paper.pdf.

[77] W. Ley, K. Wittmann, and W. Hallmann, *Handbook of Space Technology*. John Wiley & Sons, Ltd, United Kingdom, 2009.

[78] P. Fortescue, G. Swinerd, and J. Stark, *Spacecraft Systems Engineering*. John Wiley & Sons, Ltd, Chichester, United Kingdom, 2011.

[79] B. Zandbergen, *Thermal rocket propulsion reader*. Delft University of Technology, Delft, 2016.

[80] A. Cervone, "AE3534-I Spacecraft Technology course lecture slides, lectures 5-6," Delft University of Technology, Faculty of Aerospace Engineering, 2015-2016.

[81] D. M. Goebel and I. Katz, *Fundamentals of Electric Propulsion: Ion and Hall Thrusters*. National Aeronautics and Space Administration Jet Propulsion Laboratory, California Institute of Technology, California, 2008.

[82] H. Kuninaka, "The potential of ion engines," japan Aerospace Exploration Agency, Cited 01-06-2016 from: http://global.jaxa.jp/article/special/hayabusa/kuninaka_e.html.

[83] E. Y. Choueiri, "New dawn for electric rockets," *Scientific American*, vol. 300, pp. 58–65, February 2009, doi:10.1038/scientificamerican0209-58.

[84] J. J. Lissauer and I. de Pater, *Fundamental Planetary Science, Physics, Chemistry and Habitability*. Cambridge university press, New York, United states of America, 2013.

[85] "In-Space Propulsion," Moog In-Space Propulsion, moog ISP, Cited 07-06-2016 from: http://www.moog.com/markets/space/in-space-propulsion.html.

[86] N. Grumman, "Northrop Grumman Aerospace Systems," Cited 07-06-2016 from: http://www.northropgrumman.com/AboutUs/BusinessSectors/AerospaceSystems/Pages/default.aspx.

[87] M. E. Sansaturio and O. Arratia, "Apophis: the Story Behind the Scenes," *Earth Moon Planet, Springer*, vol. 102, pp. 425–434, September 2007, doi: 10.1007/s11038-007-9165-3.

[88] A. Ketsdever, "MAE 5595: Space Mission Analysis course lecture slides, lecture 13," University of Colorado, Colorado Springs, 2015-2016.

[89] "Space Propulsion: Ion Propulsion Systems," Airbus Defence and Space, Cited 08-06-2016 from: http://www.space-propulsion.com/spacecraft-propulsion/ion-propulsion/.

[90] R. P. Welle, "Propellant Storage Considerationsfor Electric Propulsion," *22nd International Electric Propulsion Conference*, pp. 91–107, 1991, AIAA-91-2589.

[91] S. Technologies, "Sun Sensors for Satellites," Cited 07-06-2016 from: http://www.solar-mems.com/en/products/space.

[92] Sodern, "SCMOS Star Trackers: Hydra Family," Cited 07-06-2016 from: http://www.sodern.com/sites/en/ref/Star-Trackers-HYDRA_51.html.

[93] M. Blanke and M. B. Larsen, "Satellite Dynamics and Control in a Quaternion Formulation," http://orbit.dtu.dk/files/98594729/Satdyn_mb_2010f.pdf.

[94] J. Peraire and S. Widnal, " 3D Rigid Body Dynamics: Equations of Motion; Euler's Equations," http://ocw.mit.edu/courses/aeronautics-and-astronautics/16-07-dynamics-fall-2009/lecture-notes/MIT16_07F09_Lec28.pdf.

[95] L.-P. Chang, *On efficient wear leveling for large-scale flash-memory storage systems*. ACM, New York, NY, 2007.

[96] C. T. Russell *et al.*, "Dawn: A journey in space and time," *Planetary and Space Science*, vol. 73, pp. 341–365, January 2003, doi:10.1016/j.pss.2003.06.013.

[97] C. Russell, *The Dawn Mission to Minor Planets 4 Vesta and 1 Ceres*. Springer, 2012.

[98] L. W. Couch, *Digital and Analog Communication Systems*. Pearson Education, Harlow, United Kingdom, 2013.

[99] M. K. Simon, *Bandwidth-Efficient Digital Modulation with Application to Deep-Space Communications*. Jet Propulsion Laboratory, California Institute of Technology, 2001.

[100] J. H. Yuen, *Deep Space Telecommunication Systems Engineering*. JPL Publication 82-76, Jet Propulsion Laboratory, California Institute of Technology, 1983.

[101] C. Peirera, "Mechanisms of the Rosetta High Gain Antenna," in *Proc. 9th European Space Mechanisms & Tribology Symposium, Liege, 19-21 September 2001, ESA SP-480*, September 2001.

[102] T. W. Davies, "Fourier's law," *Thermopedia*, february 2011, http://dx.doi.org/10.1615/AtoZ.f.fourier_s_law.

[103] D. G. Gilmore *et al.*, *Spacecraft Thermal Control Handbook*. American Institute of Aeronautics and Astronautics, 2002.

[104] "Basotect," B6 group, http://b6tech.dk/uk/products-competencies/-basotect-foam.html.

[105] "AZ-93 White Thermal Control, Electrically Conductive Paint / Coating," AZ Technology, 2004, http://www.aztechnology.com/materials-coatings-AZ-93.html.

[106] "Thermally Efficient Deployable Radiators," Thermal Management Technologies, 2012, http://tmtsdl.com/forms/deployableRadiatorFactSheet.pdf.

[107] "Boeing-601," Forecast International, Cited 13-06-2016 from: https://www.forecastinternational.com/archive/disp_pdf.cfm?DACH_RECNO=306.

[108] N. Picciano, "Battery aging and characterization of nickel metal hydride and lead acid batteries," 2007, Cited 15-06-2016 from: https://kb.osu.edu/dspace/bitstream/handle/1811/25087/Picciano_Nicholas_Thesis_AgingCharacterizationofNiMHandLeadAcidBAtteries.pdf.

[109] "Nickel Metal Hydride (NiMH," Energizer, 2010, Cited 15-06-2016 from: http://data.energizer.com/PDFs/nickelmetalhydride_appman.pdf.

[110] J. Kopera, "Inside the Nickel Metal Hydride Battery," 2004, Cited 15-06-2016 from: http://www.cobasys.com/pdf/tutorial/inside_nimh_battery_technology.pdf.

[111] "The Rosetta Orbiter," ESA, 2014, http://www.esa.int/Our_Activities/Space_Science/Rosetta/The_Rosetta_orbiter.

[112] P. on Small Spacecraft Technology, *Technology for Small Spacecraft*. National Academic Press, 1994.

[113] T. J. Patrick, "Space environment and vacuum properties of spacecraft materials," *Vacuum*, pp. 351–357, 1981, Cited 31-05-2016 from:http://www.sciencedirect.com/science/article/pii/S0042207X81800425.

[114] J. Wijker, *Spacecraft Structures*. Springer, 2008, ISBN: 978-3-540-75552-4.

[115] A. S. Metals, "Aerospace Aluminium Distributor," Cited 01-06-2016 from: http://www.aerospacemetals.com/aluminum-distributor.html.

[116] B. S. . T. Association, "Properties of Pure Beryllium," Cited 01-06-2016 from: http://beryllium.eu/about-beryllium-and-beryllium-alloys/properties-of-beryllium/properties-of-pure-beryllium/.

[117] M. S. Online, "Alloy Steels D6AC," Cited 01-06-2016 from: http://www.suppliersonline.com/propertypages/D6AC.asp.

[118] C. Hanks and D. Hamman, *Radiation Effects Design Handbook*. NASA, 1971.

[119] "Metal Index," Argus Media Ltd., Cited 01-06-2016 from: https://www.metalprices.com/p/metal_index.

[120] R. Hibbeler, *Mechanics of Materials, 8th Edition*. Pearson Education, Inc, 2011.

[121] M. I. O. Technology, "Stresses: Beams In Bending," 2004, Cited 15-06-2016 from: http://ocw.mit.edu/courses/civil-and-environmental-engineering/1-050-solid-mechanics-fall-2004/readings/emech9_04.pdf.

[122] arianespace, "Soyuz users manual," March 2012, Cited 14-06-2016 from: http://www.arianespace.com/wp-content/uploads/2015/09/Soyuz-Users-Manual-March-2012.pdf.

[123] D. D. J. Smith, *Reliability, Maintainability and Risk, 6th Edition*. Butterworth-Heinemann, Jordan Hill, Oxford, 2001.

[124] "Reliability, multi-state failures and survivability of spacecraft and space-based networks," Thermal Management Technologies, 2012, https://smartech.gatech.edu/bitstream/handle/1853/45871/castet_jeanfrancois_201212_phd.pdf.

[125] D. E. Koelle, *Handbook of Cost Engineering for Space Transportation Systems with TRANSCOST 7.0*. TCS-TransCostSystems, November 2000.

[126] "Space Project Management - Project Phasing and Planning," ECSS–M–30A, ESA Publications Division, Noordwijk, The Netherlands, April 1996.

[127] "NPR 7120.5, NASA Space Flight Program and Project Management Handbook," NASA, Cited 13-06-2016 from: http://www.nasa.gov/pdf/423715main_NPR_7120-5_HB_FINAL-02-25-10.pdf.

[128] "Rosetta - Mission Operations," European Space Agency, July 2015, Cited 19-05-2016 from: http://sci.esa.int/rosetta/2276-mission-operations/.

[129] J. González, M. Belló, J. Martín-Albo, and A. Gálvez, "Don quijote: An esa mission for the assessment of the neo threat," *International Astronautical Congress, IAC-04-Q.P.21*, October 2010.

[130] ESA, "Call for ideas: Neo encounter 2029," Cited 16-06-2016 from: http://emits.sso.esa.int/emits-doc/ESTEC/AO-1-5680-AnnexC-SOW-Study-Description.pdf.

[131] *Overview of Mission Design for NASA Asteroid Redirect Robotic Mission Concept*. 33rd International Electric Propulsion Conference, The George Washington University, October 2010.

[132] A. Cheng *et al.*, "Asteroid impact and deflection assessment mission," *Acta Astronautica*, vol. 115, p. 262–269, October–November 2015.

[133] NASA, "Fy 2017 budget estimates," 2016, Cited 16-06-2016 from: http://www.nasa.gov/sites/default/files/atoms/files/fy_2017_budget_estimates.pdf.

[134] H. Yano *et al.*, "Touchdown of the hayabusa spacecraft at the muses sea on itokawa," *Science*, vol. 312, no. 5778, pp. 1350–1353, June 2006.

[135] *Japan's future plans for missions to primitive bodies: Hayabusa-2, Hayabusa-mk2, and Marco Polo*. 39th Lunar and Planetary Science Conference, held March 10-14, 2008 in League City, Texas. LPI Contribution No. 1391., p.1747, March 2008.

A. Work distribution

The students names are abbreviated with numbers as follows. M.F. van Amerongen (S1), J. Anckaert (S2), P.M. van den Berg (S3), J.M. Fisser (S4), J.M. Heywood (S5), A. Hutan (S6), T.A.J. Meslin (S7), U.B. Mukhtar (S8), A.S. Parkash (S9), J. Ramos de la Rosa (S10).
The work packages are presented in bold font and italic fonts, the latter is for subdividing the packages. The bold font work packages are then the totals if there are subdivisions. The mentioned hours include writing, in addition to the time spent obtaining the findings and results. The 192 hours per person stand for the time from the mid-term until handing in the final report, or 24 days of 8 hours.

Table A.1: Work distribution final report

Work package	Time	**S1**	**S2**	**S3**	**S4**	**S5**	**S6**	**S7**	**S8**	**S9**	**S10**
Introduction			5								
Mission Overview					1		6				
Mission timeline					1		1				
Functional analysis							5				
Astrodynamics				14	88					16	
Model of the solar system					10						
Trajectory				9	10					8	
Results					60						
Verification of results					8						
Launcher Selection				5						3	
Gravity tractor				15						50	
Fundamental concept										15	
Gravity tractor mass estimation				10						20	
Gravity tractor deflection distance				5						15	
Scientific Payload			40			32	40				42
Scientific Objectives			10			16	10				
Scientific Instruments			30			16	25				30
Mass & Power budget							5				12
Propulsion & Orbit control				108						56	
Requirements and constraints				1						2	
Thruster type trade-off				10						15	
Propulsion system sizing methodology				50						19	
Verification				5						5	
Thruster selection				10						5	
Propulsion system sizing results				33						10	
Propulsion system layout				4							
Attitude Determination and Control			83			16	40				47
Introduction			2								
ADCS sizing method			28			16	20				25
Actuator and sensor sizing results			8				20				22
ADCS sizing assessment and conclusion			5								
Attitude model			40								
Command & Data Handling			25			16	45				46
C&DH sizing method			18			16	20				25
Results			5				20				21
Conclusion			2				5				
Communications					60						15
Requirements and constraints					2						
Telemetry and Command of the spacecraft					10						
Tracking the spacecraft					2						
Chosen characteristics					15						
Link budgets					15						
Subsystem components selection					10						
Antenna sizing											15
Integration into spacecraft					4						
Conclusion					2						
Thermal Control System		16						120	8		
Requirements		4						10	4		
Inputs/Outputs		4						7	4		
Method		8						80			
Results								11			
Conclusion								2			
Verification and validation								10			

Work package	Time	S1	S2	S3	S4	S5	S6	S7	S8	S9	S10
Electrical Power System		118						18	16		
Requirements		10						4			
Power system architecture		36						2			
Power system model		72						12	16		
Spacecraft Structure		30						15	142		
Requirements		4						5	6		
Material Selection		18							8		
Structural Analysis		8						5	30		
Sizing The Structure									30		
Vibrational Analysis									58		
Verification & Validation								5	10		
Spacecraft configuration				8		24					
Catia Model				8		24		22			
Layout optimization						70		2		10	
Design analysis			4	10					2		20
Risk management					10						
Reliablility, Availability, Maintainability & Safety											20
Sustainable development								5			
Sensitivity Analysis				10							
Compliance & Feasibility			4						2		
Resource Allocation				5						25	
Mission budgets				5							
Cost estimation										25	
Future Activities			10	10			24			15	10
Planning of future activities					10						
Verification & Validation			10								
Production							12				5
Operations and logistics							12				5
Market Analysis				10						15	
Conclusion and recommendations			2						8		
Jury summary				4							
Poster				4		4	7				
Executive summary			3				5				
Quality control		26	20	14	22	25	25	10	16	20	12
Total	1920	192	192	192	192	192	192	192	192	192	192